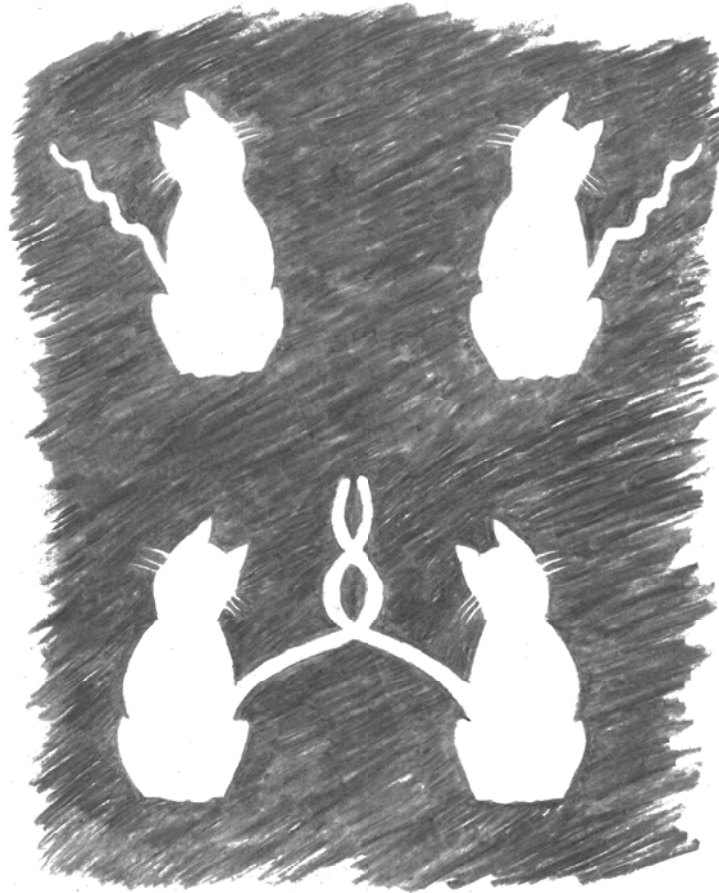


Quantum properties of nanostructured semiconductors: Spin-orbit, entanglement and valley physics



by

José Carlos García-Abadillo Uriel

Memoria presentada para optar
al grado de Doctor en Ciencias Físicas

UNIVERSIDAD AUTÓNOMA DE MADRID

Directora: María José Calderón Prieto
Instituto de Ciencia de Materiales de Madrid, CSIC

Madrid, Jan 2018

We are trying to prove ourselves wrong as quickly as possible, because only in that way can we find progress.

Richard Feynman

Acknowledgements

En primer lugar quiero agradecer a María José Calderón por acogerme desde el primer día y darme la oportunidad de escribir la tesis. Agradezco su apoyo, buenas ideas y paciencia sobrenatural a lo largo de estos años, en especial estas últimas vacaciones de Navidad con la escritura de la tesis, los procesos burocráticos y demás pesadillas navideñas.

Gracias también a mi familia. A mis abuelos, a mis hermanas y, particularmente, a mis padres, sin los que no habría llegado hasta aquí.

Of course, I'd like to thank all my collaborators, without them this thesis would not be the same: Joe, Belita, Dimi, Sven, Xuedong, Mark Friesen, Mark Eriksson and Sue Coppersmith. Also those who were there, during my stays abroad: Adam, Cameron, Richard, Brandur, Yuan-Chi, Ekmel, Guilherme.

No puedo dejar sin mencionar a los colegas del ICMM que han amenizado todo el largo proceso de la tesis: Robert, Sigmund, Fernando, Leandro, Guillem, Álvaro, Mónica, Jorge, Yago, Jordi, Bea, Chema, Miguel, Yue, Jesús y alguno mas que me olvidaré. Mención especial a los colegas del fútbol: Roberto, Rafa, Jorge... sin ellos ahora sería obeso y/o tendría 90 pulsaciones en reposo.

Debo, además, reconocer el impacto de mis musas en mi trabajo: Gracias Gabi (GabiStark), Peluco (chega826) y Camilo (krestakaa). Sin olvidar por supuesto a grandes como Pablo (eres el siguiente) y Mario Increliche.

Finalmente, quiero dar las gracias a Inma por haberme sufrido todos estos años, particularmente los últimos días de escribir la tesis, en los que apenas he cocinado y he convertido al gato en un adicto al juego. Mención especial al dibujo que me has hecho para la portada.

Para Inma.

Quantum properties of nanostructured semiconductors: Spin-orbit, entanglement and valley physics

by

José Carlos García-Abadillo Uriel

Abstract

Silicon is the most important semiconducting material, being present in all the electronic devices around us. Silicon has also drawn attention for its very interesting properties for the construction of a scalable quantum computer which, at the same time, would be compatible with classical devices. Among these properties, its extraordinary quantum coherence, due to the negligible spin-orbit interaction for electrons and the ability to get rid of nuclear spins by isotopic purification, stands out. However, quantum state manipulation requires the application of oscillating magnetic fields and, often, localized magnetic fields which require too much power while being experimentally challenging. Besides, the original proposals for entanglement protocols impose complex restrictions to the devices, which are technologically challenging.

In this thesis, alternatives for quantum computation in semiconductors are proposed. The first of these alternatives is the use of hole bound states instead of electron states. Holes bound to acceptors in Silicon are inherently susceptible to the spin-orbit interaction, which allows the possibility to define an electrically manipulable quantum bit (qubit), potentially much more efficient than magnetic field manipulation. At the same time, it paves the way for new possibilities to generate entanglement between qubits. The effects of spin-orbit interactions on the qubit coherence will also be addressed.

When electrons are considered, the degenerate minima (valleys) in the conduction band add a new degree of freedom which has to be taken into account. In this thesis, the valley physics of quantum dot bound states is analyzed in two different geometries. These states also allow the interaction with electric fields, simplifying the scalability. In exchange, the coherence properties can be affected. The valley degree of freedom is affected by the nanostructure confinement and electric fields, which gives a particular flexibility that can be used to improve the coherence properties.

Finally, the use of two dimensional materials will be proposed as another alternative. Two dimensional materials are being studied for their many interesting properties and potential applications. We explore the feasibility of using dopants in these materials to define qubits.

Keywords: Qubit, holes, spin-orbit, entanglement, magic angles, confinement, valley physics, electrical manipulation, 2D materials

Propiedades cuánticas de semiconductores nanoestructurados: Espín-órbita, entrelazamiento y física de valles

por

José Carlos García-Abadillo Uriel

Resumen

El Silicio es el material semiconductor mas importante, estando presente en todos los aparatos electronicos que nos rodean. El Silicio también ha llamado la atención por tener propiedades interesantes para la construcción de un ordenador cuántico escalable y compatible con dispositivos clásicos. Entre estas propiedades, destacarían sus extraordinarias propiedades de coherencia cuántica debidas a una interacción espín-órbita despreciable para electrones y la posibilidad de purificar isotópicamente. Sin embargo, la manipulación de los estados cuánticos requiere aplicar campos magnéticos oscilantes y, en muchos casos, localizados, lo que requiere mucha energía y es experimentalmente muy complicado. Además los protocolos de entrelazamiento propuestos inicialmente imponen restricciones muy complicadas de superar tecnológicamente.

En esta tesis se proponen alternativas para la computación cuántica en semiconductores. La primera de estas alternativas es el uso de estados ligados de huecos en lugar de electrones. Los huecos ligados a aceptores en Silicio son inherentemente susceptibles a la interacción espín-órbita, lo que permitiría la posibilidad de definir un qubit manipulable con campos eléctricos, potencialmente mucho mas eficientes que campos magnéticos. A su vez, abre nuevas posibilidades para generar entrelazamiento entre qubits. Se discutirán también los efectos de espín-órbita en la coherencia de los qubits.

Se analizan también de la física de valles en estados ligados a puntos cuánticos en distintas geometrías. Estos estados también permiten la interacción con campos eléctricos, facilitando la escalabilidad. A cambio, las propiedades de coherencia se ven afectadas. Sin embargo, la complejidad de la banda de conducción en Si añade un nuevo grado de libertad: los valles. Este grado de libertad es influenciado por el confinamiento en la nanoestructura, así como campos eléctricos, lo que le da cierta flexibilidad que se podrá utilizar para mejorar las propiedades de coherencia.

Finalmente, se propondrá el uso de semiconductores en dos dimensiones como alternativa. Este tipo de materiales han sido estudiados recientemente, demostrando propiedades cuánticas muy interesantes. Exploramos la posibilidad de usar estados ligados a dopantes en estos materiales para definir qubits.

Palabras clave: Qubit, huecos, espín-órbita, entrelazamiento, ángulos mágicos, física de valles, manipulación eléctrica, materiales 2D

Contents

Abstract	vi
Resumen	vii
List of Figures	xiii
Abbreviations	xvi
1 General Introduction	1
1.1 Quantum computation	1
1.2 Semiconductor based quantum computing	3
1.2.1 Basic electronic properties of Si	4
1.2.2 Kane Quantum Computer	5
1.2.3 Loss-DiVincenzo Quantum Computer	7
1.3 State of the art	9
1.3.1 Dopants	9
1.3.2 Quantum dots	11
1.4 Theoretical description	14
1.4.1 Effective mass theory	14
1.4.2 Kohn-Luttinger Hamiltonian	16
1.4.3 Tight-Binding methods	17
1.5 This thesis	18
1.5.1 Part I: Acceptor bound states	19
1.5.2 Part II: Quantum dots	19
1.5.3 Part III: 2D materials	20
I Acceptor bound states	21
2 Confinement effects on acceptor levels	22
2.1 Introduction	22
2.2 Confined acceptors Hamiltonian	25
2.2.1 Selection rules and effective mass model	27
2.2.2 Application to hard wall interfaces	28
2.2.2.1 Variational method	28

2.2.3	Application to SiGe quantum wells	29
2.2.3.1	Variational method for quantum wells	31
2.3	Central cell corrections	32
2.4	Interface effects on the spectrum	33
2.5	Hard wall effective Hamiltonian	35
2.5.1	HH-LH splitting	38
2.5.2	Dipolar coupling p	39
2.5.3	Rashba coefficient	40
2.6	Confinement and strain effects on acceptors in quantum wells	41
2.7	Effective low energy Hamiltonian for SiGe quantum wells	42
2.7.1	HH-LH splitting	43
2.7.2	g -factor	45
2.7.3	Dipolar coupling p	46
2.7.4	Rashba coefficient	46
2.8	Conclusions	47
3	Qubit manipulation in SiGe quantum wells	49
3.1	Introduction	49
3.2	Heavy-hole based qubit	51
3.2.1	Electron Spin Resonance	52
3.2.2	Electric Dipole Spin Resonance	53
3.2.3	g -Tensor Modulation Resonance	54
3.3	Light-hole based qubit	55
3.3.1	Convex LH qubit	57
3.3.2	Concave LH qubit	58
3.4	Decoherence processes	59
3.5	Conclusions	61
4	Full tunability, coherence and entanglement of acceptors near an interface	63
4.1	Introduction	63
4.2	Qubit basis	64
4.3	In-plane anisotropy	68
4.3.1	Sweet spots	69
4.3.2	Induced spin-polarization	70
4.4	Manipulability: EDSR	72
4.5	Coherence	74
4.5.1	Charge noise	74
4.5.2	Phonon-induced relaxation	76
4.5.3	Decoherence Free Subspace	77
4.6	Two-qubit coupling: Entanglement	79
4.6.1	Magic angles	82
4.6.2	Protocol 1	83
4.6.3	Protocol 2	83
4.7	Discussion: Experimental implications	84
4.7.1	Single-qubit operations	84
4.7.2	Entanglement	86

4.8	Conclusions	87
II	Quantum dots	88
5	Disorder effects on Tunneling and Valley physics in Si Double Quantum Dots.	89
5.1	Introduction	89
5.2	Tight binding model	91
5.2.1	Valley degree of freedom	92
5.2.2	Confinement and fields	92
5.2.3	Disordered interface	93
5.3	Effective Hamiltonian	93
5.4	Vertical electric field effects	94
5.4.1	Intervalley Tunneling	95
5.4.2	Valley splitting	96
5.5	Detuning effects	96
5.5.1	Intervalley Tunneling	97
5.5.2	Valley splitting	98
5.6	Comparison with experiments	98
5.6.1	Typical behavior	99
5.6.2	Hotspot behavior	100
5.6.3	Sweet spot behavior	101
5.7	Conclusions	103
6	Valley physics of corner dots in Si nanowires.	104
6.1	Introduction	104
6.2	Nanowire simulations	105
6.2.1	Gate voltages	107
6.2.1.1	Analytical approximation	107
6.2.2	Corner angles	108
6.2.2.1	Adding angles to the analytical expression	109
6.2.3	Split gates	109
6.2.3.1	Analytical expression for the split gates	110
6.3	Valley splitting in the EMA	110
6.4	Valley splitting in TB simulations	113
6.5	Conclusions	116
III	2D materials	118
7	Dopants in 2D materials for Quantum Computing.	119
7.1	Introduction	119
7.2	Effective mass method	120
7.2.1	Hydrogen atom: H	121
7.2.2	Hydrogen ion: H ⁻	121
7.2.3	Hydrogen molecule ion: H ₂ ⁺	122
7.2.4	Hydrogen molecule: H ₂	124

7.2.4.1	Binding energies	126
7.2.4.2	Bohr radius	126
7.3	Parameters of 2D materials	126
7.4	Application to quantum computing	129
7.5	Conclusions	130
8	Conclusions	132
9	Conclusiones	135
	Appendices	138
A	Relevant integrals for Chapter 2	139
B	Schrieffer-Wolff transformation	141
	References	143

List of Figures

1.1	Representation of the Bloch sphere.	2
1.2	Silicon unit cell.	4
1.3	Silicon band structure.	4
1.4	Valley ellipsoids in Si.	5
1.5	Scheme of the valence band.	5
1.6	Scheme of Kane’s quantum computer.	6
1.7	Sketch of Loss and DiVincenzo’s quantum computer	8
1.8	Cartoon of the nuclear spin-bath in GaAs.	9
1.9	Hybrid qubit double quantum dot device, and its energy level diagram. . . .	13
1.10	Cross section of the Nanowire Field Effect Transistor.	14
2.1	Hard wall and quantum well geometries.	23
2.2	Valence subbands.	24
2.3	Linear g-factor as a function of Ge composition.	29
2.4	Energy spectrum of an acceptor in Si near an interface.	33
2.5	Spectrum of an acceptor near an interface in Ge, and ground state splittings. .	34
2.6	Wavefunctions of a hole bound to an acceptor near an interface.	36
2.7	Ground state splitting of an acceptor as a function of the electric field.	38
2.8	Dipolar coupling p as a function of the vertical electric field.	39
2.9	Rashba coefficient α as a function of the electric field.	40
2.10	Acceptor energy levels in a quantum well for different positions.	41
2.11	Ground state splitting of an acceptor in a quantum well as a function of different parameters for a heavy-hole ground state.	44
2.12	Ground state splitting of an acceptor in a quantum well as a function of different parameters for a light-hole ground state.	45
2.13	Effective g-factor of a heavy-hole ground state in a quantum well as a function of different parameters.	45
2.14	Dipolar coupling p of a hole state in a quantum well as a function of different parameters.	46
2.15	Rashba coupling α of a heavy-hole ground state in a quantum well as a function of different parameters.	47
3.1	Sketch of the quantum well heterostructure and the bound hole envelope wave- function.	50
3.2	Electron Spin Resonance Rabi frequency of a heavy-hole ground state as a function of different parameters.	52

3.3	Electric Dipole Spin Resonance Rabi frequency of a heavy-hole ground state as a function of different parameters.	53
3.4	g-Tensor Modulation Resonance Rabi frequency of a heavy-hole ground state as a function of different parameters.	54
3.5	Level scheme of a light-hole based qubit.	55
3.6	Larmor frequency and Electric Dipole Spin Resonance Rabi frequency of a convex light-hole ground state as a function of the electric field.	58
3.7	Larmor frequency and Electric Dipole Spin Resonance Rabi frequency of a concave light-hole ground state as a function of the electric field.	58
3.8	Relaxation and coherence times of a heavy-hole based qubit.	59
4.1	Sketch of the device geometry of an acceptor qubit near an interface.	64
4.2	Eigenenergies and Larmor frequency of a light-hole qubit as a function of the vertical electric field.	65
4.3	Eigenenergies and Larmor frequency of a light-hole qubit for a magnetic field not aligned with the main crystal axes.	69
4.4	Value of the electric field for the anisotropic sweet spot.	70
4.5	Movie of the upper branch effective spin polarization as a function of ϕ and the electric field.	71
4.6	Polar plot of the effective g -factor of a light-hole qubit.	72
4.7	Estimate of dephasing due to second order charge noise for a light-hole qubit near an interface.	76
4.8	Estimate of the relaxation times as a function of ϕ for a light-hole qubit near an interface.	77
4.9	Angular distribution of the entanglement coupling as a function of ϕ for two light-hole qubits near an interface.	82
4.10	Movie of the two-qubit coupling angular distribution as a function of the magnetic field orientation.	83
4.11	Schemes of the two proposed entanglement protocols.	84
4.12	Number of single qubit operations per qubit lifetime as a function of ϕ for a light-hole acceptor.	85
4.13	Charge noise exposure during the entanglement protocols during the adiabatic swept.	87
5.1	Scanning electron microscope image of the double dot device, and scheme of the theoretical model.	90
5.2	Schematic representation of the tight binding model.	91
5.3	Energy diagram of the double-dot lowest states obtained from the tight binding simulations.	93
5.4	Tunnel couplings and valley splitting in a disordered nanostructure as a function of the vertical field.	95
5.5	Example of a valley-orbit effect.	96
5.6	Experimentally measured qubit frequency of a double dot hybrid qubit, and simulated qubit frequencies of the tight binding model.	97
5.7	Tunnel couplings and valley splitting in a disordered double dot device as a function of detuning.	97
5.8	Experiment vs theory comparison of a typical case as a function of detuning, showing qubit frequency and center of mass.	99
5.9	Wavefunctions of the lowest valley states in the typical case.	100

5.10	Experiment vs theory comparison of a hotspot behavior as a function of detuning, showing qubit frequency and center of mass.	101
5.11	Wavefunctions of the lowest valley states in the hotspot case.	101
5.12	Experiment vs theory comparison of a sweet spot behavior as a function of detuning, showing qubit frequency and center of mass.	102
5.13	Wavefunctions of the lowest valley states in the sweet spot case.	102
6.1	Sketch of the Nanowire Field Effect Transistor.	105
6.2	Discretized nanowire geometry simulated in the finite difference software COM-SOL.	106
6.3	Gate voltage distribution in a cross section with the single and back gates. . .	107
6.4	Gate voltage distribution in a cross section with the single and back gates with non right angles.	109
6.5	Gate voltage distribution in a cross section with the split and back gates. . .	110
6.6	Corner state energies under the effective mass approximation as a function of the angle.	111
6.7	Valley splitting of the corner states as a function of the angle.	112
6.8	Corner state valley splitting as a function of different gate voltages.	113
6.9	Corner state wavefunctions obtained in the tight-binding simulations.	114
6.10	Corner state energies obtained in the tight binding simulations as a function of the angle.	115
6.11	Corner state valley splitting in the tight binding simulations as a function of the angle.	116
6.12	Corner state valley splitting in the tight binding simulations as a function of different gate voltages.	116
7.1	Dopant placed in a 2D Silicene layer.	119
7.2	Energy of the 2D hydrogen molecule ion in the effective mass approximation as a function of R	122
7.3	Energy of the four lowest molecular states in the effective mass approximation as a function of R	124
7.4	Bohr radius of the two electrons in the lowest molecular states at large R . . .	124
7.5	Critical value of ϵ for the validity of the effective mass approximation when considering a single donor atom.	127
7.6	Critical value of ϵ for the validity of the effective mass approximation when considering a double donor molecule.	128
7.7	Exchange interaction as a function of R	129

Abbreviations

0D	0-Dimensional
1D	1-Dimensional
2D	2-Dimensional
3D	3-Dimensional
AC	Alternating Current
BOX	Buried Oxide
CMOS	Complementary Metal-Oxide-Semiconductor
COM	Center Of Mass
cQED	cavity Quantum Electrodynamics
DC	Direct Current
DFS	Decoherence Free Subspace
EDSR	Electric Dipole Spin Resonance
EMA	Effective Mass Approximation
EMT	Effective Mass Theory
ESR	Electron Spin Resonance
FET	Field Effect Transistor
FinFET	Fin Field Effect Transistor
GS	Ground State
g-TMR	g-Tensor Modulation Resonance
HH	Heavy-Hole
LH	Light-Hole
MOS	Metal-Oxide-Semiconductor
MOSFET	Metal-Oxide-Semiconductor Field Effect Transistor
NMR	Nuclear Magnetic Resonance
NWFET	Nanowire Field Effect Transistor
QDHQ	Quantum Dot Hybrid Qubit
qubit	Quantum bit
SET	Single Electron Transistor
SOC	Spin Orbit Coupling
SOI	Spin Orbit Interaction
STM	Scanning Tunneling Microscopy
SW	Schrieffer Wolff
TB	Tight Binding
TLS	Two Level System

General Introduction

1.1 Quantum computation

Since the development of the metal-oxide-semiconductor field effect transistor (MOSFET) in the late fifties [1], silicon (Si) has become the most important semiconductor material, leading the digital and electronics revolution of the 20th century. In this period the development of the semiconductor industry has followed with great accuracy Moore's law which states that every two years the number of transistors in a single wafer is doubled [2]. These transistors are used to encode the information of computers in bits with electrical signals, and calculations our computers make are performed by applying logic gates to these bits.

Nowadays, Moore's law is still alive and both server and high-end graphics cards processors contain around 20 billions of transistors, which is more than the double of the global population, being the size of the node of 14 nm [3]. In 2018 both Intel and AMD expect to commercialize transistors of 7 nm, but the shrinking of transistors has an expiration date. Once the transistor dimensions start to go below 5 nm the semiclassical approximation used to describe this devices will start to fail, and other quantum mechanisms such as tunneling or entanglement will become relevant, dramatically affecting the reproducibility of the electrical properties from device to device [4].

When the laws of quantum mechanics become relevant, we can reconsider how to cipher the information in quantum bits (qubits) which, instead of simply encoding the information in two classical values 0 and 1, would store the information in two possible quantum states $|0\rangle$ and $|1\rangle$ [5–7]. These two states can be built from any quantum two level system (TLS), which in practice requires the existence of a ground and excited state separated from higher excited states such that the latter can be considered irrelevant states. This construction can be extremely powerful since a classical bit can only take two possible values while the quantum states of a qubit can be written as the general expression

$$|\psi\rangle = \cos\theta|0\rangle + e^{i\phi}\sin\theta|1\rangle . \quad (1.1)$$

This means that a qubit can encode any quantum superposition of the two classical states in the Bloch sphere characterized by the phases ϕ and θ [8], see Fig. 1.1.

Quantum computers also allow the possibility of addressing some problems that are intractable with classical computers. The most known example is the prime factorization of

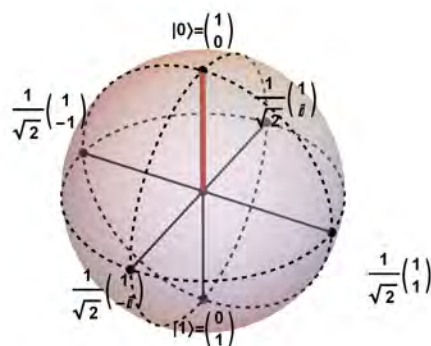


FIGURE 1.1: Bloch sphere representing the state of a qubit. The qubit can take any value in the surface of the sphere, including any superposition of the two allowed classical states 0 and 1.

large numbers: with the current classical algorithms this problem can not be solved in polynomial time, particularly for prime numbers used in classical cryptography such as the RSA algorithm [9] the decryption with classical algorithms would require more time than the age of the universe. However, Shor's quantum algorithm could solve this type of problems in polynomial time, eventually breaking the most reliable classical algorithms for cryptography [10]. At the same time, several schemes for quantum cryptography have been developed [11, 12]. This kind of algorithms would theoretically be unbreakable due to the no-cloning theorem of quantum mechanics [13]. Speed up of database searching would also be possible due to Grover's algorithm [14].

A more interesting application for scientists would be the possibility of performing quantum simulations [15]. Since a quantum computer obeys the laws of quantum mechanics, its efficiency simulating specific quantum systems would be overwhelming in comparison to their classical counterparts. Quantum simulators could help in the calculation of complex molecules, with applications on material science, biology and medicine among many others [16, 17]. Constructions with several qubits have already been successfully built to simulate the 2D Ising model, magnetism frustration and quantum magnets, among others [18–20].

However, the construction of a quantum computer is a herculean task. A quantum computer not only needs to be able to manipulate each qubit individually with high precision but it also must beat the decoherence of the quantum states due to the interaction with the environment. In 2000 D. P. DiVincenzo proposed the criteria that an experimental device must satisfy in order to efficiently work as a working quantum computer [21]. These criteria consists of five conditions. (1) **Scalability** is the capacity of a system to accommodate as many qubits as possible: a quantum computer must be able to store and manipulate hundreds or thousands of qubits. (2) **Initialization** is the capacity of a quantum computer to initialize each qubit to a reference state. (3) It would also need a **universal** set of gates, meaning that the quantum computer must be able of manipulating the qubits with a set of gates such that every quantum operation can be performed. In general, this requires the ability to perform both single- and two-qubit operations in any qubit pair. For single qubit operations, it is enough with implementing Pauli operators σ_x , σ_y , σ_z , and the Hadamard gate (U_H). Two-qubit operations, require the implementation of the quantum controlled

NOT (U_{CNOT}), that changes the second qubit depending on the first qubit state:

$$U_H = \frac{1}{\sqrt{2}} \begin{pmatrix} 1 & 1 \\ 1 & -1 \end{pmatrix} \quad (1.2)$$

$$U_{CNOT} = \begin{pmatrix} 1 & 0 & 0 & 0 \\ 0 & 1 & 0 & 0 \\ 0 & 0 & 0 & 1 \\ 0 & 0 & 1 & 0 \end{pmatrix} \quad (1.3)$$

(4) **Long coherence times**, which means that the quantum states must endure decoherence and relaxation processes long enough to allow for a sufficiently large number of operations such that quantum error algorithms can be applied. (5) **Qubit specific measurement**, which means that each qubit can be measured at any time during the execution of a quantum algorithm. These criteria is often extended with two more conditions for quantum communications: (6) The ability to take the quantum computer qubits to **interconvert stationary and flying qubits**. (7) These flying qubits would also need the ability to be **transmitted** to other quantum computing devices.

The physical realization of a quantum computer that fits into DiVincenzo's criteria has led to several possible implementations in the scientific community. Some of the most known examples are: (I) trapped ions, where the qubit is encoded in the states of ions confined by electromagnetic fields [22]. (II) Nitrogen-vacancy centers in diamond (N-V centers), where the spins can be addressed by using optical transitions [23]. (III) Superconducting circuits, where the information can be encoded in the charge, phase or flux degrees of freedom [24]. (IV) Topological quantum computation [25], where the degrees of freedom of anyonic systems are used to define the qubit. (V) Semiconductor quantum devices, where the qubit is often defined in the charge or spin degrees of freedom [26, 27]. This last platform is the one that will be treated in this thesis, particularly silicon based quantum devices.

In Si, qubits can be constructed with the different degrees of freedom of electrons or holes confined to dopants or quantum dots [28]. Each approach could be suitable for satisfying DiVincenzo's criteria, mainly due to the extraordinary coherence times in this material and its compatibility with the current semiconductor microelectronics.

1.2 Semiconductor based quantum computing

Semiconducting quantum devices can take advantage of the current fabrication technology for microelectronics. There is a powerful industry behind that makes this field grow rapidly. In the quantum limit, however, semiconductor devices present too many degrees of freedom hence its applicability to quantum computing devices is not trivial. The most widely investigated semiconducting materials for quantum computation are Si and GaAs. GaAs devices grew rapidly due to the maturity of its lithographically design quantum dots while Si has overall better coherence properties due to the presence of zero nuclear spin isotopes. The fast growth of GaAs slowed down due to the short coherence times and, nowadays, quantum control over Si devices is almost at the same level. However, Si also presents a more complex bandstructure that gives rise to certain electronic properties that need to be considered.

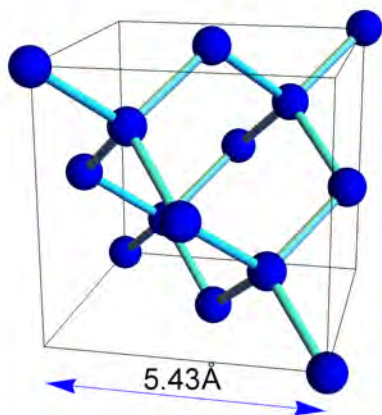


FIGURE 1.2: Silicon unit cell. The lattice constant is 0.543 nm.

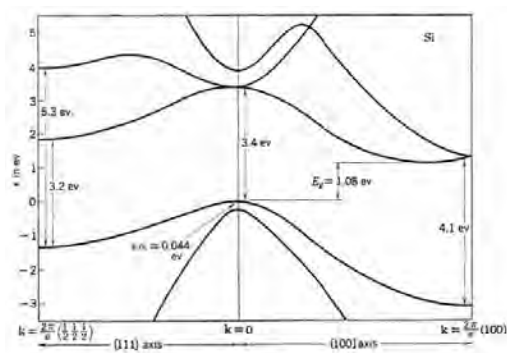


FIGURE 1.3: Silicon band structure. From [29].

1.2.1 Basic electronic properties of Si

Before getting into details of the most known proposals and the state of the art in the field, it is convenient to enumerate some basic electronics properties of Si. This way, the advantages and disadvantages of the different proposals will be easier to understand.

As shown in Fig. 1.2 Si has a diamond structure with lattice constant $a = 0.543$ nm [30]. Each atom has four nearest neighbors and since it is part of the group IV of semiconductors, it has four valence electrons. The group symmetry of this lattice is the cubic group O_h . Once a silicon atom is replaced by a group III atom, this atom adds an extra hole, behaving as an acceptor. On the other hand, if replacement is made with a group V atom, this new atom donates an extra electron, becoming a donor. Independently of which of these two types of dopant atoms we add to our system, from Fig. 1.2 it can be deduced that the symmetry is locally reduced to the tetrahedral symmetry T_d .

Important properties of both electrons and holes in Si can be deduced from the band structure in Fig. 1.3. Si has an indirect gap, with the maximum of the valence band at Γ but the minimum of the conduction band close to the zone boundary in the crystallographic (100) directions. This implies that there are six equivalent conduction band minima, named valleys. In these valleys the effective mass of the electron is anisotropic, with different longitudinal and transverse effective masses. This is represented by the conduction band ellipsoids in Fig. 1.4.

The valence band in Si does have its maximum at the Γ point, hence holes avoid the valley degeneracy. However, there is still a four-fold degeneracy at the top of the valence band due to the confluence of the light-hole (LH) and heavy-hole (HH) bands [31], named accordingly to their effective masses. There is another band, the split-off band, separated by the spin-orbit coupling (44 meV in Si). In comparison, the binding energy of a boron acceptor in Si is 45 meV, meaning that the spin-orbit interaction in the valence band of Si is a very relevant interaction.

Electrons and holes in Si inherit the behavior of the conduction and valence band respectively. The bound states of a donor lie below the conduction band while the bound states of acceptors are on top of the valence band.

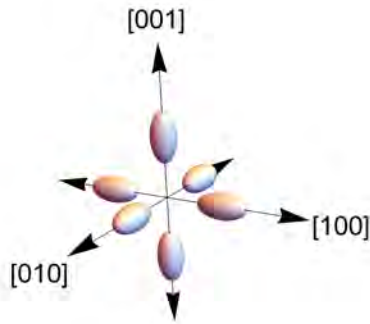


FIGURE 1.4: Valley ellipsoids of same energy.

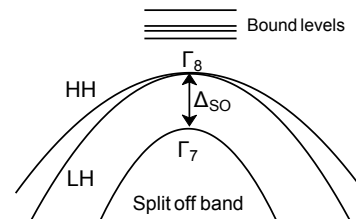


FIGURE 1.5: Scheme of the valence band and the acceptor bound states.

1.2.2 Kane Quantum Computer

In his 1998 seminal paper, Bruce Kane introduced the idea of using dopants in Si for developing a quantum computer [27]. The proposal, see Fig. 1.6, consisted in an array of phosphorus donors in a Si device, 20 nm below a SiO₂ interface approximately. The metallic gates A and J are there to perform different operations on the donors in order to implement single- and two-qubit gates.

The phosphorus donors behave as effective gigantic hydrogen atoms with Bohr radius around 2.5 nm [32]. Both the electron and the nucleus of the donor have spin 1/2 so both spins offer obvious TLS than can be used potentially to encode a qubit. In this particular proposal the nuclear spin was chosen to be the qubit, following the Nuclear Magnetic Resonance schemes [33]. Interestingly, since the most common isotope of Si is ²⁸Si, whose nuclear spin is $I = 0$, each qubit would be isolated from the potential noise of a spin bath [34], quite common in group III-V semiconductors such as GaAs. Moreover, the remaining 4.7% abundance of natural ²⁹Si, whose nuclear spin is 1/2, can be removed by isotopic purification techniques [35]. The removal of the nuclear spin bath further increases the coherence properties of the nuclear spin in a way that its coherence times can be beyond 30 seconds, which is the most extraordinary coherence times in a solid state device [36]. The extraordinary coherence properties of Si were not a big surprise, as relaxation times of the nuclear spin, already being measured in the late fifties [37], were also remarkable, exceeding 10 hours. This extraordinary coherence and relaxation times give this platform a great advantage over other quantum computing proposals.

Scalability was another of the advantages of Kane's scheme. Thousands of dopants can be placed in a silicon wafer, potentially allowing the manipulation of all these qubits by correctly applying gate voltages. Not to mention the intrinsic compatibility with microelectronics that would make possible the interaction between classical and quantum information processors.

The hyperfine interaction between the electron spin and the nuclear spin is a key ingredient of Kane's proposal for both single- and two-qubit manipulation. The magnetic Hamiltonian of the electron spin-nuclear-spin system is

$$H = g_e \mu_e B \sigma_z^e - g_n \mu_n B \sigma_z^n + A \sigma^e \cdot \sigma^n, \quad (1.4)$$

being μ_e , μ_n and g_e , g_n the Bohr magneton for electron and nuclear spins, and the g -factors of electron and nuclear spins. B is the magnetic field, σ are the Pauli matrices for each spin and

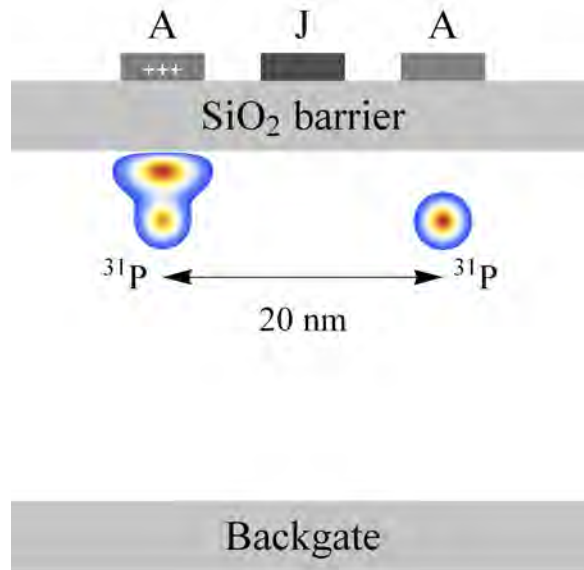


FIGURE 1.6: Scheme of Kane's quantum computer. The left electron is attracted by the activated A-gate, tuning the hyperfine interaction. The J-gate can be used to activate the exchange interaction between neighboring electrons.

A is the hyperfine coupling. By inspection of Eq. 1.4 it is clear that a static magnetic field can be applied to split the two states of both the electron and nuclear spins with different Larmor energies. Interestingly, the hyperfine coupling is a function of the electron probability density at the nucleus:

$$A = \frac{4}{3} g_e \mu_B g_n \mu_n |\psi_e(0)|^2. \quad (1.5)$$

We can look at Fig. 1.6 to understand the role of the A-gate. By applying a gate voltage the electron wavefunction can be pushed towards the SiO₂ barrier, which plays the role of preventing ionization. Through this operation, the electron probability density at the nucleus is changed and, by virtue of Eq. 1.5, the hyperfine coupling is modified, so as the frequencies of the different possible transitions between the different eigenstates of Eq. 1.4. In other words, the A gate can be used to tune the different frequencies of each single-qubit subsystem individually. An in-plane AC magnetic field can then be applied in resonance with the particular transition that we want to perform in an individually selected qubit.

The two-qubit gates are more complicated, requiring the action of both the A and J gates. It is important to note that, in order to fulfill DiVincenzo's universality criterion, two-qubit operations together with single-qubit operations are necessary. In this original scheme, the donors are expected to be distanced by 20 nm, long enough to avoid direct interaction between the nuclear spins. Again, the electron spin plays an important role for two-qubit operations. By correctly applying the A-gate voltage, the nuclear spin can be transferred into the electron spin. By applying a gate voltage in the J-gate two nearest neighbor donor electrons can be drawn into an intermediate region, where they can interact via exchange interactions. The effective Hamiltonian of such interaction is

$$H_{ee} = J \sigma_e^1 \cdot \sigma_e^2 \quad (1.6)$$

Where J is the exchange coupling, proportional to the overlap between electrons. In this way, by controlling the J gate, a SWAP operation (swaps two qubit states) between the electron spins can be performed. With more complex pulses in the J gate, the CNOT two-qubit gate

can be performed. The electron spins are then translated again into the nuclear spins by the action of the magnetic field and the A gate. For universality, it is enough to perform any single qubit operation together with SWAP or CNOT operations [6].

Still, there are two requirements for a potential quantum computer yet to be fulfilled: initialization and readout of the qubits. Both of them can be done by the same mechanism. Phosphorus donors can bind two electrons but, due to the Pauli exclusion principle, in order to bind two electrons at the same time they must have opposite spin orientations. It is possible to take advantage of this mechanism by applying electric fields with the gates to encourage tunneling between the donors. If the electron spins have opposite spins tunneling is allowed and a charge signature can be projectively measured using sensitive electrometers. With this mechanism not only would be possible to measure the states but also to initialize the computer by carefully injecting electrons into the donors and rejecting those with opposite spin.

In summary, this proposal fulfills DiVincenzo's criteria. Both single- and two-qubit gates are addressable to perform multiple operations within the remarkable coherence times that the Si platform provides. The platform itself, as some other solid state proposals, does have good scalability prospects. A quantum computer with this characteristics could be initialized and individual measurements are feasible.

However, after almost two decades, several challenges have aroused. Some of them were already pointed out by Bruce Kane in its original paper, and some others were discovered later. The most important of them are related to the two-qubit operations and the initialization/readout mechanism. As it was pointed out in the previous section, donors in Si have an extra degeneracy due to the valley degree of freedom. As a result, the electron wavefunction is affected, its hydrogenic envelope is modified by extremely fast oscillations that change sign in the order of magnitude of atomic steps [38]. This is of capital relevance for two-qubit operations because the exchange interaction is proportional to the overlap between electrons. If these electrons have extremely fast oscillations its overlap will also oscillate, implying a very complicated dependence of the exchange interaction with the donor position. Solving this problem would require perfect atomic precision in the placement of donors. The other major issue, comes from the original proposal for the readout mechanism itself. When the tunneling between neighboring donors happens, one of the donors goes to the D^- charge state, which strongly couples to the environment. Its short coherence time together with the short lifetime (it has a very small binding energy and hence easily tunnels into the conduction band) dramatically reduces the probability of success for this readout mechanism [39].

Still after this issues, the scientific community considers Si as one of the most promising candidates for solid state quantum computing and a lot of effort has been made to dodge this problems or even overcome them as challenges.

1.2.3 Loss-DiVincenzo Quantum Computer

The other relevant architecture for this thesis is the Loss-DiVincenzo quantum computer [26]. Proposed in 1998 too, it also shows a possible way towards the construction of a quantum computer with a solid state device, see Fig. 1.7. In this case, the spins of electrons confined in electrostatically defined quantum dots encode the qubits. In this platform, each quantum dot contains a single electron. The electrons of different quantum dots are separated by a tunnel barrier, whose height can be modified by applying different gate voltages to a tunnel

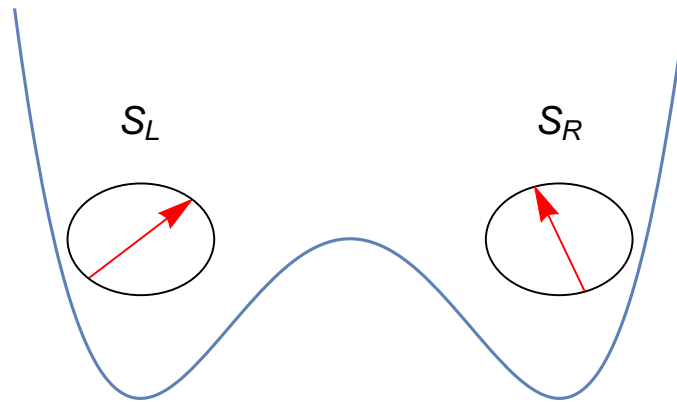


FIGURE 1.7: Sketch of Loss and DiVincenzo’s quantum computer. Electrons with spin S_L and S_R are confined in the left and right dots. The spin is manipulated via oscillating local magnetic fields.

gate in between the dots. The scalability of this platform would be guaranteed since it is potentially possible to place thousands of quantum dots in a semiconductor device.

Each individual electron spin is addressed via local oscillating magnetic fields, allowing any single-qubit operation. The individual application of magnetic fields can also be used to get reliable individual qubit initialization. This method has the challenging requirement of being able to apply localized magnetic fields for each quantum dot.

Two-qubit operations are performed in a similar manner to Kane’s proposal: using the exchange interaction. In this case a pulsed gate voltage in the tunnel barrier between two quantum dots is applied such that the exchange constant J becomes time dependent. By carefully choosing the pulse duration and time dependence, it is possible to make a SWAP operation. Single-qubit gates together with this SWAP operation can be used to perform more complex two-qubit gates like the CNOT.

This proposal started to evolve much faster in GaAs devices. During the first few years Si quantum dots lagged behind the rapid growth of this field in GaAs devices [40–42]. This rapid growth was limited by the problem of non-zero nuclear spins in the natural isotopes of its constituents, leading to a big susceptibility to magnetic noise decoherence processes [43]. The GaAs nuclear spin bath can be seen schematically in Fig. 1.8. On the other hand, electrons in Si have a larger effective mass, making harder to confine them in electrostatically defined quantum dots. Once this problem was solved, this approach could take advantage of the good coherence properties due to the existence of zero nuclear spin natural isotopes in Si.

Finally, the last DiVincenzo’s criterion was the ability to perform high precision measurements. This again is made with spin-to-charge conversion schemes that take advantage of the Pauli spin blockade. The tunnel barrier could be tuned to allow electron tunneling, which would be suppressed if the two electron spins are in the same quantum state, otherwise there would be a charge signature measurable by high precision electrometers.

Time has shown that this scheme is not perfect either. In this case the individual single-qubit operations require local magnetic fields. This kind of magnetic fields are hard to control experimentally and require too much power, complicating the scalability of the scheme. For two-qubit gates Si quantum dots do not have the same problem as the Kane proposal since

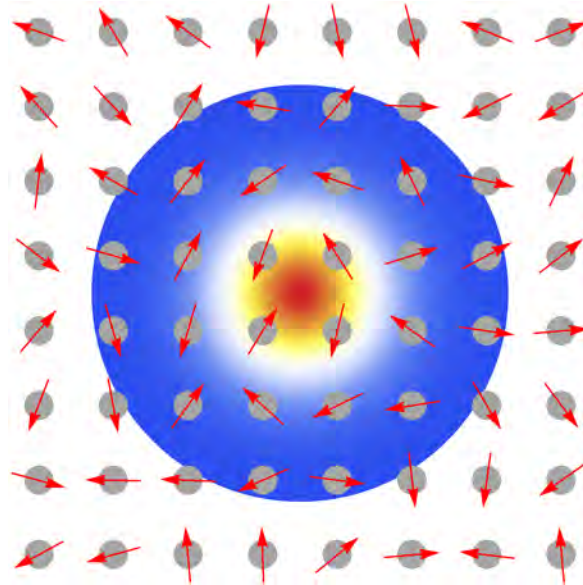


FIGURE 1.8: Cartoon of the nuclear spin-bath in GaAs.

the quantum dots have no pinning center (dopant), still the valley degeneracy increases the complexity of the Hilbert space giving rise to valley related relaxation mechanisms. GaAs, on the other hand, has a direct bandgap at Γ so the valley degeneracy would not be a problem but, as stated before, the magnetic nuclei bath is a detrimental hazard for the coherence of the qubits.

Just like Kane's proposal, the experimental challenges have not intimidated the scientific community and this scheme has evolved since the original paper, giving rise to several modifications both in Si and GaAs that could potentially overcome the original difficulties.

1.3 State of the art

In this section a small review of the current research in the field of semiconductor based quantum computer proposals. For the curious reader, a more throughout review of the Si quantum nanoelectronics field, in both dopants and quantum dots, can be found in [28].

1.3.1 Dopants

Since Kane's proposal there has been a general and constant improvement of the theoretical approaches for understanding the physics of the donors in the experimental conditions of the scheme. The first approaches used variational gaussian or hydrogenic wavefunctions adapted to the phosphorus Bohr radius in silicon. These wavefunctions were used to solve the Hamiltonian of the donor under the effective mass approximation (EMA) [32, 44–52]. The potential of the A-gate was included so the Stark effect of the donor was also taken into account [53, 54]. Tight-binding methods were also developed in parallel to include the Bloch components of the wavefunctions [55–58].

For the single electron control, realistic effects that appear in the experiments also had to be taken into account, such as the presence of an insulating interface due to the presence of a

perpendicular electric field. The confining potential of the A-gate together with the presence of this interface gave rise to three different regimes: (i) electron confined to the Coulomb impurity, (ii) electron confined to the effective triangular well formed at the interface, (iii) hybridization of both confinement regimes [59–63]. Central cell corrections had also to be included to account for the differences between donor species too [64–67]. Some early [32, 68] and recent works [53, 69] also showed that the valley degeneracy was not a real problem for the single electron physics, since the strong confinement of the donor potential already lifts the valley degeneracy, separating a non degenerate ground state from a three-fold degenerate valley excited state. Donor molecule dynamics were also necessary for the understanding of the readout process [39, 70–72] and spin-to-charge conversion mechanisms [39, 73]. Improvements in the understanding of the donor physics were also necessary for the interaction with magnetic fields. The g -factor was found to be valley and gate voltage dependent [74].

Regarding electron-electron interactions, the real applicability of the exchange coupling to generation of entanglement and the construction of two-qubit gates has been extensively investigated [66, 75–79]. However, as previously stated, the valley degeneracy gives rise to oscillations in the exchange as a function of position [38, 49, 80–83]. These oscillations are not commensurate with the atomic lattice and hence exact positioning of the dopants would be required for reproducibility. Strain can be used to partially break the degeneracy, but it still requires atomic precision in the donor placement [84]. The strict characterization of two qubit gates [79, 85–87] can optimize the fidelities for the Kane scheme despite the valley oscillations. Another issue with the exchange interaction is its inherent charge noise susceptibility. Since the exchange interaction depends on the overlap of the two electrons, electric field fluctuations could potentially modify the exchange coupling, requiring a higher control and optimization of the interface and gates [88, 89].

These difficulties led to alternative proposals where some of the problems were removed. Some of the mechanisms that this proposals consider are: electric manipulation of the g -factor in a SiGe heterostructures [90], resonant transferring of the a single electron for qubit-qubit coupling [91], qubit encoding in electron and nuclear spins at the same time [92], optical transitions of qubits [93], magnetic dipolar coupling for two-qubit operations [94], qubit encoding in the charge degree of freedom [95], 2D spin transport with non-local qubit-qubit interactions [96].

In all the cases, the accurate positioning of the impurities is, at least, an important factor. In particular, in the original scheme, the exchange oscillations require lattice site precision of donor implantation so this became an experimental challenge. One way to overcome this challenge was the use of the already standard technique of ion implantation [97–103]. With this technique a P ion (or any other ion) can be shot into a Si device, but the dopant position is only approximated. By carefully applying external electric fields, the vertical positioning of the donor ion can be adjusted with a precision of ± 10 nm [104]. The main issues of this method are the difficulty of achieving and registering individual ion shots, and that once the ions are implanted, the surface is reconstructed by an annealing process that inevitably causes diffusion and segregation of the dopants [105]. Single dopant implantation was demonstrated in a MOSFET [106, 107], and it is still under constant improvement [108].

An alternative to single-ion implantation is the Scanning tunnelling microscopy (STM) technique. This technique not only allows imaging of surfaces with high resolution, it also allows to pattern surfaces at the atomic scale [109–113]. The atomic position of dopants in Si with STM follows a multiple step process: (i) First, a monolayer of hydrogen is positioned on the surface of the Si device. (ii) The STM tip is used to remove selected H atoms, leaving several

empty spots in the surface. (iii) Phosphine (PH_3) molecules are then sent to the interface, the molecule then fuses with the surface, leaving the P atoms in the empty spots. (iv) A new silicon overgrowth process is done to bury the P atoms. Again, some accuracy is lost during the overgrowth process. This method is also under constant improvement [114].

Regarding spin-readout, the first experiments of using high precision electrometers to measure the spin states of qubits were done in GaAs quantum dots [40]. In this case a quantum point contact was coupled to the qubit to perform the measurement, however, the charge sensitivity can be enhanced by employing a single electron transistor tunnel coupled to the qubit, like in this work in Si [115]. Soon after that, high-fidelity single shot readout of the electron spin was achieved in a Si device. Since this milestone, the field rapidly grew and some other key milestones in the Kane quantum computer were achieved such as the manipulation of the electron spin to perform Rabi oscillations and work as a qubit [116]. The high fidelity measurement of the nuclear spin [117]. The electron spin coherence of the electron spin was shown to be above 2s [35]. Even higher coherence times were achieved for the nuclear spin [36], allowing the storage of quantum information for 30 seconds. Experimental proof of a high-fidelity A-gate operation has been obtained [118]. Extraordinary gate fidelities of 99.95% and 99.99% were achieved for the manipulation of the electron spin and the nuclear spin [119].

Still, after the remarkable experimental growth of the field, multiple qubit operations are still hard to achieve due to the exchange oscillations problem. Some new alternatives have aroused, for example the use of hybrids of quantum dots and dopants would open new paths for two-qubit operations [120, 121], the use of electric dipole-dipole interactions between different donors [104], coupling to superconducting resonators [122] or interactions with photons (dressed states) [123].

One alternative, particularly important for this thesis, is to use acceptor dopants instead of donors [124–126]. Since the top of the valence band is at the Γ point there is no valley degree of freedom, so there are no exchange oscillations as a function of the acceptor position. Instead, as the top of the valence band is four-fold degenerate, the ground spin state behaves effectively as a spin 3/2 system. Strain and confinement can be used to partially lift this degeneracy and keep a two level system that works as a qubit. Some interesting features of this approach are the higher spin-orbit interaction of the valence band, that would allow all-electrical single-qubit manipulation without local magnetic fields, or the dipole-dipole coupling between acceptors, which can be potentially used for entanglement generation or multi-qubit gates. Experimental work involving holes in semiconductors is a vibrant field [127–136]. Particularly on acceptor spin qubits many of the experimental milestones have already been achieved, from the measurement of single-acceptor states [137], the Stark effect [138], strain induced lifting of the four-fold degeneracy [139], and the placement of acceptors near an interface [140], to the measurement of the coupling between two acceptors [141, 142]. More details on acceptor based proposals and its physics will be presented along Chapters 2-4.

1.3.2 Quantum dots

Soon after Loss and DiVincenzo's proposal, there were several experimental advances in GaAs/AlGaAs quantum dots. Single-shot readout of the electron spin was achieved [40], coherent control of single-qubit [41], and even two-qubits [42]. This brilliant start was slowed down by the inevitable presence of a bath of nuclear spins in GaAs, leading to relatively short

relaxation and coherence times. Several techniques have been developed to suppress this type of noise and increase their coherence times [143–145]. On the other side, the large effective mass of electrons in Si made single electron occupation in quantum dots an experimental challenge. Despite of the existence of Coulomb blockade measurements [146], it was not until 2007 that single carrier occupation was achieved for both electrons [147] and holes [148, 149].

In contrast to dopant devices where the valley degeneracy for electrons is lifted such that the ground state is non-degenerate and separated 11 meV from excited valley states, the valley physics in quantum dots requires more analysis. The majority of Si quantum dot devices are made of Si grown on a $\text{Si}_x\text{Ge}_{1-x}$ substrate alloy, or based on Si MOS (with a SiO_2 interface). Strain in these devices gives rise to a huge lifting of the degeneracy from a six-fold degenerate valley states to a two-fold degeneracy. This two-fold degeneracy would correspond to the valleys in the growth direction [150]. The confinement of the electron wavefunction in the heterostructure also favors this separation, that can be up to tens of meV. The presence of sharp interfaces and gate voltages further reduce the symmetry, lifting the remaining degeneracy. The lowest two-valley states are then separated by an energy quantity called the valley splitting, which can be in the order of hundreds of μeV s as calculated from both tight binding methods and the effective mass approach [151–156]. In general, it was shown that valley splitting has a complicated dependence on disorder and other structural conditions [156, 157]. For instance, since the interface of both Si/ SiO_2 and Si/SiGe quantum dots is not perfectly flat, interfacial disorder strongly changes the valley physics from device to device [158]. In general, and again due to the disorder of realistic devices, the ground states of electrons in Si quantum dots are never purely valley states. Instead, mixing of the valley and orbital degrees of freedom occurs [159]. The valley degree of freedom generates fast oscillations in the confinement direction, the presence of steps in an interface creates a local position dependent the valley phase of this oscillations, which is responsible for the mixing of valley and orbit degrees of freedom.

Due to the small value of the valley splitting in quantum dots, the valley physics is a very relevant degree of freedom, affecting the relaxation times [160, 161], the exchange interaction [162] or the g -factors anisotropies [163]. This complex physics of the two-fold valley states in quantum dots, has also given rise to different proposals of using the valley degree of freedom to encode qubits [164, 165].

Independently on the kind of quantum computation scheme, quantum dots need a way for non-invasive measuring the spin states of the confined electrons. Quantum point contact sensors have demonstrated its use in both Si/SiGe and Si/ SiO_2 quantum dots [166–168]. Just like for dopants, Single Electron Transistors (SET) can also be used [169].

To achieve quantum computation, two-qubit interactions are necessary too. Double quantum dots have also been constructed [170, 171], and now there are even proposals and experiments involving more quantum dots [172]. The first reported double quantum dot in Si [170] was coupled to a SET that was used to identify the charge state of each quantum dot but single electron occupation was not achieved. The first Si/SiGe double quantum dot was made in 2009 [173], and by carefully applying gate voltages on each dot and a tunnel gate the demonstration of singly occupied dots was done [174]. Finally, quantum dots have also taken advantage of the isotopic purification methods, giving rise to an enriched ^{28}Si double dot [175]. Eventually, Pauli spin blockade was observed in different Si double quantum dot systems [176–179].

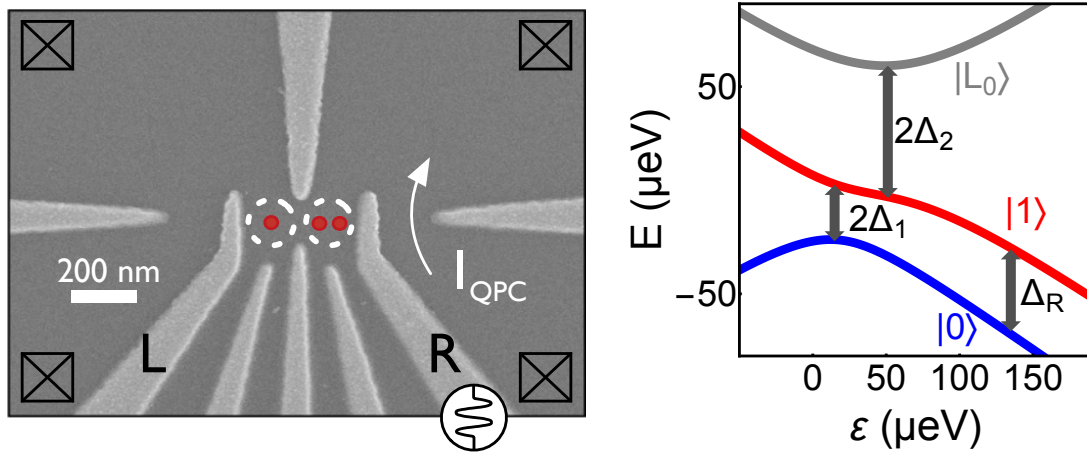


FIGURE 1.9: (Left) Hybrid qubit double quantum dot device. (Right) Its energy level diagram.

Once double quantum dots are formed, charge occupation is controlled and the Pauli spin blockade mechanism is observed, there are enough ingredients to try to implement a universal set of quantum operations in quantum dot systems. The need of local magnetic fields for spin qubits like those in the Loss and DiVincenzo's proposal gave rise to other different approaches like charge-qubits and singlet-triplet qubits. For a charge-qubit the information is encoded in the position of the electron in the double dot, for example one left localized electron in the left dot (configuration $(1,0)$) can be considered the $|0\rangle$ state while the localization at the right dot (charge configuration $(0,1)$) is considered the $|1\rangle$ state [180]. In this case the manipulation is done by electric means only: carefully tuning the dot gate voltages and the tunnel coupling it is possible to perform Landau-Zener transitions between one state and the other, or even create superposition of states. The biggest problem with this kind of qubits is its inherent sensitivity to charge noise: while the manipulation can be made in a very fast way, this sensitivity makes the qubit to decohere easily under small fluctuations of the gate voltages or by fluctuating defects. In contrast, singlet-triplet qubits use the two-electron spin states to encode the qubit. This gives rise to four possible configurations, one singlet state $|S\rangle$ and three triplet states $|T_-\rangle$, $|T_0\rangle$, $|T_+\rangle$. The Pauli exclusion principle creates a spin dependent Coulomb repulsion that can be used in the readout since the singlet states can be obtained in the $(0,2)$ charge configuration while the triplet states are obtained in the $(1,1)$. This qubit can be manipulated by changing the detuning of the system to perform rotations between the singlet and triplet states. This type of qubits are also sensitive to charge noise due to its dependence on detuning and Coulomb repulsion, however they are not as susceptible as the charge qubit, though their manipulation is slower than that of charge qubits.

Spin qubits have the problem of slow manipulation and local magnetic fields. Charge and singlet-triplet qubits can be faster and do not need local magnetic fields but are more susceptible to charge noise. This gave rise to a search for new types of qubits for quantum dots. In particular, systems with high spin-orbit couplings could be interesting due to the possibility of electric manipulation of the spin. Examples of this include new geometries [120, 179, 181] or interfacial induction of spin-orbit interaction due to the Rashba mechanism or valley-orbit mechanisms [159, 182, 183]. Two relevant approaches for this thesis are the hybrid qubit [165] and the corner dots [181] defined in Si nanowires.

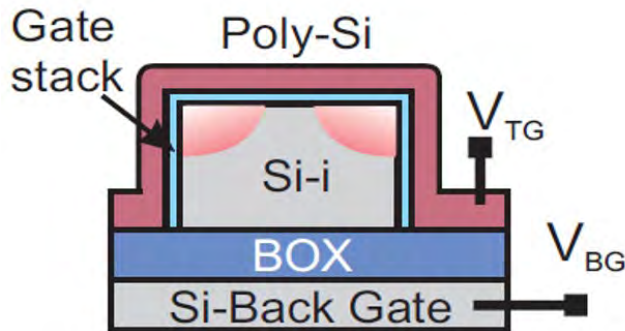


FIGURE 1.10: From [184]. Cross section of the Nanowire Field Effect Transistor. Top left and top right angles have localized electron states.

In the hybrid qubit proposal, a double quantum dot is occupied with two electrons localized in the left dot and the other in the right dot, see Fig. 1.9. The qubit is encoded in the states $|0\rangle = |S\rangle|\downarrow\rangle$ and $|1\rangle = \sqrt{1/3}|T_0\rangle|\downarrow\rangle - \sqrt{2/3}|T_-\rangle|\uparrow\rangle$, being $|S\rangle, |T_0\rangle, |T_-\rangle$ the singlet or triplet spin states of the doubly occupied dot. Qubit manipulations are made through tunneling events between the left and right dot. Single qubit rotations can then be done by all electrical means by changing the tunnel gates and detuning. This process does not require the application of oscillating magnetic fields, enabling fast qubit operation. Particularly, near the anticrossings this qubit effectively works as a charge qubit while for large values of detuning it works as an effective spin qubit. These two regimes have different properties. In the "charge" regime the operations can be made faster but the sensitivity to charge noise is more important in comparison to the "spin" regime. In the latter the singlet-triplet splitting is related to the valley splitting of the right dot so the far detuning regime inherits the valley physics of the double quantum dot system.

The other interesting system for this thesis consist of a nanowire based transistor [120, 179, 181], similar to FinFETs, where application of different gate voltages allows the confinement of electrons in a double quantum dot system in the two top corners, see Fig. 1.10. Charge occupation, charge dynamics and Pauli spin blockade have already been observed in this system. One of the particularities of this system is that the quantum dot is confined against two interfaces rather than one (corner state), making more relevant the physics of not only the two valleys in the growth direction, whose valley splitting would be now affected by two interfaces, but also the two valleys in the horizontal direction of confinement. Charge manipulation can be made between the dots and dopants can also be inserted in this system to make use of a donor nuclear spin as a quantum memory. The now relevant two extra valley states can be of great importance for pure electrical manipulation and tunneling events.

1.4 Theoretical description

In this section the key basic mathematical background for this thesis is introduced. More specific analysis will be presented in the following chapters as required.

1.4.1 Effective mass theory

Near each of the conduction band minima of silicon k_0 , the energy dispersion relation can be expanded in terms of parabolic functions of the wavevectors whose curvature is directly

related to the effective mass [32, 44], see Fig.1.3:

$$E = E_0 + \hbar^2 \left(\frac{(k_l - k_0)^2}{2m_l} + \frac{k_{t_1}^2 + k_{t_2}^2}{2m_t} \right) \quad (1.7)$$

Where k_0 is the value where the conduction band has a minimum for a certain valley index, l indicates the longitudinal component while t_1 and t_2 indicate the transversal components. For example, for the valley minimum in the [100] direction, $l = x$, $t_1 = y$ and $t_2 = z$. The longitudinal mass is $0.916m_e$ and the transversal mass is $0.19m_e$.

An electron state then satisfies the equation:

$$\left(-\frac{\hbar^2}{2m} \nabla^2 + V(\mathbf{r}) + V_c(\mathbf{r}) \right) \Psi(\mathbf{r}) = E\Psi(\mathbf{r}) \quad (1.8)$$

Where $V(\mathbf{r})$ is the potential felt by an electron in the periodic lattice of Si, and $V_c(\mathbf{r})$ is the confinement potential. This confinement potential can be, for example, the donor potential or SiGe barriers in a quantum well.

Using the Bloch theorem it is clear that the solutions of Eq. 1.8 are combinations of envelope functions $F^\mu(\mathbf{r})$ and periodic Bloch wavefunctions $u_{n\mathbf{k}}^\mu(\mathbf{r})e^{i\mathbf{k}\mathbf{r}}$, where μ indicates the valley index. Putting the pieces together we have

$$\Psi^\mu(\mathbf{r}) = F^\mu(\mathbf{r})u_{n\mathbf{k}}^\mu(\mathbf{r})e^{i\mathbf{k}\mathbf{r}} \quad (1.9)$$

The envelope functions must be properly normalized $\int_{space} |F^\mu(\mathbf{r})|^2 d\mathbf{r} = 1$ and so must the Bloch part to the lattice volume Ω : $\int_{lattice} |u_{n\mathbf{k}}^\mu(\mathbf{r})e^{i\mathbf{k}\mathbf{r}}|^2 d\mathbf{r} = \Omega$.

This is called the single-valley effective mass theory. Generalizations can be made to include interactions between different valleys and valley-orbit mechanisms. To do so the wavefunction in 1.9 has to be generalized to include the contribution of each valley:

$$\Psi(\mathbf{r}) = \sum_{\mu=1}^6 \alpha_\mu F^\mu(\mathbf{r})u_{n\mathbf{k}}^\mu(\mathbf{r})e^{i\mathbf{k}\mathbf{r}} \quad (1.10)$$

This multi-valley effective mass method can be used, for instance, to correctly obtain the valley splitting in donors and, adapted to quantum wells by applying the correct confinement potential [67, 154].

For donors $V_c(\mathbf{r}) = -\frac{e^2}{4\pi\epsilon_{Si}r}$, it can be shown that the envelope functions for each valley state satisfy the hydrogenic wavefunction

$$\left(-\hbar^2 \left(\frac{1}{2m_l} \partial_l^2 + \frac{1}{2m_t} \partial_{t_1}^2 + \frac{1}{2m_t} \partial_{t_2}^2 \right) - \frac{e^2}{4\pi\epsilon_{Si}r} \right) F^\mu(\mathbf{r}) = EF^\mu(\mathbf{r}) \quad (1.11)$$

It is possible to use group theory to obtain the valley combinations α_μ with correct symmetry. From the irreducible representations of the group T_d it follows that the six-fold degenerate ground state splits into a ground state with A_1 symmetry, three excited states with T_2 symmetry and two excited states with E symmetry. The valley combinations for these states

are:

$$\alpha_{A_1} = \frac{1}{\sqrt{6}}(1, 1, 1, 1, 1, 1) \quad (1.12)$$

$$\alpha_{T_2^x} = \frac{1}{\sqrt{2}}(1, -1, 0, 0, 0, 0) \quad (1.13)$$

$$\alpha_{T_2^y} = \frac{1}{\sqrt{2}}(0, 0, 1, -1, 0, 0) \quad (1.14)$$

$$\alpha_{T_2^z} = \frac{1}{\sqrt{2}}(0, 0, 0, 0, 1, -1) \quad (1.15)$$

$$\alpha_{E^{xy}} = \frac{1}{2}(1, 1, -1, -1, 0, 0) \quad (1.16)$$

$$\alpha_{E^z} = \frac{1}{\sqrt{12}}(1, 1, 1, 1, -2, -2) \quad (1.17)$$

These combinations together with Eq. 1.11 are then used to obtain the energies and wavefunctions of the ground state donor.

In quantum wells, strain and confinement in the z-direction split the in-plane valley states from the z-valley states, hence only the latter are relevant for the analysis:

$$\Psi(\mathbf{r}) = \sum_{\mu=\pm z} \alpha_{\mu} F^{\mu}(\mathbf{r}) u_{k_{\mu}}(\mathbf{r}) e^{ik_{\mu}z} \quad (1.18)$$

For perfectly flat interfaces $|\alpha_z| = |\alpha_{-z}| = 1/\sqrt{2}$ and the envelope functions for each valley state are the same. Hence, the two eigenstates are the symmetric and anti-symmetric combinations of z-valley states. The envelope function is then determined by

$$\sum_{\mu=\pm z} \alpha_{\mu} e^{ik_{\mu}z} \left[-\hbar^2 \left(\frac{1}{2m_t} \partial_x^2 + \frac{1}{2m_t} \partial_y^2 + \frac{1}{2m_l} \partial_z^2 \right) + V_c(\mathbf{r}) + V_v(z) - E \right] F_{\mu} = 0 \quad (1.19)$$

where $V_v(z)$ is the valley coupling potential that can be described within the effective mass approximation as a delta function at the interface, located at z_i :

$$V_v(z) = v_v \delta(z - z_i) \quad (1.20)$$

The value of the coupling v_v can be determined from experiments or atomistic simulations [185, 186]. When the quantum wells consider realistic effects such as atomistic disorder at the interfaces the valley and orbital degrees of freedom become mixed and the effective mass approximation requires some improvements [159, 187].

1.4.2 Kohn-Luttinger Hamiltonian

The atomic p states in group IV semiconductors contribute predominantly to the valence band, which means that spin-orbit effects are relevant [31]. Once the SOC is included, the total angular momentum J associated to the valence band is made of the orbital angular momentum $L = 1$ and the spin angular momentum $S = 1/2$. This gives rise to two different bands: the one with $J = 1/2$, known as the split-off band, the other, with $J = 3/2$, is four-fold degenerate at the top of the valence band and is often divided in two subbands according to the effective masses of the holes. These are the light-hole (LH) and heavy-hole

(HH) subbands. These two subbands are separated from the split-off band by the SOC (44 meV in Si, 290 meV in Ge).

Unlike the bottom of the conduction band, the top of the valence band of both Si and Ge can not be approximated by a single band. Both the LH and HH subbands converge to a four-fold degenerate valence band maximum at the Γ point and, due to the proximity of the split-off band, the latter also needs to be considered for accurate calculations of acceptor states.

The development of an effective mass theory requires then the use of Löwdin's degenerate perturbation method in the $k.p$ framework [182, 188]. In total, this theory gives rise to a Hamiltonian that includes the HH, LH and split-off bands, including their spin counterparts. The resulting 6×6 Hamiltonian is

$$H_{KL} = \begin{pmatrix} P+Q & L & M & 0 & \frac{i}{\sqrt{2}}L & -i\sqrt{2}M \\ L^* & P-Q & 0 & M & -i\sqrt{2}Q & i\sqrt{\frac{3}{2}}L \\ M^* & 0 & P-Q & -L & -i\sqrt{\frac{3}{2}}L^* & -i\sqrt{2}Q \\ 0 & M^* & -L^* & P+Q & -i\sqrt{2}M^* & -\frac{i}{\sqrt{2}}L^* \\ -i\sqrt{2}L^* & i\sqrt{2}Q & i\sqrt{\frac{3}{2}}L & i\sqrt{2}M & P+\Delta_{SO} & 0 \\ i\sqrt{2}M^* & -i\sqrt{\frac{3}{2}}L^* & i\sqrt{2}Q & i\sqrt{2}L & 0 & P+\Delta_{SO} \end{pmatrix} \quad (1.21)$$

After defining the effective Rydberg unit as $Ry^* = e^4 m_0 / 2\hbar^2 \epsilon_s^2 \gamma_1$ and the effective Bohr radius as $a^* = \hbar^2 \epsilon_s \gamma_1 / e^2 m_0$ [44]. The differential operators in Eq. (1.21) are

$$\begin{aligned} P &= -k^2 \\ Q &= -\frac{\gamma_2}{\gamma_1}(k_x^2 + k_y^2 - 2k_z^2) \\ L &= i2\sqrt{3}\frac{\gamma_3}{\gamma_1}(k_x - ik_y)k_z \\ M &= -\sqrt{3}\frac{\gamma_2}{\gamma_1}(k_x^2 - k_y^2) + i2\sqrt{3}\frac{\gamma_3}{\gamma_1}k_x k_y, \end{aligned} \quad (1.22)$$

with m_0 the free electron mass, ϵ_s the semiconductor static dielectric constant, Δ_{SO} the SOC of the semiconductor, and γ_1 , γ_2 and γ_3 material dependent Luttinger parameters. The values of the Luttinger γ_i can be easily related to the effective masses of light- and heavy-holes in different directions [31].

The Kohn-Luttinger Hamiltonian can be used as an effective mass approach to describe the HH, LH and split-off bands. To include the Coulomb potential of an acceptor it is possible to proceed like in the effective mass approach for electrons including directly the Coulomb potential with possible central cell corrections if necessary.

1.4.3 Tight-Binding methods

In this subsection the basic 1D tight-binding method to describe the fundamental properties of the valley states, is shown. Despite of its simplicity this model already captures the basic physics of the valley oscillations and can be applied for the simulation of valley states in 2D and 3D devices. This method was developed by Boykin et al. in Ref. [151], and improved in the following years [156, 157].

Consider a chain of $2N+1$ Si atoms, for the tight binding method we can use a position basis in which $|n\rangle$ denotes the n th atom such that the wavefunction $|\Psi\rangle$ of an electron can be represented as

$$|\Psi\rangle = \sum_n b_n |n\rangle \quad (1.23)$$

Once we add a Hamiltonian with t_1 as a nearest neighbor hopping, its action on the wavefunction is

$$H|\Psi\rangle = \sum_n b_n t_1 (|n+1\rangle + |n-1\rangle) \quad (1.24)$$

We can assume periodic boundary conditions such that applying a Fourier transform with a lattice constant a we have

$$|q\rangle = \sum_{j=-N}^{j=N} e^{ijqa}$$

$$H|q\rangle = t_1(e^{iqa} + e^{-iqa})|q\rangle = \epsilon|q\rangle \quad (1.25)$$

Its eigenvalues are then $\epsilon = 2t_1 \cos(qa)$. Since this dispersion relation has its minimum at $q = 0$, this nearest neighbor tight-binding can only be used to describe the physics in directions where the valley degree of freedom is not relevant. In order to describe indirect bandgap semiconductors, at least hopping terms to second nearest neighbors t_2 are required. In this case the action of the Hamiltonian becomes

$$H|\Psi\rangle = \sum_n b_n (t_1|n+1\rangle + t_1|n-1\rangle + t_2|n+2\rangle + t_2|n-2\rangle) \quad (1.26)$$

Imposing again periodic boundary conditions, the dispersion relation is now

$$\epsilon = 2t_1 \cos(qa) + 2t_2 \cos(2qa) \quad (1.27)$$

Now this dispersion relation has a minimum that depends on the values of t_1 and t_2 . We can choose this values to get the Si parameters of longitudinal effective mass $m_l = 0.916m_0$ and the minimum position in the dispersion relation $q_0 = 0.82(2\pi/a)$. The obtained values for the hopping parameters that describe a band with valley degeneracy in Si are $t_1 = 0.683\text{eV}$ and $t_2 = 0.612\text{eV}$. To account for the effective mass in transversal directions the single band tight binding can be used. The hopping value that gives the correct transversal effective mass $m_t = 0.191m_0$ is $t = 10.91$. An on-site energy of 23.23 eV can be used such that the energy minimum is zero.

In this way we can get a tight binding method that reproduces the longitudinal mass and oscillations of two-valley states in one direction and the transversal mass in other direction. This method is particularly suited to account for fast variations that are relevant for the valley physics and are hard to account in effective mass theories, like atomic disorder at the interface.

1.5 This thesis

As has been stated along this introduction, the silicon quantum computing field has grown very rapidly in the last few years. However, there are still several remaining challenges as the need for faster operations while keeping the extraordinary coherence properties of Si or the search for new ways to overcome the lattice precision donor placement to get repeatability

entanglement or multi-qubit gates. In this thesis we propose the use of 2D materials to overcome the donor placement problem, and high spin-orbit systems in Si will be studied such as acceptors, corner states in nanowires and valley states in quantum dots. The contents are divided in three parts, each one divided in chapters with its own introduction and conclusion.

1.5.1 Part I: Acceptor bound states

This part is divided in three chapters: (2) description of all the relevant parameters of acceptor states under different confinement conditions. (3) Manipulation of acceptor states in SiGe quantum wells. (4) Anisotropies in the g -factor and experimental consequences.

In Chapter 2 we deal with the basic physics and calculations of acceptor states. Since acceptor states lie near the valence band, they can take advantage of the SOC of Si. This SOC could in principle be used to perform all-electrical qubit manipulation and two-qubit procedures in which the valley degeneracy of the conduction band is not relevant. The Kohn-Luttinger Hamiltonian is solved together with the Coulomb impurity with a variational effective mass method to obtain the HH-LH splitting due to the quantum confinement of interfaces and quantum wells. The HH-LH splitting due to the presence of strain in Si/SiGe quantum wells is also calculated. Other relevant parameters like the T_d symmetry coupling p and the effective g -factors are also calculated.

In Chapter 3 the three different possible manipulation methods are analyzed for acceptors in Si/SiGe quantum wells. The parameters calculated in Chapter 2 are used to develop an effective Hamiltonian for the low energy states, relevant for qubit operations. Magnetic field induced manipulation through direct Electron Spin Resonance (ESR), electrical manipulation by Electric Dipole Spin Resonance (EDSR), and g -Tensor Modulation Resonance (g-TMR) are discussed. The strong spin-orbit coupling and tunability of the g -tensor allow fast electrical manipulation of both LH and HH based qubits.

In Chapter 4 the relevance of the T_d symmetry terms of acceptors is analyzed and its consequences for the manipulation and coherence of single- and two-qubit operations are discussed. It is shown that the spin 3/2 physics of the lowest energy states, together with the T_d symmetry gives rise to an anisotropic magnetic field dependence. This anisotropy is relevant for qubit manipulation since it modulates the existence of sweet spots and can give rise to a Decoherence Free Subspace (DFS). The two-qubit coupling is also affected by this anisotropy, allowing the activation and deactivation of two-qubit operations by just applying vertical electric fields.

1.5.2 Part II: Quantum dots

This part is divided in two Chapters: Chapter 5 on valley tunneling physics of double quantum dots, and Chapter 6 on the theory of corner states.

In Chapter 5 the valley physics in Si/SiGe double quantum dot system is analyzed. This double quantum dot system has analogies with the more complex system of the hybrid qubit double quantum dot, where all electrical fast manipulation is feasible. A tight binding method is used to describe the valley physics of a single electron inside a double quantum dot in the presence of interfacial disorder. The valley physics of this system is analogous to the valley and spin physics in the hybrid qubit. The tight binding method is used to understand

how disorder can affect the different relevant parameters of double quantum dot qubits. In particular, the tunneling rates between dots for same and different valley states is calculated, so is the valley splitting, showing how different disorder realizations can dramatically change their values and its dependence on electric fields. Consequences for the manipulability and coherence are discussed.

In Chapter 6 the valley physics of an electron based quantum computing device with strong spin-orbit interaction is analyzed. In the relevant device, the electrons are tightly confined against not only one, but two interfaces forming corner dots. The gate voltages of the system can be used to tune some devices from a regime of confinement where only two valley states are relevant, like in other devices, to regimes in which four valley states are physically relevant. The interaction with the excited valley states, even in the two valley approximation, gives rise to a strong SOC that has already shown to be relevant for all-electrical electron spin qubit manipulation in Si.

1.5.3 Part III: 2D materials

In the last part of this thesis the use of 2D materials to overcome the placement of donors in Si devices will be analyzed. The purpose of this chapter is to analyze the viability of donor states in 2D materials assuming the stability of the materials themselves. The energies of different donor atom and molecule states are obtained as a function of different parameters of the 2D host. The viability of these states for quantum computation purposes is discussed.

Part I

Acceptor bound states

Confinement effects on acceptor levels ¹

2.1 Introduction

Most spin-qubits rely on the use of time dependent magnetic fields to perform operations, but experimentally it is quite difficult to localize a time dependent magnetic field on a single qubit. This makes desirable to look for ways to manipulate the qubit states only by electric fields. The search for electric field manipulable qubits has focused the attention in the recent years to high spin orbit systems [125, 126, 191–195]. These systems mix the spin with the orbital degrees of freedom. As the orbital wavefunction is sensitive to electric fields, this mixing allows the possibility of manipulating spins entirely by electric means. In silicon and germanium, the conduction band has a small spin orbit interaction, but in the valence band this interaction can be much stronger. As holes in group IV semiconductors have an orbital momentum $I = 1$ and spin $S = 1/2$ in their atomic wavefunctions, holes can be described by a total effective spin $J = 3/2$ [31, 44], which implies inherently high spin orbit interactions. Confined hole systems are then very interesting platforms to explore spin orbit coupling effects for quantum computing. Moreover, since the total spin of the hole is not the usual value $1/2$ but $3/2$, there is physics in holes with no equivalent for electrons [182, 196–199].

Acceptors provide a natural way of confining holes in Si and Ge. Proposals of acceptor-based qubits may make use of the long range strong dipolar inter-qubit coupling [124], and exploit the spin-orbit interaction to couple spin to phonons [200], or to oscillating electric fields [125, 126]. The relative importance of the different sources of decoherence is different in electrons and holes: spin-orbit interactions would make holes more sensitive to charge noise while hyperfine interaction (which can cause spin decoherence due to coupling to nuclear spins [43]), while not entirely suppressed, is smaller for holes than for electrons [201–206]. The effective suppression of the latter by Si isotopic purification, which gets rid of nuclear spins in Si, leads to very long electron coherence times [35]. In practical dopant-based quantum computer proposals, dopants are introduced in nanostructures and close to surfaces or interfaces, where their bound states can be manipulated by applying gate voltages. Under these conditions, the energies of bound carriers can be shifted by quantum confinement

¹Results published in [189] and [190].

and dielectric mismatch [48, 207, 208] potentially modifying the working parameters of the devices.

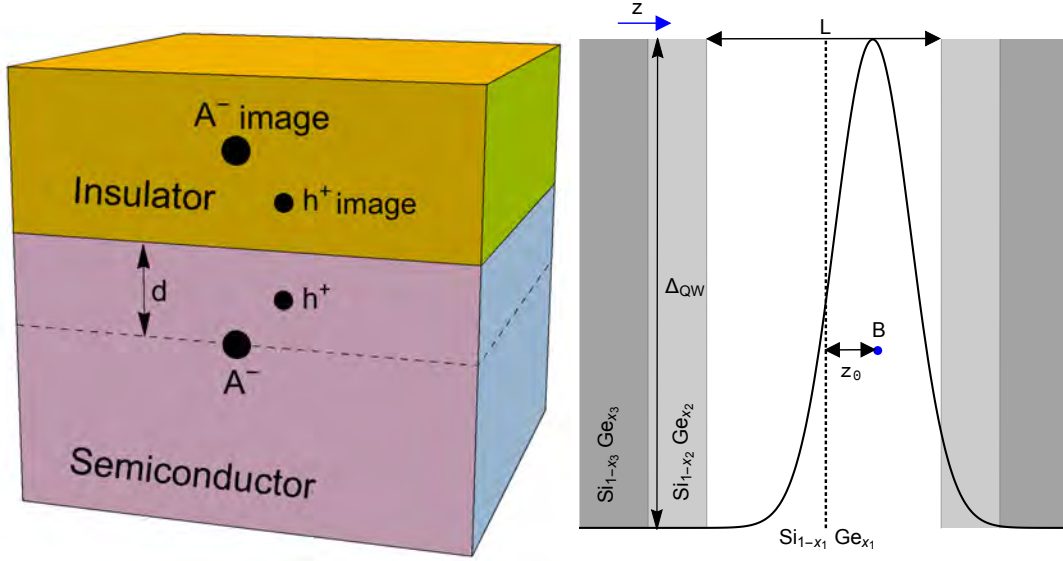


FIGURE 2.1: (Left) Schematic view of the of the hard wall geometry. The acceptor A is at a distance d from the (001) interface between the semiconductor (Si or Ge) and an insulating barrier. Image charges appear due to the dielectric mismatch between the semiconductor and the barrier. (Right) Sketch of the quantum well heterostructure and the bound hole envelope wave-function along the perpendicular z direction. L is the width of the well, z_0 determines the acceptor position from the well center, Δ_{QW} is the barrier height, and x_1 , x_2 , and x_3 indicate the proportion of Germanium on each of the layers. $x_1 > x_2$ for defining the quantum well for holes. The substrate (with composition $\text{Si}_{1-x_3}\text{Ge}_{x_3}$) is relaxed and fixes the lattice parameter in the whole heterostructure. This determines the sign of the strain on the quantum well and is hence related to whether the doublet ground state is heavy-hole ($x_3 = x_2$) or light-hole ($x_3 > x_1$) like.

Quantum confinement may alter the shape of the wavefunctions through the boundary conditions, consequently affecting the binding energy. For instance, in a very thin (compared to the bound state wave-function size a_B) nanowire, the extra confinement enhances the binding energy deactivating the dopants as carrier providers [209, 210]. However, when the dopant is close (compared to a_B) to one interface/surface but not confined in other directions, the wave-function can be deformed in such a way that the density probability of the bound state decreases on the dopant, leading to a reduction of the binding energy. The dielectric mismatch gives rise to image charges which, depending on the relative magnitude of the dielectric functions of the nanostructure components, can lead to an enhanced or decreased binding. In the case of a semiconductor surrounded by insulators, the image charges have the same sign as the charges originating them, enhancing the binding energies.

Not only the energies but also the symmetry of the bound states may be modified. To develop an understanding of the low energy physics of acceptor states, we then need to account for the confinement, since it breaks the ground state degeneracy. At the same time the lack of inversion symmetry gives rise to a Rashba spin orbit interaction [125]. Strain [139, 198, 211, 212] and electric fields [54, 138] also affect the ground state degeneracy. Important terms are also those that come from the local T_d symmetry of the acceptor [199], since they can couple the spin degree of freedom to linear electric fields.

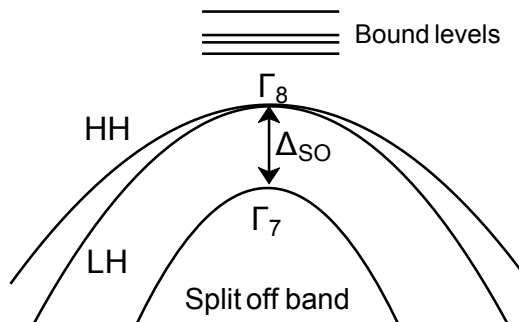


FIGURE 2.2: Sketch of the valence subbands. HH indicates the heavy hole subband while LH indicates the light hole subband. The energies of the bound states are positive and defined with respect to the top of the valence band.

Characterization of dopants embedded in nanostructures can be performed via transport measurements [213, 214] while STM can give information of the wave-function of subsurface dopants [140, 215, 216].

Here we consider an acceptor under two types of confinement: near a hard wall interface and within a SiGe quantum well, see Fig. 2.1. We perform an analysis of all the relevant parameters of each type of confinement, and evaluate their effects on the energy spectrum and the symmetry of the bound states for substitutional acceptors (group III elements). Our study is based on effective mass theory (EMT) with the Kohn Luttinger Hamiltonian, see 1.4.2, for a bulk acceptor in a group IV semiconductor host [44, 217–219]. EMT exploits the analogy with free atoms but includes information about the host crystal through the bands. Both quantum confinement and dielectric mismatch are included. Central cell corrections [219] are also considered in order to reproduce the energy spectra of different acceptor species. We study the energy spectra of acceptors, including the Kramers doublet splitting of the ground state observed recently experimentally [140]. Our approach allows a complete analysis of the symmetry breaking induced by the interface. The effects of strain, due to the lattice mismatch in SiGe quantum wells, is also taken into account for the analysis. Other relevant parameters to the construction of an effective Hamiltonian for the quantum dynamics, such as the Rashba coupling due to the lack of inversion symmetry and the change in the coupling to the T_d symmetry term, are considered.

	Si	Ge
Ry* (meV)	24.8	4.4
a_0 (nm)	2.55	10.85
γ_1	4.22	13.35
γ_2	0.39	4.25
γ_3	1.44	5.69
Δ_{SO} (meV)	44	290
ε_s	11.4	15.36
a (nm)	0.5431	0.5658
C_{11} (MN/cm ²)	16.772	13.112
C_{12} (MN/cm ²)	6.498	4.923
b (eV)	-2.2	-3.0
g_1	-1.07	6.82

TABLE 2.1: Relevant parameters for Si and Ge. From [31].

2.2 Confined acceptors Hamiltonian

From 1.4.2 we know that the description of the valence band in group IV semiconductors requires the inclusion of the HH, LH and split-off bands, see Fig. 2.2, through the Kohn-Luttinger Hamiltonian in the basis $|J, J_z\rangle$:

$$H_{KL} = \begin{pmatrix} |3/2, 3/2\rangle & |3/2, 1/2\rangle & |3/2, -1/2\rangle & |3/2, -3/2\rangle & |1/2, 1/2\rangle & |1/2, -1/2\rangle \\ P + Q & L & M & 0 & \frac{i}{\sqrt{2}}L & -i\sqrt{2}M \\ L^* & P - Q & 0 & M & -i\sqrt{2}Q & i\sqrt{\frac{3}{2}}L \\ M^* & 0 & P - Q & -L & -i\sqrt{\frac{3}{2}}L^* & -i\sqrt{2}Q \\ 0 & M^* & -L^* & P + Q & -i\sqrt{2}M^* & -\frac{i}{\sqrt{2}}L^* \\ -i\sqrt{2}L^* & i\sqrt{2}Q & i\sqrt{\frac{3}{2}}L & i\sqrt{2}M & P + \Delta_{SO} & 0 \\ i\sqrt{2}M^* & -i\sqrt{\frac{3}{2}}L^* & i\sqrt{2}Q & i\sqrt{2}L & 0 & P + \Delta_{SO} \end{pmatrix} \quad (2.1)$$

Being these differential operators in Rydberg units (see 1.4.2):

$$\begin{aligned} P &= -k^2 \\ Q &= -\frac{\gamma_2}{\gamma_1}(k_x^2 + k_y^2 - 2k_z^2) \\ L &= i2\sqrt{3}\frac{\gamma_3}{\gamma_1}(k_x - ik_y)k_z \\ M &= -\sqrt{3}\frac{\gamma_2}{\gamma_1}(k_x^2 - k_y^2) + i2\sqrt{3}\frac{\gamma_3}{\gamma_1}k_xk_y, \end{aligned} \quad (2.2)$$

See table 2.1 for the relevant parameters of Si and Ge. The effect of the proximity to interfaces is considered also by including in the Hamiltonian the image charges that arise due to the dielectric mismatch between the host crystal and the barrier [220, 221]. We consider two different types of confinement $H_{\text{confinement}}$: In one case a (001) interface is considered at a distance d from the acceptor, while in the other the acceptor is inside a quantum well at a distance z_0 from the center, see Fig. 2.1. Finally, the Coulomb potential produced by the acceptor impurity is given by $H_c = e^2/(4\pi\varepsilon_s\varepsilon_0r)$, with the relative permittivity ε_s .

Together, $H_{KL} + H_{\text{confinement}} + H_c$ are enough to describe the physical effects of an interface on the acceptor bound states. However, as can be seen in Refs. [125, 126] and will be discussed in the following Chapters, an acceptor based quantum computer will be also affected by strain, electric and magnetic fields.

The Bir-Pikus Hamiltonian H_{BP} [198, 199] includes the effect of strain in the nanostructure

$$\begin{aligned} H_{\text{BP}} &= a\epsilon\mathbb{1} \\ &+ b \left((J_x^2 - \frac{5}{4}\mathbb{1})\epsilon_{xx} + (J_y^2 - \frac{5}{4}\mathbb{1})\epsilon_{yy} + (J_z^2 - \frac{5}{4}\mathbb{1})\epsilon_{zz} \right) \\ &+ d/\sqrt{3} (\{J_x, J_y\}\epsilon_{xy} + \{J_y, J_z\}\epsilon_{yz} + \{J_x, J_z\}\epsilon_{xz}). \end{aligned} \quad (2.3)$$

The parameters a, b and d are the deformation potentials, \mathbf{J} is the angular momentum, ϵ_{ii} are the deformation tensor components, and $\mathbb{1}$ is the identity matrix. In this thesis, only uniaxial strain will be considered, hence, the deformation tensor is diagonal with components $\epsilon = \epsilon_{xx} = \epsilon_{yy}$, and

$$\epsilon_{zz} = -2 \frac{C_{12}}{C_{11}} \epsilon \quad (2.4)$$

where C_{12} and C_{11} are the elasticity moduli. The uniaxial strain breaks the fourfold degeneracy of the valence band at the Γ point, separating the HH, LH subbands [222]. For $\epsilon > 0$ (tensile strain) the top of the valence band has HH character, while it is LH like for $\epsilon < 0$ (compressive strain).

The electric field interaction with the hole is given by the Stark Hamiltonian $H_{\text{F}} = e\mathbf{F} \cdot \mathbf{r}$ whose in-plane components, when the inversion symmetry is lost in the heterostructure, act like a Rashba-type interaction [125, 126].

The interaction with magnetic fields is given by

$$H_{\text{B}} = \mu_{\text{B}} (g_1 \mathbf{B} \cdot \mathbf{J} + g_2 \mathbf{B} \cdot \mathcal{J}) \quad (2.5)$$

where g_1 and g_2 are the linear and cubic bulk g-factor of the host material. The operator \mathcal{J} is $\mathcal{J} = (J_x^3, J_y^3, J_z^3)$. The cubic term can be neglected for most of the cases as, in general, $g_1 \gg g_2$ [223].

Finally, due to the local T_d symmetry of the acceptor, there are some allowed electromagnetic extra terms [198, 199]. We consider here the only allowed term with a coupling constant big enough to be of relevance for the order of magnitude of the electric (MV/m) and magnetic fields (T). This is the term H_{T_d} , which is an interaction that couples the acceptor spin with electric fields \mathbf{F} .

$$H_{T_d} = p/\sqrt{3} (\{J_y, J_z\}F_x + \{J_x, J_z\}F_y + \{J_x, J_y\}F_z). \quad (2.6)$$

This linear coupling is only possible because the local T_d symmetry of the acceptor central cell does not fulfill the inversion symmetry. This coupling is hence stronger the larger the probability density at the acceptor [223]. A very relevant particularity of this term is that it allows the mixing of HH and LH states in the presence of an electric field. The parameter p is an effective dipole moment that can be estimated [223] by $p = e \int_0^a f^*(r) r f(r)$ with a the lattice constant of the host material, and $f(r)$ the radial envelope function. In bulk silicon $p = 0.26$ Debye for a B acceptor and it would be larger for deeper acceptors.

The total Hamiltonian of a confined acceptor is then given by:

$$H_{\text{total}} = H_{\text{KL}} + H_{\text{c}} + H_{\text{confinement}} + H_{\text{BP}} + H_{\text{T}_d} + H_{\text{F}} + H_{\text{B}}. \quad (2.7)$$

2.2.1 Selection rules and effective mass model

In bulk, Si has cubic with inversion symmetry so the transformation elements form the O_h group. The three double irreducible representations (IRs) Γ_6 and Γ_7 with dimension two and Γ_8 with dimension four are all allowed in this group. As a result, the acceptor states are doubly or four-fold degenerate. Due to the inversion symmetry, parity is conserved and the states can be separated in well defined parity states (Γ_6^+ , Γ_6^- , Γ_7^+ , Γ_7^- , Γ_8^+ and Γ_8^-). However, central cell effects break the inversion symmetry, reducing the symmetry of the system to the tetrahedral double group \bar{T}_d . The \bar{T}_d group also has IRs Γ_6 , Γ_7 and Γ_8 but in this case parity is not a good quantum number. A consequence of the inversion symmetry breaking is the appearance of weak transitions between states with nominally identical parity, which would be forbidden if inversion symmetry were actually preserved [224]. However, as will be shown in the following sections, without external fields the central cell corrections are only important at small distances from the acceptor (see Table 2.2), their effect is very local and hence the parity can be in general considered a good quantum number in bulk.

The selection rules of the Hamiltonian Eq. (2.1) can be obtained after examining the differential operators and the couplings between different sets of the pseudo-angular momentum $|J, J_z\rangle$. Being the dopant orbital angular momentum \mathbf{L} , we can define a total angular momentum \mathbf{K} as $\mathbf{K} = \mathbf{L} + \mathbf{J}$ [218, 224]. The selection rules for the quantum numbers \mathbf{K} and $K_z = L_z + J_z$, which can be obtained applying the Wigner-Eckart theorem to the terms of cubic symmetry, are

$$\langle \mathbf{K}', K'_z | H_{\text{acceptor}} | \mathbf{K}, K_z \rangle \propto \delta_{K'_z, (K_z + (0, \pm 4))}. \quad (2.8)$$

We can use these selection rules to relate the quantum numbers \mathbf{K} and K_z to the IRs of the O_h (or \bar{T}_d) group. Doubly degenerate eigenstates of the cubic symmetry with $K_z = \pm 1/2 + 4n$ transform under the group O_h as Γ_6 states, while two-fold degenerate states with $K_z = \pm 3/2 + 4n$ transform like Γ_7 symmetry states. The four-fold degenerate eigenstates of the cubic symmetric terms in the Hamiltonian correspond to the Γ_8 representation and can have any half-integer K_z , always according to the selection rules.

The confinement will be assumed to be in the (001) direction. The considered confinement conditions imply that neither \mathbf{L} nor the parity can be well defined quantum numbers. An immediate consequence is that the total angular momentum $\mathbf{K} = \mathbf{L} + \mathbf{J}$ is not well defined and states with different \mathbf{K} are not orthogonal to each other. However, the z projection of the atomic angular momentum is associated to the φ spherical coordinate so L_z is not affected by the presence of a nearby interface and, since K_z is the sum of L_z and J_z , the selection rule Eq. (2.8) holds. In terms of symmetry, the global O_h symmetry is reduced. The Γ_8 symmetry becomes a reducible representation, but the IRs Γ_6 and Γ_7 remain. This implies that, under confinement in one direction, the four-fold degeneracy of the Γ_8 states is broken into two doubly degenerate states with symmetries Γ_6 and Γ_7 respectively. This effect of symmetry reduction by the interface is analogous to the effect of uniaxially strained silicon in the (001) direction [211, 212, 222]. The ground state split doublets with Γ_6 and Γ_7 symmetry are often referred as light-hole states and heavy-hole states, due to the higher contribution of states coming from the LH and HH valence bands respectively.

The selection rules are useful then to define uncoupled variational basis sets to solve the total Hamiltonian of the problem. A variational wavefunction basis can already be built to fulfill the confinement conditions and selection rules while being based on the solutions of the Coulomb potential, since those are the most relevant terms in the Hamiltonian.

2.2.2 Application to hard wall interfaces

For an acceptor near a hard wall interface, such as a SiO₂ interface the confinement potential becomes $H_{\text{confinement}} = H_{\text{interface}}$:

$$H_{\text{interface}} = V_b \Theta(z - d) - \frac{2Q'}{\sqrt{\rho^2 + (z + 2d)^2}} + \frac{Q'}{2(z + d)} \quad (2.9)$$

The hard wall boundary condition of the single interface is equivalent to making the approximation $V_b \rightarrow \infty$. The second and third terms are the acceptor and hole image charges respectively with $Q' = (\epsilon_b - \epsilon_s)/(\epsilon_b + \epsilon_s)$. ϵ_b is the barrier static dielectric constant [220]. Note that for an insulating barrier $Q' < 0$, namely the acceptor image is attractive for holes, and hence an enhancement of the binding energy is expected.

The total Hamiltonian, now with the hard wall interface confinement in Eq. 2.7, is then:

$$H_{\text{HW}} = H_{\text{KL}} + H_{\text{c}} + H_{\text{interface}} + H_{\text{BP}} + H_{\text{T}_d} + H_{\text{F}} + H_{\text{B}}. \quad (2.10)$$

2.2.2.1 Variational method

The barrier potentials considered for this case are much larger than the typical binding energies and hence a hard-wall boundary condition $\Psi(z \leq -d) = 0$ is assumed for the wave function. The interface boundary condition implies that the spherical symmetry usually assumed for the bound hole variational wave-function in bulk is not valid and it is more appropriate to work in cylindrical variables with the z-axis perpendicular to the interface. With the information of the symmetries and the selection rules we can define a hydrogen-like variational basis set in cylindrical variables and with quantum numbers J and J_z :

$$\psi(\rho, z, \varphi, \alpha_i) = (z + d) z^{l'} \rho^{|L_z|} r^{n'} e^{-\alpha_i r + i L_z \varphi} |J, J_z\rangle, \quad (2.11)$$

where $l' = L - |L_z|$ and $n' = n - L - 1$ with $n > L$. A set of different α_i values is considered. ρ is the cylindrical variable $\rho = \sqrt{r^2 - z^2}$. The $(z + d)$ prefactor assures that the basis set satisfies the hard wall boundary condition. Given an L_z , the quantum number J_z is chosen such that K_z belongs to a given IR. For example, for calculating Γ_7 states, given $L_z = 1$, the possible J_z are 1/2 and 3/2 ($K_z = 3/2, 5/2$ respectively), while for Γ_6 states J_z can be both -1/2 and -3/2 ($K_z = \pm 1/2$). This basis set is truncated at a certain L_{max} with $n_{\text{max}} = L_{\text{max}} + 1$. L_{max} is chosen such that the condition for the energy $(E_{L_{\text{max}}} - E_{L_{\text{max}}-1}) = 0.1$ meV is fulfilled in bulk, which in silicon corresponds to $L_{\text{max}} = 11$. The number of different α_i considered is not as determinant for the convergence as the value of L_{max} . For instance, for the ground state energy of an acceptor in bulk silicon, including $\alpha_1 = 1$ and $\alpha_2 = 2$ with $L_{\text{max}} = 11$ gives $(E_{L_{\text{max}}} - E_{L_{\text{max}}-1}) = 0.1$ meV. However, the excited states require a larger set of different α_i due to their different Bohr radii. Adding $\alpha_3 = 0.5$ and $\alpha_4 = 0.25$ gives results with $(E_{L_{\text{max}}} - E_{L_{\text{max}}-1}) < 0.2$ meV for the first 8 states. For Ge, the set is truncated at $L_{\text{max}} = 11$ for the $J = 3/2$ states while for the $J = 1/2$ states $L_{\text{max}} = 6$ since the split-off band is less relevant in this case ($\Delta_{\text{SO}}^{\text{Ge}} = 290$ meV) and the convergence is faster.

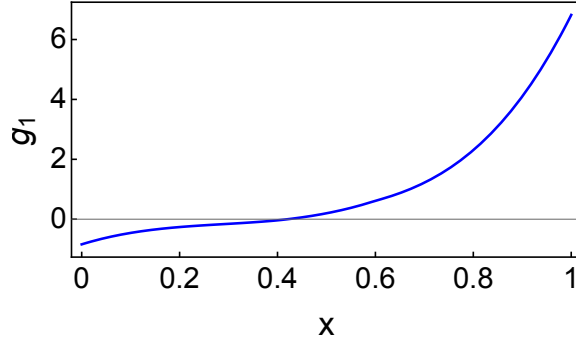


FIGURE 2.3: Value of the linear g-factor g_1 in $\text{Si}_{1-x}\text{Ge}_x$ as a function of the Ge content. The bulk g-factors in Silicon and Germanium have opposite signs, hence around $x = 0.4$ the $\text{Si}_{1-x}\text{Ge}_x$ g-factor goes through zero.

Since the basis set defined in Eq. (2.11) is not orthonormal, it is necessary to consider the overlap matrix $S_{i,j}$

$$\begin{aligned} S_{i,j} &= \langle \psi(\alpha_i) | \psi(\alpha_j) \rangle \\ H_{i,j} &= \langle \psi(\alpha_i) | H_{\text{acceptor}} | \psi(\alpha_j) \rangle, \end{aligned} \quad (2.12)$$

and the problem becomes a generalized eigenvalue problem

$$H_{i,j} |\Psi\rangle = E S_{i,j} |\Psi\rangle. \quad (2.13)$$

Most of the integrals used to obtain the matrix elements of $H_{i,j}$ and $S_{i,j}$ can be solved formally, as detailed in Appendix A.

2.2.3 Application to SiGe quantum wells

Now consider an acceptor acceptor is placed in a quantum well of width L , see Fig. 2.1. Starting from the total Hamiltonian in Eq. 2.7, the confinement potential is now

$$H_{\text{QW}} = \Delta_{\text{QW}} (\Theta(z - L/2) + \Theta(-z - L/2)) + H_{\text{ic}}, \quad (2.14)$$

being Δ_{QW} is the quantum well barrier. The image charges and hole self-energy are included in H_{ic} and are more complex in this case than in the hard wall case [225]. However, this contribution is negligible as the dielectric constants of the well and barrier materials are similar ($Q \approx 0$) and is not considered here. The Hamiltonian for this confinement is then

$$H_{\text{SiGe}} = H_{\text{KL}} + H_{\text{c}} + H_{\text{QW}} + H_{\text{BP}} + H_{\text{Td}} + H_{\text{F}} + H_{\text{B}}. \quad (2.15)$$

To obtain the values of the Luttinger γ_i parameters for $\text{Si}_{1-x}\text{Ge}_x$ we use the interpolating functions given in Ref. [226]:

$$\begin{aligned}
\gamma_1 &= 4.22 + 1.234x + 3.988x^2, \quad 0 \leq x \leq 0.8, \\
\gamma_1 &= -104.315 + 447.266x - 601.113x^2 + 271.542x^3, \quad 0.8 \leq x \leq 1, \\
\gamma_2 &= 0.39 - 0.185x + 2.203x^2, \quad 0 \leq x \leq 0.8, \\
\gamma_2 &= -58.16 + 238.533x - 318.8x^2 + 142.667x^3, \quad 0.8 \leq x \leq 1, \\
\gamma_3 &= 1.44 + 0.266x + 1.928x^2, \quad 0 \leq x \leq 0.8, \\
\gamma_3 &= -59.74 + 250.855x - 366.675x^2 + 151.25x^3, \quad 0.8 \leq x \leq 1.
\end{aligned} \tag{2.16}$$

The relaxed lattice constant of a generic $\text{Si}_{1-x}\text{Ge}_x$ alloy can be obtained using the interpolating function [227] $a_0(x) = 0.541(1-x) + 0.5658x - 0.00188x(1-x)$, where the lattice parameter increases with the Ge content. While for SiO_2 interfaces we use the hard wall approximation, justified since the barrier height is 3 eV, the barrier height of the quantum well Δ_{QW} is related to the valence band offset of the SiGe heterostructure, and hence depends on both the quantum well and barrier compositions. It is given in eV by (see Refs. [226, 227]):

$$\Delta_{\text{QW}} = (0.74 - 0.06x_2)(x_1 - x_2) \tag{2.17}$$

The deformation potential b , dielectric constants and elasticity moduli C_{11} , C_{12} are calculated by linear interpolation [228]. The g -factors are calculated by interpolation of the bulk data from Ref. [229], see Fig. 2.3. In comparison to hard wall confinement conditions, for SiGe quantum wells show several new features: the material dependence of several parameters, the barrier height and the inherent uniaxial strain. The acceptor Coulomb potential now has an extra z dependence $H_c = e^2/(4\pi\epsilon_s(z)\epsilon_0 r)$, due to the different value of $\epsilon_s(z)$ in the barrier and in the quantum well.

Due to the lattice mismatch between well and barrier, there is an intrinsic uniaxial strain in SiGe quantum wells. The ϵ_{ii} depend on the relative values of x_1 , x_2 and x_3 (see Fig. 2.1), the Ge content of each of the layers of the heterostructure. For a $\text{Si}_{1-x_1}\text{Ge}_{x_1}$ layer with lattice constant $a_0(x_1)$ grown on a relaxed $\text{Si}_{1-x_3}\text{Ge}_{x_3}$ substrate with lattice constant $a_0(x_3)$ the deformation tensor is diagonal with components:

$$\begin{aligned}
\epsilon_{xx} &= \epsilon_{yy} = \frac{a_0(x_3) - a_0(x_1)}{a_0(x_1)} \\
\epsilon_{zz} &= -2\frac{C_{12}}{C_{11}}\epsilon_{xx}.
\end{aligned} \tag{2.18}$$

In general, $x_2 < x_1$ is required to define a p-type quantum well. When $x_3 < x_1$ strain is compressive and Γ_7 symmetry (HH) ground states are favored, so the simplest case $x_3 = x_2$ implies a HH ground state. On the other hand, if $x_3 > x_1$, strain is tensile and always favors Γ_6 symmetry ground states (LH). The latter case is more complex in terms of fabrication, but allows a LH ground state and, as will be shown in the following chapters, the competition between strain favored LH states and confinement favored HH states gives an extra flexibility to define the qubit, giving rise to very interesting properties for quantum computation.

The only remaining term that includes an extra dependence is the magnetic field, due to the material dependence of the g -factor:

$$H_{\text{B}} = \mu_{\text{B}} (g_1(z)\mathbf{B} \cdot \mathbf{J} + g_2(z)\mathbf{B} \cdot \mathcal{J}) \tag{2.19}$$

However, as the linear g -factors of confined heavy holes are known to be suppressed for in plane magnetic fields [130], there can be situations in which the cubic g -factors (g_2) dominate. This cubic term is also important when considering a heavy-hole qubit as it can mix the ground state heavy-hole Kramer doublet through in-plane magnetic fields. This is particularly the case when $x_3 = x_2$ and $x_2 < x_1$.

2.2.3.1 Variational method for quantum wells

We split the total Hamiltonian in Eq. (2.15) into a static Hamiltonian H_0 and an interacting Hamiltonian H_{int}

$$\begin{aligned} H &= H_0 + H_{\text{int}} \\ H_0 &= H_{\text{KL}} + H_c + H_{\text{QW}} + H_{\text{BP}} + H(\mathbf{F}_z)_{\text{Td}} \\ &\quad + H_{\text{F}_z} + H_{\text{Bstatic}} + H_{\text{ic}} \\ H_{\text{int}} &= H_{\text{F}_{\parallel}} + H_{\text{Bint}} \end{aligned} \quad (2.20)$$

H_0 includes the contribution of the terms related to the well parameters – length, uniaxial strain and acceptor position. It also includes static contributions of both the vertical electric field, which due to the acceptor ion term gives an extra mixing of HH and LH, and the static magnetic field, which breaks time reversal symmetry lifting the remaining degeneracy. This static magnetic field is in the perpendicular direction for the HH case, and in the in-plane direction for the LH case. The interacting Hamiltonian H_{int} includes the oscillating in-plane electric and, in the HH case, also in-plane magnetic fields. These terms mix the HH and LH subspaces such that after solving the static Hamiltonian their contribution is mostly off-diagonal in the qubit subspace.

The variational basis set used for solving the static Hamiltonian for the acceptor bound states is

$$|\psi_i(\rho, z, \varphi)\rangle = N_i \rho^n e^{-\alpha_i \rho} \phi_i(z) e^{iLz\varphi} |J, J_z\rangle, \quad (2.21)$$

where N_i is the normalization coefficient. The set of α_i parameters is chosen to be $\alpha_1 = 4$, $\alpha_2 = 2$, $\alpha_3 = 1$ and $\alpha_4 = 0.5$. The functions $\phi_i(z)$ are odd and even solutions to the finite quantum well problem, including excited states with different depths outside the quantum well in the form:

$$\phi_{k_c^+}^+(z) = \begin{cases} N_L e^{\beta z} & x \leq -L/2 \\ N_C \cos(k_c^+ z) & -L/2 \leq x \leq L/2 \\ N_R e^{-\beta z} & x \geq L/2 \end{cases} \quad (2.22)$$

$$\phi_{k_c^-}^-(z) = \begin{cases} N_L e^{\beta z} & x \leq -L/2 \\ N_C \sin(k_c^- z) & -L/2 \leq x \leq L/2 \\ N_R e^{-\beta z} & x \geq L/2 \end{cases} \quad (2.23)$$

where N_L , N_R , N_C and β are chosen to normalize and fulfill boundary conditions of the wavefunctions. The value of k_c is split into the number of nodes l and a phase $\theta \in (0, 1)$ that can be related to the relative density of wavefunction inside and outside the well: $k_c^+ = (2l + \theta)\pi/L$ and $k_c^- = (2l + \theta + 1)\pi/L$. The values of θ are chosen to maximize the energy for each case. This value is usually in between 0.7 and 0.99 and strongly depends on the vertical electric field and dopant position. The number of different α_i and θ_i parameters are

		B	Al	Ga	In	Tl
Si	E_{GS} (meV)	45.83	69.03	74.16	157	246
	r_{cc} (nm)	-	0.078	0.082	0.12	0.15
Ge	E_{GS} (meV)	10.82	11.15	11.32	11.99	13.45
	r_{cc} (nm)	-	0.077	0.089	0.12	0.16

TABLE 2.2: Central cell parameter r_{cc} [219] that reproduces the measured bulk ground state energy E_{GS} for the different acceptor species [30]. A single r_{cc} suffices to reproduce the full spectrum [67]. Boron binding energies are well reproduced without the central cell correction.

not as important for the energy convergence as the value of n and l at which the basis set is truncated. We take $n_{\text{max}} = 8$, $l_{\text{max}} = 10$. The difference in energy between the calculated ground state using $l_{\text{max}} = 10$ and $n_{\text{max}} = 9$ is smaller than 0.1 meV.

An acceptor bound ground state in bulk is fourfold degenerate (due to the degeneracy of the top of the valence band at the Γ point). In these heterostructures this degeneracy is not only broken by the mechanisms described in chapter 2 but also by strain (tensile strain gives rise to a LH ground state while compressive strain leads to a HH ground state [222, 230]) and quantum confinement in one direction (which, as will be shown, always favours a HH ground state). A LH ground state may then be produced if the tensile strain splitting overcomes the one produced by the quantum confinement.

2.3 Central cell corrections

In order to account for the dependence of the binding energy on the acceptor species, the so-called central cell corrections have to be included [219]. We adopt here a central cell potential which takes into account the incomplete screening of the Coulomb potential at very short distances from the dopant [67]

$$V_{\text{cc}} = \frac{2(\epsilon_s - 1)e^{-r/r_{\text{cc}}}}{r}, \quad (2.24)$$

with r_{cc} a semiempirical parameter [67] calculated such that for a given acceptor the measured bulk ground state energy is reproduced, see Table 2.2. A single r_{cc} characteristic of each dopant species is sufficient to get also the excited spectrum. The values are very similar for Si and Ge. However, due to the much smaller binding energies of the acceptor states in Ge (which corresponds to much more extended wave functions) the effect of the central cell correction on the binding energies is not as large in Ge as in Si. The central cell correction is not needed to reproduce the energy spectrum for the boron acceptor (namely, r_{cc} for boron is negligibly small). A larger binding energy corresponds to a larger r_{cc} . Typical central-cell parameter values are very small, $r_{\text{cc}} \sim 1 \text{ \AA}$, and hence we do not expect it to be affected by the presence of the interface.

Other relevant central cell corrections correspond to the value of the coupling p in Eq. 2.6. In this thesis, coupling to electric fields is only calculated with a boron acceptor whose value is $p = 0.26D$. The value for deeper acceptors can be found in Ref. [223] and table 2.3.

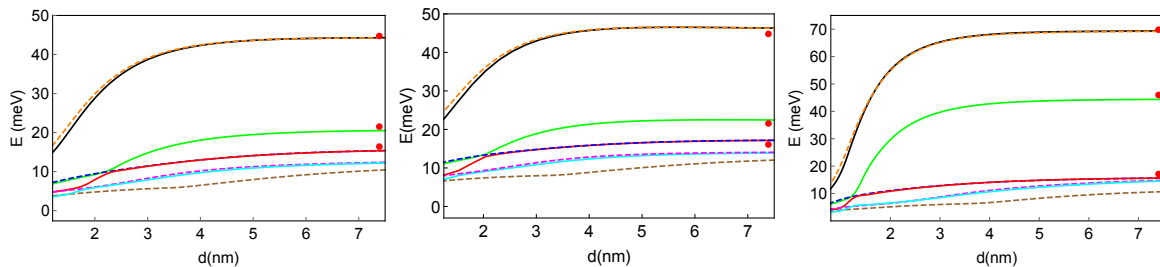


FIGURE 2.4: Energy dependence on distance to the hard wall interface of the ground state and some excited states of an acceptor in Si. The highest energy corresponds to the ground state which is four-fold degenerate in bulk and split in two Kramers doublets near the interface. Dashed lines indicate Γ_7 states while solid lines indicate Γ_6 states. The red dots are the experimental values for the bulk energies of the lowest three states [30, 31]. As the excited states have a less localized wave function than the ground state, they become affected by the interface at larger distances. (a) For B acceptors, neglecting the image charges. (b) Same as (a) including the image charges corresponding to a SiO_2 barrier. Note the enhancement of the binding energies in (b) with respect to (a) due to the attractive character of the acceptor image. (c) Same as (a) for Al acceptors. Holes are more strongly bound for Al in bulk, see Table 2.2, but the energies at small d are very similar to the B case in (a), indicating a suppression of the central cell effects.

2.4 Interface effects on the spectrum

Fig. 2.4 illustrates the effect of a hard wall interface on the energy spectrum as a function of the interface-acceptor distance d in Si. The superimposed dots at large d correspond to the three lowest energies measured in bulk for the corresponding acceptors [30, 31]. The bulk energies are well reproduced but the interface boundary condition and the image charges affect the calculated energies up to the distances shown in the figure. Fig. 2.4 (a) corresponds to a B acceptor and neglects the image charges (namely, $Q' = 0$). Fig. 2.4 (b) considers a SiO_2 barrier ($Q' = -1/2$), and Fig. 2.4 (c) is the result for Al acceptors with $Q' = 0$. Fig. 2.5(a) shows the corresponding results for B acceptors in Ge with $Q' = 0$. There are two main qualitative interface induced effects on the energy levels: (i) the binding energies are smaller close to the interface and (ii) the ground state (which is four-fold degenerate in bulk) splits in two Kramers doublets [140].

The *reduction of the binding energies* close to the interface is due to the quantum confinement [207, 208, 221] produced by the boundary condition on the wave function, which has to be zero at the interface. The wave-function is hence deformed with its probability density shifting away from the interface, see Fig. 2.6. This effect is more significant for the levels coming from the four-fold degenerate bulk ground-state than for the excited states leading to the compression of the full energy spectrum [231]. This compression also appears in bulk strained systems [211, 212] due to the splitting of the heavy-hole and the light-hole bands.

The reduction of the ground state binding energy due to the quantum confinement is partially compensated by the dielectric mismatch with the insulating barrier [208], compare panels (a) and (b) in Fig. 2.4: the holes are more strongly bound when the image charges are included (because $Q' < 0$). The extra binding effect of the acceptor image can be still appreciated at the longest distances shown in Fig. 2.4 (b) by comparing to the bulk values. A vacuum barrier, with $Q' = -0.84$, would further increase the ground state binding energy such that, for $d = 2$ nm, $E_{\text{GS}} = 40.3$ meV, consistent with the reported experimental values in Ref. [208].

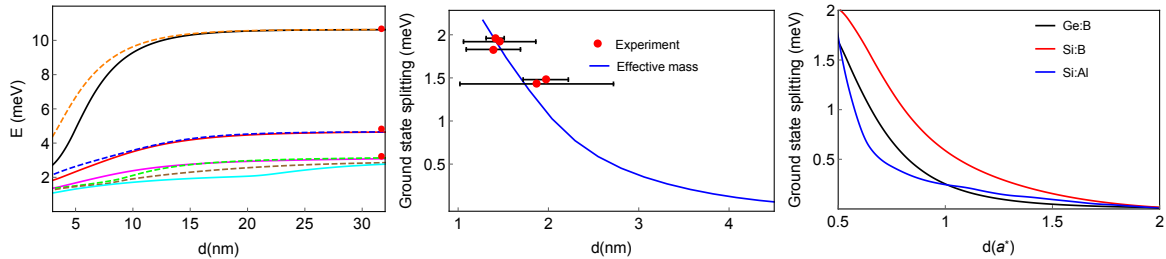


FIGURE 2.5: (Left) Spectrum of a B acceptor in Ge. The notation for the curves is the same as in Fig. 2.4. The binding energy is much smaller in Ge than in Si, however, the ground state splittings are of the same order. (Center) Splitting of the B ground state in Si as a function of the distance d . The red dots are the experimental values taken from Ref. [140]. Although an interface with vacuum has been considered in this plot ($Q' = -0.84$), the value of the splitting is basically independent of Q' down to the distance d considered here. (Right) Comparison of the splitting of the ground state in Si (with two different acceptors) and Ge in effective units of distance.

For doped Si, the energy difference between the two doublets and the excited spectrum can be lowered (for $Q' = 0$) to values < 8 meV, a significant reduction from the > 25 meV typical splitting in bulk. This energy splitting is enhanced when the dielectric mismatch is included, as in Fig. 2.4 (b), but it is still smaller than its bulk value. The compression of the spectrum should be kept in mind when interpreting experimental measurements of bound states in field effect transistor geometries where SiO_2 is a common barrier material. A strong compression could bring the excited states closer to the HH LH manifold ground states, although this energy separation is expected to still be several meV long.

Qualitatively similar results are found for Al acceptors in Fig. 2.4 (c). In the bulk limit, the energies of the two first levels are enhanced with respect to B by the central cell corrections. However, the third level has a binding energy very similar to that in B. This difference is due to the first 2 energy levels being s-like (and hence more affected by central cell corrections). Notably, although the Al acceptors have much larger binding energies in bulk, close to the interface the values are very similar to B acceptors. This is a consequence of the hole probability density shifting away from the dopant, significantly reducing the effect of the central cell correction on the energy. Therefore, distinction among different acceptors in terms of measured binding energies may be blurred by the proximity to an interface.

The *splitting of the ground state* is due to the symmetry reduction produced by the interface. As explained in subsec. 2.2.1, the Γ_8 IR becomes reducible and hence the states with Γ_8 symmetry in bulk acquire a Γ_6 or Γ_7 symmetry. This is the case in particular of the four-fold degenerate bulk ground state which is split in two doublets. The two doublets have a predominant LH (Γ_6) or HH (Γ_7) character. Both corresponding wavefunctions have s-like envelopes, however, the light-hole ground state is more affected by the interface because it has a higher contribution of high order spherical harmonics parallel to the surface as shown in Fig. 2.6. The slightly different shapes of the heavy-hole and light-hole wave functions leads to the energy splitting of the two doublets [140].

The solid and dashed lines in Fig. 2.4 correspond to Γ_6 and Γ_7 symmetries respectively. Whenever those curves are degenerate towards the bulk (increasing d), the Γ_8 symmetry is recovered. The level crossings (anticrossings) in the excited spectrum occur between states with different (same) symmetry. For small values of d there are some near degeneracies between Γ_6 and Γ_7 states which are accidental and not related to the (reducible) Γ_8 symmetry.

Fig. 2.5(b) shows the energy difference between the two lowest doublets for B in Si. The energies for this plot have been obtained considering an interface with vacuum ($Q' = -0.84$) but results are qualitatively (not quantitatively) independent of the value of Q' considered. The energy difference is enhanced as the acceptor gets closer to the interface. Distances $d \leq 0.5a^*$ require the inclusion of higher spherical harmonics $L \geq 11$ to maintain the accuracy due to the relatively larger weight of interfacial states.

The dots with error bars in Fig. 2.5(b) are experimental values as reported in Ref. [140]. The agreement with the calculated splitting is very good even in comparison to more sophisticated tight-binding calculations [140]. The giant splitting ~ 6 meV found at very short distances $d \sim 0.5$ nm $< d_{\min}$ in Ref. [140] is not included in this figure. We stress that the doublet splitting barely depends on Q' , namely it is independent of the nature of the insulator, but the energy spectrum compression does, see discussion of Fig. 2.4. Therefore, in order to keep the excited states away from the lowest doublet in case of a giant splitting, an insulator with a very low dielectric constant should be used.

The same considerations can be made in the case of doped Ge, see Fig. 2.5(c) for the energy spectrum. The main difference with Si is that holes are much less bound in Ge, leading to a larger effective Bohr radius and hence the effect of the interface is more noticeable for much deeper acceptors.

Although the energy spectrum is quantitatively affected by the host crystal and the acceptor species, the interface induced ground state splitting is very similar in different systems, as illustrated in Fig. 2.5(c). Here the doublet splitting is shown for B in Si, Al in Si and B in Ge as a function of the distance in effective units. The three curves are very similar and, in all cases, splittings $\gtrsim 1$ meV can be found.

2.5 Hard wall effective Hamiltonian

In bulk the four-fold degenerate ground state of the acceptor is separated by 21 meV from the following excited states. Although this splitting can be reduced to ≈ 10 meV, it is still enough for quantum computation since the thermal energy in the dilution fridge would be below 1 μ eV. This allows us to build the effective low energy Hamiltonian for the four-fold ground state in Ref. [125]. This effective Hamiltonian will be used to understand the qubit dynamics in Chapter 4.

We split the total Hamiltonian Eq. (2.10) into the variationally solved Hamiltonian H_0 , related to the static terms, and the interacting terms H_{int} that will be accounted by a Schrieffer-Wolff (SW) transformation (see Appendix B)

$$\begin{aligned} H &= H_0 + H_{\text{int}} \\ H_0 &= H_{\text{KL}} + H_{\text{c}} + H_{\text{interface}} + H_{\text{BP}} + H_{\text{F}_z} \\ H_{\text{int}} &= H_{\text{B}_{\parallel}} + H_{\text{E}_{\parallel}} + H_{\text{T}_d} \end{aligned} \quad (2.25)$$

H_0 includes the contribution of the terms related to static terms, such as the interface and strain, and also the effect of a vertical electric field that could be used to further confine the hole wavefunction. The interacting Hamiltonian H_{int} includes the in-plane magnetic field, that will be used in chapter 4 to lift the remaining degeneracy, the oscillating in-plane electric

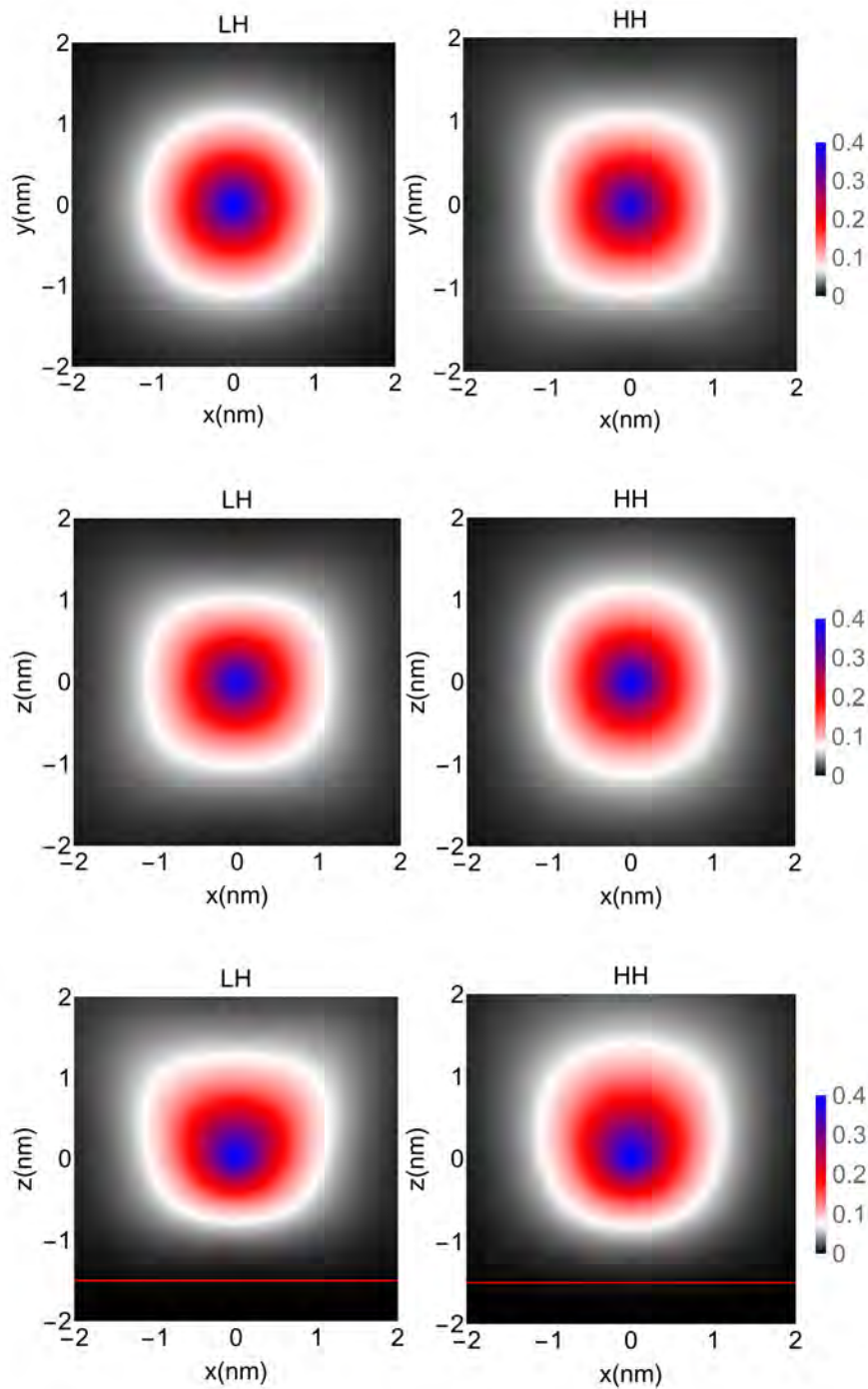


FIGURE 2.6: Spatial probability distribution of the two ground state doublets for B in Si considering a SiO_2 interface: (left) Γ_6 state with a predominant light-hole (LH) character, and (right) Γ_7 state with a predominant heavy-hole (HH) character. The acceptor is located at $(0, 0, 0)$. Top figures are the in-plane ($x - y$) images for $d = 2$ nm. The shape of the wave-functions is the same at all distances. Differences with d can be noticed in the $x - z$ plane (images are equivalent in the $y - z$ plane). The middle panels correspond to $d = 7.5$ nm and the bottom ones to $d = 1.5$ nm. The red line in the bottom panels represents the interface position. The wave-functions are deformed by the interface proximity. The LH wave-function is more affected than the HH one leading to the energy splitting.

field and the T_d symmetry terms that mix the HH and LH subspaces such that after solving the static Hamiltonian their contribution is mostly off-diagonal in the qubit subspace.

An acceptor bound ground state in bulk is fourfold degenerate (due to the degeneracy of the top of the valence band at the Γ point). As seen in the previous section, quantum confinement lifts this degeneracy favoring a Γ_7 (HH) ground state. Strain also lifts this degeneracy: tensile strain gives rise to a LH ground state while compressive strain leads to a HH ground state [222, 230]. Different strain conditions will be considered in chapters 3 and 4.

H_0 is solved variationally as in the previous sections, obtaining both the energies and eigenfunctions of the first eight states. The interaction with in-plane electric and magnetic fields is evaluated taking into account this first eight states manifold through a SW transformation up to third order. Due to the lack of inversion symmetry these in-plane electric and magnetic fields will give off-diagonal terms in the heavy-hole ground state manifold, allowing the manipulation of the qubit state.

Since H_0 does not mix Γ_6 and Γ_7 states, the only relevant term in the effective H_0 Hamiltonian is the HH-LH splitting. Since HH are associated to states with $m_J = \pm 3/2$ and LH with $m_J = \pm 1/2$, the effective low energy Hamiltonian of H_0 in the basis $\{3/2, 1/2, -1/2, -3/2\}$ is

$$H_0^{\text{eff}} = \begin{pmatrix} 0 & 0 & 0 & 0 \\ 0 & \Delta_{HL} & 0 & 0 \\ 0 & 0 & \Delta_{HL} & 0 \\ 0 & 0 & 0 & 0 \end{pmatrix}, \quad (2.26)$$

where Δ_{HL} can be divided into the contribution from the interface, the vertical electric field and strain. Following Refs. [125, 126] we set the zero of energy at the HH ground state. This way the sign of Δ_{HL} determines whether the ground state is HH or LH like. The value of Δ_{HL} as a function of F_z , d and strain will be discussed in the following subsection.

Note that for the numeric results we are considering an 8×8 effective Hamiltonian. The highest four states are important for the quantitative results since they can be close in energy to the lowest LH and HH states, however the qualitative picture can already be understood in terms of this effective 4×4 Hamiltonian involving the Kramer doublets of the first HH and LH states. In the same basis, the effective Hamiltonians of the H_{int} terms are:

$$H_{E_{\parallel}}^{\text{eff}} = \begin{pmatrix} 0 & \alpha F_- & -ipF_z & 0 \\ \alpha F_+ & 0 & 0 & -ipF_z \\ ipF_z & 0 & 0 & -\alpha F_- \\ 0 & ipF_z & -\alpha F_+ & 0 \end{pmatrix} \quad (2.27)$$

$$H_{T_d}^{\text{eff}} = \begin{pmatrix} 0 & -ipF_+ & 0 & 0 \\ ipF_- & 0 & 0 & 0 \\ 0 & 0 & 0 & -ipF_- \\ 0 & 0 & ipF_+ & 0 \end{pmatrix} \quad (2.28)$$

$$H_{B_{\parallel}}^{\text{eff}} = g\mu_B B \begin{pmatrix} 0 & \frac{\sqrt{3}}{2}e^{i\phi} & 0 & 0 \\ \frac{\sqrt{3}}{2}e^{-i\phi} & 0 & e^{i\phi} & 0 \\ 0 & e^{-i\phi} & 0 & \frac{\sqrt{3}}{2}e^{i\phi} \\ 0 & 0 & \frac{\sqrt{3}}{2}e^{-i\phi} & 0 \end{pmatrix} \quad (2.29)$$

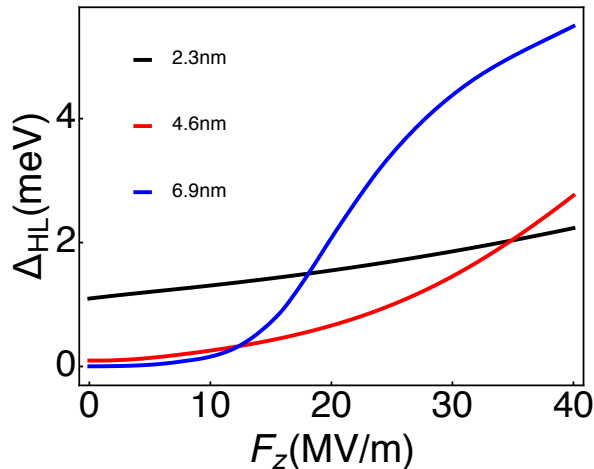


FIGURE 2.7: HH-LH splitting for three different distances d from the interface as a function of the electric field.

The in-plane electric field is defined in tensorial spherical coordinates $F_{\pm} = F_x \pm iF_y$, while the in-plane magnetic field is in polar coordinates $B(\cos(\phi), \sin(\phi))$ for convenience. Here α is the Rashba coupling parameter that appears as an effective interaction with in-plane electric fields due to the lack of inversion symmetry [125]. The g -factor in this submanifold g , is similar to the bulk $g \approx 1.07$. Finally, the value of p is obtained by using the formula from [223] $p = e \int_0^a f^*(r) r f(r)$. The values of both p and α are affected by confinement and the applied vertical field. Both parameters will be discussed in the following subsections.

From the form of Eqs. 2.27, 2.28, and 2.29, it is clear that these terms are of particular relevance for the dynamics since all of them mix HH and LH degrees of freedom. Eq. 2.27 is telling that manipulation of qubit states can be performed by performing transitions from the HH to the LH states. Eq. 2.28 also has this interaction terms, but also implies that the vertical electric field is already mixing HH and LH, which means that this interaction might be enhanced by F_z , see Eq. 2.6. Finally, Eq. 2.29 shows the typical structure of an in-plane magnetic field interacting with a spin 3/2 system. It also mixes naturally HH and LH.

In the following subsections the values of the different parameters as a function of d and F_z are discussed. Since these values are relevant for Chapter 4, where quantum computation with acceptors near a SiO₂ interface is discussed, the main purpose of the following subsections is the comparison with the values of the effective Hamiltonian obtained by finite difference calculations in Ref. [126].

2.5.1 HH-LH splitting

As thoroughly discussed in this Chapter, the Γ_7 ground state, related to a higher HH composition, splits away from the Γ_6 ground state Kramer doublet under the confinement conditions. While this splitting can be already seen in Fig. 2.5(b), it can be modified by the application of a vertical electric field. This field can further increase the confinement by pushing the hole wavefunction towards the interface.

To obtain results with a similar precision as those obtained with a finite differences method in Ref. [126], where they include a high electric field, we require the inclusion of higher angular momentum wavefunctions. This way it is possible to compensate the lack of triangular

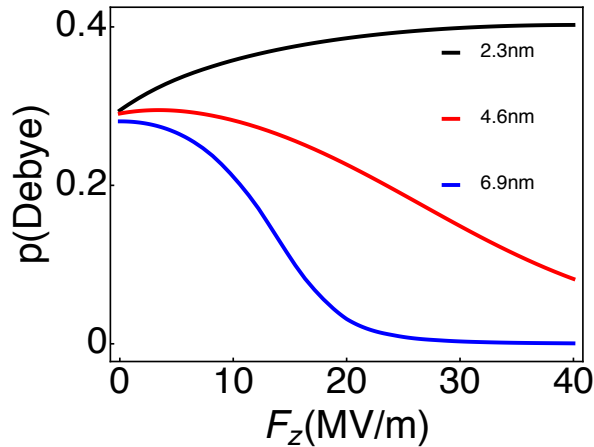


FIGURE 2.8: T_d symmetry dipolar coupling p for three relevant distances from the interface as a function of the electric field.

well wavefunctions within the variational basis set. These results were then obtained with $L_{\max} = 16$. By comparison with Ref. [126], the values with this variational method are in good agreement with those obtained with a finite difference method, though the high electric fields requires a higher variational basis set that reduces the effectiveness of the simulations.

In figure 2.7 the value of the HH-LH splitting for three different values of d are shown as a function of the vertical electric field. As expected, by increasing the vertical electric field the splitting is enhanced. The reason for this is the increased confinement against the interface with F_z . It can also be seen that the farther the acceptor is from the interface, the easier to push the wavefunction against the interface. The reason for this is that the same vertical electric field for two different distances from the interface the same electric field can induces a bigger voltage difference for the most separated acceptor. The results for these three distances are in very good agreement with those in Ref. [126].

2.5.2 Dipolar coupling p

	B	Al	Ga	In
$p(\text{D})$	0.26 ± 0.06	0.8 ± 0.12	0.6 ± 0.1	0.9 ± 0.12

TABLE 2.3: Value of the dipolar coupling p for acceptors in bulk Si. From [223].

The value of the dipolar coupling p related to the T_d symmetry terms in Eq. 2.28 is tabulated in Tab. 2.3. Its value can be estimated by accounting for the wavefunction density at the acceptor central cell [223]

$$p = e \int_0^a f^*(r) r f(r). \quad (2.30)$$

In this formula $f(r)$ is the envelope of the hole ground state wavefunction while a is the lattice constant. Since the density of the wavefunction at the central cell is altered by the presence of the interface, see Fig. 2.6, it is also expected that the deformation due to the presence of vertical electric fields is also going to affect strongly this value. To calculate the value of p we first use the variational method to obtain the ground state envelope wavefunction $f(r)$, and then Eq. 2.30. A large number of variational wavefunctions is again required to obtain accurate results ($L_{\max} = 16$), such as described in subsection 2.2.2.1.

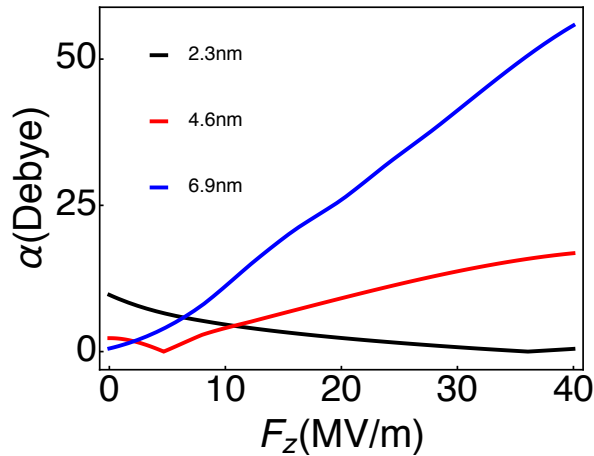


FIGURE 2.9: Estimation of the Rashba coupling α for three different distances as a function of the vertical electric field.

The results can be seen in Fig. 2.8. The value when no field is applied, $F_z = 0$, is very close to the bulk value of $p = 0.26D$, being slightly affected by the wavefunction position. Distances below 2 nm start to deviate from this behavior since the wavefunction starts to be repelled away from the acceptor due to the close presence of the interface. This effect was already found in the previous central cell subsection 2.3, where the central cell effects are lost for acceptors very close to the interface. Higher electric fields move the hole wavefunction away from the impurity and, as a result, the value of p is increased. When the acceptor is at a distance $d \leq a_B$, the wavefunction is repelled by the interface and an increasing electric field pushes it back to the interface, hence increasing the density at the acceptor center. Acceptors at larger distances can be partially ionized by the electric field, reducing the value of p with F_z . In particular, in the case $d = 6.9$ nm, the value is very close to zero for > 20 MV/m. This implies that the hole wavefunction is almost totally ionized from this value, the effects of the Hamiltonian term in Eq. 2.28 becomes irrelevant ($p \approx 0$), and the hole becomes bound to the interface in the z direction.

2.5.3 Rashba coefficient

Since the silicon lattice does not have inversion symmetry, the Rashba coupling is, in this case, a consequence of the presence of the interface [125]. This Rashba coupling allows spin-orbit interactions with in-plane electric fields, which can then be used to manipulate a qubit encoded in the degrees of freedom of the acceptor. As can be seen in Eq. 2.27, this Rashba interaction is off-diagonal in the $|m_J\rangle$ basis of the four-fold ground state. It couples the HH submanifold with the LH submanifold, in a similar way to the T_d symmetric terms. The calculation of this coupling is performed by perturbation theory. After obtaining the results from the variational method of the first eight states, the value of α is obtained by mapping onto Eq. 2.27 by a SW transformation, see Appendix B.

The values of α can be seen in Fig. 2.9. The stronger dependence on F_z for acceptors farther from the interface is clear again. For $d = 6.9$ nm this Rashba coefficient strongly grows with F_z since in this case the electric field is further reducing the inversion symmetry. Interestingly, in the other two cases there is a change of sign in α . This is due to the interplay between the interface and the vertical field. For small d the interface repels the wavefunction, while the vertical electric field pushes the wavefunction against the interface. For these two regimes

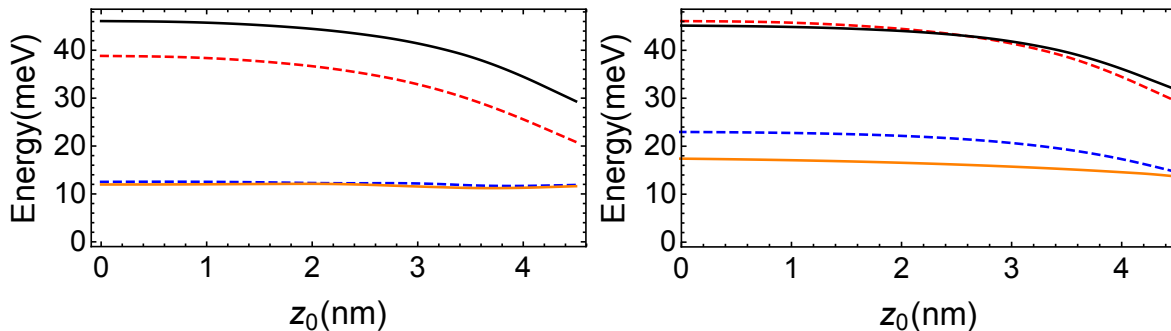


FIGURE 2.10: Acceptor energy levels in a quantum well versus z_0 for $x_1 = 0.05$ and $L = 10$ nm. No external fields applied in the two cases. Solid (dashed) curves correspond to heavy-hole (light-hole) like states. Note that the energy is calculated from the top of the valence band being the bound states positive in energy. In (Left) the ground state is heavy-hole like. The plot corresponds to $x_2 = x_3 = 0$. In (Right) the ground state is light-hole like for centred acceptors (small z_0) but the level crosses the heavy hole excited one when the acceptor gets close to the barrier due to the effect of quantum confinement. This plot uses $x_2 = 0$ and $x_3 = 0.06$. Larger values of x_3 would increase the LH-HH splitting.

the inversion symmetry is broken in opposite ways for low F_z and high F_z . Alternatively, this effect can be already seen in Fig. 2.8 since the maximum of the density of the wavefunction, related to p , is expected to happen near the sign flip of α . The obtained values are again in good agreement with those in Ref. [126].

2.6 Confinement and strain effects on acceptors in quantum wells

We have seen that the proximity of an acceptor to an interface decreases its binding energy due to the repulsion of the wave-function produced by the hard wall. In a narrow well, this competes with the fact that the confinement between the two walls increases the binding energy. This increase, which could seem good news in terms of robustness of the ground state, limits very strongly the sensitivity of the wave-function shape under external fields, limiting its manipulability. An extra ingredient that arises here is the uniaxial strain produced by the different lattice parameters on the x_1 , x_2 , and x_3 layers. This uniaxial strain induces the dominating HH-LH splitting. As has been discussed in the previous section, by choosing the parameters of the heterostructure, the ground state can become of HH or LH character (see Fig. 2.1). HH and LH acceptor qubits in Si have been discussed in Refs. [124–126, 200]. In fig 2.1 two spectra, with different strain configurations in a $L = 10$ nm quantum well, are shown. In (a) $x_2 = x_3 = 0$ while the well is $\text{Si}_{0.9}\text{Ge}_{0.1}$, which already corresponds to several meV separation between HH and LH. On the other hand, in (b) the parameters are chosen to obtain a LH ground state for certain distances. In this case the HH-LH splitting from strain competes against the splitting from the quantum confinement. Basically, the strain induced splitting is constant while increasing the confinement by getting closer to the interface reduces the binding energy of LH states. In the following we will consider two regimes for acceptors confined in quantum wells: (i) $x_2 = x_3 < x_1$, will give a HH ground state, independently on the degree of confinement. (ii) $x_3 > x_1 > x_2$, but with a small difference between x_3 and x_1 , implying a LH ground state. Increasing the confinement by vertical electric fields recovers the HH ground state.

2.7 Effective low energy Hamiltonian for SiGe quantum wells

Similarly as with hard wall interface conditions, H_0 includes the contribution of the terms related to the confinement parameters – strain and acceptor position. It also includes static contributions of both the vertical electric field, which due to the acceptor T_d term gives an extra mixing of Γ_6 and Γ_7 , and the static magnetic field, which breaks time reversal symmetry lifting the remaining degeneracy. This static magnetic field is in the perpendicular direction for the HH case, and in the in-plane direction for the LH case. The reason for this is the different anisotropy of the effective g -factors for HH and LH states: Vertical magnetic fields are coupled strongly to heavy-holes since $|m_J(\text{HH})| = 3|m_J(\text{LH})|$, while in-plane fields only couple to HH via LH states, implying a suppressed effective in-plane g -factor for pure HH states. The interacting Hamiltonian H_{int} includes the oscillating in-plane electric and, in the HH case, also in-plane magnetic fields. These terms mix the HH and LH subspaces such that after solving the static Hamiltonian their contribution is mostly off-diagonal in the qubit subspace.

H_0 is solved variationally, obtaining both the energies and eigenfunctions of the first eight states. Note that, unlike the unstrained bulk acceptor states, the excited states beyond the first two doublets are close in energy (see Fig. 2.1) and hence should not be neglected. The interaction with in-plane electric and magnetic fields is evaluated taking into account this first eight states manifold through a SW transformation up to third order, see Appendix B. Due to the lack of inversion symmetry in the well (except when $z_0 = 0$ and $F_z = 0$) and the extra mixing of HH-LH states via the T_d symmetry interaction with electric fields, these in-plane electric and magnetic fields will give off-diagonal terms in the heavy-hole ground state manifold, allowing the manipulation of the qubit state.

For clarity we separate the perpendicular and parallel terms of the effective Hamiltonian. This Hamiltonian accounts for the low energy physics of only the first four bound states (lowest LH and HH Kramer doublets) in the m_J basis $\{3/2, -3/2, 1/2, -1/2\}$:

$$\begin{aligned}
 H_{\perp}^{\text{eff}}(F_z, B_z) = & \begin{pmatrix} E_{\text{HH}}(F_z) & 0 & 0 & -ipF_z \\ 0 & E_{\text{HH}}(F_z) & ipF_z & 0 \\ 0 & ipF_z & E_{\text{LH}}(F_z) & 0 \\ -ipF_z & 0 & 0 & E_{\text{LH}}(F_z) \end{pmatrix} \\
 & + \mu_B B_z \begin{pmatrix} g_{\perp}^{\text{HH}} & 0 & 0 & 0 \\ 0 & -g_{\perp}^{\text{HH}} & 0 & 0 \\ 0 & 0 & g_{\perp}^{\text{LH}} & 0 \\ 0 & 0 & 0 & -g_{\perp}^{\text{LH}} \end{pmatrix}. \quad (2.31)
 \end{aligned}$$

Where the values g_{\perp}^{HH} , g_{\perp}^{LH} are the perpendicular g -factors of the first HH and LH bound states respectively. These g -factors include the contributions of both the linear and cubic g -factors. The energies E_{HH} and E_{LH} depend on L , z_0 and the electric field applied in the z direction F_z . Note that for the numeric results we are considering an 8×8 effective Hamiltonian. The last four states are important for the quantitative results as they can be close to both the first LH and HH states, however the qualitative picture can already be understood in terms of this effective 4×4 Hamiltonian involving the Kramer doublets of the first HH and LH states.

In the same basis, the effective Hamiltonian of the in-plane terms is, neglecting small non-linear terms for simplicity,

$$\begin{aligned}
H_{\parallel}^{\text{eff}}(\mathbf{E}_{\parallel}, \mathbf{B}_{\parallel}) &= \begin{pmatrix} 0 & 0 & -ipE_+ + \alpha E_- & 0 \\ 0 & 0 & 0 & -ipE_- - \alpha E_+ \\ ipE_- + \alpha E_+ & 0 & 0 & 0 \\ 0 & ipE_+ - \alpha E_- & 0 & 0 \end{pmatrix} \\
&+ \mu_B \begin{pmatrix} 0 & \tilde{g}'_{\parallel} B_+ & \frac{\sqrt{3}}{2} \tilde{g}_{\parallel} B_- & 0 \\ \tilde{g}'_{\parallel} B_- & 0 & 0 & \frac{\sqrt{3}}{2} \tilde{g}_{\parallel} B_+ \\ \frac{\sqrt{3}}{2} \tilde{g}_{\parallel} B_+ & 0 & 0 & \tilde{g}_{\parallel} B_- \\ 0 & \frac{\sqrt{3}}{2} \tilde{g}_{\parallel} B_- & \tilde{g}_{\parallel} B_+ & 0 \end{pmatrix}. \quad (2.32)
\end{aligned}$$

Here α is the Rashba coupling parameter, and the g -factors \tilde{g}_{\parallel} and \tilde{g}'_{\parallel} are the effective linear and cubic g -factors, respectively.

When the confinement and strain conditions are such that our ground state allows the definition of a HH qubit, we will consider the Hamiltonian Eq. (2.31) as an effective static Hamiltonian, with Eq. (2.32) the interacting Hamiltonian. When these conditions lead to a LH ground state however, the static magnetic field will be in the in-plane direction since LHs couple strongly to in-plane fields, and it will be manipulated only by electric means.

From Eq. 2.32 it can be seen that the linear g -factor does not couple heavy-hole states. This occurs because it is only coupled to the linear spin operator \mathbf{J} , see Eq. 2.19. Under compressive strain in the SiGe quantum well, the HH and LH subbands are separated by a few meV, and the ground state g -factor in the in-plane directions is suppressed as it is off-diagonal, being proportional to the HH-LH mixing. This implies that the linear in-plane g -factor in the ground state manifold is tunable through the electric field mixing of HH and LH.

On the other hand, the cubic g -factor couples magnetic fields with the operator $\mathcal{J} = (J_x^3, J_y^3, J_z^3)$. This third order spin operator is the only term in the total Hamiltonian Eq. (2.15) that directly couples HH Kramer doublets. Although the cubic g -factor is small, it is not negligible when the linear g -factor is suppressed and can even be the dominant term for an in-plane magnetic field.

Regarding the interaction with electric fields, in the effective static Hamiltonian Eq. (2.31) it can be seen that non-zero vertical electric fields already mix the HH and LH states through the off-diagonal T_d symmetry interaction with the acceptor ion. This extra mixing is quite important in the case of electric manipulation of a HH state, as it allows the interaction with in-plane electric fields via both the Rashba and the T_d symmetry terms in Hamiltonian Eq. (2.32).

2.7.1 HH-LH splitting

The HH-LH splitting is sensitive to confinement and strain. This implies that this parameter is strongly affected by several of the fixed conditions of the quantum well and acceptor such as the difference in composition between the quantum well and the barrier x_1 , x_2 and x_3 , the quantum well width L , the relative acceptor position z_0 and even the vertical electric field F_z . The strain conditions are determined by the quantum well composition and, as discussed previously, can favor HH or LH ground states depending on whether strain is compressive or

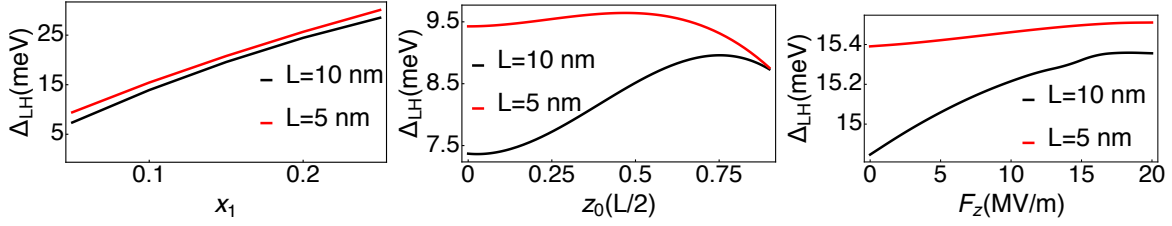


FIGURE 2.11: HH-LH ($\Delta_{\text{LH}} = E_{\text{HH}} - E_{\text{LH}}$) splitting as a function of different parameters assuming $x_2 = x_3 = 0$. (Left) The acceptor is positioned at the center of the quantum well ($z_0 = 0$) and no electric field is applied. The splitting is shown as a function of the Germanium composition in the quantum well x_1 . (Center) For $x_1 = 0.05$ and zero electric field, the splitting is shown as a function of the acceptor position in units of $L/2$. (Right) $x_1 = 0.1$ and $z_0 = 0.6L/2$ are constant and the splitting is shown as a function of the vertical electric field. Positive electric field pushes the wavefunction against the closest interface in this case.

tensile respectively. On the other hand, as discussed for hard walls, confinement also splits the four-fold degeneracy but in this case, it always favors the HH ground state.

In Fig. 2.11 the dependence on all these parameters is shown for different cases for which the ground state is HH like. In the left-hand figure the effects of strain are shown. Simply by going to $x_1 = 0.05$ the strain induced splitting is bigger than 5 meV. This splitting grows fast with x_1 and, for $x_1 \geq 0.25$ (keeping $x_2 = 0$) the first LH Kramer doublet is no longer the first excited state. The acceptor position slightly modifies the splitting from the strain conditions by increasing the splitting when getting closer to an interface. There is now a new effect coming from the difference in effective masses between Si and SiGe. This difference in effective masses reduces the binding energy in the SiGe barrier and gives rise to a reduction in the binding energy that competes against the increase coming from the confinement conditions. Finally, the vertical electric field can be used to further increase the confinement against one of the interfaces. In Fig. 2.11(c) $x_1 = 0.1$, reducing the wavefunction density inside the SiGe barrier even for high fields so the reduction of the binding energy in the quantum well is not relevant in this case. The increasing confinement translates again into an increase in the energy separation. Another general effect in these figures is the effect of the quantum well width. In the three cases it can be seen that a quantum well with smaller L has intrinsically a higher HH-LH separation, due to the increased confinement. It has also an effect on the dependence on z_0 and F_z since the tight confinement reduces the freedom of movement in the hole wavefunction, which is translated into a reduced effect of z_0 and F_z in comparison to wider quantum wells where the hole only sees a single interface.

In Fig. 2.12 two cases where $x_3 > x_1$ are shown. The dependence of Δ_{LH} on the parameters z_0 and F_z is the same than in Fig. 2.11, being the tensile strain the main difference. In these cases it can be seen how the tensile strain forces a LH ground state ($\Delta_{\text{LH}} < 0$) but an increased confinement via vertical fields can be used to change the sign of Δ_{LH} and get to a HH ground state.

In summary, the strain conditions imposed by the quantum well composition dominate the value of $\Delta_{\text{LH}} = E_{\text{HH}} - E_{\text{LH}}$ in Si/SiGe quantum wells but other effects coming from the hole wavefunction confinement can slightly modify this behavior. In particular under compressive strain the ground state is always HH like, but carefully selecting x_3 to create tensile strain conditions allows the possibility of getting a LH ground state. In the latter case, the ability to increase confinement via electric fields allows a higher tunability since both HH and LH ground states can be achieved.

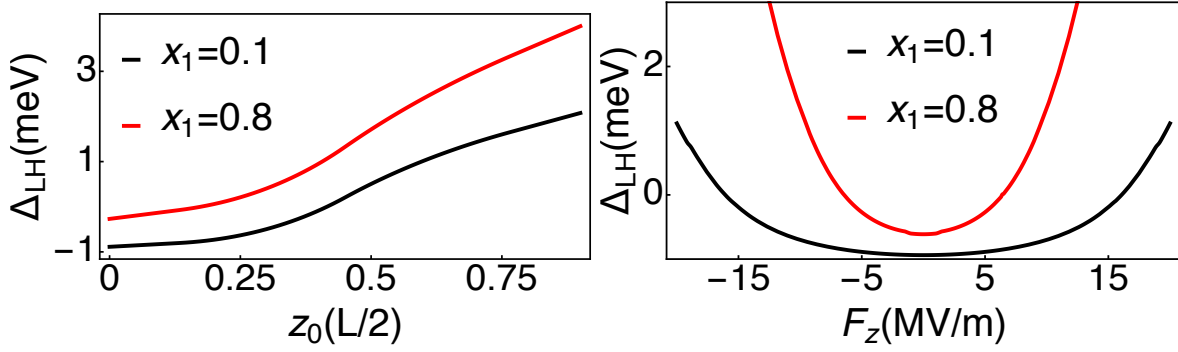


FIGURE 2.12: HH-LH ($\Delta_{LH} = E_{HH} - E_{LH}$) splitting as a function of different parameters assuming $x_3 = x_1 + 0.05$ and $x_2 = x_1 - 0.1$. (Left) For two values of x_1 and $F_z = 5$ MV/m, the splitting is shown as a function of the acceptor position in units of $L/2$. (Right) For two values of x_1 and $z_0 = 0$ the splitting is shown as a function of the vertical electric field.

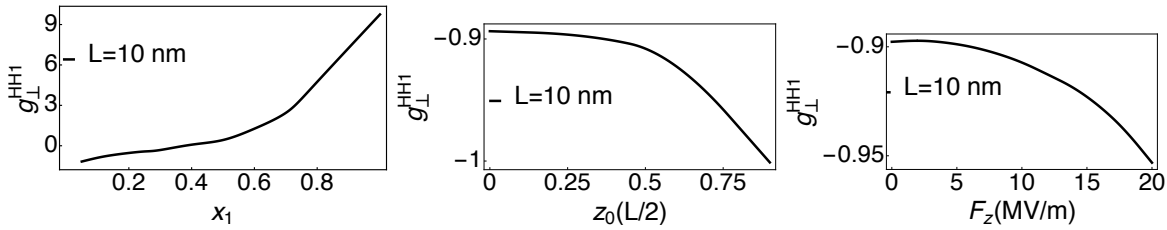


FIGURE 2.13: Effective g -factor g_{\perp}^{HH} as a function of different parameters assuming $x_2 = x_3 = 0$. (Left) The acceptor is positioned at the center of the quantum well ($z_0 = 0$) and no electric field is applied. The g -factor is shown as a function of the Germanium composition in the quantum well x_1 . (Center) For $x_1 = 0.1$ and zero electric field, the g -factor is shown as a function of the acceptor position in units of $L/2$. (Right) $x_1 = 0.1$ and $z_0 = 0.3L/2$ are constant and g_{\perp}^{HH} is shown as a function of the vertical electric field.

2.7.2 g -factor

In this subsection the focus is on the perpendicular g -factor g_{\perp}^{HH} for simplicity, since all other effective g -factors behave similarly. At the same time Hs are more susceptible to this g_{\perp} than g_{\parallel} , so g_{\perp} already gives the qualitative picture. As can be seen in Fig. 2.13 the effective g -factor g_{\perp}^{HH} is affected by all the parameters of the quantum well. Fig. 2.13(Left) shows how this g -factor changes with x_1 for an acceptor in the middle of the well and no electric field. The behavior is analogous to the observed in Fig. 2.3, as expected. Si has a negative g -factor, and it is smaller than in Ge in absolute value. The effective g -factor inherits the properties of the bulk values. Comparing with Fig. 2.3 the value of g_{\perp}^{HH} is enhanced. This is because the effective g -factor of a HH state is expected to be around $3/2g_{bulk}$ since HH is associated to the $m_J = 3/2$ state. More interestingly, the value of the g -factor strongly depends on the density of the wavefunction in the barriers. 2.13(Left) shows how by placing the acceptor near a single barrier, the g -factor is modified. In general since the bulk g -factor is negative for $x < 0.4$ and positive for $x > 0.4$ we can expect that an acceptor close to the interface is going to have a reduced (more negative) effective g -factor near the interface in all the cases, being bigger in absolute value when $x < 0.4$ and smaller when $x > 0.4$. This behavior is also obtained under the influence of a vertical electric field. By increasing F_z the density of the wavefunction inside the barriers is increased, allowing the tunability of the g -factor by electrical means. This will be of particular interest for manipulation via the g -Tensor Modulation Resonance technique that will be discussed in the following chapter.

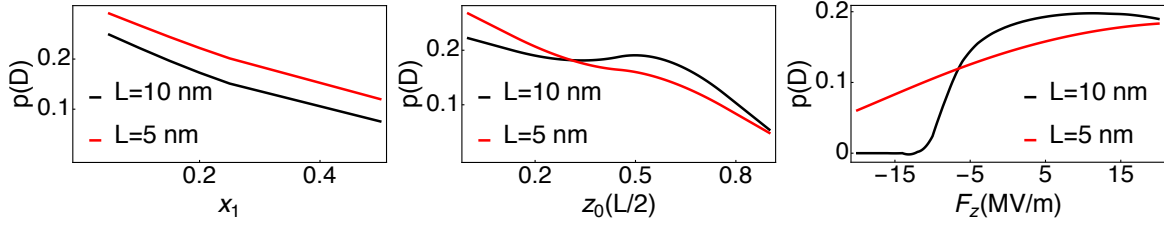


FIGURE 2.14: Estimate of the dipolar coupling p . (Left) The acceptor is positioned at the center of the quantum well ($z_0 = 0$) and no electric field is applied. The value of p is shown as a function of the Germanium composition in the quantum well x_1 . (Center) For $x_1 = 0.1$ and zero electric field, p is shown as a function of the acceptor position in units of $L/2$. (Right) $x_1 = 0.1$ and $z_0 = 0.6L/2$ are constant and p is shown as a function of the vertical electric field.

2.7.3 Dipolar coupling p

The value of the dipolar coupling is calculated using the formula in Eq. 2.30. For a B acceptor in Si, its value is $0.26D$. Its value for other acceptors are tabulated in [223] and can be seen in Table 2.3, but there is no available data for acceptors in Ge or SiGe. In any case, Eq. 2.30 already has a material dependent component since it is a measurement of the wavefunction density at the central cell. In Ge the hole wavefunction is more spread due to the much bigger Bohr radius compared to Si. As a result, the obtained value for Ge will be suppressed in comparison to the value in Si.

This can be seen in Fig. 2.14(Left). The value of p is strongly reduced by increasing the Ge content of the quantum well x_1 . Narrower wells show an increased value of p . This is due to the fact that a narrower well further compresses the hole wavefunction, increasing the density wavefunction near the acceptor impurity. As the position of the acceptor is closer to one of the interfaces, p is reduced due to the repulsion of the hole wavefunction away from the interface, similar to what happens with a single interface. The electric field in Fig. 2.14(Right) can strongly affect its value too. By pushing the wavefunction away from the impurity, p is reduced. On the other hand p can be enhanced when F_z compensates the position of the acceptor, reaching a maximum. It is important to note that, depending on parameters such as L and z_0 , under strong electric field conditions, such as when $F_z < -15$ MV/m in Fig. 2.14(Right), the hole can be completely ionized from the acceptor impurity making $p = 0$.

2.7.4 Rashba coefficient

The Rashba coefficient α is non-zero as a result of the lack of inversion symmetry. This means that an acceptor in the center of the quantum well with no electric field applied has $\alpha = 0$. The value of α is particularly relevant for manipulation because it couples in-plane electric fields with the spin degree of freedom. The Rashba coefficient can be increased by placing the acceptor away. Its value is obtained by a SW transformation, see Appendix B.

Fig. 2.15 shows the value of this coefficient as a function of several parameters. Fig. 2.15(Left) shows a material dependence through the parameter x_1 . This is related to the same material dependence mechanism in the dipolar coupling p . The more Ge content, the bigger Bohr radius of the hole wavefunction, and the wavefunction becomes more sensitive to the presence of interfaces such that the inversion symmetry is easily reduced. While a hole in Si may start

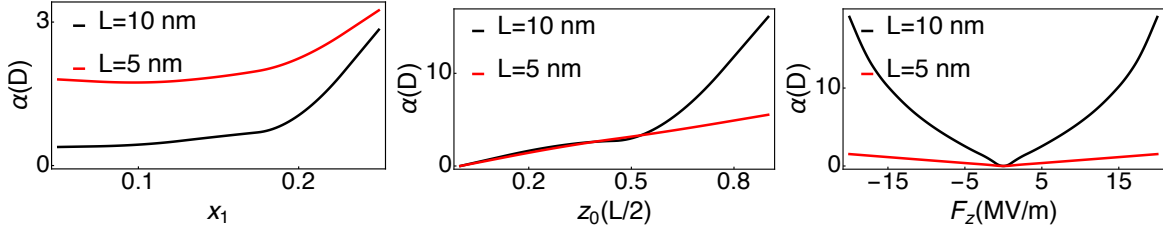


FIGURE 2.15: Rashba coupling α as a function of different parameters. (Left) The acceptor is positioned at $z_0 = 0.3L/2$ and no electric field is applied. The value of α is shown as a function of the Germanium composition in the quantum well x_1 . (Center) For $x_1 = 0.1$ and zero electric field, α is shown as a function of the acceptor position in units of $L/2$. (Right) $x_1 = 0.1$ and $z_0 = 0$ are constant and α is shown as a function of the vertical electric field.

feeling the interface at a distance around 5 nm, in Ge it starts to feel it more than 10 nm away. Another clear dependence comes from L : the narrower the quantum well, the more confined the wavefunction is and then the harder its inversion symmetry is affected by the two interfaces. This gives higher α for wider quantum wells and higher x_1 . In Fig. 2.15(Center) the value of z_0 shows that the closer the acceptor to a single interface the higher α . The large value of α is not only due to the Ge content but also because the two interfaces reduce the symmetry further than a single interface, although this mechanism is detrimental when $z_0 \approx 0$ due to an increase in the symmetry. Fig. 2.15(Right) shows that even for an acceptor near $z_0 = 0$ big values of α can be obtained by moving the hole wavefunction against one interface. Here it is also shown that narrow quantum wells are not only detrimental due to the higher symmetry that provides the further confinement but also because the envelope becomes more insensitive to electric fields in comparison to wider wells.

2.8 Conclusions

In this chapter we have used an effective mass approach to study the effect of confinement on the group III acceptor energy spectra and bound states symmetry in group IV semiconductors. This method, though computationally less demanding than tight-binding, has been proven to be very reliable not only for the calculation of binding energies but also for the wavefunctions [232]. A semiconductor/insulator interface introduces a specific boundary condition and the corresponding dielectric mismatch implies new attractive potential terms in the Hamiltonian. The combined effect of the quantum confinement and the dielectric mismatch gives rise to energy shiftings which depend on the distance between the acceptor and the interface and the value of the insulator dielectric constant. In general terms the full energy spectrum is compressed, namely, the distance between the ground state and the excited states is reduced by the confinement but this reduction is partially compensated by the dielectric mismatch [208]. Central cell effects, which account for the binding energies dependance on the acceptor species, become less important when acceptors get closer to the interface with the insulator. Therefore, different acceptors close to an interface may be difficult to distinguish by the values of their binding energies.

We have also followed the modifications on the symmetry of the bound states which can be qualitatively understood via the analysis of the symmetry breaking induced by the interface. One of the consequences of this symmetry reduction is the splitting of the four-fold ground state in two Kramers doublets, as reported in Ref. [140]. This doublet splitting is independent of the dielectric mismatch for a particular host:acceptor combination. Different acceptors lead

to comparable values of the interface induced doublet splitting, which is typically $\gtrsim 1$ meV. Our results are in very good agreement with the measurements in Ref. [140].

The variational method was also adapted for SiGe quantum wells, allowing us to perform a similar analysis for a different type of confinement. In this case the results can be easily related to those obtained from the single interface case, being the natural appearance of strain the biggest difference. This strain dominates the ground state splitting and depending on the difference between lattice constants between the well and the substrate, both tensile and compressive strain can be achieved. When the well is under compressive strain the ground state is inevitably of HH nature. On the other hand, tensile strain favors LH states and competes against the quantum confinement. This competition is interesting since it allows the possibility of tuning the nature of the ground state by changing the confinement within the well via external fields, which is useful to define a flexible qubit where the interaction between LH and HH states is also tunable.

Finally, together with the Schrieffer-Wolff transformations described in Appendix B, this method allows the mapping of the four-fold ground state onto an effective Hamiltonian that includes the effect of the interface, electric fields and magnetic fields. The values of the different parameters for a single interface are in excellent agreement with those obtained with a finite differences method in Refs. [125, 126]. These effective Hamiltonians are the cornerstones of Chapters 3 and 4.

Qubit manipulation in SiGe quantum wells ¹

3.1 Introduction

In the previous chapter we justified the interest in acceptor states by the intrinsic spin-orbit interaction in the valence band in silicon. It was shown that confinement can strongly affect the effective Hamiltonian of the lowest states, but it is in this chapter where the impact of quantum confinement on holes for manipulating the quantum states is characterized. The strong spin-orbit interaction of this system makes desirable to look for ways to manipulate the qubit states only by electric fields, in particular, we focus on techniques such as electric dipole spin resonance (EDSR) [191, 233] or g-tensor modulation resonance (g-TMR) [234].

Quantum confinement has an important influence on the ground state mixing between light holes $m_J = \pm 1/2$ and heavy holes $m_J = \pm 3/2$ [127]. The manipulation by electric means of holes in silicon has been recently achieved in nanowires [235]. Acceptors in silicon have an intrinsic T_d symmetry term that allows an extra heavy hole - light hole mixing under the application of electric fields [198, 199]. This T_d symmetry term, together with the lack of inversion symmetry that can be provided through electric fields or by the nanostructure confinement itself, can lead to the enhancement of the SOI via a Rashba type interaction. This interaction can create a sweet spot for specific values of the electric field in an EDSR manipulated light-hole acceptor qubit, allowing both fast operations and high coherence times [125, 126].

A strong SOI, together with quantum confinement, can also result in electrically tunable g -factors [127, 131]. It has also been shown that the confinement can generate an anisotropy in the g -factor for different states [128–130]. A heavy hole state in a quantum well has a suppressed g -factor in the plane parallel to the quantum well, while in the case of a light hole the g -factor is suppressed in the perpendicular direction. Both the anisotropy and the tunability of the g -factor are requirements for an electrically manipulated spin qubit by g-TMR [234, 236]. Indeed, the control of g -factors of holes in silicon nanowires has been proven [237].

¹Results published in [190].

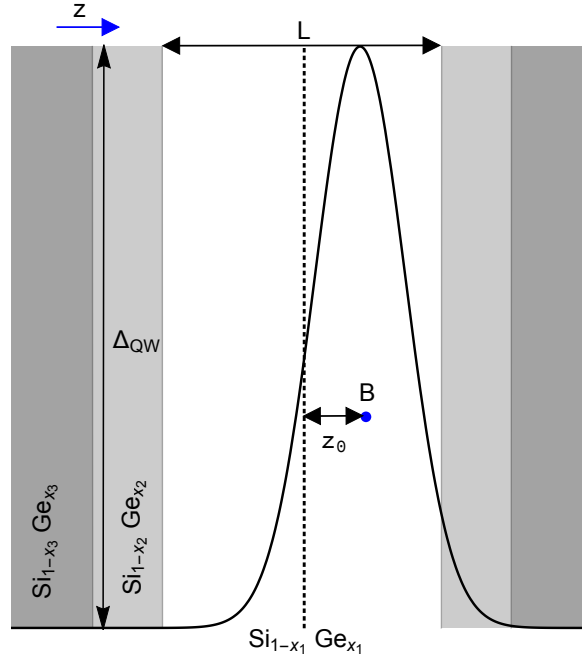


FIGURE 3.1: Sketch of the quantum well heterostructure and the bound hole envelope wave-function along the perpendicular z direction. L is the width of the well, z_0 determines the acceptor position from the well center, Δ_{QW} is the barrier height, and x_1 , x_2 , and x_3 indicate the proportion of Germanium on each of the layers. $x_1 > x_2$ for defining the quantum well for holes. The substrate (with composition $\text{Si}_{1-x_3}\text{Ge}_{x_3}$) is relaxed and fixes the lattice parameter in the whole heterostructure. This determines the sign of the strain on the quantum well and is hence related to whether the doublet ground state is heavy-hole ($x_3 = x_2$) or light-hole ($x_3 > x_1$) like.

Good coherence and relaxation times together with the different possibilities of manipulation with electric fields is what make hole systems in silicon an interesting platform for quantum computing. The intrinsic T_d symmetry of the acceptor together with the symmetry reduction due to the quantum confinement allows the possibility of manipulation by electric means. In this chapter we are interested in exploring spin qubit manipulation with acceptors in SiGe heterostructure quantum wells. The different germanium content of the barrier and quantum well allows g -factor manipulation and also changes the sensitivity to Rashba interacting terms due to a larger Bohr radius. Depending on the type of strain in the $\text{Si}_{1-x}\text{Ge}_x$ quantum well, HH or LH qubits can be defined. For HH qubits, we explore three different ways of manipulating the acceptors: electron spin resonance with magnetic fields (ESR), EDSR and g -TMR. For LH qubits, we focus on pure electric manipulation (EDSR).

To explore all these alternatives, we use the effective mass approach described in the previous chapter with the Kohn-Luttinger Hamiltonian for a bulk acceptor in a group IV semiconductor host [44, 217–219], together with the effects of the quantum well barriers, the Bir-Pikus Hamiltonian [198, 199] for including the strain in the quantum well, and the effect of electric and magnetic fields. The result of these EMT simulations is mapped onto the effective Hamiltonian obtained in subsection 2.7. We will show how strain, which dominates the HH-LH splitting, hinders the manipulation by both electric and magnetic fields, while the asymmetry due to the acceptor position within the well or the presence of a vertical electric field facilitates the electric field manipulability. The g -factors dependence on the heterostructure composition is also an important factor for both magnetic and electric field manipulation.

We find that a LH qubit can be manipulated much faster than a HH one but the latter benefits of much longer relaxation times due to a larger HH-LH splitting. On the other hand, the presence of sweet spots in the LH qubit protects it from charge noise.

3.2 Heavy-hole based qubit

Typically, p-type SiGe quantum wells are compressively strained as they require $x_2 < x_1$, and the strain is maintained in the simplest experimental case $x_3 = x_2$. In this case both the quantum confinement and strain favor the HH states over LH states, see Fig. 2.10(Left), with a few meV HH-LH splitting. As the HH in-plane g -factors are known to be suppressed under these circumstances we will consider a perpendicular magnetic field to split the HH Kramer doublet. From Eq. 2.31, we know that the effective static Hamiltonian of a HH qubit in the $\{3/2, -3/2, 1/2, -1/2\}$ basis is:

$$H_0^{\text{HH}}(\mathbf{F}_z, \mathbf{B}_z) = \begin{pmatrix} E_{\text{HH}}(\mathbf{F}_z) & 0 & 0 & -ip\mathbf{F}_z \\ 0 & E_{\text{HH}}(\mathbf{F}_z) & ip\mathbf{F}_z & 0 \\ 0 & ip\mathbf{F}_z & E_{\text{LH}}(\mathbf{F}_z) & 0 \\ -ip\mathbf{F}_z & 0 & 0 & E_{\text{LH}}(\mathbf{F}_z) \end{pmatrix} + \mu_B \mathbf{B}_z \begin{pmatrix} g_{\perp}^{\text{HH}} & 0 & 0 & 0 \\ 0 & -g_{\perp}^{\text{HH}} & 0 & 0 \\ 0 & 0 & g_{\perp}^{\text{LH}} & 0 \\ 0 & 0 & 0 & -g_{\perp}^{\text{LH}} \end{pmatrix}. \quad (3.1)$$

The Hamiltonian for the interaction with in-plane magnetic and electric fields is then:

$$H_{\text{int}}^{\text{HH}}(\mathbf{E}_{\parallel}, \mathbf{B}_{\parallel}) = \begin{pmatrix} 0 & 0 & -ip\mathbf{E}_+ + \alpha\mathbf{E}_- & 0 \\ 0 & 0 & 0 & -ip\mathbf{E}_- - \alpha\mathbf{E}_+ \\ ip\mathbf{E}_- + \alpha\mathbf{E}_+ & 0 & 0 & 0 \\ 0 & ip\mathbf{E}_+ - \alpha\mathbf{E}_- & 0 & 0 \end{pmatrix} + \mu_B \begin{pmatrix} 0 & \tilde{g}'_{\parallel} B_+ & \frac{\sqrt{3}}{2} \tilde{g}'_{\parallel} B_- & 0 \\ \tilde{g}'_{\parallel} B_- & 0 & 0 & \frac{\sqrt{3}}{2} \tilde{g}'_{\parallel} B_+ \\ \frac{\sqrt{3}}{2} \tilde{g}'_{\parallel} B_+ & 0 & 0 & \tilde{g}'_{\parallel} B_- \\ 0 & \frac{\sqrt{3}}{2} \tilde{g}'_{\parallel} B_- & \tilde{g}'_{\parallel} B_+ & 0 \end{pmatrix}. \quad (3.2)$$

from which we can already tell that the two HH states can only be coupled to first order with in-plane magnetic fields. In order to manipulate a HH or LH Kramer doublet through electric fields, a HH-LH coupling is required. From Eq. (3.1) it can be seen that vertical electric fields can increase this coupling via the local T_d symmetry term, however the interaction is inversely proportional to the HH-LH energy separation.

The Rabi frequencies for each type of manipulation can be obtained by applying a SW transformation to get the effective Hamiltonian of the qubit levels. The off-diagonal terms can be used to perform rotations in the qubit basis. The energy of these off-diagonal terms can be trivially transformed into the Rabi frequency ($E_{01} = \hbar\omega_{\text{Rabi}}$). The linear terms in the in-plane magnetic field give the Electron Spin Resonance (ESR) Rabi frequency, while the linear terms in the in-plane electric field give rise to the EDSR Rabi frequency.

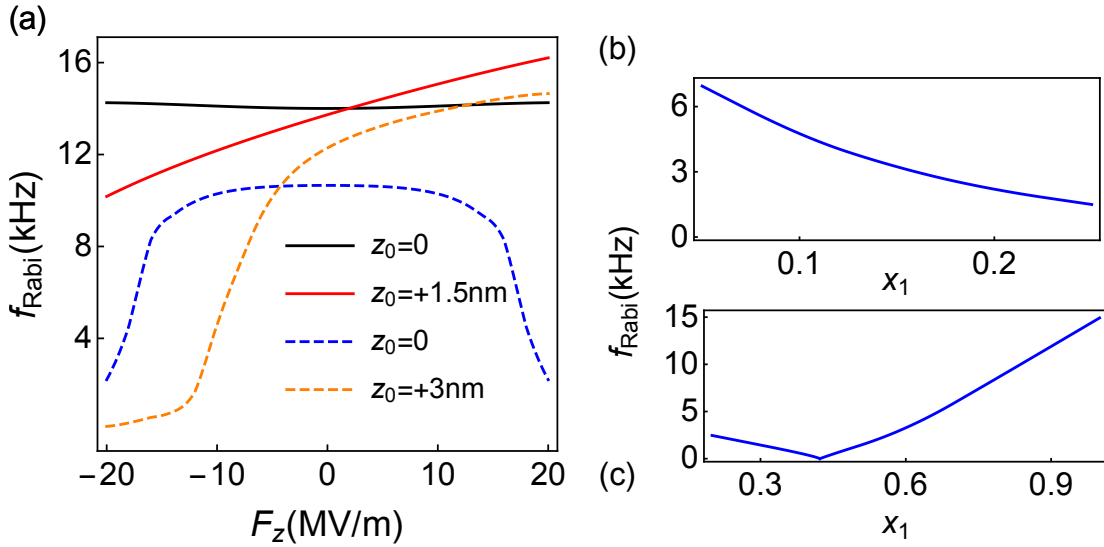


FIGURE 3.2: ESR Rabi frequency (a) as a function of the perpendicular electric field for $L = 5$ nm (solid lines) and $L = 10$ nm (dashed lines) and different values of z_0 . $x_1 = 0.05$, and $x_2 = x_3 = 0$; (b) for $L = 10$ nm as a function of x_1 with $x_2 = x_3 = 0$, $z_0 = 0.6\frac{L}{2}$ and $F_z = 10$ MV/m; (c) same as (b) with $x_3 = x_2 = x_1 - 0.05$. The amplitude of the in-plane oscillating magnetic field applied is 0.1 mT and the constant magnetic field applied in the z -direction is 1 T.

3.2.1 Electron Spin Resonance

Spin manipulation can be readily achieved by applying oscillating in-plane magnetic fields, see Eq. 3.2, which directly couple the two heavy hole states proportionally to \tilde{g}_{\parallel} . Therefore, the Rabi frequency can be enhanced by increasing the in-plane g -factor. As the quantum well and the quantum barrier have different g -factors, increasing the density of the hole wavefunction in the region with a larger g -factor in absolute value will also increase the Rabi frequency of the ESR manipulation. Here we evaluate the effect on the in-plane effective g -factors of three different parameters: The proportion of Germanium x in the SiGe alloy, the applied perpendicular electric field F_z , and the position of the acceptor within the quantum well z_0 .

The dependence of the (bulk) g -factor on the Germanium content x is shown in Fig. 2.3 and is clearly inherited by the effective g -factors, see Fig. 2.13(Left). This implies that, for instance, for $x_1 < 0.4$ and $x_2 < x_1$, increasing the wavefunction density in the barrier enhances the g -factor. The opposite happens for $x_1 > 0.6$ and $x_2 < x_1$. On the other hand, as $x_1 - x_2$ increases so does the barrier height due to the strain (see Eq. 2.17), making it harder for the wavefunction to penetrate the barrier. z_0 also affects the penetration in the barriers: the closer the acceptor is to the barriers, the larger the density probability in them.

The role of F_z is more complex. On one hand, it can modulate the wave-function probability density in the different layers. However, the electric field has more consequences on the acceptor physics as it changes the HH-LH mixing through the T_d symmetry term (the ipF_z components in Eq. 3.1). In principle, increasing F_z would increase the linear g -factor but the effective dipole moment p , which is proportional to the wave function probability density near the acceptor, can be simultaneously reduced, limiting the effect of this term in the total

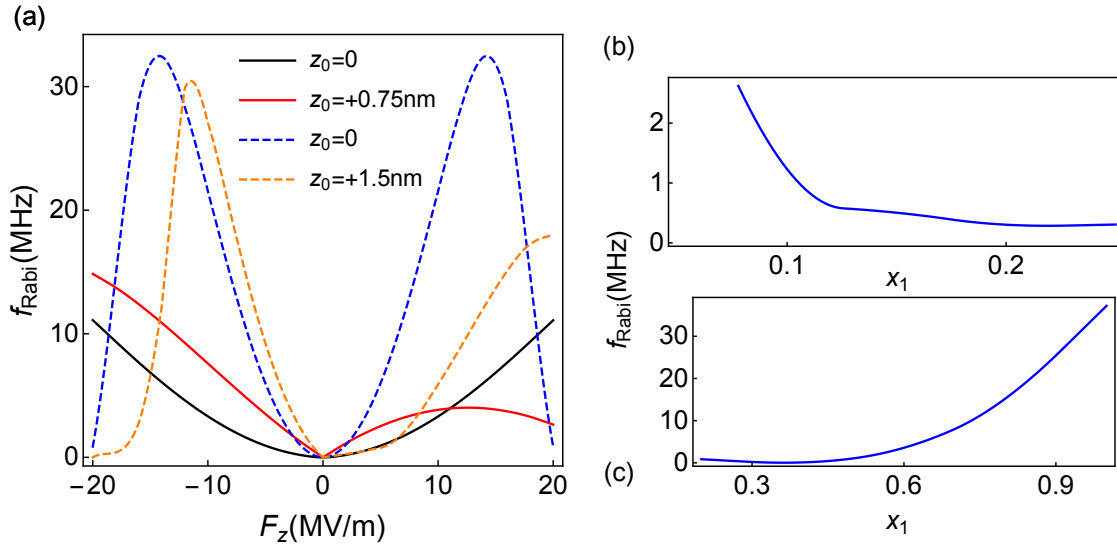


FIGURE 3.3: EDSR Rabi frequency as (a) a function of the perpendicular electric field for $L = 5$ nm (solid lines) and $L = 10$ nm (dashed lines) and different values of z_0 . $x_1 = 0.05$, and $x_2 = x_3 = 0$; (b) for $L = 10$ nm as a function of x_1 with $x_2 = x_3 = 0$, $z_0 = 0.6\frac{L}{2}$ and $F_z = 10$ MV/m; (c) same as (b) with $x_3 = x_2 = x_1 - 0.05$. The in-plane oscillating electric field is taken as 50 kV/m and the constant magnetic field applied in the z -direction is 1 T.

Hamiltonian. The value of p can also be affected by L (smaller widths increases probability density) and by x (as the Bohr radius in Ge is larger than in Si), see Fig. 2.14.

Fig. 3.2 illustrates the previous remarks. For small values of L ($L = 5$ nm for the solid lines in Fig. 3.2(a)) the effect of F_z is small as the wave function is more constrained. Off-centered acceptors ($z_0 \neq 0$) are more easily manipulated by electric fields which push the wavefunction towards the farthest away interface. With Si barriers ($x_2 = 0$), Fig. 3.2(b), the Rabi frequency is suppressed as a function of x_1 but a significant enhancement can be achieved in all-SiGe heterostructures, as $\text{Si}_{1-(x_1-0.05)}\text{Ge}_{x_1-0.05}/\text{Si}_{1-x_1}\text{Ge}_{x_1}/\text{Si}_{1-(x_1-0.05)}\text{Ge}_{x_1-0.05}$, once $x_1 > 0.6$, as shown in Fig. 3.2(c). In summary, the best conditions to enhance the ESR Rabi frequency are achieved by quantum wells with large x_1 and by choosing the acceptor position and electric fields such that most of the wavefunction density is in the region with larger g -factor. Wider quantum wells make it easier to tune the Rabi frequency with electric fields.

Note that the Rabi frequencies achieved by magnetic field manipulation are orders of magnitude smaller than the ones obtained by electric field manipulation, as shown in the following, so in practice the magnetic field manipulation would not be advisable.

3.2.2 Electric Dipole Spin Resonance

Spin-orbit interaction provides us with an electric knob to manipulate spins. The spin-orbit interaction is produced by the inversion symmetry breaking (Rashba α terms in Eq. 3.2) in the heterostructure and by the acceptor T_d symmetry (p terms in Eq. 3.2). These terms induce an extra mixing between the HHs and LHs allowing a purely electric field manipulation with in-plane oscillating fields.

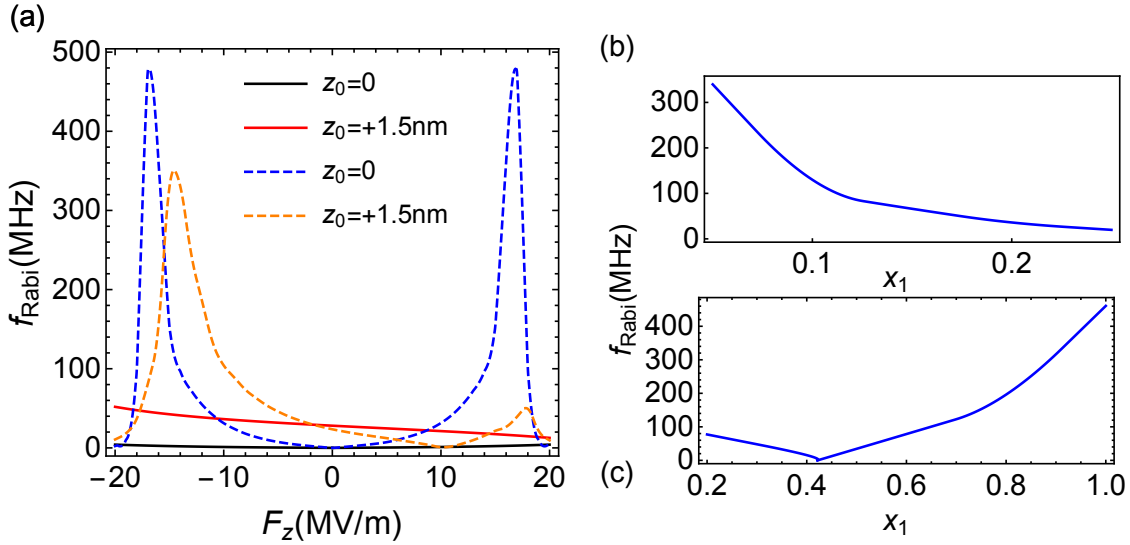


FIGURE 3.4: g-TMR Rabi frequency as (a) a function of the perpendicular electric field for $L = 5$ nm (solid lines) and $L = 10$ nm (dashed lines) and different values of z_0 . $x_1 = 0.05$, and $x_2 = x_3 = 0$; (b) for $L = 10$ nm as a function of x_1 with $x_2 = x_3 = 0$, $z_0 = +3$ nm, $F_z = -10$ MV/m, and $|\mathbf{B}| = 1$ T; (c) same as (b) with $x_3 = x_2 = x_1 - 0.05$.

The HH-LH coupling is limited by excessive strain and by large $x_1 - x_2$, both splitting the HH-LH manifolds by several meV and hence reducing drastically the EDSR term. As shown in Fig. 3.3 the absence of a perpendicular electric field F_z leads to zero coupling.

As discussed in the previous chapter the Rashba term gets stronger by reducing the inversion symmetry. This symmetry is broken by placing the acceptor on an off-centered position and by applying a perpendicular electric field. The barrier height can also increase the Rashba coupling but in exchange this implies higher strain and lower HH-LH coupling. The quantum well width can also be important: the wider the quantum well, the more room the wavefunction has to shift, allowing higher Rashba couplings. Another interesting factor is the Bohr radius in the material. Contrary to the T_d term, which is suppressed when the Bohr radius is big (namely, for large Ge content), the Rashba term is enhanced due to the higher sensitivity to the inversion asymmetry induced by one of the barriers.

Figs. 3.3 (b) and (c) show the dependence of the EDSR Rabi frequency on x_1 for a Si and a $\text{Si}_{1-(x_1-0.05)}\text{Ge}_{x_1-0.05}$ barrier, respectively. A large Ge content in the well, together with a small $x_1 - x_2$ difference, gives rise to a significant enhancement of the Rabi frequency due to the increasing Bohr radius.

3.2.3 g-Tensor Modulation Resonance

The quantum confinement and the strain suppresses the in-plane g -factor in comparison to the out of plane g -factor of heavy-holes, creating an anisotropy in the g -tensor. This anisotropy depends on applied perpendicular electric fields by means both of the spin-orbit interaction and the different content of Ge on the heterostructure layers. The dependence of the Rabi frequency on the g -factor modulation g -TMR by F_z can be obtained using the Bloch equations, as was done in [236]:

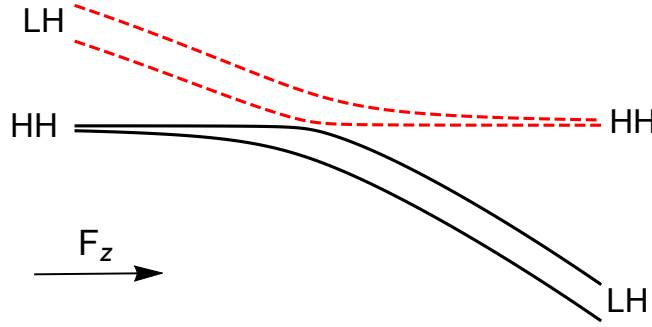


FIGURE 3.5: Sketch of the first four energy levels under tensile strain and an in-plane constant magnetic field as a function of an electric field F_z . For larger values of F_z , due to the proximity to a barrier interface, the quantum confinement competes with strain and eventually the ground state becomes of HH character. The anticrossing occurs due to the LH-HH mixing induced by the applied fields. For simplicity, the g -factor is assumed to be constant. In practice, it can decrease (increase) as a function of F_z in the concave (convex) case.

$$f_R^{gTMR} = \frac{\mu_B E_{ac}}{2h} \left[\frac{1}{g_{\parallel}} \left(\frac{\partial g_{\parallel}}{\partial F_z} \right) - \frac{1}{g_{\perp}} \left(\frac{\partial g_{\perp}}{\partial F_z} \right) \right] \frac{g_{\parallel} g_{\perp} |B|}{|g_{\parallel}| + |g_{\perp}|} \quad (3.3)$$

where E_{ac} is the oscillating component of the applied perpendicular electric field, assumed to be small enough to consider a linear dependence of the g -tensor. This oscillating field is superimposed to the static vertical electric field F_z (already considered in the Hamiltonian H_0) and is taken as $E_{ac} = 1$ MV/m in the following. The magnetic field is applied in a direction that maximizes the Rabi frequency, $\theta = \arctan\left(\sqrt{\frac{g_{\parallel}}{g_{\perp}}}\right)$ where θ is defined with respect to the in-plane direction [236]. As $g_{\parallel} < g_{\perp}$, $\theta \approx 0$.

In order to enhance the g -TMR Rabi frequency, the derivatives of the g -factors with respect to the electric field F_z have to be maximized. This condition is fulfilled for large values of x_1 and small $x_1 - x_2$ as Ge g -factors are larger. A narrow quantum well would restrain the effect of F_z on the wave-function so wide quantum wells are more desirable. For the same reason, off-centered acceptors give larger frequencies. These results are summarized in Fig. 3.4 where it is also patent that the frequencies achieved with this method are at least one order of magnitude larger than with EDSR.

3.3 Light-hole based qubit

To form a p-type quantum well with SiGe, $x_2 < x_1$ is required. If we take a substrate with different Germanium content x_3 (see Fig. 3.1) it is possible to get a tensile strained p-type quantum well when $x_3 > x_1$. In this case, the splitting caused by the tensile strain competes against the one from quantum confinement such that when the strain is large enough the ground state in the quantum well is of LH nature. Here we will focus on a regime where the ground state is LH for $F_z = 0$, but the HH-LH splitting can be tuned with the vertical field such that the ground state can become of HH character, see Fig. 2.10(Right). Proximity to the interface with the barrier (by choosing a particular z_0 or by applying large electric fields) tend to favour a HH ground state. This LH-HH proximity can lead to sweet spots in the LH

qubit subspace [125] when in-plane magnetic fields are applied to break the Kramers doublet degeneracy.

As the magnetic field here is applied in the $x - y$ plane and gives rise to an off-diagonal interaction, LH and HH are naturally mixed under in-plane magnetic fields. We consider this magnetic field in the x direction for simplicity. In the qubit subspace then, neither in-plane nor out-of-plane magnetic fields will give purely off-diagonal interaction. Moreover, as the first four states are close in energy and have different g -factor dependences, the g -TMR manipulation gives rise to complex four state dynamics, which is not considered in this thesis. Therefore, for a LH qubit we focus only on purely electric field manipulation through EDSR.

The effective Hamiltonian for a LH qubit is, in the $\{3/2, -3/2, 1/2, -1/2\}$ basis:

$$H_0^{\text{LH}}(\mathbf{F}_z, \mathbf{B}_x) = \begin{pmatrix} E_{\text{HH}}(\mathbf{F}_z) & 0 & 0 & -ip\mathbf{F}_z \\ 0 & E_{\text{HH}}(\mathbf{F}_z) & ip\mathbf{F}_z & 0 \\ 0 & ip\mathbf{F}_z & E_{\text{LH}}(\mathbf{F}_z) & 0 \\ -ip\mathbf{F}_z & 0 & 0 & E_{\text{LH}}(\mathbf{F}_z) \end{pmatrix} + \mu_B \begin{pmatrix} 0 & 0 & \frac{\sqrt{3}}{2}g_{\parallel}B_x & 0 \\ 0 & 0 & 0 & \frac{\sqrt{3}}{2}g_{\parallel}B_x \\ \frac{\sqrt{3}}{2}g_{\parallel}B_x & 0 & 0 & g_{\parallel}B_x \\ 0 & \frac{\sqrt{3}}{2}g_{\parallel}B_x & g_{\parallel}B_x & 0 \end{pmatrix}, \quad (3.4)$$

where the g -factor is mostly determined by the linear g -factor ($g_{\parallel} \approx \tilde{g}_{\parallel}$) since the in-plane g -factor of LH is not suppressed. The interaction with in-plane electric fields is

$$H_{\text{int}}^{\text{LH}}(\mathbf{E}_{\parallel}) = \begin{pmatrix} 0 & 0 & -ipE_+ + \alpha E_- & 0 \\ 0 & 0 & 0 & -ipE_- - \alpha E_+ \\ ipE_- + \alpha E_+ & 0 & 0 & 0 \\ 0 & ipE_+ - \alpha E_- & 0 & 0 \end{pmatrix} \quad (3.5)$$

Following [125] we can perform a rotation to the Hamiltonian in Eq. 3.4 to the qubit basis in the operating point F_z :

$$H_{\text{qubit}}^{\text{LH}} = \begin{pmatrix} E_l - \frac{1}{2}\varepsilon_{Zl} & 0 & Z_1 & Z_2 \\ 0 & E_l + \frac{1}{2}\varepsilon_{Zl} & Z_2 & Z_1 \\ Z_1 & -Z_2 & E_u - \frac{1}{2}\varepsilon_{Zu} & 0 \\ -Z_2 & Z_1 & 0 & E_u - \frac{1}{2}\varepsilon_{Zu} \end{pmatrix} \quad (3.6)$$

Being E_l , E_u the lower (qubit) and upper (excited) branches, with Larmor energies ε_{Zl} and ε_{Zu} respectively. Naming a_L and a_H the amplitude probability of a LH or a HH in the qubit branch, these Larmor energies are:

$$\begin{aligned} \varepsilon_{Zl} &= 2g_{\parallel}(z_0, F_z)\mu_B B \sqrt{3a_L^2 a_H^2 + a_L^4} \\ \varepsilon_{Zu} &= 2g_{\parallel}(z_0, F_z)\mu_B B \sqrt{3a_L^2 a_H^2 + a_H^4}. \end{aligned} \quad (3.7)$$

Which means that the Larmor energy of each branch is the Zeeman energy modulated by the HH-LH composition of the branches (tunable by F_z). The coupling between branches is

quantified by Z_1 and Z_2 :

$$\begin{aligned} Z_1 &= \frac{1}{2}\varepsilon_{Z_0} \cos(\theta_l/2 - \theta_u/2 - \theta_o) \\ Z_2 &= \frac{i}{2}\varepsilon_{Z_0} \sin(\theta_l/2 - \theta_u/2 - \theta_o), \end{aligned} \quad (3.8)$$

where θ_l , θ_u and θ_o are phases related to the HH-LH mixing of each branch; whose physical meaning will be discussed in the next chapter. More importantly, ε_{Z_0} is the Zeeman coupling between branches:

$$\varepsilon_{Z_0} = 2g_{\parallel}(z_0, F_z)\mu_B B \sqrt{3(a_H^4 + a_L^4) - 2a_L^2 a_H^2} \quad (3.9)$$

Using a SW transformation (see Appendix B) we can now obtain the effects of the interacting Hamiltonian 3.5 in the qubit subspace. This becomes:

$$H_{int}^{(2)} = DE_{\parallel}\sigma_x \quad (3.10)$$

Which means that an oscillating in-plane electric field can be used to perform single-qubit rotations with a dipolar moment D :

$$D = \frac{1}{2} \frac{\varepsilon_{Z_0}}{E_l - E_u} \left(\alpha \cos(\theta_o - \theta_{\parallel}) + p \sin(\theta_o - \theta_{\parallel}) \right), \quad (3.11)$$

being θ_{\parallel} the EDSR angle $E_{\parallel}(\cos \theta_{\parallel}, \sin \theta_{\parallel})$. θ_o is the phase associated to the qubit-excited coupling and whose value is $\theta_o \approx \pi/4$ in the sweet spots, regions in the F_z parameter space where the qubit is insensitive to charge noise, that are going to be considered. Since in general $\alpha \gg p$, choosing $\theta_{\parallel} = \pi/4$ maximizes the coupling D in Eq. 3.11. The main difference with previous work [125, 126] is the electric field dependence of the g -factor. Depending on the behavior of the g -factor as a function of the electric field (which can push the wave-function inside the barriers) we will distinguish two cases: The *convex* LH qubit, where the g -factor grows when increasing the density wavefunction within the barriers (for $x_1 \lesssim 0.4$), and the *concave* LH qubit where the g -factor decreases when increasing the density wavefunction in the barriers (for $x_1 \gtrsim 0.4$). This behavior shows in the Larmor frequency and affects the conditions for the sweet spots.

3.3.1 Convex LH qubit

The Larmor frequency inherits the convex behavior of the g -factor as long as the ground state is LH (namely, for small values of F_z). The implications are shown in Fig. 3.6: there is a sweet spot at the minimum of the g -factor and from there the qubit frequency grows due to both the g -factor increasing and the interaction with the T_d symmetry term. For larger values of F_z , there is a HH-LH anticrossing at which the g -factor decreases because the HH in-plane g -factor is suppressed, giving rise to another sweet spot. This last sweet spot appears both at positive and negative electric fields due to the symmetry of the quantum well. In total there might be up to three sweet spots, with positions that depend on several parameters, particularly the acceptor position z_0 .

Regarding the Rabi frequencies, the off-diagonal terms in the qubit subspace come mostly from the Rashba interaction so they grow by reducing the inversion symmetry, becoming maximal at the HH-LH anticrossing. Near the sweet spots, this gives rise to very large Rabi frequencies compared with the HH qubit ones.

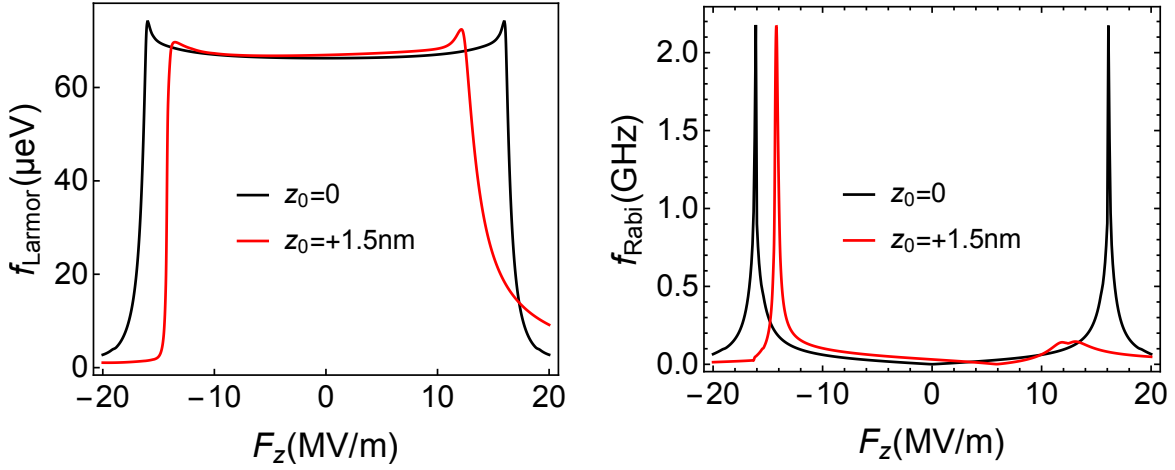


FIGURE 3.6: (Left) Larmor frequency of the convex LH qubit in μeV as a function of the electric field for $x_1 = 0.1$, $x_2 = 0$, $x_3 = 0.06$, $B = 1\text{ T}$, $L = 10\text{ nm}$. (Right) Rabi frequency of the LH qubit for the same parameters as (Left) and assuming an in-plane oscillating electric field of 50 kV/m .

3.3.2 Concave LH qubit

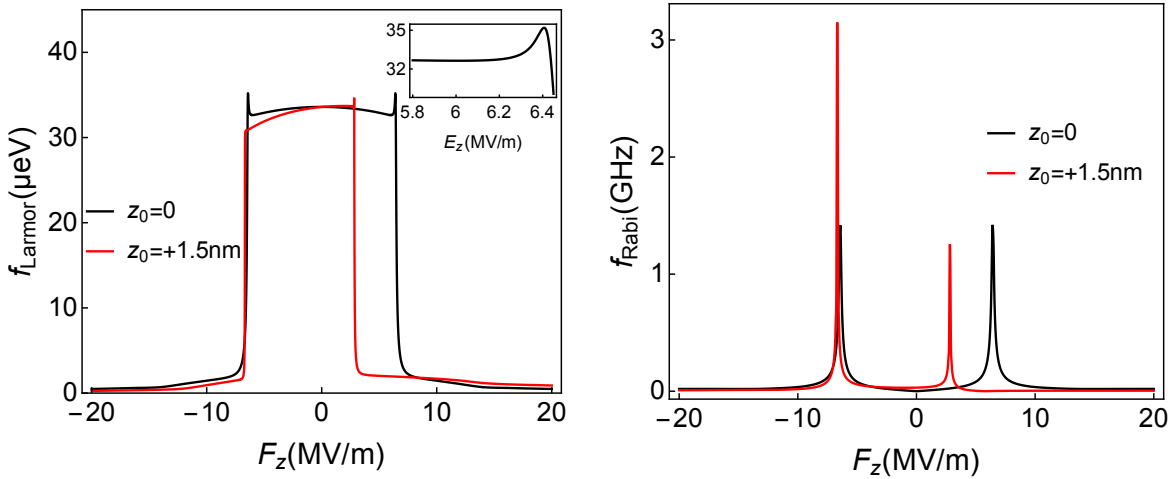


FIGURE 3.7: (Left) Larmor frequency of the concave LH qubit in μeV as a function of the electric field for $x_1 = 0.8$, $x_2 = 0.7$, $x_3 = 0.82$, $B = 0.1\text{ T}$, $L = 10\text{ nm}$. (Right) Rabi frequency of the LH qubit for the same parameters as (Left).

In this case the Larmor frequency inherits the concave behavior of the g -factor. The derivative of the Larmor frequency has now two opposite contributions as a function of the electric field: the decreasing g -factor, and the small positive contribution from the T_d symmetry. If the contribution to the derivative of the g -factor is larger than the contribution of the T_d term,

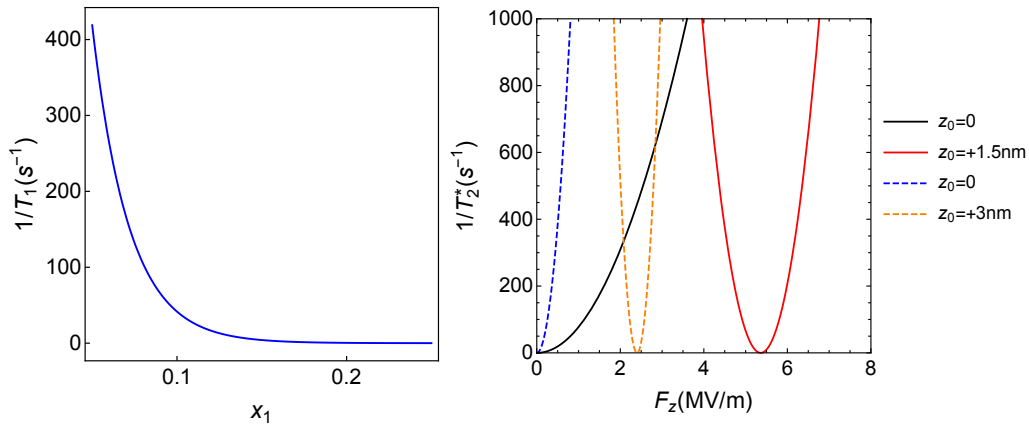


FIGURE 3.8: (Left) Inverse of the relaxation times of a HH qubit as a function of x_1 when $L = 10$ nm and the acceptor is at z_0 . (Right) Inverse of the coherence times due to the charge noise induced by a defect at 40 nm from the acceptor. Dashed lines correspond to $L = 10$ nm.

which is the case for high magnetic fields, there is only one sweet spot which corresponds to the maximum of the g -factor. When the contribution from the g -factor is small such that the T_d term can partially surpass it near the anticrossing, there will be two extra sweet spots. In total there can be up to five sweet spots: at the maximum of the g -factor, when the T_d term surpasses the g -factor in the derivative, and at the final decrease just before the anticrossing due to the mixing with the HH component. Note that the last two might appear both for positive and negative F_z due to the quantum well symmetry. This kind of behavior can be seen in the case $z_0 = 0$ in Fig. 3.7 where there are five sweet spots. The five sweet spots appear only for small enough magnetic fields: for instance, in the case of Fig. 3.7, with $x_1 = 0.8$ and $B = 0.1$ T, in the case of negative electric field and $z_0 = +1.5$ nm, the five sweet spots cannot be attained. Higher x_1 would increase the effective g -factor, reducing even further this maximum magnetic field. On the other hand, a smaller x_1 could allow higher magnetic fields.

The Rabi frequencies have the same behavior as in the convex case: the reduction of inversion symmetry clearly increases the Rabi frequencies, being maximal near the sweet spots. The numbers however can be larger as the Rabi frequency of the EDSR in a LH qubit is directly proportional to the Zeeman field, and in this case the effective g -factors are much larger.

3.4 Decoherence processes

For the HH qubit, the Rabi frequencies obtained by electric field manipulation are of the order of MHz, see Figs. 3.3-3.4. The magnetic field manipulation, see Fig. 3.2, is around three orders of magnitude slower. The manipulation frequency has to be benchmarked against relaxation and coherence times in order to get an estimate of the number of qubit rotations allowed before losing coherence. Hence, the faster electric field manipulation is more advisable. Estimates of the relaxation times using the formula for small temperature phonon-induced spin relaxation of acceptor heavy hole qubits in Ref. [126]:

$$\frac{1}{T_1} = \frac{[\hbar\omega]^3}{20\hbar^4\pi\rho} C_d \left[\frac{\varepsilon Z_0}{\Delta} \right]^2, \quad (3.12)$$

and using the relevant parameters for the considered materials [238], are of the order of milliseconds in the worst case scenario (small quantum well barriers) and can be significantly improved by increasing $x_1 - x_2$ as the relaxation times are directly proportional to the HH-LH splitting, see Fig. 3.8(Left). Since the relaxation times are proportional to the HH-LH splitting, T_1 grows very fast with x_1 due to strain. Experiments in natural Ge/Si nanowires double quantum dots have measured coherence times in the order of tenths of microseconds [239], more than one order of magnitude longer than for III-V semiconductors. These measurements show a dominant nuclear-spin dephasing, but isotopic purification is expected to make charge noise the dominant source of dephasing.

The Larmor frequency is, for the HH qubit, mostly determined by the Zeeman splitting, other factors, such as the HH-LH mixing due to the spin-orbit terms, are negligible in comparison. This means that the largest contribution to charge noise dephasing comes from the fluctuations in the g -factor. The regions in which the g -factors vary more strongly under the effect of an electric field are also those in which the qubit is more sensitive to charge noise dephasing. On the other hand, as the quantum well is symmetric, there is a value of F_z at which the g -factor is not sensitive to variations of the electric field. This value is $F_z = 0$ when the acceptor is placed at the center of the quantum well. Therefore, the best conditions for g-TMR coincide with a large effect of charge noise dephasing and a compromise between the two has to be achieved. This can be seen in Fig. 3.8(Right) where the dephasing times due to charge noise fluctuations coming from a defect 40 nm away from the acceptor are estimated [240]:

$$1/T_2^* = \frac{\Delta E_{\text{Larmor}}^2 \tau}{2\hbar^2}, \quad (3.13)$$

being τ the fluctuating times (considered $\tau = 1 \mu\text{s}$ in this case) and ΔE_{Larmor} the change in Larmor energy due to the fluctuating charge. The charge noise effects in dephasing are minimized ($T_2^* \rightarrow \infty$ to first order) where $dg_{\perp}^{\text{HH1}}/dF_z = 0$ since in this case the qubit energy is insensitive to charge noise to first order. The curvature of this *sweet spots* depends a lot on the quantum well width. This is because a narrower quantum well makes the g -factor less sensitive to electric fields and hence, the sweet spots are wider in F_z .

Regarding the LH qubit, there are two desirable properties: strong couplings that allow fast EDSR manipulation together with the existence of sweet spots [125]. The estimated Rabi frequencies are much higher in the LH qubit than in the HH one. In return, relaxation and coherence times are expected to be much smaller. For instance, applying the phonon-induced spin relaxation formula in Eq. 3.12, we get T_1 of the order of microseconds or tens of microseconds. Up to five sweet spots can be achieved depending on the heterostructure composition. In the case in which the g -factor is smaller in the barrier (concave LH qubit), the sweet spots near the anticrossing are very close to each other and a better resilience against electric field noise is expected.

The Ge content in the heterostructure has an important effect on the achieved Rabi frequencies and coherence times. The larger Bohr radius in Ge gives rise to an enhanced Rashba coupling, and hence increases EDSR couplings in both HH and LH qubits. On the other hand, the larger Bohr radius reduces the effective dipolar coupling p which, together with the larger effective g -factor, suppresses T_1 [125], particularly for the LH qubit. This negative impact on T_1 can be reduced in two ways: (i) applying small Zeeman fields, which is also a requirement for obtaining the five sweet spots in the concave LH qubit, and (ii) using deep acceptors, such as Al, Ga, In or Tl, as they are affected by non-negligible central cell corrections [189] that produce higher dipolar couplings p [223].

It is experimentally advantageous to use Si ($x_3 = 0$) or Ge ($x_3 = 1$) as substrates. In the case of Si the compressive strain would produce a HH qubit while in the case of Ge both HH and LH are possible, depending on the interplay between the tensile strain, which favours LH, and the confinement, which favours HH giving rise to good relaxation times. In the case of a Ge substrate, high concentrations of Ge are also needed within the well in order to reach the LH-HH anti crossing condition as a function of the applied vertical electric field. This LH type of qubit would have several sweet spots where charge noise is suppressed but T_1 is not as big as in a HH qubit since the energy difference between branches is small (near an anti-crossing). In the next chapter the improvement of T_1 , among other things, will be addressed for an acceptor near a SiO₂ interface.

3.5 Conclusions

We have calculated the Rabi frequencies of three different ways of manipulating a single qubit for a hole bound to an acceptor inside a quantum well. Depending on the strain conditions, the acceptor ground state has a heavy-hole or light-hole character. The results show that it is possible to get Rabi frequencies for a HH ground state in the range of MHz for the electric field based manipulation methods while it is possible to reach the GHz in the case of an electrically manipulated LH state. In comparison the Rabi frequencies obtained with magnetic field manipulation are only in the order of kHz.

The Rabi frequency of the electron spin resonance of a HH state can be enhanced by increasing the g -factor in the heterostructure (this can be achieved by a large Ge content) and by raising the hole density wave-function in the barriers, which have a larger g -factor. It is hence interesting to use small barriers, for instance Si_{1-x₂}Ge_{x₂}/Si_{1-x₁}Ge_{x₁}/Si_{1-x₂}Ge_{x₂} quantum wells with $x_2 = x_1 - 0.05$. An electric field can shift the hole wave-function within the heterostructure and hence can be applied to increase or decrease the Rabi frequency.

Purely electric field manipulation of a HH spin-qubit via electric dipole spin resonance can also produce MHz frequencies thanks to the presence of the acceptor T_d symmetry and spin-orbit Rashba terms. The required lack of inversion symmetry can be obtained by applying a vertical electric field. The HH-LH mixing given by this electric field and the T_d symmetry term is also very important. The Rabi frequencies are proportional to the asymmetry of the hole wave function. A large Bohr radius (or smaller binding energy) allows an easier manipulation of the wave-function by electric field. The HH-LH mixing is inversely proportional to the strain, hence large strains are not desirable as they reduce the Rabi frequency.

The g -TMR method of spin qubit manipulation is the one that gives the best Rabi frequencies for HH qubits. In exchange, this method is also the most exposed one to charge noise. The quantum well composition is not very important as long as the g -factors are not suppressed (this happens around $x \approx 0.4$) and the barrier is not very high. The best Rabi frequencies are obtained when the acceptor is close to one barrier and pushed by an electric field to the opposite barrier. At the sweet spots, however, the Rabi frequencies are much smaller but still larger than those obtained through EDSR.

The LH qubit, can be easily manipulated by electrical means with frequencies of the order of GHz around the sweet spots, allowing both fast manipulation and good coherence properties. Several sweet spots can be found and the qubit becomes limited by the relaxation time T_1 due to the small energy separation between the qubit branch and the excited branch.

In general, the presence of the spin-orbit terms due to the acceptor (T_d symmetry) and lack of inversion symmetry (Rashba type) allow the possibility of several ways of manipulating the spin state of a hole bound to an acceptor inside a quantum well. Due to the HH-LH splitting in the HH case, the relaxation and coherence properties are expected to be optimal, making this type of quantum wells good candidates as quantum memories. The LH ground states have good properties of coherence and still high manipulability near the sweet spots, making this type of quantum wells good candidates for quantum computation. This type of devices would also have good compatibility with electrically defined quantum dots, allowing the possibility of hybrid dot-acceptor qubits.

Full tunability, coherence and entanglement of acceptors near an interface ¹

4.1 Introduction

One of the main issues with solid state quantum computing is generating high fidelity entanglement protocols. Some of the proposals for long range entanglement require complex circuitry to couple different devices. Proposals to simplify the circuitry to create entanglement often involve dipolar interactions [94, 104, 242, 243] since exchange is a too short range interaction. The main problem with dipolar interactions is that it behaves as an always on Ising or XY type interaction between neighboring qubits, meaning that the two-qubit interactions are always generating dynamics. Detuning one qubit with respect to the other can be used to reduce the two-qubit dynamics [243], but this does not entirely suppresses the mechanism. Reducing the dipole of one of the qubits deactivates that qubit for single-qubit interactions too [104, 242]. For magnetic dipolar interactions, particular choices of the magnetic field can be used to turn off the coupling [94], but this requires the ability to dynamically change the magnetic field orientation.

In this chapter we propose a new mechanism that allows to turn on and off the electric dipolar coupling of two-acceptor based qubits. To do so, we generalize the theory of the acceptor qubit defined in Ref. [125]. In this reference, an acceptor-based quantum information platform was introduced, in which inversion symmetry breaking by the SiO₂ interface (Fig. 4.1) gives rise to a Rashba interaction that couples the spin to in-plane electric fields, enabling fast electrical manipulation via electric dipole spin resonance techniques (EDSR). Sensitivity to charge noise is suppressed to first order at particular values of the electric field (sweet spots). Two qubit operations can be performed by using the electric dipolar interaction between acceptors. There are two main limitations in this scheme: (i) in the sweet spots the coherence time is limited by T_1 , controlled by phonons and hence, cannot be easily enhanced, and (ii) entanglement, performed via electric dipole-dipole interactions, shares the same problem of other dipolar based entanglement protocols, it can only be turned off by deactivating one of the qubits.

¹Results published on [241].

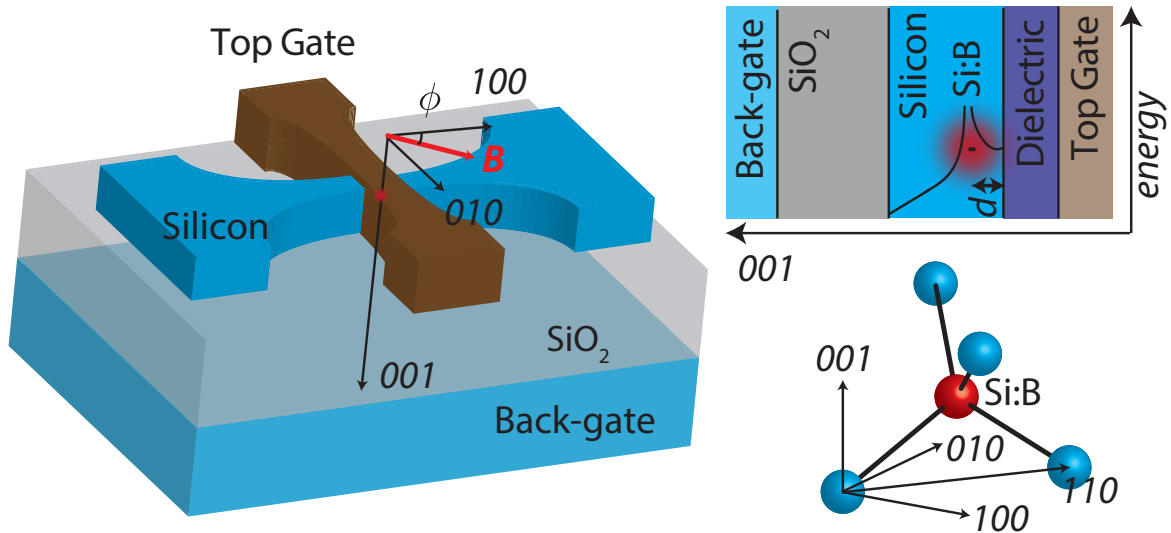


FIGURE 4.1: Sketch of the device geometry and layered heterostructure in the (001) direction. The orientation of the magnetic field within the plane is given by ϕ , the angle with respect to the (100) direction. d denotes the depth of the acceptor beneath the top gate interface.

By generalizing the theory of this acceptor qubit with the EMT used in Chapter 2, we show that a magnetic field in a *fixed* in-plane orientation away from the main crystal axes can be used to overcome these limitations for an acceptor based Si quantum computer with full electrical control. The T_d symmetry of the acceptor in the Si lattice enables an unconventional interaction between the acceptor bound hole and the in-plane magnetic field. Certain magnetic field orientations make qubits insensitive to charge noise to second order, and a decoherence free subspace (DFS) is found, where the qubit is insensitive to *both* charge noise *and* phonon-induced relaxation. More importantly, particular orientations of the magnetic field (*magic angles*) can be chosen beforehand to switch off entanglement, which can then be reestablished purely by electrical means. In this way, single qubit operations can still be performed while entanglement is switched off. As a result, optimal magnetic field orientations at magic angles can both enhance T_1 and allow for a maximum electric based tunability of the two qubit coupling. We propose two possible protocols for full electrical control of acceptor entanglement that do not require atomic placement accuracy, exploiting the DFS in one case and reducing the exposure to charge noise in the other.

4.2 Qubit basis

The effective Hamiltonian given in Ref. [125] is obtained here by applying the effective mass approach from 2.5. As described in that section, this Hamiltonian is given by the contribution of different terms in Eqs. 2.26, 2.27, 2.28, 2.29. Now we consider a magnetic field \mathbf{B} with an arbitrary in-plane orientation characterised by an angle ϕ . This angle is defined such that $\phi = 0$ corresponds to the (001) direction. The qubit is defined under a vertical electric field

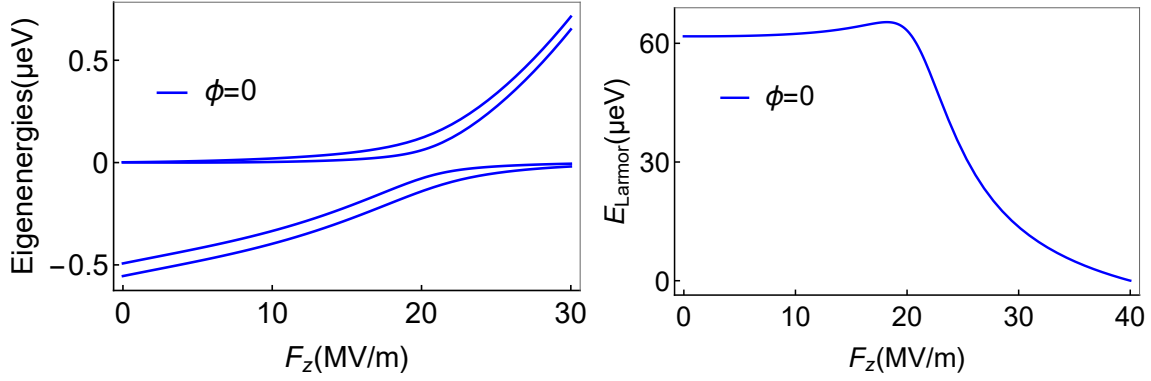


FIGURE 4.2: In both plots $B = 0.5$ T and $d = 4.6$ nm. (Left) Eigenenergies of H_{eff} as a function of the vertical field when the magnetic field is aligned to the (001) direction. Up to a field $F_z \sim 20$ MV/m, the lower branch is of LH character, the LH-HH mixing increasing with F_z . After the anticrossing, the lower branch is of HH character. (Right) Larmor energy, when the magnetic field is aligned to the (001) direction, as a function of the vertical electric field. The Larmor energy has a local minimum at $F_z = 0$ and a maximum at $F_z = 18.1$ MV/m. At these values of F_z the Larmor energy is flat, indicating insensitivity to charge noise.

and a fixed in-plane magnetic field. The total effective Hamiltonian of the qubit is:

$$H_{\text{eff}} = \begin{pmatrix} 0 & \frac{\sqrt{3}}{2}\varepsilon_Z e^{-i\phi} & -ipF_z & 0 \\ \frac{\sqrt{3}}{2}\varepsilon_Z e^{i\phi} & \Delta_{HL} & \varepsilon_Z e^{-i\phi} & -ipF_z \\ ipF_z & \varepsilon_Z e^{i\phi} & \Delta_{HL} & \frac{\sqrt{3}}{2}\varepsilon_Z e^{-i\phi} \\ 0 & ipF_z & \frac{\sqrt{3}}{2}\varepsilon_Z e^{i\phi} & 0 \end{pmatrix} \quad (4.1)$$

Where the Zeeman term is $\varepsilon_Z = g_1 \mu_B B$. Note that here the HH energy is set to zero for $F_z = 0$. The qubit is defined by the two levels making up the spin-split ground state (qubit branch), defined this time as the more negative energies. The excited branch is then formed by the next two excited states. At zero fields, the strain conditions are $\Delta_{HL} < 0$ such that the qubit branch is of LH character. As shown in Fig. 4.3(a) the HH and LH branches are clearly separated by the magnitude of Δ_{HL} , which decreases as F_z increases. At large gate fields, as the bound hole wave-function is pushed towards the interface, the LH and HH levels eventually anticross and the qubit branch acquires a predominantly HH character [125].

As Fig. 4.1 shows, the local tetrahedral symmetry of the acceptor makes a clear distinction between the main crystal axes and any other direction. It is represented by the term H_{T_d} in the Hamiltonian, which governs the qubit interaction with electric fields, and becomes more pronounced as the top gate voltage is increased, generating a mixing between HH and LH in the two branches. The interplay between the terms with tetrahedral symmetry H_{T_d} and the usual Zeeman interaction H_B gives rise to a new and counterintuitive magnetic field orientation dependence of the qubit properties with no analog for spin-1/2 electrons. This is due to the quadrupolar spin operators involved in the T_d terms, not allowed for spin 1/2 (spin quadrupolar terms are reducible to either a dipolar Pauli matrix or the identity matrix). In Fig. 4.3 this magnetic field orientation dependence can already be seen, the eigenvalues and hence, the qubit frequency, strongly depend on the magnetic field orientation.

To define the qubit, we consider first the action of the vertical electric field only:

$$H_{op}(\varepsilon_Z = 0) = \begin{pmatrix} 0 & 0 & -ipF_z & 0 \\ 0 & \Delta_{HL} & 0 & -ipF_z \\ ipF_z & 0 & \Delta_{HL} & 0 \\ 0 & ipF_z & 0 & 0 \end{pmatrix} \quad (4.2)$$

Defining $E_l = \frac{1}{2}(\Delta_{HL} - \sqrt{\Delta_{HL}^2 + 4p^2F_z^2})$, $E_u = \frac{1}{2}(\Delta_{HL} + \sqrt{\Delta_{HL}^2 + 4p^2F_z^2})$, the previous Hamiltonian is diagonalized being E_l and E_u the energies of the lower and upper branches respectively. The eigenstates are then:

$$|l_-\rangle = a_L| -1/2\rangle + ia_H|3/2\rangle \quad (4.3)$$

$$|l_+\rangle = a_L|1/2\rangle - ia_H| -3/2\rangle \quad (4.4)$$

$$|u_-\rangle = ia_H|1/2\rangle + a_L| -3/2\rangle \quad (4.5)$$

$$|u_+\rangle = -ia_H| -1/2\rangle + a_L|3/2\rangle, \quad (4.6)$$

being $a_L = E_l/\sqrt{E_l^2 + p^2F_z^2}$ and $a_H = pF_z/\sqrt{E_l^2 + p^2F_z^2}$. Physically, the values of a_L and a_H can be associated to the probability amplitudes of LH and HH of the qubit branch respectively. The amplitudes a_L and a_H change with the vertical electric field. In particular, due to the strain conditions, when $F_z = 0$ the composition is $a_L = -1$ and $a_H = 0$, and each branch has a clear LH and HH behavior. By increasing F_z , each branch increases the mixing of HHs and LHs, until the qubit branch starts to become more HH-like ($a_H > a_L$). Eventually, when F_z is large enough, the lower and upper branches become mostly HH-like and LH-like respectively. The unitary transformation that diagonalizes to the new basis $\{|l_-, l_+, u_-, u_+\rangle\}$ is:

$$U_0 = \begin{pmatrix} -ia_H & 0 & 0 & a_L \\ 0 & a_L & ia_H & 0 \\ a_L & 0 & 0 & -ia_H \\ 0 & ia_H & a_L & 0 \end{pmatrix} \quad (4.7)$$

Applying this unitary transformation to the original Hamiltonian we get:

$$\hat{H}_{op} = \begin{pmatrix} E_l & \frac{1}{2}\lambda_{Zl}^* & \frac{1}{2}\lambda_{Zo}^* & 0 \\ \frac{1}{2}\lambda_{Zl} & E_l & 0 & \frac{1}{2}\lambda_{Zo} \\ \frac{1}{2}\lambda_{Zo} & 0 & E_u & \frac{1}{2}\lambda_{Zu}^* \\ 0 & \frac{1}{2}\lambda_{Zo}^* & \frac{1}{2}\lambda_{Zu} & E_u \end{pmatrix} \quad (4.8)$$

In this basis the Zeeman interaction is the only off-diagonal term, with

$$\begin{aligned} \lambda_{Zl} &= 2\varepsilon_Z(a_L^2e^{-i\phi} - i\sqrt{3}a_La_He^{i\phi}) \\ \lambda_{Zu} &= 2\varepsilon_Z(-a_H^2e^{i\phi} + i\sqrt{3}a_La_He^{-i\phi}) \\ \lambda_{Zo} &= 2\varepsilon_Z(-ia_Ha_Le^{-i\phi} + \sqrt{3}(a_L^2 - a_H^2))e^{i\phi/2} \end{aligned} \quad (4.9)$$

Physically, the absolute value of λ_{Zl} and λ_{Zu} is the Zeeman splitting of the lower and upper branches respectively, while the absolute value of λ_{Zo} indicates a Zeeman coupling between branches. These off-diagonal couplings are orientation dependent. We can now do the last transformation to define the qubit. The Larmor energy of each branch is included in this transformation while the coupling between branches is considered a perturbation. Let the

unperturbed Hamiltonian be:

$$U_0^\dagger H_{op,0} U_0 = \begin{pmatrix} E_l & \frac{1}{2}\lambda_{Zl}^* & 0 & 0 \\ \frac{1}{2}\lambda_{Zl} & E_l & 0 & 0 \\ 0 & 0 & E_u & \frac{1}{2}\lambda_{Zu}^* \\ 0 & 0 & \frac{1}{2}\lambda_{Zu} & E_u \end{pmatrix} \quad (4.10)$$

This Hamiltonian is diagonalized by U_{Z0} to give the eigenenergies $E_\pm = E_l \pm \frac{1}{2}|\lambda_{Zl}|$ and $E_{u\pm} = E_u \pm \frac{1}{2}|\lambda_{Zu}|$. Writing $\lambda_{Zl} = \varepsilon_{Zl} \exp(i\theta_l)$, $\lambda_{Zu} = \varepsilon_{Zu} \exp(i\theta_u)$, and $\lambda_{Zo} = \varepsilon_{Zo} \exp(i\theta_o)$,

$$\begin{aligned} \theta_l &= \arctan(a_L^2 \cos(\phi) + \sqrt{3}a_L a_H \sin(\phi), -a_L^2 \sin(\phi) - \sqrt{3}a_L a_H \cos(\phi)) \\ \theta_u &= \arctan(-a_H^2 \cos(\phi) + \sqrt{3}a_L a_H \sin(\phi), -a_H^2 \sin(\phi) + \sqrt{3}a_L a_H \cos(\phi)) \\ \theta_o &= \arctan(-a_L a_H \sin(\phi) + \sqrt{3}/2(a_L^2 - a_H^2) \cos(\phi), -a_L a_H \cos(\phi) + \sqrt{3}/2(a_L^2 - a_H^2) \sin(\phi)) \end{aligned} \quad (4.11)$$

$$\begin{aligned} \varepsilon_{Zl} &= 2\varepsilon_Z \sqrt{3a_L^2 a_H^2 + a_L^4 + 2\sqrt{3}a_L^3 a_H \sin(2\phi)} \\ \varepsilon_{Zu} &= 2\varepsilon_Z \sqrt{3a_L^2 a_H^2 + a_H^4 - 2\sqrt{3}a_H^3 a_L \sin(2\phi)} \\ \varepsilon_{Zo} &= 2\varepsilon_Z \sqrt{3(a_L^2 - a_H^2)/4 + a_H^2 a_L^2 + \sqrt{3}a_H a_L (a_H^2 - a_L^2) \sin(2\phi)} \end{aligned} \quad (4.12)$$

The unitary transformation that diagonalizes the previous Hamiltonian is then:

$$U_{Z0} = 2^{-\frac{1}{2}} \begin{pmatrix} e^{-i\theta_l/2} & e^{-i\theta_l/2} & 0 & 0 \\ -e^{i\theta_l/2} & e^{i\theta_l/2} & 0 & 0 \\ 0 & 0 & e^{-i\theta_u/2} & e^{-i\theta_u/2} \\ 0 & 0 & -e^{i\theta_u/2} & e^{i\theta_l/2} \end{pmatrix} \quad (4.13)$$

The Hamiltonian in this basis is:

$$H_{qubit} = \begin{pmatrix} E_l - \frac{1}{2}\varepsilon_{Zl} & 0 & Z_1 & Z_2 \\ 0 & E_l + \frac{1}{2}\varepsilon_{Zl} & Z_2 & Z_1 \\ Z_1 & -Z_2 & E_u - \frac{1}{2}\varepsilon_{Zu} & 0 \\ -Z_2 & Z_1 & 0 & E_u - \frac{1}{2}\varepsilon_{Zu} \end{pmatrix} \quad (4.14)$$

where

$$\begin{aligned} Z_1 &= \frac{1}{2}\varepsilon_{Zo} \cos(\theta_l/2 - \theta_u/2 - \theta_o) \\ Z_2 &= \frac{i}{2}\varepsilon_{Zo} \sin(\theta_l/2 - \theta_u/2 - \theta_o) \end{aligned} \quad (4.15)$$

Here Z_i are the Zeeman interactions between the lower and upper branches. Note that Z_1 is a real number while Z_2 is a purely imaginary number. The lower branch with Zeeman energy ε_{Zl} is the qubit branch while the upper branch with ε_{Zu} can be seen as a leakage excited states branch that interacts with the qubit branch via Z_1 and Z_2 . Noting that the next excited states are at least 10 meV away from this 4×4 manifold, this means that all the dynamics and decoherence of a qubit defined in the lower branch will be dominated by the interaction terms Z_1, Z_2 with the upper branch.

In the original proposal the magnetic field is assumed along one of the main crystal axes [125]. In this case, the values of the different parameters in Eqs. 4.11 and 4.12 are simply:

$$\begin{aligned}\theta_l &= \arctan(\sqrt{3}a_H a_L, a_L^2) \\ \theta_u &= \arctan(\sqrt{3}a_H a_L, -a_H^2)\end{aligned}\quad (4.16)$$

$$\begin{aligned}\theta_o &= \arctan\left(\frac{\sqrt{3}}{2}(a_L^2 - a_H^2), a_L a_H\right) \\ \varepsilon_{Zl} &= 2\varepsilon_Z \sqrt{3a_L^2 a_H^2 + a_L^4} \\ \varepsilon_{Zu} &= 2\varepsilon_Z \sqrt{3a_L^2 a_H^2 + a_H^4} \\ \varepsilon_{Zo} &= 2\varepsilon_Z \sqrt{3(a_L^2 - a_H^2)/4 + a_H^2 a_L^2}\end{aligned}\quad (4.17)$$

The value of the qubit Larmor frequency is given, to first order, by ε_{Zl} . Its value depends explicitly on the electric field via a_H and a_L . We can find the sweet spots for $\phi = 0$ by simply finding the solutions to $d\varepsilon_{Zl}/dF = 0$:

$$\frac{d\varepsilon_{Zl}}{dF_z} = \varepsilon_Z \frac{(-3 + 4a_L^2)a'_L(F_z)}{\sqrt{3 - 2a_L^2}} = 0 \quad (4.18)$$

This has two solutions for $F_z \geq 0$: $a_L = -\sqrt{3}/2$ and $a'_L = 0$. The values of the electric field corresponding to these sweet spots are at $F_z = 0$ and $F_z \approx 18$ MV/m, for an acceptor at $d \approx 5$ nm and with a strain splitting of $\Delta_{LH}^{\text{strain}} = -0.6514$ meV, corresponding to $\varepsilon_{\parallel} \approx 0.1\%$. The sweet spot at $F_z = 0$ only requires $a_L = -1$ so it is independent of the exact amount of strain as long as the ground state is LH like. The sweet spot at large field, however, happens when the quantum confinement partially compensates the strain splitting such that $a_L = -\sqrt{3}/2$ and $a_H = 1/2$. It can also be proven, that the qubit is also insensitive to first order to in-plane charge noise. This is the reason why, the qubit is operated at these sweet spots. In the large field sweet spot, the values of the Rashba coefficient can be high enough to allow single qubit operations in 0.2 ns while the dipolar two qubit operations can be performed in 2 ns. Since the sweet spot with $F_z = 0$ has a suppressed α , qubits with $F_z = 0$ could be potentially used as quantum memories with improved coherence times (in the order of hundreds of μs).

For $\phi = n\pi/2$ (main crystal axes) the qubit is limited by phonon-induced relaxation, with a T_1 estimate of 20 μs . This means that 10^5 single-qubit and 10^4 two qubit operations could be performed during the qubit lifetime [125]. The phonon-induced relaxation can not be significantly improved simply by changing F_z , like with charge noise, so this mechanism can be considered the main limitation.

4.3 In-plane anisotropy

The Zeeman couplings ε_{Zl} , ε_{Zu} and ε_{Zo} in Eq. 4.12 dominate the qubit physics and depend on ϕ . This means that the Larmor energy of both the qubit and upper branches, and the coupling between them, are anisotropic in the xy plane. This can be seen in Fig. 4.3, where the energy diagram and the Larmor energy are shown as a function of the electric field for different magnetic field orientations. It can even be seen that particular orientations can give rise to a crossing between the levels within one of the branches.

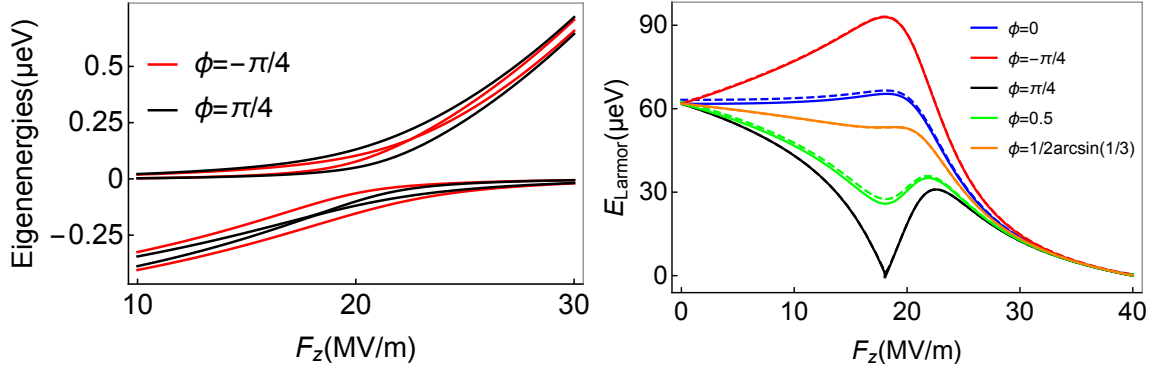


FIGURE 4.3: In all plots $B = 0.5$ T and $d = 4.6$ nm. (Left) Eigenenergies of H_{eff} as a function of the vertical field for two particular cases $\phi = \pi/4$ (black lines) and $\phi = -\pi/4$ (red lines). (Right) Larmor energy for different magnetic field orientations as a function of the vertical electric field. The Larmor energy at the isotropic sweet spot ($F_z = 18.1$ MV/m) is enhanced for $\pi/2 < \phi < \pi$ and depressed for $0 < \phi < \pi/2$ with a minimum at $\phi = \pi/4$. At this point the two lowest levels cross. The dashed lines correspond to the numerical results. When $\phi = 1/2 \arcsin(1/3)$ the isotropic and anisotropic sweet spots coincide in a single one which is robust to charge noise up to second order.

This anisotropic behavior has no analog for spin 1/2 electrons. As Fig. 4.1 shows, the local tetrahedral symmetry of the acceptor makes a clear distinction between the main crystal axes and any other direction. It is represented by the term H_{T_d} in the Hamiltonian, which governs the qubit interaction with electric fields, and becomes more pronounced as the top gate voltage is increased ($H_{T_d} \propto pF_z$), generating a mixing between HH and LH in the two branches. This is a spin quadrupolar term, product of two J matrices (spin dipoles), that is not allowed in a spin 1/2 Hilbert space since the product of two spin dipolar operators in spin 1/2, the Pauli matrices, can only give another dipole (Pauli matrix) or the identity. Without this term, the Zeeman interaction would be perfectly isotropic. The interplay between the terms with tetrahedral symmetry H_{T_d} and the usual Zeeman interaction H_B gives rise to this new and counterintuitive magnetic field orientation dependence. Since the H_{T_d} mixes the HH and LH through the action of F_z , this in-plane anisotropy is a clear signature of the LH-HH mixing.

4.3.1 Sweet spots

This in-plane anisotropy not only affects the splittings but can also affect other properties such as the sensitivity to charge noise. In particular, Fig. 4.3 shows the Larmor energy as a function of the vertical electric field, and the different orientations of the magnetic field ϕ also change the derivative dE_{Larmor}/dF_z . As a consequence the values of F_z for which the qubit energy is insensitive to charge noise are affected by ϕ . As calculated in Eq. 4.18, we can obtain the sweet spots as a function of ϕ :

$$\frac{d\varepsilon_{ZI}}{dF_z} = \varepsilon_Z \frac{(-3 + 4a_L^2)(a_H + \sqrt{3}a_L \sin(2\phi))a'_L(F_z)}{a_H \sqrt{3 - 2a_L^2 + 2\sqrt{3}a_L a_H \sin(2\phi)}} = 0 \quad (4.19)$$

One of the solutions corresponds to the *isotropic sweet spot* that occurs when $a_L = -\sqrt{3}/2$ ($a_H = 1/2$). This corresponds to the large field sweet spot for $\phi = 0$ and has no magnetic field orientation dependence. Considering that $a'_L \propto a_H$, the other solution is equivalent to solve $a_H + \sqrt{3}a_L \sin(2\phi) = 0$. Considering positive electric fields, there is a ϕ dependent

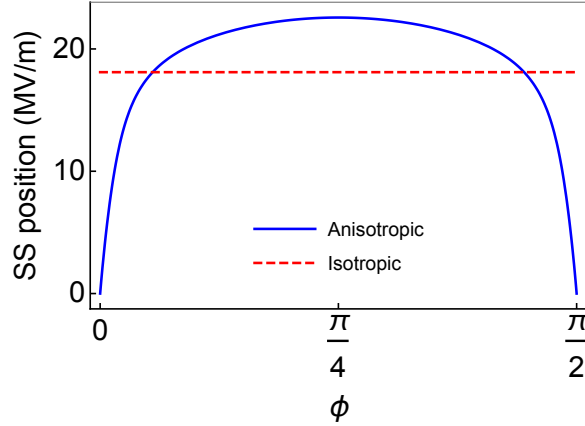


FIGURE 4.4: Value of the electric field F_z at which the sweet spots occur as a function of the in-plane magnetic field orientation for $d = 4.6$ nm. The isotropic sweet spot is fixed at 18.1 MV/m while the anisotropic one is a non-monotonic function of ϕ . The maximum value of F_z for the anisotropic sweet spot is ≈ 22.5 MV/m, where $a_L = -1/2$ and $a_H = \sqrt{3}/2$. The sweet spots merge at $\phi = 1/2 \arcsin(1/3)$ and $\phi = \pi/2 - 1/2 \arcsin(1/3)$ where the qubit energy is particularly flat and insensitive to charge noise up to second order, see Fig. 4.3(Right).

sweet spot solution for $0 \leq \phi \leq \pi/2$ and $\pi \leq \phi \leq 3\pi/2$. This sweet spot is then called the *anisotropic sweet spot*. Solutions in the other two quadrants in ϕ can be found for a electric field that pulls the wavefunction away from the interface, but in this case the acceptor would ionize due to the lack of a close interface. The position of both sweet spots as a function of the vertical field is shown in Fig. 4.4.

Particularly, at $\phi = \pi/4 + n\pi$, this sweet spot is at $a_H = \sqrt{3}/2$ and $a_L = -1/2$ while, for a magnetic field aligned with the main axes of the crystal, this sweet spot corresponds to the value $F_z = 0$. Also, when $\phi = \pi/4 + n\pi$ the value of the Larmor frequency at the isotropic sweet spot is zero. At this point there is an inversion of the effective spin polarization of the lower branch, meaning that an effective g -factor flip occurs in this particular case.

4.3.2 Induced spin-polarization

[movie](#)

When separating the absolute value and the phase of each Zeeman coupling in Eq. 4.2 we wrote $\lambda_{Zl} = \varepsilon_{Zl} \exp(i\theta_l)$, $\lambda_{Zu} = \varepsilon_{Zu} \exp(i\theta_u)$, and $\lambda_{Zo} = \varepsilon_{Zo} \exp(i\theta_o)$. To understand better what are physically the values of the phases, we can construct an analogy with a spin 1/2 electron under an in-plane magnetic field $B(\cos \phi, \sin \phi)$ whose Hamiltonian is:

$$\hat{H}_e = \begin{pmatrix} E_0 & \frac{1}{2}g\mu_B B e^{-i\phi} \\ \frac{1}{2}g\mu_B B e^{i\phi} & E_0 \end{pmatrix} \quad (4.20)$$

The diagonalization of this simple Hamiltonian gives two eigenvalues separated by the Zeeman energy of the magnetic field. These energies are associated to eigenstates with well defined spin polarization. In particular, the ground state spin points towards the magnetic field direction while excited state points against the magnetic field direction (assuming $g > 0$). Analogously, the values of θ_l and θ_u can be associated to spin polarizations of each branch.

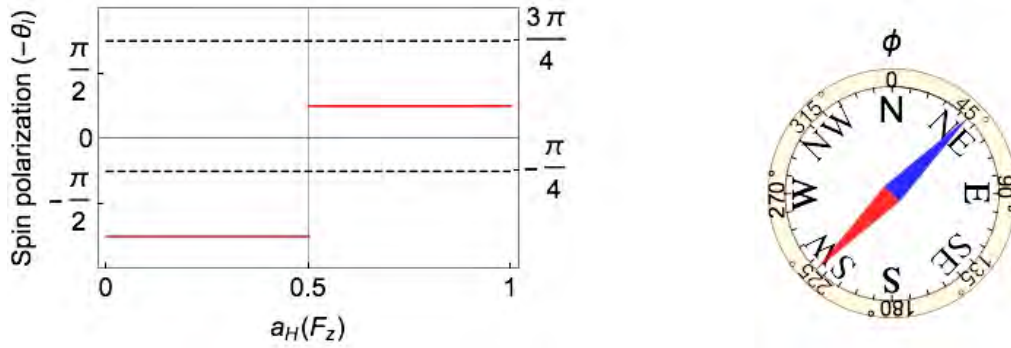


FIGURE 4.5: (Quicktime Movie in the pdf version.) Spin polarization of the lower branch as a function of the vertical electric field via $a_H(F_z)$. Click to see this for different values of ϕ . At the isotropic sweet spot ($a_H = 1/2$) this spin polarization is fixed in one direction, independently of the magnetic field orientation. When the magnetic field orientation is at $\phi = \pi/4 + n\pi$ the value is not defined and shows a jump discontinuity, this is because the qubit cannot see the magnetic field as $g_{\text{eff}} = 0$. On the other hand, when $\phi = -\pi/4 + n\pi$ the spin polarization is a constant of motion.

Rigorously however, these spin polarizations can only be considered *effective* spin polarizations of each branch, in the sense that this is a spin $3/2$ system and its spin polarization is more complex. For instance, the value of θ_o would be an interacting spin polarization with no real physical meaning in this picture. The HH-LH splitting that separates the two branches is what makes this effective spin polarization physical picture of these phases a powerful tool to understand the behavior of each branch under the presence of magnetic fields in analogy with the dynamics of a spin $1/2$ doublet.

This picture of the effective spin polarizations of each branch is particularly interesting due to the intrinsic dependence of θ_l , θ_u and θ_o not only on the magnetic field orientation ϕ but also on the vertical electric field F_z via a_L and a_H . The spin polarization of the ground state as a function of the vertical electric field when changing ϕ can be seen in the movie 4.5. At $F_z = 0$ the T_d symmetry term is zero and the effective spin polarization is simply ϕ just like for a single electron. This is clearly modified for different values of F_z .

At the two sweet spots the spin polarization is spin-orbit induced and, in particular cases, independent of the magnetic field. At the isotropic sweet spot ($a_L = -\sqrt{3}/2$, $a_H = 1/2$) the spin of the qubit is polarized in the $-\pi/4 + n\pi$ direction while, when $a_L = -1/2$ and $a_H = \sqrt{3}/2$ it is the upper branch the one with fixed spin polarization in the $\pi/4 + n\pi$ direction. In this latter case, applying the magnetic field in the spin polarization corresponds to the anisotropic sweet spot. The fixed spin polarization has several consequences as can be seen in Fig. 4.6. When a magnetic field is applied perpendicularly to the induced spin polarization the effective g -factor goes to zero, see Fig. 4.3(c), and these states cannot sense the magnetic field. In this case the effective spin polarization is not defined (jump discontinuity). On the other hand, the effective g -factor is maximized when the in-plane magnetic field is parallel to the spin polarization. As will be shown, this case corresponds to a decoupling of the qubit and upper branches in a decoherence free subspace (DFS), with $\varepsilon_{Z_o} = 0$.

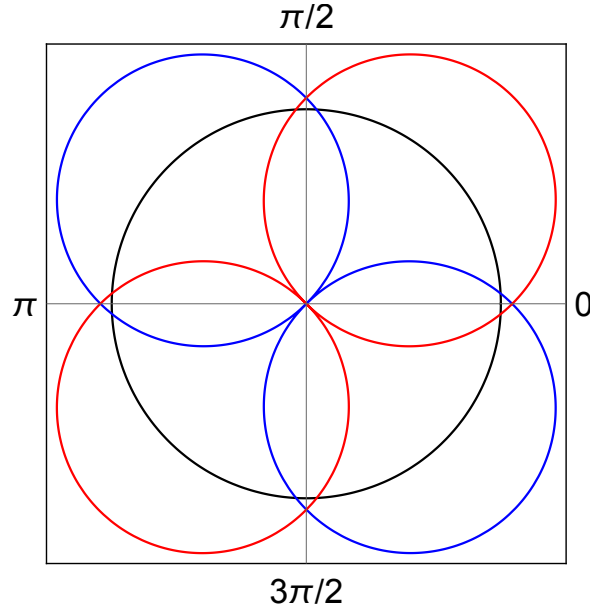


FIGURE 4.6: Polar plot of the effective g -factor. The black curve corresponds to when $F_z = 0$ and the g -factor is perfectly isotropic. The blue curve shows the effective g -factor of the qubit branch at the isotropic sweet spot. The blue curve corresponds to the effective g -factor of the upper branch when $a_L = -1/2$ and $a_H = \sqrt{3}/2$.

4.4 Manipulability: EDSR

As shown in the previous chapter, the qubit operations are performed by applying in-plane oscillating electric fields. The presence of the interface breaks the inversion symmetry of the envelope wavefunctions allowing the mixing of states with different behavior under the parity operator. This lack of inversion symmetry allows the action of an in-plane linear Stark effect $H_E = e(E_x x + E_y y) = eE_{\parallel}(\cos \theta_{\parallel} + \sin \theta_{\parallel})$. The effect of this interaction of the acceptor hole is calculated considering several excited states and mapped onto the effective 4×4 Hamiltonian in the $|m_J\rangle$ basis:

$$H_E = E_{\parallel} \begin{pmatrix} 0 & \alpha e^{i\theta_{\parallel}} & 0 & 0 \\ \alpha e^{-i\theta_{\parallel}} & 0 & 0 & 0 \\ 0 & 0 & 0 & -\alpha e^{i\theta_{\parallel}} \\ 0 & 0 & -\alpha e^{-i\theta_{\parallel}} & 0 \end{pmatrix} \quad (4.21)$$

Where α is an effective Rashba coupling, associated to the lack of inversion symmetry, and related to the applied vertical electric field and the distance to the interface. This effective Rashba Hamiltonian, rotated into the qubit basis becomes

$$\hat{H}_E = \begin{pmatrix} 0 & 0 & E_{1R} & E_{2R} \\ 0 & 0 & E_{2R} & E_{1R} \\ -E_{1R} & E_{2R} & 0 & 0 \\ E_{2R} & -E_{1R} & 0 & 0 \end{pmatrix} \quad (4.22)$$

Being

$$\begin{aligned} E_{1R} &= i\alpha E_{\parallel} \sin(\theta_{\parallel} + \theta) \\ E_{2R} &= -\alpha E_{\parallel} \cos(\theta_{\parallel} + \theta) \end{aligned} \quad (4.23)$$

Where $\theta = \theta_u/2 - \theta_l/2$, see Eq. 4.11. Note that E_{1R} is a purely imaginary number while E_{2R} is real.

We can use a SW transformation to obtain the action of an in-plane electric field in the qubit submanifold. The off-diagonal terms of the effective Hamiltonian in the qubit basis provide the EDSR coupling:

$$H_{-+}^{(2)} = \frac{2\varepsilon_{Zu}\text{Re}(-Z_1Z_2)}{(E_l - E_u)^2} + \frac{2\varepsilon_{Zu}\text{Re}(-E_1E_2)}{(E_l - E_u)^2} + \frac{2\text{Re}(E_2Z_1 - E_1Z_2)}{(E_l - E_u)} \quad (4.24)$$

The first two terms are identically zero because Z_1 and E_2 are real numbers while Z_2 and E_1 are purely imaginary. The last term is linear in the electric field so it can be used to perform operations via EDSR. This off-diagonal term can be written:

$$H_{-+}^{(2)} = DE_{\parallel} = \frac{1}{2} \frac{\varepsilon_{Z_o}(\phi)}{E_l - E_u} E_{\parallel} (\alpha \cos(\theta_o(\phi) - \theta_{\parallel}) + p \sin(\theta_o(\phi) - \theta_{\parallel})), \quad (4.25)$$

being D the EDSR dipolar coupling. At the sweet spot θ_o does not depend on ϕ so the only dependence on ϕ comes from ε_{Z_o} . Substituting the expressions at the isotropic sweet spot we get:

$$D_{\text{iso}} = \sqrt{3/2} \frac{\varepsilon_Z}{E_l - E_u} \sqrt{1 + \sin(2\phi)} (\alpha \cos(\pi/4 - \theta_{\parallel}) + p \sin(\pi/4 - \theta_{\parallel})) \quad (4.26)$$

Which in the high-field approximation, where $\alpha \gg p$ becomes:

$$D_{\text{iso}} = \alpha \sqrt{3/2} \frac{\varepsilon_Z}{E_l - E_u} \sqrt{1 + \sin(2\phi)} \cos(\pi/4 - \theta_{\parallel}) \quad (4.27)$$

This means that the off-diagonal term can be shut down when $\phi = -\pi/4$ or $\phi = 3\pi/4$, killing EDSR. At the same time EDSR can be maximized, for a given ϕ , by choosing the angle of the in-plane electric field $\theta_{\parallel} = \pi/4$. Being $\phi = \pi/4$ the in-plane magnetic field orientation with higher EDSR coupling.

In the anisotropic sweet spot the EDSR term is more complex due to the intrinsic ϕ dependence of the sweet spot. In the limit $\alpha \gg p$ it reduces to:

$$D_{\text{aniso}} = \alpha \sqrt{3/2} \frac{\varepsilon_Z}{E_l - E_u} \frac{|\cos 2\phi|}{\sqrt{2 - 3/2 \cos 4\phi}} \cos \left(\theta_{\parallel} - \arctan(2 \cos \phi - \cos 3\phi + 3 \cos 5\phi, 2 \sin \phi + \sin 3\phi + 3 \sin 5\phi) \right) \quad (4.28)$$

In this case the ideal θ_{\parallel} depends on ϕ . In any case this interaction can be switched off for $\phi = \pi/4$.

This EDSR coupling can be calculated with the parameters obtained from the effective Hamiltonian and, by optimizing the magnetic field, can improve the Rabi frequencies that in the original case allowed a π rotation in 0.2 ns. Particularly at the anisotropic sweet spot where α is bigger than in the isotropic sweet spot in a big ϕ window, the EDSR coupling can be even bigger, allowing faster single-qubit operations.

4.5 Coherence

As already shown, there are two sweet spots in F_z where the qubit is insensitive to charge noise δF_z to first order. In [125] it was also shown that the qubit is also insensitive to any in-plane charge noise δF_{\parallel} to first order. The main coherence limitation was then the phonon-induced relaxation, estimated around 20 μs for realistic parameters. In this section, the magnetic field orientation is shown to affect second order charge noise and phonon-induced relaxation, allowing the extension of the qubit lifetime.

4.5.1 Charge noise

The analysis of charge noise can be performed similarly to the previous section but with an in-plane electric field coming from a fluctuation $(\delta E_x, \delta E_y, 0) = \delta E_{\parallel}(\cos(\theta_{\parallel}), \sin(\theta_{\parallel}))$. Its Hamiltonian in the qubit basis is:

$$\hat{H}_{noise} = \begin{pmatrix} 0 & 0 & E_1 & E_2 \\ 0 & 0 & E_2 & E_1 \\ -E_1 & E_2 & 0 & 0 \\ E_2 & -E_1 & 0 & 0 \end{pmatrix} \quad (4.29)$$

where now

$$E_1 = i\delta E_{\parallel}(p \cos(\theta_{\parallel} - \theta) + \alpha \sin(\theta_{\parallel} + \theta)) \quad (4.30)$$

$$E_2 = -\delta E_{\parallel}(p \sin(\theta_{\parallel} - \theta) + \alpha \cos(\theta_{\parallel} + \theta)) \quad (4.31)$$

We focus now on the diagonal terms to get the dephasing produced by these terms. The dephasing term is then:

$$\begin{aligned} \Delta H_{--}^{(2)} - \Delta H_{++}^{(2)} &= (E_1 + Z_1)(E_1^* + Z_1^*) \left(\frac{1}{E_l - E_u - \varepsilon_{Zl}/2 + \varepsilon_{Zu}/2} - \frac{1}{E_l - E_u + \varepsilon_{Zl}/2 - \varepsilon_{Zu}/2} \right) \\ &+ (E_2 + Z_2)(E_2^* + Z_2^*) \left(\frac{1}{E_l - E_u - \varepsilon_{Zl}/2 + \varepsilon_{Zu}/2} - \frac{1}{E_l - E_u + \varepsilon_{Zl}/2 - \varepsilon_{Zu}/2} \right) \end{aligned} \quad (4.32)$$

As for a given i the terms Z_i and E_i are one purely imaginary and the other purely real, we have:

$$(E_i + Z_i)(E_i^* + Z_i^*) = |E_i|^2 + |Z_i|^2 + (E_i Z_i^* + E_i^* Z_i) = |E_i|^2 + |Z_i|^2 \quad (4.33)$$

This means that terms linear in the in-plane electric fields are identically zero. Moreover, the terms involving $|Z_i|^2$ are static so they do not dephase the qubit and can be ignored. Expanding to first order the denominator terms, the expression for second order charge noise dephasing becomes:

$$\Delta E_{Larmor}^{noise} = |E_1|^2 \frac{\varepsilon_{Zl} - \varepsilon_{Zu}}{(E_l - E_u)^2} + |E_2|^2 \frac{\varepsilon_{Zu} + \varepsilon_{Zl}}{(E_l - E_u)^2} \quad (4.34)$$

Which, after substituting expressions becomes:

$$\begin{aligned} \Delta E_{Larmor}^{noise} &= \frac{\delta E_{\parallel}^2}{(E_l - E_u)^2} \left[(\alpha \sin(\theta + \theta_{\parallel}) + p \cos(\theta - \theta_{\parallel}))^2 (\varepsilon_{Zl} - \varepsilon_{Zu}) \right. \\ &\quad \left. + (\alpha \cos(\theta + \theta_{\parallel}) - p \sin(\theta - \theta_{\parallel}))^2 (\varepsilon_{Zu} + \varepsilon_{Zl}) \right] \end{aligned} \quad (4.35)$$

In the limit of large α , which is valid for example at the isotropic sweet spot and within a big window of the anisotropic sweet spot, we can further simplify this expression:

$$\Delta E_{Larmor}^{noise} = \alpha^2 \frac{\delta E_{\parallel}^2}{(E_l - E_u)^2} \left[\varepsilon_{Zl}(\phi) + \varepsilon_{Zu}(\phi) \cos(2(\theta(\phi) - \theta_{\parallel})) \right] \quad (4.36)$$

This expression can be set to zero by carefully choosing ϕ for several values of θ_{\parallel} but not always. For those cases in which this is not possible it is still possible to minimize as a function of ϕ .

One minimal condition to have noise insensitive to second order is $\varepsilon_{Zl} \leq \varepsilon_{Zu}$. Substituting expressions this is equivalent to the condition:

$$\Delta_{HL} + 2\sqrt{3}pF_z \sin(2\phi) \geq 0 \quad (4.37)$$

This means that in the small electric field limit the mitigation is not possible but for high enough F_z it could be. For example, we take again the sweet spot values and this condition is equivalent to:

$$\frac{1}{2} \arcsin\left(\frac{1}{3}\right) \leq \phi \leq \frac{\pi}{2} - \frac{1}{2} \arcsin\left(\frac{1}{3}\right) \quad (4.38)$$

This is indeed the window where the anisotropic sweet spot is at bigger or equal electric field than the isotropic sweet spot. Within this window it is possible to find an orientation ϕ such that the in-plane noise is canceled out.

Another interesting limit is $F_z = 0$. In this case $a_L = -1$ and $a_H = 0$. Taking the corresponding limits we get:

$$\Delta E_{Larmor}^{noise}(F_z = 0) = \varepsilon_Z \frac{\delta E_{\parallel}^2}{(E_l - E_u)^2} (\alpha^2 + p^2 + 2\alpha p \sin(2\theta_{\parallel})) \quad (4.39)$$

At $F_z = 0$ the limit $|\alpha| \gg |p|$ holds for several values of d , so:

$$\Delta E_{Larmor}^{noise}(F_z = 0) \approx \alpha^2 \varepsilon_Z \frac{\delta E_{\parallel}^2}{(E_l - E_u)^2} \quad (4.40)$$

This means that at $F_z = 0$ the in-plane noise is independent on the magnetic field orientation. This is an expected result because at $F_z = 0$ there is no mixing of HH and LH that can create the magnetic field anisotropy.

In Fig. 4.7 we assume a particularly harmful defect at 40 nm from the acceptor such that it induces a fluctuation with $\delta E_{\parallel} = 3$ kV/m oriented in the (001) direction. In the worst case scenario we can assume a correlation time of this defect of 1 μ s (slower fluctuating defects can be suppressed by a well coordinated pulse sequence and faster defects decohere slower than slow defects.). We can relate this parameters to the dephasing time [244]:

$$1/T_2 = \frac{\Delta E_{Larmor}^2 \tau}{2\hbar^2} \quad (4.41)$$

Using Eq. 4.36 to obtain the change in Larmor energy, T_2 is obtained. It can be seen that it depends on ϕ and for both sweet spots there are values for which $1/T_2 = 0$.

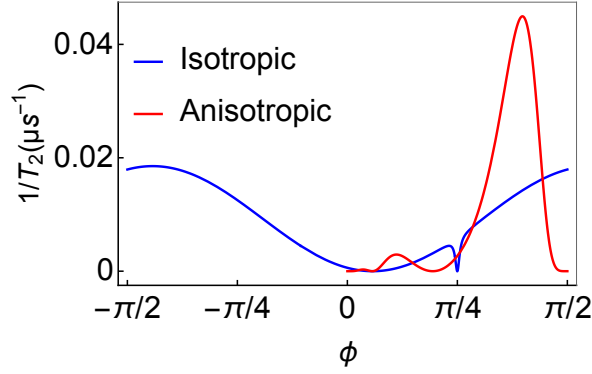


FIGURE 4.7: Estimate of dephasing due to second order charge noise for a given defect with $\delta E_{\parallel} = 3\hat{x}$ kV/m with $\tau = 10^{-6}$ s. It can be seen that both sweet spots have values of ϕ where the qubit is insensitive to this particular defect.

4.5.2 Phonon-induced relaxation

At low temperatures the expression for the relaxation times of the acceptor qubit is [125]:

$$\frac{1}{T_1} = \frac{(\hbar\omega)^3}{20\hbar^4\pi\rho} \left[\sum_i |\langle -|D_{ii}|+\rangle|^2 \left(\frac{2}{v_l^5} + \frac{4}{3v_t^5} \right) + \sum_{i \neq j} |\langle -|D_{ij}|+\rangle|^2 \left(\frac{2}{3v_l^5} + \frac{1}{v_t^5} \right) \right] \quad (4.42)$$

Where the parameters ρ , v_l and v_t are material dependent parameters, see [30]. Going to second order in the SW transformation we get:

$$\langle -|D_{ij}|+\rangle = \frac{1}{E_l - E_u} (\hat{H}'_{-,u-} \hat{H}'_{u-,+} + \hat{H}'_{-,u+} \hat{H}'_{u+,+}) \quad (4.43)$$

Where \hat{H}' can be split into the off-diagonal Zeeman and the phonon contributions $\hat{H}' = \hat{H}'_B + \hat{H}'_{ph}$. The elements of the Hamiltonian \hat{H}'_{ph} are:

$$\begin{aligned} D_{ii} &= b'(J_i^2 - \frac{5}{4}) \\ D_{ij} &= 2d'/\sqrt{3}\{J_i, J_j\} \quad i \neq j \end{aligned} \quad (4.44)$$

Where the values of b' and d' are deformation potential constants of Si [30]. The values of $|\langle -|D_{ij}|+\rangle|^2$ at the isotropic sweet spot are independent of the angle ϕ except for the intrinsic dependence of ε_{Z_o} . These values are

$$\begin{aligned} |\langle -|D_{xx}|+\rangle|^2 &= |\langle -|D_{yy}|+\rangle|^2 = 3b^2\varepsilon_{Z_o}^2/64\Delta^2 \\ |\langle -|D_{zz}|+\rangle|^2 &= 3b^2\varepsilon_{Z_o}^2/16\Delta^2 \\ |\langle -|D_{xy}|+\rangle|^2 &= d^2\varepsilon_{Z_o}^2/16\Delta^2 \\ |\langle -|D_{xz}|+\rangle|^2 &= |\langle -|D_{yz}|+\rangle|^2 = d^2\varepsilon_{Z_o}^2/8\Delta^2 \end{aligned} \quad (4.45)$$

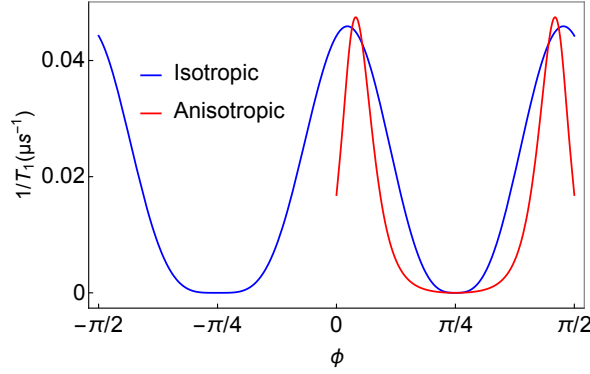


FIGURE 4.8: Estimate of the relaxation times as a function of ϕ for both sweet spots. Two mechanisms allow the suppression of this decoherence mechanism which corresponds to different values of ϕ for which $T_1 \rightarrow \infty$ to first order.

In the case of the anisotropic sweet spot the values of $|\langle -|D_{ij}|+\rangle|^2$ are

$$\begin{aligned}
 |\langle -|D_{xx}|+\rangle|^2 &= |\langle -|D_{yy}|+\rangle|^2 = 3b^2\varepsilon_{Z_o}^2/64\Delta^2 \\
 |\langle -|D_{zz}|+\rangle|^2 &= 3b^2\varepsilon_{Z_o}^2/16\Delta^2 \\
 |\langle -|D_{xy}|+\rangle|^2 &= d^2\varepsilon_{Z_o}^2/16\Delta^2 \\
 |\langle -|D_{xz}|+\rangle|^2 &= d^2\varepsilon_{Z_o}^2\cos^2\theta_o/4\Delta^2 \\
 |\langle -|D_{yz}|+\rangle|^2 &= d^2\varepsilon_{Z_o}^2\sin^2\theta_o/4\Delta^2
 \end{aligned} \tag{4.46}$$

Collecting terms, the new dependence on the phase θ_o cancels out so we arrive to the original formula in Ref. [125], except for the intrinsic ϕ dependence of ε_{Z_o} and the energy difference $\hbar\omega$.

The general formula for phonon-induced relaxation, valid at both sweet spots, is then

$$\frac{1}{T_1} = \frac{(\hbar\omega(\phi))^3}{20\hbar^4\pi\rho} \left(\frac{\varepsilon_{Z_o}(\phi)}{E_l - E_u} \right)^2 \left[\frac{3b'}{32} \left(\frac{2}{v_l^5} + \frac{4}{3v_t^5} \right) + \frac{5d'}{48} \left(\frac{2}{3v_l^5} + \frac{1}{v_t^5} \right) \right] \tag{4.47}$$

Interestingly, as shown in Fig. 4.8 the phonon-induced relaxation can be suppressed under certain circumstances. These are those for which $\varepsilon_{Z_o} = 0$ and when $\hbar\omega(\phi) = 0$. The former corresponds to when the qubit and upper branches do not interact in such a way that the qubit branch is isolated not only from phonon-induced relaxation but also from any charge noise to first order. This is the case of the isotropic sweet spot when $\phi = -\pi/4$, while in the anisotropic sweet spot it happens when $\phi = \pi/4$. The latter mechanism corresponds to when the magnetic field points perpendicularly to the fixed effective spin polarization of the isotropic sweet spot, in this case the qubit is insensitive to the magnetic field and the phonon-induced relaxation is irrelevant. In this case however, other mechanisms would arise since the temperature is not exactly zero and $k_B T > \hbar\omega$.

4.5.3 Decoherence Free Subspace

As previously shown, under certain circumstances the qubit becomes isolated from the excited states and $\varepsilon_{Z_o} = 0$. This only happens when one of the branches has a fixed spin polarization and the magnetic field points in parallel to this polarization. We distinguish then two ways of achieving this DFS: (i) magnetic field pointing in the same direction of the spin polarization

of the qubit branch in the isotropic sweet spot. In this case θ_l becomes a constant of motion and the Zeeman interaction is perfectly diagonal. This happens when $\phi = -\pi/4 + n\pi$; (ii) magnetic field pointing in the same direction of the spin polarization of the upper branch in the anisotropic sweet spot. In this case θ_u becomes a constant of motion and the Zeeman interaction is again perfectly diagonal. This happens when $\phi = \pi/4 + n\pi$.

Compared to conventional DFSs, where decoherence is suppressed via the symmetries of the encoded states, the DFS here is achieved by actively controlling the strength of its interaction with the environment. The magnetic field orientation can be chosen beforehand, and F_z can be used to go to the DFS in a particular sweet spot. Both cases correspond to a particular mixing of HH-LH in one of the branches. In both branches, when the amplitude probability of LH is $|a_L| = \sqrt{3}/2$ and the amplitude probability of HH is $|a_H| = 1/2$ the particular branch becomes decoupled from the other branch. It is a property of the states with this particular mixing of HH and LH. Any interaction term that allows such mixing would have similar properties.

We can see this by trying to find the DFS from the Hamiltonian level. As the qubit interacts with the upper states through the Zeeman interaction, we can see this subspace as a leakage submanifold. The interaction terms between the qubit states and the leakage states are then given by the off-diagonal Zeeman terms in the qubit Hamiltonian. A decoherence free subspace would be a subspace in which the Zeeman interaction is purely diagonal in the qubit basis, or equivalently $[H_{T_d} + H_{\text{interface}}, H_B] = 0$. In this subspace, all the interactions would be suppressed to first order. To find such subspace we use the following elements that form part of a bigger basis of the space of spin 3/2:

$$\begin{aligned}
e_1 &= \frac{\mathbb{1}}{2} \\
e_2 &= 1/6(2J_z^2 - J_x^2 - J_y^2) \\
e_3 &= 1/\sqrt{5}J_x \\
e_4 &= 1/\sqrt{5}J_y \\
e_5 &= 1/\sqrt{12}\{J_x, J_y\} \\
e_6 &= 1/\sqrt{12}\{J_y, J_z\} \\
e_7 &= 1/\sqrt{12}\{J_z, J_x\}
\end{aligned} \tag{4.48}$$

In this basis the elements of the effective Hamiltonian are

$$\begin{aligned}
H_{\text{inter}} &= \Delta_{HL}(e_1 - e_2) \\
H_{T_d} &= 2pF_z e_5 \\
H_B &= \sqrt{5}(B_x e_3 + B_y e_4)
\end{aligned} \tag{4.49}$$

The commutators are then

$$\begin{aligned}
[H_{\text{inter}}, H_B] &= i2\sqrt{3}\Delta_{HL}(B_y e_7 - B_x e_6) \\
[H_{T_d}, H_B] &= -4ipF_z(B_x e_7 - B_y e_6)
\end{aligned} \tag{4.50}$$

The total commutator is

$$\begin{aligned}
[H_{\text{inter}} + H_{T_d}, H_B] &= e_7(-4ipF_z B_x + i2\sqrt{3}\Delta_{HL}B_y) \\
&+ e_6(4ipF_z B_y - i2\sqrt{3}\Delta_{HL}B_x)
\end{aligned} \tag{4.51}$$

As e_7 and e_6 are different elements of the basis, $[H_{\text{inter}} + H_{T_d}, H_B] = 0$ is equivalent to solve the following system

$$\begin{aligned}\Delta_{HL}B_y - \frac{2pF_z}{\sqrt{3}}B_x &= 0 \\ \Delta_{HL}B_x - \frac{2pF_z}{\sqrt{3}}B_y &= 0\end{aligned}\quad (4.52)$$

The system has non-trivial solutions if and only if $B_x = \pm B_y$ which corresponds to the orientations $\pm\pi/4 + n\pi$. These are the most symmetric directions as the main axes of the crystal remain indistinguishable.

In the case $B_x = -B_y$, the solution requires $\Delta_{HL} = -\frac{2pF_z}{\sqrt{3}}$ which corresponds to the isotropic sweet spot. The case $B_x = B_y$ requires $\Delta_{HL} = \frac{2pF_z}{\sqrt{3}}$ corresponding to the anisotropic sweet spot. These conditions are indeed equivalent to the previous conditions of the amplitude probabilities of LH and HH being $|a_L| = \sqrt{3}/2$ and $|a_H| = 1/2$ respectively. In these two cases the Zeeman interaction can be diagonalized simultaneously with the interface and T_d symmetry terms, so the qubit becomes isolated from the upper branch.

It is also interesting to express the different contributions in terms of the spherical tensors J_+ and J_-

$$\begin{aligned}H_{T_d} + H_{\text{inter}} &= -\frac{3}{4}\mathbf{1} - \frac{i}{8}(\Delta_{HL} + 2pF_z/\sqrt{3})(J_+ + iJ_-)^2 \\ &+ \frac{i}{8}(\Delta_{HL} - 2pF_z/\sqrt{3})(J_+ - iJ_-)^2 \\ H_B &= \frac{1+i}{4}(B_x - B_y)(J_+ - iJ_-) \\ &+ \frac{1-i}{4}(B_x + B_y)(J_+ + iJ_-)\end{aligned}\quad (4.53)$$

From here it can be seen how for the sweet spots, and for particular values of the magnetic fields, the non-magnetic and the magnetic terms share eigenvectors. The operators of $H_{T_d} + H_{\text{inter}}$ form a spin quadrupole which is the square of the dipolar spin interaction with the magnetic field. Consequently, both operators commute.

4.6 Two-qubit coupling: Entanglement

In this section the dipolar coupling between two acceptors is calculated for an arbitrary ϕ . Due to the spin-orbit interaction and the electric dipole moment of each acceptor a spin-dependent dipolar interaction is expected between the two acceptors. Let the subspace of the two qubits be $\{|l^{-a}, l^{-b}\rangle, |l^{-a}, l^{+b}\rangle, |l^{+a}, l^{-b}\rangle, |l^{+a}, l^{+b}\rangle\}$. The total Hamiltonian is $H^\Sigma = H_{op}^a + H_{op}^b + V^{ab}$, where H_{op} are the single acceptor Hamiltonians and V^{ab} is the Hamiltonian of the electrostatic interaction given by $V^{ab}(\mathbf{r}_a - \mathbf{r}_b) = e^2/4\pi\epsilon|\mathbf{r}_a - \mathbf{r}_b|$.

Here we assume that each qubit may have different energies and applied fields. The single qubit Hamiltonians are:

$$\langle m|H_{op}^i|m'\rangle = \begin{pmatrix} -\frac{\varepsilon_i^i}{2} & 0 & Z_1^i & iZ_2^i \\ 0 & \frac{\varepsilon_i^i}{2} & iZ_2^i & Z_1^i \\ Z_1^i & -iZ_2^i & \Delta^i - \frac{\varepsilon_u^i}{2} & 0 \\ -iZ_2^i & Z_1^i & 0 & \frac{\varepsilon_u^i}{2} + \Delta^i \end{pmatrix} \quad (4.54)$$

Where the superindex i indicates acceptor a or b.

We assume two acceptors separated by a distance \mathbf{R} . When the two acceptors are far enough we can use the multi-pole expansion for the Coulomb interaction:

$$\langle mn|V^{12}|m'n'\rangle = \frac{R^2 \langle m|e\mathbf{r}'_1|m'\rangle \cdot \langle n|e\mathbf{r}'_2|n'\rangle - 3(\langle m|e\mathbf{r}'_1|m'\rangle \cdot \mathbf{R})(\langle n|e\mathbf{r}'_2|n'\rangle \cdot \mathbf{R})}{4\pi\epsilon R^5} \quad (4.55)$$

Being $\mathbf{r}'_i = \mathbf{r}_i - \mathbf{R}_i$ the hole coordinate relative to the ion, and assuming an arbitrary relative position in the xy plane $\mathbf{R} = R \cos(\theta_E)\hat{x} + R \sin(\theta_E)\hat{y}$, so

$$\begin{aligned} \langle mn|V^{12}|m'n'\rangle &= \frac{(1 - 3 \cos^2 \theta_E) \langle m|ex'_1|m'\rangle \cdot \langle n|ex'_2|n'\rangle + (1 - 3 \sin^2 \theta_E) \langle m|ey'_1|m'\rangle \cdot \langle n|ey'_2|n'\rangle}{4\pi\epsilon R^3} \\ &+ \frac{\langle m|ez'_1|m'\rangle \cdot \langle n|ez'_2|n'\rangle}{4\pi\epsilon R^3} \end{aligned} \quad (4.56)$$

The dipole matrix elements relevant for the Coulomb interaction are:

$$\langle m|e(x', y')^i|m'\rangle = \begin{pmatrix} 0 & 0 & iq_{1x,y}^i & q_{2x,y}^i \\ 0 & 0 & q_{2x,y}^i & iq_{1x,y}^i \\ -iq_{1x,y}^i & q_{2x,y}^i & 0 & 0 \\ q_{2x,y}^i & -iq_{1x,y}^i & 0 & 0 \end{pmatrix} \quad (4.57)$$

where $q_{1x}^i = \alpha^i \sin \theta^i$, $q_{2x}^i = -\alpha^i \cos \theta^i$, $q_{1y}^i = \alpha^i \cos \theta^i$, and $q_{2y}^i = \alpha^i \sin \theta^i$ (assuming the approximation $\alpha \gg p$ valid for both qubits).

We can project the interactions into the 4×4 subspace using a SW transformation. Working out $H^{(2)}$ gives a spin-independent shift:

$$H^{(2)} = - \left[\frac{((q_1^a)^2 + (q_2^a)^2) \left((q_1^b)^2 + (q_2^b)^2 \right)}{\Delta^a + \Delta^b} + \frac{(Z_1^a)^2 + (Z_2^b)^2}{\Delta^a} + \frac{(Z_1^b)^2 + (Z_2^a)^2}{\Delta^b} \right] \mathbf{1} \quad (4.58)$$

The third-order correction is

$$\begin{aligned} H_{mm'}^{(3)} &= -\frac{1}{2} \sum_{l,m''} \left[\frac{H'_{ml} H'_{lm''} H'_{m''m}}{(E_{m'} - E_l)(E_{m''} - E_l)} + \frac{H'_{mm''} H'_{m''l} H'_{lm'}}{(E_m - E_l)(E_{m''} - E_l)} \right] \\ &+ \frac{1}{2} \sum_{l,l'} H'_{ml'} H'_{ll'} H'_{l'm'} \left[\frac{1}{(E_m - E_l)(E_m - E_{l'})} + \frac{1}{(E_{m'} - E_l)(E_{m'} - E_{l'})} \right] \end{aligned} \quad (4.59)$$

The result of the third order correction to zeroth order in ε_i is

$$H^{(3)} = J_{dd} \begin{pmatrix} 0 & 0 & 0 & 1 \\ 0 & 0 & 1 & 0 \\ 0 & 1 & 0 & 0 \\ 1 & 0 & 0 & 0 \end{pmatrix} \quad (4.60)$$

where

$$J_{dd} = \frac{4(q_2^a Z_1^a + q_1^a Z_2^a)(q_2^b Z_1^b + q_1^b Z_2^b)}{\Delta^a \Delta^b} \quad (4.61)$$

Which is an Ising type spin-spin interaction

$$H^{(3)} = J_{dd}(\sigma_{a+} + \sigma_{a-})(\sigma_{b+} + \sigma_{b-}).$$

After adding all the contributions and substituting, the value of J_{dd} is:

$$J_{dd} = \frac{\alpha^a \alpha^b \varepsilon_{Z_o}^a \varepsilon_{Z_o}^b (\sin \theta_o^a \sin \theta_o^b (1 - 3 \sin^2 \theta_E) + \cos \theta_o^a \cos \theta_o^b (1 - 3 \cos^2 \theta_E))}{4\pi\epsilon R^3 (E_l^a - E_u^a)(E_l^b - E_u^b)} \quad (4.62)$$

This dipole-dipole coupling J_{dd} is inversely proportional to the qubit-upper branch energy separation Δ , and it is directly proportional to the qubit-upper branch couplings ε_{Z_o} of each qubit, and their Rashba couplings α , such that

$$J_{dd} = \frac{\alpha^a \alpha^b \varepsilon_{Z_o}^a \varepsilon_{Z_o}^b}{8\pi\epsilon R^3 \Delta^a \Delta^b} G(F_z^a, F_z^b, \phi, \theta_E), \quad (4.63)$$

with $G(F_z^a, F_z^b, \phi, \theta_E)$ a modulating function that depends on the operating point of each qubit, the magnetic field orientation ϕ and the relative orientation θ_E . In the original proposal [125], with $\phi = 0$, this coupling allows 10^4 two qubit operations per qubit lifetime when both qubits are at the isotropic sweet spot and separated by 20 nm. Since each qubit is operated at a sweet spot, we can consider three ideal situations: (i) both qubits at their isotropic sweet spots; (ii) one qubit at the isotropic and the other at the anisotropic one; (iii) both qubits at their anisotropic sweet spots. Note that gate voltages alone can switch between these cases. Substituting for each case we get:

Case (i): We get:

$$J_{dd} = \frac{3}{2} \varepsilon_Z^2 (1 + \sin(2\phi)) \frac{\alpha^a \alpha^b}{8\pi\epsilon R^3 (E_l^a - E_u^a)(E_l^b - E_u^b)} \quad (4.64)$$

Case (ii): Omitting the complex dependence in the dynamic sweet spot of θ_o on ϕ :

$$J_{dd} = \frac{3\varepsilon_Z^2 \sqrt{1 + \sin(2\phi)} \alpha^a \alpha^b |\cos(2\phi)|^2}{16\pi\epsilon R^3 (E_l^a - E_u^a)(E_l^b - E_u^b) \sqrt{7 + 4 \cos 4\phi - 3 \cos 8\phi}} \times \frac{(3 \cos(3\phi - \theta_o^a) - \cos(\phi + \theta_o^a) - 3 \cos(2\theta_E)(\cos(\phi - \theta_o^a) - 3 \cos(3\phi + \theta_o^a)))}{(4.65)}$$

Case (iii):

$$J_{dd} = 3\varepsilon_Z^2 \frac{\alpha^a \alpha^b \cos^2(2\phi) [(1 - 3 \cos^2 \theta_E) \cos \theta_o^a \cos \theta_o^b + (1 - 3 \sin^2 \theta_E)] \sin \theta_o^a \sin \theta_o^b}{8\pi\epsilon R^3 (E_l^a - E_u^a)(E_l^b - E_u^b) (3 \cos(4\phi) - 5)} \quad (4.66)$$

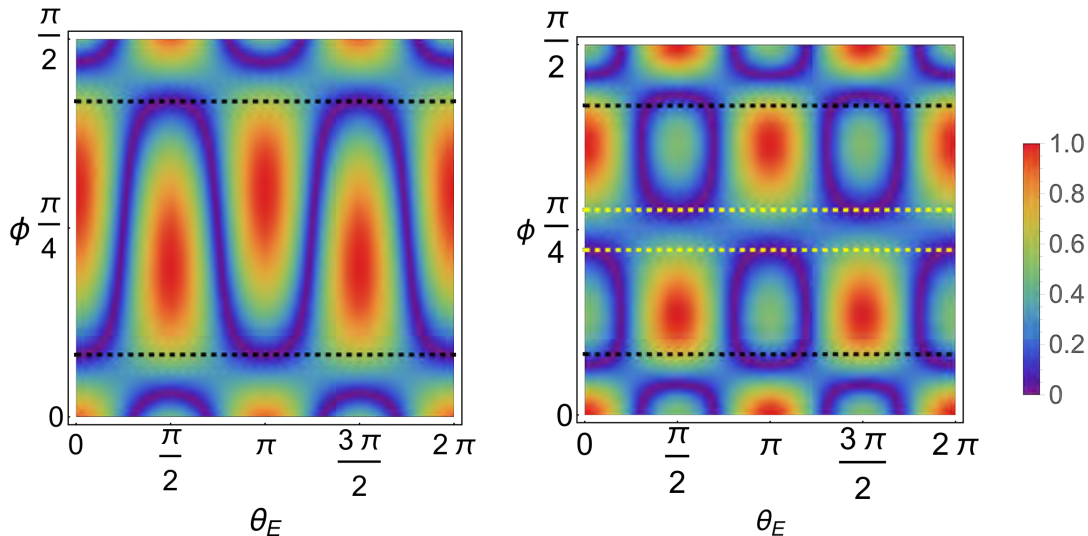


FIGURE 4.9: Normalized function $G(F_z^a, F_z^b, \phi, \theta_E)$ that modulates the entanglement coupling, see Eq. 4.63. In case (i) $G(F_z^a, F_z^b, \phi, \theta_E) = 1$ independently of the relative orientation. (Left) Case (ii): Qubit a is at the isotropic sweet spot while qubit b is at the anisotropic. The black dashed lines indicate 15° and 75° , orientations for which the coupling is suppressed in one main axis while enhanced in the other. (Right) Case (iii): Both qubits are at the anisotropic sweet spot. The black dashed line shows that 15° and 75° maintain their behavior qualitatively. The yellow lines correspond to 40° and 50° , which have now a qualitative behavior similar to 15° and 75° in case (ii) respectively.

The normalized angular distribution of cases (ii) and (iii) as a function of the relative orientation θ_E can be seen in Fig. 4.9. An alternative way of visualizing this coupling dynamically as a function of θ_E is in movie 4.10, where the blue and red curves correspond to case (ii) and (iii) respectively.

4.6.1 Magic angles

[movie](#)

The coupling J_{dd} can be suppressed by two mechanisms that do not involve deactivating any of the qubits: (i) eliminating the qubit dynamics in a DFS (namely, making $\varepsilon_{Z_o} = 0$), though this mechanism is not efficient as the J_{dd} suppression with $\varepsilon_{Z_o}^2$ is as fast as the increase in T_1 , thus the number of allowed two qubit operations is maintained; (ii) by choosing parameters such that $G(F_z^a, F_z^b, \phi, \theta_E) = 0$ (see purple areas in Fig. 4.9). The latter corresponds to magic angles of the magnetic field that depend on the relative orientation between acceptors and the operating point of the qubits.

In case (i) the dipolar coupling is perfectly isotropic $G(F_z^a, F_z^b, \phi, \theta_E) = 1$, hence neighboring qubits at isotropic sweet spots will always be coupled. Cases (ii) and (iii) are anisotropic and for certain relative orientations θ_E there are certain values of phi (magic angles) at which this dipolar coupling is zero even though the individual dipoles of each qubit are activated due to the high vertical field.

Interestingly, the existence of magic angles for different operating points also means that it is possible to turn on and off the two-qubit couplings by going from different combinations of sweet spots. This only requires the election of a particular orientation ϕ in a magic angle beforehand and then use the top gate voltage of the qubits to move adiabatically among

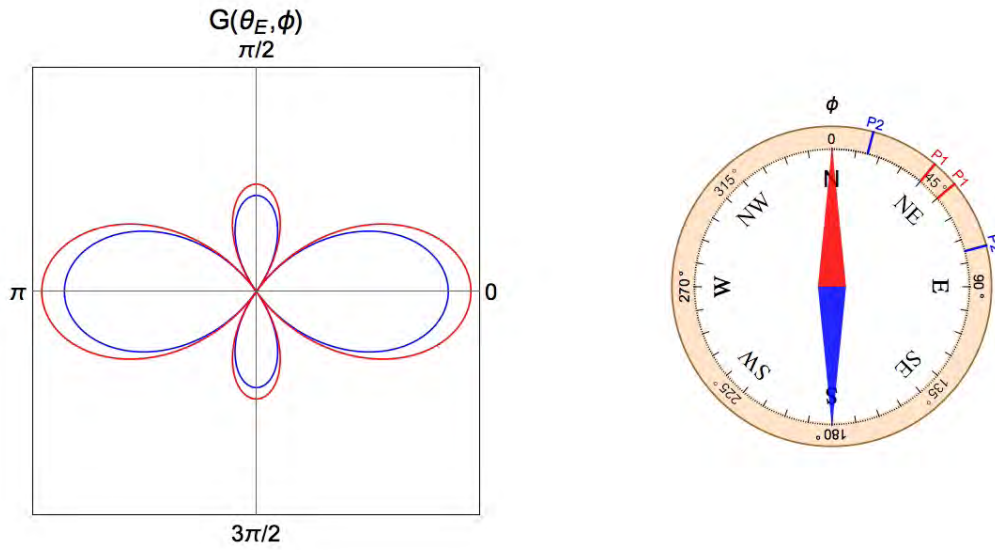


FIGURE 4.10: (Quicktime Movie in the pdf version) $J_{dd}(\theta_E)$ angular distribution for a given magnetic field. The red curve corresponds to case (iii) while the blue curve corresponds to the case (ii). The specific angles for protocols 1 and 2 are labeled as P1 and P2 respectively.

the different sweet spot combinations to switch on and off the two qubit interactions. This mechanism is the cornerstone that allows us to define protocols for entanglement based on all electrical interactions. In general, since this magic angles only suppress the coupling in one direction these protocols assume one direction for fast entanglement operations using this mechanism with a linear array while the other direction is used for entanglement via cQED with any qubit from other arrays.

4.6.2 Protocol 1

For this case we choose $\phi = 40^\circ$ ($\phi = 50^\circ$) and locate acceptors ≈ 20 nm away in the x (y) direction, such that we keep the ratio of two qubit operations per qubit lifetime $\approx 10^4$. We place acceptors at ≥ 100 nm away in the y (x) direction. Sweeping the local gates such that two neighboring qubits in the x (y) direction are taken to their anisotropic sweet spots (case (iii)), the coupling J_{dd} is suppressed in that particular direction and each qubit can be addressed individually, see Fig. 4.11(Left). Then, taking adiabatically one or both qubits to the isotropic sweet spot, the coupling is reactivated. In the perpendicular direction, J_{dd} cannot be turned off without deactivating one of the qubits at this particular ϕ , so acceptors need to be more separated and entanglement between any pair of qubits is performed via cQED [125]. An easy way to visualize the coupling distribution for each case in this protocol can be seen in the movie 4.10 where P1 indicates the first protocol angles.

4.6.3 Protocol 2

The acceptors are placed in a similar 2D array, choose $\phi = 15^\circ$ ($\phi = 75^\circ$). Sweeping the local gates such that two neighboring qubits in the x (y) direction are taken to the anisotropic-isotropic sweet spot combination (case (ii)), the coupling J_{dd} is suppressed in that particular direction and each qubit can be addressed individually, see 4.11(Right). Then the qubit

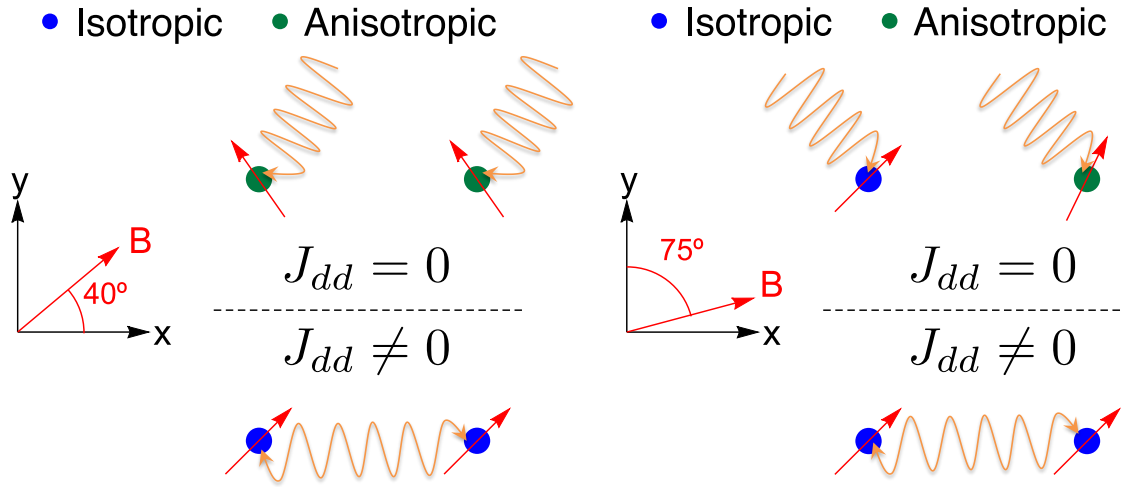


FIGURE 4.11: (Left) Scheme of protocol 1. The anisotropic-anisotropic combination is used for single qubit operations. Two-qubit operations are activated in the isotropic-isotropic combination. (Right) Scheme of protocol 2. The isotropic-anisotropic combination is used for single qubit operations. Two-qubit operations are activated in the isotropic-isotropic combination..

at the anisotropic sweet spot is adiabatically swept to the isotropic sweet spot and J_{dd} is reactivated. Again, cQED is performed in the y (x) direction.

4.7 Discussion: Experimental implications

4.7.1 Single-qubit operations

With the coupling in Eq. 4.25 and the limiting factor T_1 in Eq. 4.47 we can calculate the number of π single qubit rotations per qubit lifetime, see Fig. 4.12. The number of qubit operations diverges when T_1 tends to infinity, since $T_1 \propto 1/\varepsilon_{Z_0}^2$ while $D \propto \varepsilon_{Z_0}$. A similar tendency can be seen when the Larmor energy goes to 0. In this case the EDSR coupling is maximized while T_1 is minimized. Other processes, such as temperature, would limit this scenario since $k_B T > \hbar\omega$ at the isotropic sweet spot when $\phi = \pi/4$. Moreover, for the particular values $\phi = 1/2 \arcsin(1/3) + n\pi$, and $\phi = 1/2(\pi - \arcsin(1/3)) + n\pi$, the isotropic and anisotropic sweet spots fuse into a single sweet spot that would make the qubit insensitive to charge noise up to second order, see Fig 4.3. In this case the energy dispersion is particularly flat at the sweet spot within a 2-3 MV/m window. Hence, tuning the qubit to this second order sweet spot would further increase the coherence properties of the system, eventually allowing the observation of atomic clock transitions. Outside this second order sweet spot the magnetic field orientation provides an experimental knob to minimize the effects of second order charge fluctuations, see Fig. 4.7. In that figure the effect on the qubit strongly depends on ϕ and can be minimized and even removed at certain orientations that depend on the particular position of the charge trap relative to the acceptor. This can be used to characterize the different noise sources for a given device by measuring T_2^* for several magnetic field orientations. The information obtained from such measurements would also

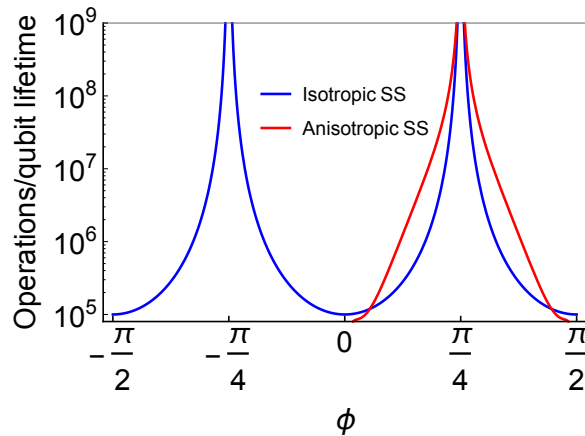


FIGURE 4.12: Number of single qubit operations per qubit lifetime as a function of ϕ for an acceptor at 4.6 nm and $B = 0.5\text{T}$.

be relevant for donor based qubits or Si/SiO₂ confined quantum dots, since those qubits operate in similar environments, as well as shedding light on $1/f$ noise.

In particular, we can use the different possible regimes in F_z and ϕ to devise a way to fully characterize how different contributions of noise affect the qubit. The most interesting configurations to analyze the noise in a particular device would be:

(a) $F_z = 0$, $\phi = n\pi/2$: With this orientation $F_z = 0$ corresponds to the anisotropic sweet spot. Since there is no vertical field applied, α is very small so charge noise is suppressed in the z direction to first order. This small value of α also implies that charge noise is also suppressed to second order in the horizontal directions. However, a slight variation in the direction of the magnetic field would move the position of this sweet spot so the qubit is sensitive to magnetic noise. With natural Si, this configuration could be used to estimate how sensitive the qubit is to this magnetic noise since, even under these circumstances, holes are expected to be more insensitive to magnetic noise than electrons.

(b) $F_z = 0$, $\phi \neq n\pi/2$: By moving ϕ when $F_z = 0$ we move the anisotropic sweet spot position and hence, we modify the sensitivity to vertical charge noise dF_z . In this configuration, in-plane charge noise would be suppressed to second order and, together with the information obtained from (a), the vertical charge noise could be characterized as a function of ϕ .

(c) F_z at the merged sweet spot, $\phi = 1/2 \arcsin(\pi/3)$: In this configuration the qubit is insensitive to vertical charge noise up to second order but, second order charge noise is relatively high due to the high value of α . The strength of second order in-plane charge noise could be characterized in this case.

(d) F_z at the isotropic sweet spot: With the information from (a), (b), and (c), second order in-plane charge noise could be characterized as a function of ϕ . This is particularly interesting since, using Eq. 4.36 with the experimental information, the relative positions of potentially harmful interfacial defects could be estimated.

(e) F_z at the anisotropic sweet spot: Changing ϕ the position of this sweet spot is modified. While the sensitivity to vertical charge noise will be suppressed, by moving the value of the sweet spot to higher F_z the value of α will smoothly increase and, hence, the sensitivity to second order in-plane charge noise would also increase. This would help to

characterize how strong the in-plane charge noise can increase with α and, together with the information of the other configurations and Eq. 4.25 could be used as a way to estimate how α changes.

(f) F_z at the isotropic sweet spot, $\phi \approx \pi/4$: In this case $\hbar\omega$ would be suppressed, but it could be used to obtain information about other mechanisms affecting T_1 .

(g) F_z at the isotropic sweet spot, $\phi \approx -\pi/4$ or F_z at the anisotropic sweet spot, $\phi \approx \pi/4$: This corresponds to the DFS. To first order the qubit would be disconnected from the environment and only second order processed would affect the qubit.

4.7.2 Entanglement

Both entanglement protocols require adiabatically sweeping the vertical electric field to move among sweet spots. This raises the issue of decoherence exposure during the procedure. The answer to this question allows to discern the advantages of each protocol. Since the exact amount of charge noise is device dependent, we account for the charge noise exposure qualitatively. In the original proposal for entanglement in the acceptor qubit [125, 126] the electric field is adiabatically swept from $F_z = 0$ to F_z at the isotropic sweet spot. Hence, the simplest qualitative way of comparing protocols is to account for the ratio $T_2^*(\phi)/T_2^*(0)$. Here $T_2^*(\phi)$ would be related to the amount of charge noise accumulated when going from the anisotropic sweet spot to the isotropic sweet spot for a given ϕ , and $T_2^*(0)$ the exposure to charge noise in the original proposal. Given a fluctuating charged defect with field δF_z we compute the change in energy δE_{Larmor} for a given value of F_z in the qubit. How much the defect affects the qubit energy depends on the derivative of the Larmor energy on F_z . From [244] we know that $1/T_2^* \propto \delta E_{\text{Larmor}}^2$. Defining F_z^* and \tilde{F}_z as the values of the vertical electric field at the isotropic and anisotropic sweet spots respectively, we account for the total charge noise exposure by integrating the Larmor energy change along the path from \tilde{F}_z to F_z^* :

$$I(\phi) = \int_{\tilde{F}_z}^{F_z^*} \delta E_{\text{Larmor}}^2(F_z) dF_z \quad (4.67)$$

By assuming a constant sweep rate, the time of exposure to charge noise is proportional to the difference between the initial and final electric fields. In total we get

$$\frac{T_2^*(\phi)}{T_2^*(0)} = \left| \frac{I(0)F_z^*}{I(\phi)(F_z^* - \tilde{F}_z)} \right| \quad (4.68)$$

Intuitively, this ratio is simply proportional to the charge noise sensitivity along the path and its length. The values of this ratio can be seen in Fig. 4.13 From Fig. 4.13 it is clear that any $\phi \neq 0$ reduces the charge noise exposure by sweeping between sweet spots. The explanation is simply that the closer the sweet spots are the less time the qubits are exposed to charge noise. Moreover, when the two sweet spots are closer, the derivative dE_{Larmor}/dF_z also becomes smaller. As a result, the exposure to charge noise by sweeping between sweet spots goes to zero when the two sweet spots merge at $\phi = 1/2 \arcsin(1/3)$ and $\phi = \pi/2 - 1/2 \arcsin(1/3)$.

Protocol 1 requires a magnetic field orientation very close to the DFS of the anisotropic sweet spot, which means single-qubit operations per qubit lifetime are extremely enhanced. However, the exposure to charge noise in the adiabatic sweeping is higher than in protocol 2 due to the difference in Larmor frequency between sweet spots. Protocol 2 is not close to the DFS, hence the single-qubit operations are not particularly enhanced, though T_1 is

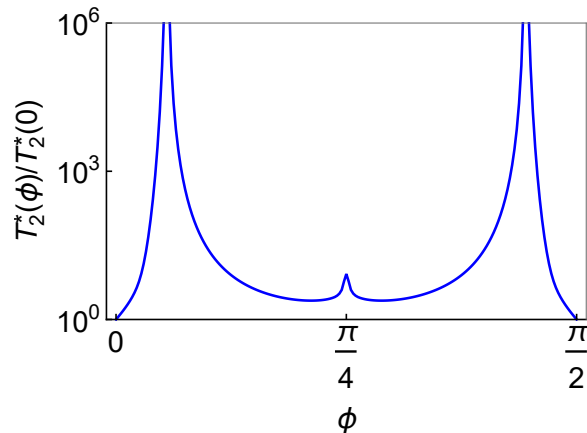


FIGURE 4.13: Ratio $T_2^*(\phi)/T_2^*(0)$ as a function of ϕ . Note that the charge noise exposure is always better for any $\phi \neq 0$, $T_2^*(\phi)/T_2^*(0) \geq 1$.

still enhanced with respect to the $\phi = 0$ case. Exposure to decoherence during the adiabatic sweep is strongly minimized since the value of ϕ is close to the one that merges the isotropic and anisotropic sweet spots (they are barely separated by ≈ 1.5 MV/m). We also note that both protocols are robust against acceptor placement imprecision. Specifically, for an accuracy of ± 5 nm in the in-plane positioning, for an inter-acceptor distance of 20 nm, the angle variation would be of $\pm 15^\circ$. Under these circumstances, J_{dd} would be small (see Fig. 4.9) rather than completely switch off in one direction. Still the ratio between the coupling enhancement in one direction and the suppression in the perpendicular one would be ≈ 10 .

4.8 Conclusions

In conclusion, we have shown that the in-plane magnetic field orientation is an effective control parameter for acceptor based qubits which is of particular relevance to experiment. As a reorientation of the magnetic field would be slow compared to typical manipulation times, it would be advisable to keep the orientation fixed during qubit operation. A particular orientation would hence be chosen beforehand in order to tune the physical system to a particular working regime. For instance, near a DFS (i.e. $\phi = -\pi/4 + n\pi$ at the isotropic sweet spot) it would be possible to increase the number of operations per qubit lifetime. An orientation $0 \leq \phi \leq \pi/2$ would allow us to get two sweet spots, at two close values of F_z , each one with different manipulability and coherence properties. For $\phi = 1/2 \arcsin(1/3) + n\pi$, or $\phi = 1/2(\pi - \arcsin(1/3)) + n\pi$, the two sweet spots merge making the qubit insensitive to charge noise up to second order, eventually allowing the observation of atomic clock transitions. The magnetic field orientation could be also used to characterize the noise sources affecting quantum computing at Si/SiO₂ interfaces. Finally, the coupling between neighboring qubits can be switched on and off by the electric field for particular values of the magnetic field orientation. This allows us to devise protocols where the exposure to charge noise is suppressed and still the qubits can be individually addressed. In summary, this unexpected parameter dependence can be used to perform experiments in different regimes, with different manipulability and coherence properties, within the same single physical system.

Part II

Quantum dots

Disorder effects on Tunneling and Valley physics in Si Double Quantum Dots.¹

5.1 Introduction

In recent years, control over Si quantum dot electronic devices has improved rapidly. For instance, controlled population has been proven not only in single quantum dots [147], but also in double dot systems [176–179]. In several quantum dot qubit systems, such as charge qubits, fast manipulation can be done solely by electric means [170]. This is a desirable quality since manipulation by local oscillating magnetic fields is experimentally more challenging and requires more power. However, manipulation via electric fields is often accompanied by sensitivity to charge noise, which limits the qubit coherence times. Charge noise has been shown to affect quantum-double-dot qubits, principally through the detuning control parameter [246], resulting in dephasing that depends on the energy dispersion as a function of detuning [247]. One method to reduce charge noise is to take advantage of the physical degrees of freedom to define a qubit with stronger coherence properties.

For Si dots, the energy dispersion is strongly affected by the physics of the conduction band minima, or *valleys* [187, 248]. Notably, atomic-scale disorder at the quantum well interface affects the valley degree of freedom, allowing mixing with the orbital degrees of freedom (valley-orbit mixing), strongly affecting the tunnel coupling between dots [155, 159, 164, 187, 249–254], and thus the qubit frequency.

We focus on a specific qubit implementation based on Si/SiGe quantum wells: the quantum dot hybrid qubit,[165, 255–261] which behaves as a charge qubit when the detuning is close to zero, and has a spin-like character for large detuning values, $\varepsilon \gg 0$. The double dot device considered for comparison in this chapter was described in ref [262]. The relevant low energy Hamiltonian is

$$H_{\text{eff}} = \begin{pmatrix} \varepsilon/2 & \Delta_1 & \Delta_2 \\ \Delta_1 & -\varepsilon/2 & 0 \\ \Delta_2 & 0 & -\varepsilon/2 + \Delta_R \end{pmatrix}. \quad (5.1)$$

¹Article in preparation [245].

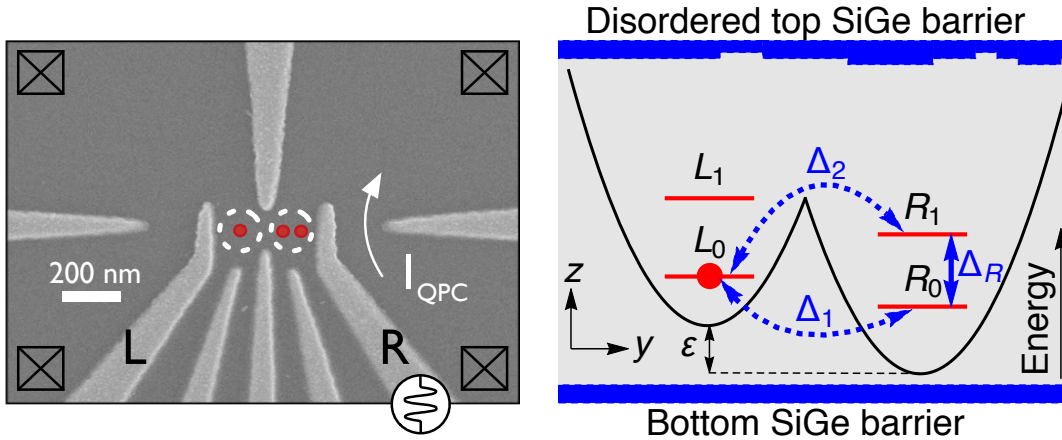


FIGURE 5.1: (Left) A scanning electron microscope image of a device nominally identical to the one used in the experiments of the quantum dot hybrid qubit. The gate voltages are tuned to form two quantum dots, located approximately within the dashed circles, where red dots represent electrons in a (1,2) charge configuration. (Right) Schematic cartoon illustrating the two-dimensional, single-electron theoretical model employed in our tight-binding simulations. The quantum well heterostructure is taken to be $\text{Si}_{0.7}\text{Ge}_{0.3}/\text{Si}/\text{Si}_{0.7}\text{Ge}_{0.3}$, and atomic-scale step disorder is added to the top interface. The lateral confinement potential is defined to be biquadratic, and the two dots are offset by energy ε . The low-energy eigenstates of the isolated dots are labelled $|L_0\rangle$, $|L_1\rangle$, $|R_0\rangle$, and $|R_1\rangle$, while the interdot tunnel couplings are labelled Δ_1 and Δ_2 . We refer to Δ_R as the “valley splitting,” although $|R_1\rangle$ can represent a valley-orbit excitation.

Specifically, the quantum dot spin-charge hybrid qubit’s main advantage is that all operations can be performed via electric fields, without any magnetic fields, resulting in fast operations and reducing the experimental complexity. This system is a double-dot device with three electrons operating near the (2,1)-(1,2) anticrossing with tunnel coupling Δ_1 , see Fig. 5.1. For three spin 1/2 electrons the resulting total spin space is formed of a spin quadruplet $S = 3/2$, and two doublets with $S = 1/2$. The logical qubit is encoded in the two states with $S = 1/2$, $S_z = -1/2$ and, since both states have same spin quantum numbers electrical operations are allowed. Regarding the charge degree of freedom, for negative values of detuning, the configuration is the (2,1). At $\varepsilon = 0$ there is a charge transition $(2,1) \rightarrow (1,2)$. This is the charge qubit regime, where electrical manipulation can be fast but, it is also more susceptible to charge noise. In the far detuning regime, however, the qubit states are encoded in the logical qubits $|0\rangle = |\downarrow\rangle|S\rangle$ and $|1\rangle = \sqrt{\frac{1}{3}}|\downarrow\rangle|T_0\rangle - \sqrt{\frac{2}{3}}|\uparrow\rangle|T_-\rangle$. Being $|S\rangle$, $|T_0\rangle$, and $|T_1\rangle$ the singlet $|S\rangle = 1/\sqrt{2}(|\uparrow\downarrow\rangle - |\downarrow\uparrow\rangle)$, the triplet $|T_0\rangle = 1/\sqrt{2}(|\uparrow\downarrow\rangle + |\downarrow\uparrow\rangle)$, and the triplet $|T_-\rangle = |\downarrow\downarrow\rangle$. The energy difference between the two qubit states in the far detuning regime, Δ_R , is mostly determined by the valley splitting of the right-hand dot, although other contributions such as the exchange interaction or the Coulomb repulsion are also relevant. In this regime the qubit behaves as a spin qubit, with slower transitions and better coherence properties since the qubit energy has a very stable energy dispersion. However, in this regime the derivative of the qubit energy with detuning $\partial f_Q/\partial\varepsilon$ is only zero asymptotically when $\varepsilon \rightarrow \infty$, hence, no true sweet spots are expected. Nonetheless, full and fast electrical control of such qubit has recently been demonstrated in this large detuning region [263].

In this chapter we theoretically show that random disorder in the position of the quantum well interface, combined with the ability to electrostatically manipulate the dot positions, allows us to find sweet spots in the energy dispersion, even in the spin-like regime. In order to simulate the low energy physics of the quantum dot hybrid qubit, we employ spinless

single electron 2D tight binding simulations that captures all the relevant physics, see Fig. 5.1(Right). The relevant states of each dot in this case are the ground and excited valley-orbit states. The electron can tunnel from the ground state of the left dot to the ground and excited states of the right dot, similar to the charge-qubit dynamics of the hybrid qubit. In the far detuning regime, the relevant states are the two right localized valley states being the qubit energy dominated by the valley splitting. As will be shown in this chapter, this simple model of a single electron in a double quantum dot captures the relevant physics both qualitatively and quantitatively. At the same time, the problem becomes much cheaper computationally and still allows to analyze the relevant valley physics.

We also compare our theoretical results with recent experiments that show evidence for a sweet spot occurring in an unexpected regime of control space, as well as the converse effect where decoherence is strongly enhanced by a *hotspot* [264]. We also provide potential explanations for these phenomena in the form of specific disorder profiles that generate similar energy dispersions in the 2D tight-binding simulations of a double-quantum dot in a SiGe/Si/SiGe quantum well.

5.2 Tight binding model

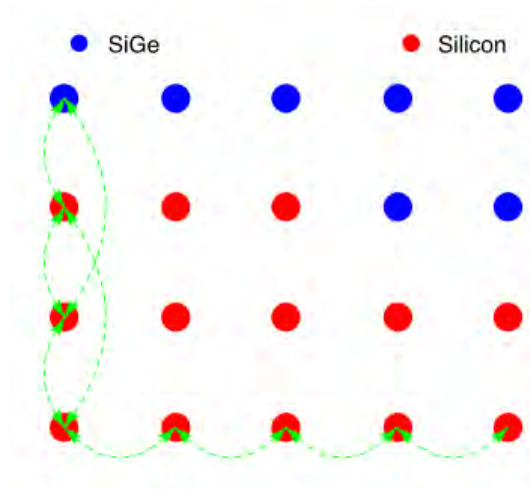


FIGURE 5.2: Schematic representation of the tight binding model. The SiGe barrier atoms have a higher on-site energy than the Si atoms. In the horizontal direction the atoms are connected to nearest neighbors, while in the vertical direction they are connected up to second nearest neighbors to include the valley oscillations. Atomic disorder is accounted by the vertical position of the SiGe barrier.

Here, we focus on atomic step disorder that arises during heterostructure growth, due to the underlying miscut of the substrate wafer, or the presence of dislocations caused by strain relaxation. Since the disordered interface has an atomistic nature, a simple EMA would overlook the atomic details that change from site to site. A TB approach is expected to give more accurate results.

This TB approach is represented schematically in Fig. 5.2. We consider a vertical direction \hat{z} as the growth direction, which we assume here to be aligned with the (001) crystal axis. In this direction there is a top and a bottom SiGe barriers that confine the electron. We consider a vertical electric field F_z that further confines the electron wavefunction against the top interface, where the interfacial disorder is going to be accounted for.

For a strained Si quantum well, the two low-lying conduction band valleys are centered at positions $\mathbf{k}_0 = \pm 0.82(2\pi/a)\hat{\mathbf{z}}$ in the Brillouin zone, where $a = 0.543$ nm is the length of the (unstrained) Si cubic unit cell. The double-dot confinement potential in the x - y plane is obviously three-dimensional (3D). However, an interfacial step is a planar feature, which generates coupling between the valley and orbital degrees of freedom (valley-orbit coupling) in the same plane [159]. If we define this as the y - z plane, and further orient the double-dot along $\hat{\mathbf{y}}$, then the essential physics of our problem is all contained within a single plane, and inclusion of the third dimension ($\hat{\mathbf{x}}$) only provides quantitative corrections, but no new physics. Our minimal model can therefore be reduced to two dimensions, corresponding to the y - z plane.

5.2.1 Valley degree of freedom

Following the theoretical background subsection 1.4.3, the minimal tight-binding model captures the valley positions as well as their longitudinal and transverse effective masses ($m_l = 0.916 m_0$ and $m_t = 0.191 m_0$, respectively) by introducing nearest- and next-nearest-neighbor hopping parameters in the z direction [151, 152] ($u_z = t_1 = 0.68$ eV and $v_z = t_2 = 0.61$ eV, respectively), and a separate nearest-neighbor hopping parameter in the x - y plane [186, 251, 265] ($u_y = t = -10.91$ eV).

The hopping parameters, described above, account for the kinetic energy, H_K , of an electron in a strained Si quantum well. The electronic potential energy is described via on-site terms, involving several contributions that include the confinement potential. A uniform on-site term $\epsilon = 23.23$ eV sets the band minimum to zero inside the quantum well.

5.2.2 Confinement and fields

We introduce a quantum well with a barrier of height $V_{\text{QW}} = 0.15$ eV, as appropriate when Si is sandwiched between strain-relaxed $\text{Si}_{0.7}\text{Ge}_{0.3}$. In all cases, we consider a quantum well width of 9.85 nm. We include a vertical electric field F , as consistent with experiments, which pulls the electron wavefunction up against the top interface:

$$H_F = -eFz. \quad (5.2)$$

Ideally, this field should be large enough that the electron feels no confinement effects from the bottom of the quantum well. We model the two dots, centered at positions y_L and y_R , with a biquadratic potential, see Fig. 5.1(Right):

$$H_{\text{DD}} = \min \left[\frac{1}{2} m_t \omega^2 (y - y_L)^2, \frac{1}{2} m_t \omega^2 (y - y_R)^2 \right], \quad (5.3)$$

where ω represents the orbital excitation frequency of the individual dots. For simplicity here, we assume both dots have the same frequency. Model parameters including y_L , y_R , F , and ω are chosen randomly, within a range of values consistent with the experiments [262]. These correspond to interdot distances around $100 \text{ nm} \leq y_R - y_L \leq 200 \text{ nm}$, $0.5 \text{ MV/m} \leq F \leq 5 \text{ MV/m}$, and $0.2 \text{ meV} \leq \hbar\omega \leq 0.6 \text{ meV}$.

Finally, we include the effects of a detuning parameter ϵ via an in-plane electric field:

$$H_\epsilon = -\frac{\epsilon}{2(y_R - y_L)} y. \quad (5.4)$$

5.2.3 Disordered interface

If we define the position of the bottom interface as z_b , and assume the top interface $z_t(y)$ is a function of position (disorder), then the barrier potential can be written as

$$H_{\text{QW}} = V_{\text{QW}} [\theta(z_b - z) + \theta(z - z_t(y))]. \quad (5.5)$$

The full Hamiltonian of the system is then written as

$$H = H_K + H_{\text{QW}} + H_F + H_{\text{DD}} + H_\varepsilon. \quad (5.6)$$

We find that the effect of a given profile on the energy dispersion can be difficult to predict, *a priori*. We have therefore performed a large number (>2500) of simulations incorporating randomly generated step profiles, such as those shown in Figures 5.9, 5.11, and 5.13. The disorder models we employ include steps of one or two different widths, ranging from narrow to wide (Figure 5.8), and we allow the interface position $z_t(y)$ to deviate from its average value by a standard deviation of 1 to 2 atomic steps.

5.3 Effective Hamiltonian

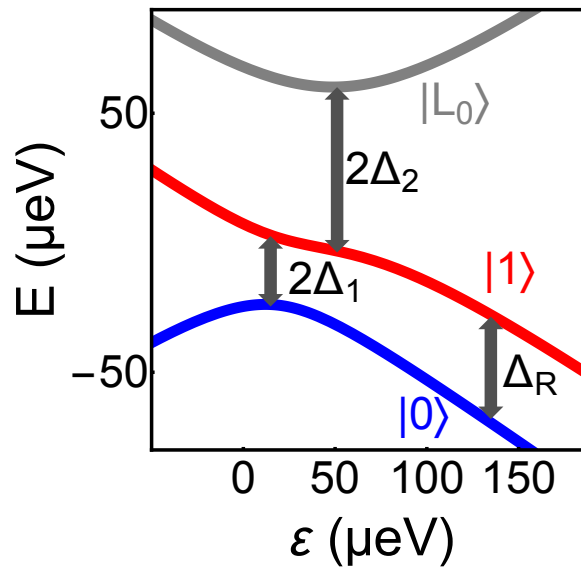


FIGURE 5.3: Low energy diagram of the lowest states obtained from the tight binding simulations as a function of detuning. Δ_1 and Δ_2 represent the two relevant tunnel couplings while Δ_R represents the asymptotic value of the right dot valley splitting.

The simulations with random parameters are evaluated as a function of ε to obtain the low energy physics. Our analysis is focused in a regime in which the left localized dot excited state $|L_1\rangle$ is more energetic than the two lowest right localized states, see Fig. 5.1. In this regime, all the dynamics can be understood in terms of the single electron tunneling dynamics and the valley splitting of the right localized states. In Fig. 5.3 we can see the detuning dependence of the relevant states. The lowest state for negative detuning is the left localized valley ground state $|L_0\rangle$. When $\varepsilon \approx 0$ an anticrossing between $|L_0\rangle$ and $|R_0\rangle$ with tunnel coupling Δ_1 occurs, corresponding to the tunneling from the (1,0) to the (0,1) configuration. A second anticrossing corresponds to the tunnel from the left dot to the excited valley state

of the right dot, with tunnel coupling Δ_2 . After this second anticrossing, the qubit states are the right localized ground and excited valley-orbit states, with qubit energy asymptotically defined by Δ_R . As a result, the effective Hamiltonian corresponds to:

$$H_{\text{eff}} = \begin{pmatrix} \varepsilon/2 & \Delta_1 & \Delta_2 \\ \Delta_1 & -\varepsilon/2 & 0 \\ \Delta_2 & 0 & -\varepsilon/2 + \Delta_R \end{pmatrix}, \quad (5.7)$$

being Δ_1 , Δ_2 , and Δ_R parameters that depend strongly on the different parameters of the quantum well, defined in each simulation. More importantly, Eq. 5.7 is identical to the effective Hamiltonian of the quantum dot hybrid qubit in Eq. 5.1. Being each parameter in the single electron TB physically analogous to the relevant parameters of the quantum dot hybrid qubit (QDHQ).

Two different methods were used to determine the fitting parameters Δ_1 , Δ_2 , and Δ_R , appearing in Eq. 5.7. The first method considers that the parameters are constants in ε . In this case the parameters were determined by fitting the qubit frequency, obtained from the two low-energy eigenvalues of Eq. 5.7 ($hf_Q \equiv E_1 - E_0$), using the least-square method. This is equivalent to obtaining an average of the different parameters in ε . As a result, the obtained values of Δ_1 and Δ_2 are mostly determined by the values at their respective anticrossings.

The second method was used for detuning dependent results, the fitting parameters for the simulations were determined as a function of ε . In the far-detuned regime ($\varepsilon \gg 0$), where the two low-energy eigenstates have charge configuration (0,1), we first determine the valley splitting, $\Delta_R(\varepsilon)$, by replacing the double-dot confinement potential, eq 5.3, with the right-localized single-dot potential,

$$H_{\text{SD}} = \frac{1}{2}m_t\omega^2(y - y_R)^2, \quad (5.8)$$

and repeating the tight-binding simulation, assuming the same interface disorder potential. Ignoring the left-hand dot in this way is acceptable, because the tails of the wave function do not play a significant role in determining the valley splitting. On the other hand, the wave function tails play an important role in determining the tunnel couplings $\Delta_1(\varepsilon)$ and $\Delta_2(\varepsilon)$. We compute these quantities by straightforwardly solving the roots of the characteristic polynomial of Eq. 5.7, using the previously computed function $\Delta_R(\varepsilon)$.

We find that each one of the different parameters of the effective Hamiltonian strongly depend, not only on the interdot distance or the dot confinement potential, but also on the particular disorder profile at the interface.

5.4 Vertical electric field effects

In order to analyze the effects of atomic interfacial disorder on the relevant low energy physics parameters, we can consider a single atom step (bump) at the top interface for simplicity. This bump has a defined width w_0 and is centered at y_0 . We can use the vertical electric field F_z to modify the electron density wavefunction near this bump, allowing us to increase or decrease its effects on the effective Hamiltonian.

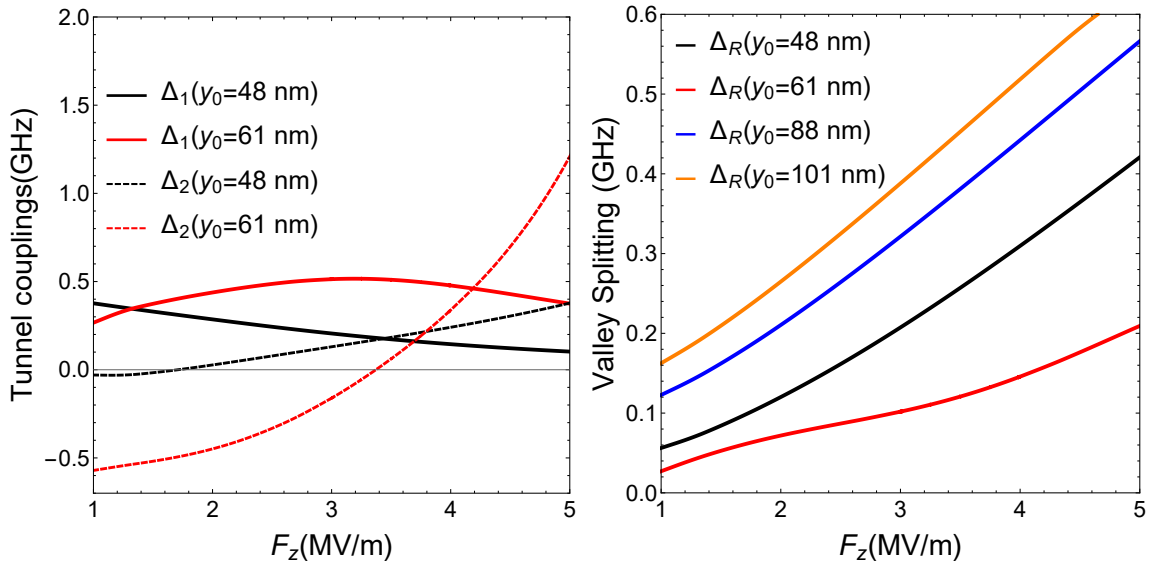


FIGURE 5.4: (Left) Tunnel couplings in GHz (1 GHz = 4.13 μeV) as a function of the vertical electric field for a $w_0 = 40$ nm single bump centered at y_0 . (Right) Value of the right dot valley splitting as a function of F_z for a $w_0 = 40$ nm bump.

5.4.1 Intervalley Tunneling

Disorder strongly affects the tunnel couplings between different valley states [251]. In a device with a perfectly flat interface, left localized and right localized valley states have coherent valley oscillations. This means that without any disorder distorting the envelope of the electron wavefunction, the valley oscillations of each dot are in phase, and the ground state of each dot oscillates coherently in z . As a result, the overlap between different valley states of each dot is necessarily zero, hence $\Delta_2 = 0$, while Δ_1 is mostly determined by the interdot distance and the dot confinement.

Interfacial disorder distorts the envelope of the wavefunction and, as a result, the valley oscillations are affected [251]. This valley-orbit effect results in a non-zero overlap between intervalley states, implying $\Delta_2 \neq 0$. Moreover, changing F_z the electron density wavefunction near a bump is strongly affected, modifying the relative phase between different localized valley states. As a consequence, the different tunnel couplings may show a non-trivial dependence on F_z , see Fig. 5.4(Left).

In particular, different realizations of a single bump (different widths and/or positions) will result in different values of the tunnel couplings and different electric field dependence. In general, the dependence is hard to predict due to the interplay between the valley and orbit degrees of freedom. For example, a single bump implies that there is a small region where the disorder is pushing away the wavefunction, but this may only be true for one of the valley states because the atomic step occurs where this valley state has a minimum due to the valley oscillations, this is schematically shown in Fig. 5.5. This may result in interesting valley-orbit effects such as one valley state being repelled by the bump, while the other is paradoxically attracted by the barrier.

As an example of these valley-orbit effects, in Fig. 5.4 there are cases where $\Delta_2 = 0$ even under the effects of interfacial disorder. In these cases the valley oscillations are affected differently as a function of the horizontal position, resulting in an overall destructive interference.

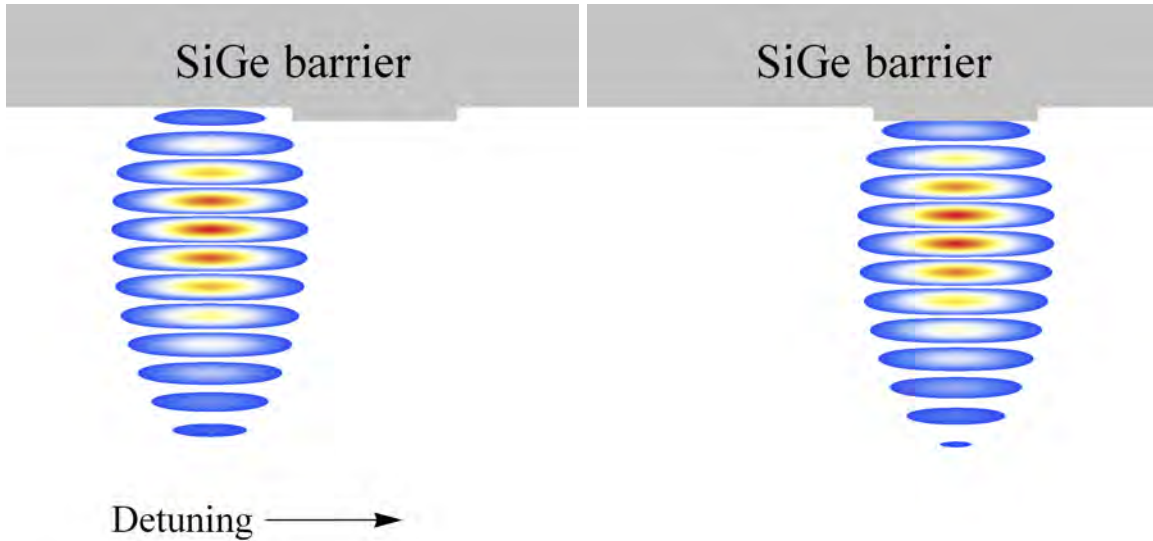


FIGURE 5.5: Example of a valley-orbit effect. (Left) Valley ground state wavefunction being pushed by detuning against a bump. The bump acts as a barrier, preventing the movement of the wavefunction. (Right) Valley excited state wavefunction being pushed by detuning against the bump. In this case the valley oscillations are such that the wavefunction does not see the bump (minimum of the oscillation) and hence, the bump does not act as a barrier and the valley state moves freely.

5.4.2 Valley splitting

As stated previously, different valley states are differently affected by atomic disorder. One valley state may feel the bump while the other is barely affected depending on the valley phase of each state. This implies that one valley state may be energetically displaced with respect to the other, or that the valley splitting is affected.

This can be seen in Fig. 5.4(Right), where different realizations of disorder are shown. Changing F_z changes how each valley state feels disorder and modifies the valley splitting. At the same time, due to the different valley phase, one of the states will always have a higher density inside the barrier so increasing the vertical field, also increases this wavefunction density difference. As a result, the valley splitting increases with F_z even when no disorder is present, until it reaches a saturation value $\hbar\omega$ related to the dot confinement potential [251].

5.5 Detuning effects

In Fig. 5.6(Left) the qubit frequency $f_Q = E_1 - E_0$ of one QDHQ device as a function of detuning is shown. The qubit frequency was obtained experimentally in Mark Eriksson's group. In Fig. 5.6(Right) the qubit frequency is obtained for three different disorder realizations. Interestingly, the values of the different effective parameters of the simulations and the experiment are almost the same. However, the simulations show that even when the effective parameters are almost identical on average, small features showing a detuning dependence may arise. Indeed, these parameters are not always constant in experiments; in particular, they have been found to depend on ε [246, 266].

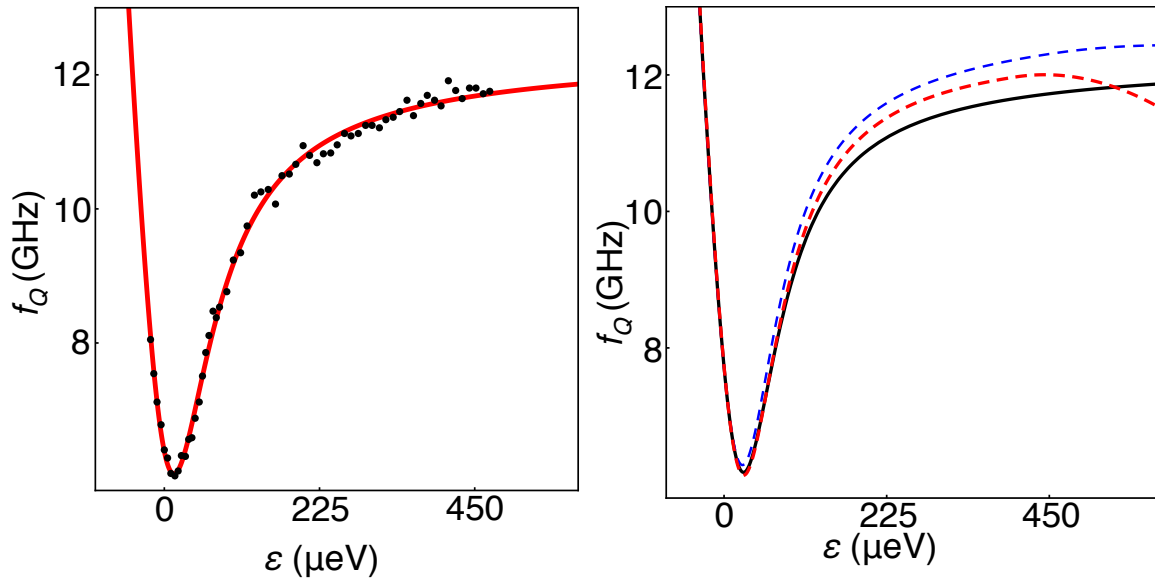


FIGURE 5.6: (Left) The experimentally measured qubit frequency of a quantum-dot hybrid qubit as a function of detuning, ε (black dots). (Right) Three qubit frequency dispersions, obtained from tight-binding simulations with different disorder profiles. The Hamiltonian parameters used in the simulations are consistent with those in the experiments, and fits of the qubit energy splitting yield results very close to (Left) but with very different detuning dependences.

5.5.1 Intervalley Tunneling

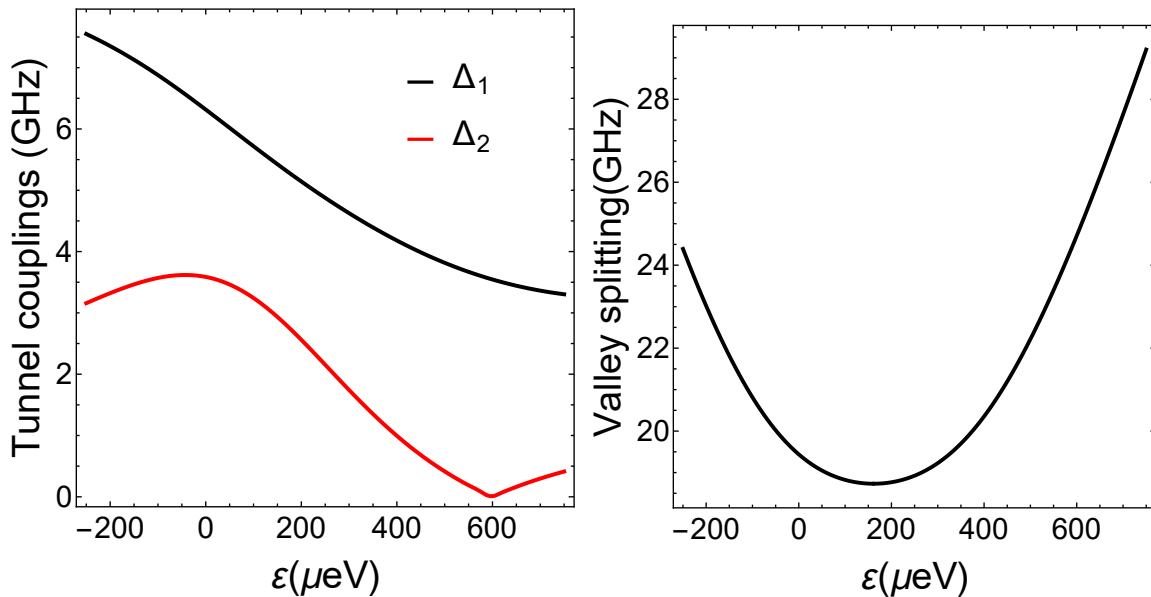


FIGURE 5.7: (Left) Tunnel couplings as a function of detuning for a disorder configuration with one narrow bump (7 nm) at $y_0 = -20$ nm. (Right) Value of the right dot valley splitting as a function of detuning for the same configuration.

We find that the different tunnel couplings, and the valley splitting depend on ε . In Fig. 5.7(Left) this tunnel coupling dependence is shown for a particular disorder realization. The mechanism behind this dependence is different to the F_z dependence. While ε does not directly push the wavefunction against an atomic step like F_z , it can move the center of mass

(COM) of each wavefunction. By slightly moving the COM, the electron wavefunction may feel different realizations of the interfacial disorder, strongly affecting the tunnel couplings or the valley splitting as seen in the previous section.

In particular, due to valley-orbit effects, one valley state may be more sensitive to ε in comparison to the other due to the different relative position of its valley oscillations and the atomic steps. This results in valley dependent COM dynamics, which may result in an interplay with the dot potential.

5.5.2 Valley splitting

In a similar way, the valley splitting is strongly affected by ε when there is interfacial disorder. This can be seen in Fig. 5.7(Right) where the valley splitting reaches a minimum around $150 \mu\text{eV}$. In this particular case the ground state increases its energy due to the atomic step, while the excited valley state barely sees the step due to the minimum of its valley oscillations. As a result the energy difference is reduced as long as the ground state can see this bump.

More complex realizations, with a higher number of atomic steps with different heights may result in more complex dependences. In most of the cases, even under complex disorder profiles, the COM movement is usually slow with ε , resulting in smooth and monotonous dependences of all the parameters in ε . These cases would be easy to average to a constant value of the parameters for the relevant detuning region in the experiments. Other cases, such as those that will be presented in the following section, with sharper behavior cannot be explained within the constant parameter approximation and may strongly affect the charge noise susceptibility of a particular device.

5.6 Comparison with experiments

In this section we compare our simulations with some experimental results obtained following the methods from [262]. In that work, applies several types of pulse sequences are applied in order to map out energy dispersions for the qubit. First, they perform a Ramsey sequence that allows the energy dispersion to be mapped out over a wide range of detunings. The qubit is initialized to its ground state, $|0\rangle$, corresponding to the north pole of the Bloch sphere. A microwave voltage pulse is then applied to the gate labeled R in Figure 5.1(Left), which is calibrated to perform an $X_{\pi/2}$ rotation, onto the equator of the sphere. The dc bias voltage on gate R is adjusted so that the detuning parameter has value ε , where free induction ensues. After a fixed time period, t_{free} , the detuning is adiabatically returned to its initial value, and a second $X_{\pi/2}$ rotation is performed. Finally, the qubit is measured, and the experiment is repeated as a function of t_{free} , to obtain Ramsey fringes. Repeating these measurements for different ε yields a dispersion curve $f_Q(\varepsilon)$. The lower panels of Figures 5.8(Left) and 5.10(Left) show two such results, obtained at different tunings of the same device, where f_Q ($\rightarrow \Delta f_Q$) has been shifted by a constant value, for clarity. As in Ref [262], we have also fit the Ramsey fringes to exponentially decaying sinusoids, yielding estimates for the decay rates Γ_2^* , which we plot in the top panels of those figures.

Secondly, they use a different pulse sequence to map the dispersion, a Larmor pulse sequence, where they start by initializing the qubit with $\varepsilon_0 \ll 0$, then they abruptly change the detuning

of the qubit such that $\varepsilon \geq 0$. This abrupt change makes the qubit state a superposition of the qubit eigenstates and free induction ensues. After a fixed time period, t_{free} , detuning is abruptly changed back to its initial value where the qubit is measured. By repeating this measurement as a function of t_{free} Larmor fringes are obtained. The qubit Larmor frequency f_Q is obtained corresponding to the detuning value ε by Fourier transforming this data. The dispersion relation is then mapped by repeating this measurements at different ε values as shown in the bottom panel of Figure 5.12. Again, the qubit frequency has been shifted by a constant amount.

Finally, a Rabi pulse sequence is performed. The qubit is first initialized at a detuning ε , microwaves are then applied to gate R for a variable time t_{RF} . The microwaves are then turned off and the qubit is measured. This measurement is then repeated at different ε values, by adjusting the voltage on gate L, yielding oscillations like those shown in the upper panel of Figure 5.12(Left). As in ref [262], we fit the slowest oscillations to a exponentially decaying sinusoid, yielding estimates for the Rabi decay rates $\Gamma_{\text{Rabi}} = 5.4$ MHz. There is mounting evidence that the form of the dispersion relation plays a crucial role in determining the qubit response to charge noise [263, 267–273]. In ref [262] it was demonstrated that a strong correlation between the measured dephasing rate $\Gamma_2^* = 1/T_2^*$ and the dispersion $f_Q(\varepsilon)$, via the relation [246, 247]

$$\Gamma_2^* = \sqrt{2\pi} |\partial f_Q / \partial \varepsilon| \sigma_\varepsilon, \quad (5.9)$$

where σ_ε represents the standard deviation of the quasi-static charge noise, which should be a constant for a given device, at a given temperature. The current data in Figures 5.8, 5.10, and 5.12 exhibit correlations which are also consistent with Eq. 5.9, with remarkable detail. Here, we observe three distinct types of dispersion phenomena.

5.6.1 Typical behavior

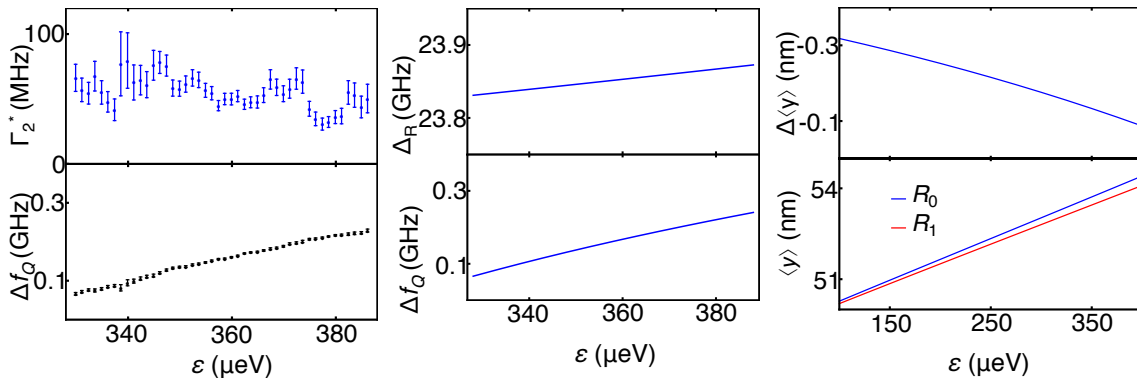


FIGURE 5.8: (Left) Energy dispersion with the typically monotonous behavior as a function of detuning. On the top panel it is shown that this monotonous behavior is inherited by the coherence properties. (Center) Identical behavior obtained through the tight binding simulations. On top the valley splitting is shown as a function of detuning. (Right) Center of mass $\langle y \rangle$ (bottom) and relative center of mass $\Delta \langle y \rangle$ (top) of the lowest two valley states. The COM physics also shows a monotonous behavior.

By far the most common type of behavior is shown in Figure 5.8(Left), where Δf_Q appears smooth and monotonous as a function of ε . In this case, no strong features are observed in Γ_2^* , as expected.

Similarly, the theoretical dispersion on the bottom of Figure 5.8(Center) is very similar to Figure 5.8(Left). These results represent the most common behavior observed in our simulations: smooth and monotonic dispersions. We note that a significant amount of disorder is needed, to suppress the valley splitting to the levels shown in the figures; however, this does not necessarily produce distinctive features in the data. The valley splitting, Δ_R (top half of Figure 5.8(Center)), the center of mass of the ground and excited states, $\langle y \rangle_0$ and $\langle y \rangle_1$, and the differential center of mass $\Delta \langle y \rangle = \langle y \rangle_1 - \langle y \rangle_0$ (Figure 5.8(Right)) also display no distinctive features. This can be understood from Figure 5.9, where we note that the wave function is centered at a location where it is not pressed against a step edge. Consequently, parameters such as the energy dispersion do not experience sudden changes as a function of detuning.

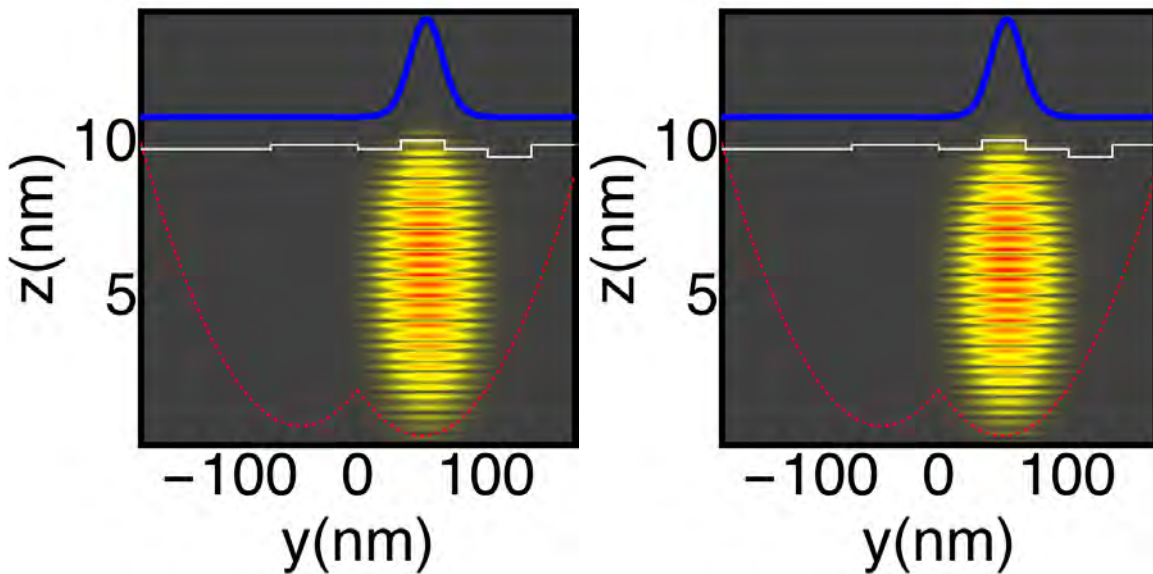


FIGURE 5.9: (Left) Lowest valley state at $\varepsilon = 360 \mu\text{eV}$ corresponding to Fig. 5.8. (Right) Excited valley state for the same configuration. In both cases the blue curve shows the horizontal probability density. The red curve shows the dot confinement potential. The white lines show the corresponding disorder profile.

5.6.2 Hotspot behavior

A more exotic behavior is observed in this case. The disorder profile in Figure 5.11 produces the energy dispersion shown in Figure 5.10(Center), which closely approximates the experimental hot spot in Figure 5.10(Left). In this case the corresponding sharp change in qubit frequency is clearly related to the sharp increase of decoherence. Our simulations indicated that the main contribution to this energy jump comes from the valley splitting, which exhibits a similar jump on the top half of Figure 5.10(Center). Such behavior arises from the fact that the eigenstates are spatially separated (a valley-orbit coupling effect) and rapidly changing with respect to ε , as observed in Figure 5.10(Right), exposing them to different local disorder potentials. The resulting valley compositions of the two eigenstates also vary rapidly. An unexpected consequence of these effects is that the excited state $|R_1\rangle$ actually moves in opposition to the electric field, for detunings around $\varepsilon \simeq 225 \mu\text{eV}$, in a striking example of valley-orbit coupling.

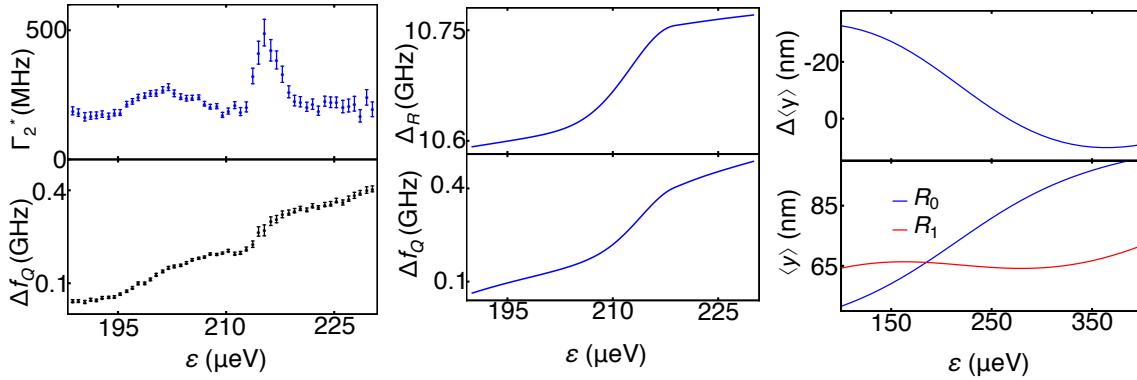


FIGURE 5.10: (Left) Energy dispersion showing an anomalous sharp change with detuning. On the top panel it is shown that this sharp change corresponds to a hotspot where decoherence is enhanced. (Center) Identical behavior obtained through the tight binding simulations. On top the valley splitting is shown as a function of detuning, showing the same sharp change. (Right) Center of mass $\langle y \rangle$ (bottom) and relative center of mass $\Delta \langle y \rangle$ (top) of the lowest two valley states. The COM dynamics shows a very different behavior for each valley state, being in both cases quite different from the typical case.

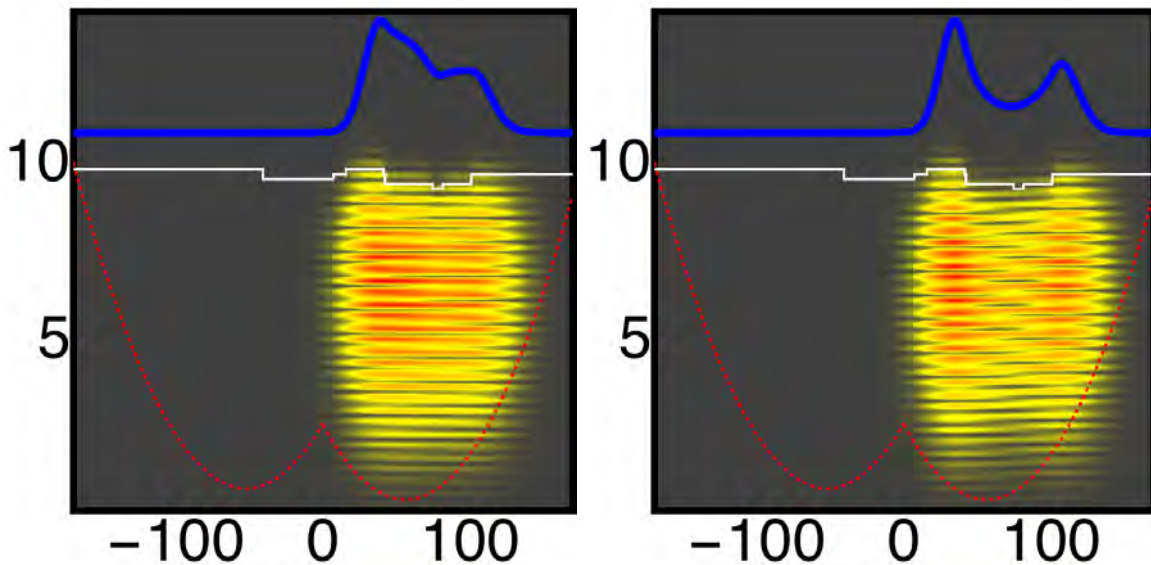


FIGURE 5.11: (Left) Lowest valley state at $\varepsilon = 210 \mu\text{eV}$ corresponding to Fig.5.10. (Right) Excited valley state for the same configuration. In both cases the blue curve shows the horizontal probability density. The red curve shows the dot confinement potential. The white lines show the corresponding disorder profile.

5.6.3 Sweet spot behavior

In the final example, the disorder profile in Figure 5.13 produces the energy dispersion shown in Figure 5.12(Center), with a sweet spot similar in width to Figure 5.12(Left). This is corresponded by an enhanced coherence as can be seen on the top half. In this case, the eigenstate positions, indicated in Figure 5.12(Right), move rather quickly compared to the typical case (Figure 5.8(Right)), yielding a differential center of mass with a dip, and a corresponding dip in the valley splitting (Figure 5.12(Center)). When this valley splitting dip is combined with the slowly increasing qubit frequency (similar to Figure 5.8(Center)), we

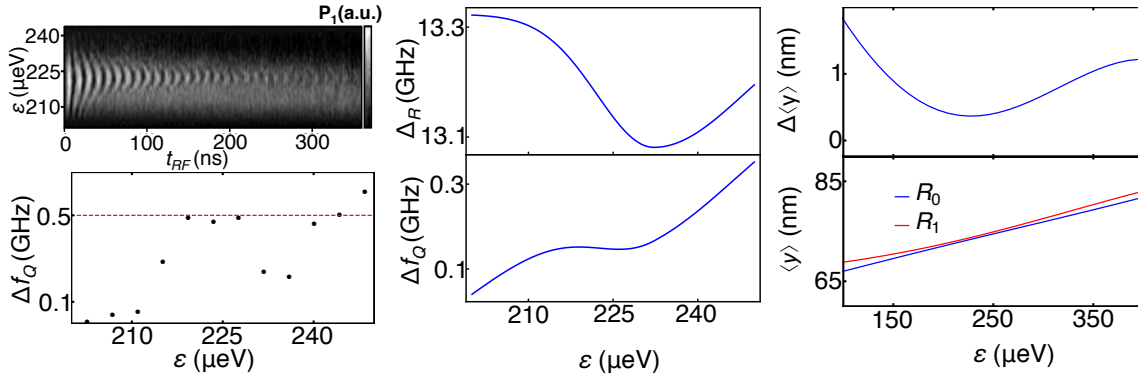


FIGURE 5.12: (Left) Energy dispersion showing flat regions in detuning. On the top panel it is shown that this flat region corresponds to a sweet spot where coherence is extremely enhanced. (Center) Identical behavior obtained through the tight binding simulations. On top the valley splitting is shown as a function of detuning, showing that the sweet spot is related to a minimum of the valley splitting. (Right) Center of mass $\langle y \rangle$ (bottom) and relative center of mass $\Delta \langle y \rangle$ (top) of the lowest two valley states. The COM of each valley state is more affected than in the typical case but relatively monotonous except for the relative center of mass that shows a local minimum.

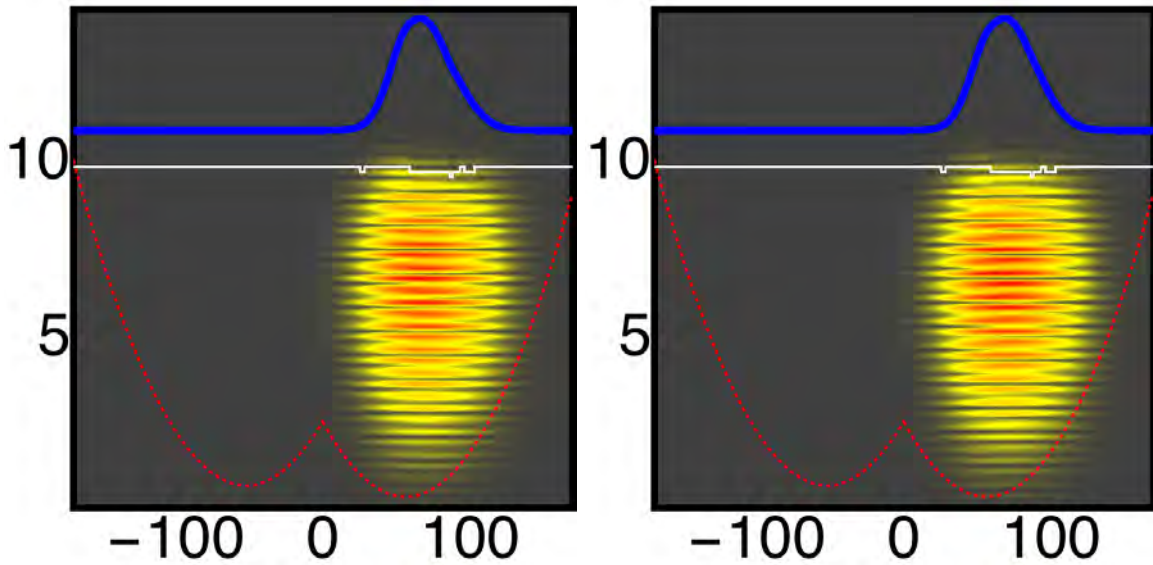


FIGURE 5.13: (Left) Lowest valley state at $\varepsilon = 225$ μeV corresponding to Fig. 5.12. (Right) Excited valley state for the same configuration. In both cases the blue curve shows the horizontal probability density. The red curve shows the dot confinement potential. The white lines show the corresponding disorder profile.

obtain a relatively flat dispersion, as shown in Figure 5.12(Center), over a 20 μeV detuning window.

5.7 Conclusions

In this chapter we have shown that a simple spinless single electron 2D TB model is sufficient to simulate the relevant physics of the more complex QDHQ. From this simple model, an effective Hamiltonian allows us to identify how interfacial disorder affects the physics of the QDHQ. In particular, it has been shown that different disorder profiles yield different dependences on electric fields, which allows the possibility of tuning the valley splitting or even the tunnel couplings electrically, within a single device.

In particular, we have shown that detuning can strongly modify the behavior of the different relevant parameters. The displacement of the center of mass of the electron bound to the quantum dot gives rise to regions of detuning where the sensitivity of the qubit to charge noise is modified: it can be enhanced or suppressed. Even though the detuning dependence is hard to predict a priori, due to the complex interplay between valley-orbit degrees of freedom and the interfacial disorder, atomic-scale disorder is ubiquitous in Si heterostructures. This suggests it could be possible to enhance the quantum coherence in future Si experiments by electrostatically tuning the dots so they are exposed to desirable disorder profiles.

Valley physics of corner dots in Si nanowires.¹

6.1 Introduction

Prospective compatibility with microtechnology is one of the main advantages of using Si as a platform for quantum computing purposes. Alternatively, the reverse process, where current microtechnology can be adapted to quantum computation has proven to be possible [179, 235, 274, 275]. In particular, in this Chapter we are interested in the applications of derivatives of the FinFET such as the Nanowire Field Effect Transistor (NWFET) [213, 274]. NWFETs are fabricated in a CMOS platform starting from silicon on insulator wafers [181]. The nanowire and gate stack can be seen in Fig. 6.1. A Si nanowire is usually in the order of hundreds of nm long, tens of nm wide, and around $\times 10$ nm thick. The nanowire is covered by a trigate electrode generally made of SiO₂, HfSiON, TiN and poly-Si. A voltage V_{TG} can be applied to this gate, allowing the 1D confinement of electron states near the top corners [275]. These confined states can then be used as 1D confined quantum dots where the electron population can be controlled [179, 181].

Quantum dots in NWFET have already been proven as interesting candidates for quantum computation in experiments. Pauli spin blockade has already been achieved [179] which can be used to remove the need for external charge sensors, simplifying the architecture. Alternatively, a gate sensor based on cQED [184] with outstanding sensitivity can be used for readout. Fast charge qubit dynamics between the two corner dots has been observed [276]. Scalability has already been shown to be possible with a quadruple quantum dot based in this architecture [277]. Even purely electrical control has been shown by taking advantage of the SOC arising from the interaction between spin and the different valley states [278].

Another possible advantage of this architecture is the possibility of adding dopants without using extra gates to drive the different states. Coupling between dopants has already been proven in this architecture by Landau-Zener-Stückelberg Interferometry [274]. This hybrid approach can benefit of the advantages of each type of qubit. For example, the nuclear spin of an implanted P donor nucleus could be used as a long-lived quantum memory while fast single qubit operations can be performed in the quantum dots via EDSR [278] or charge

¹Article in preparation.

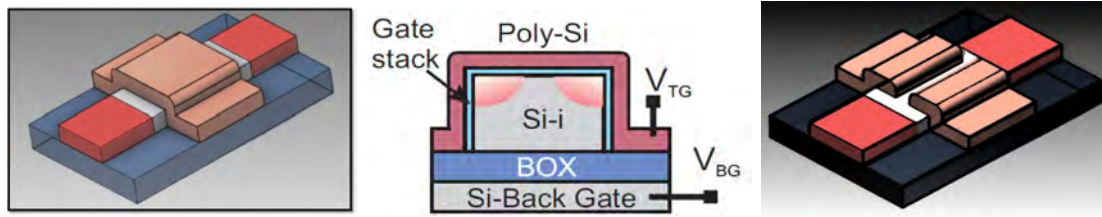


FIGURE 6.1: From [184]. (Left) Sketch of the NWFET device with a single top gate (orange). (Center) Section of a nanowire with top and back gates, with gate voltages V_{TG} and V_{BG} , respectively. The blue layer and the BOX will be assumed to be made of SiO_2 . The pink corners illustrate the quantum dots that arise naturally in this geometry. (Right) Sketch of a NWFET nanowire device with split gates. In this case the gate voltages of the left and right corners can be independently adjusted.

oscillations [276]. In particular, charge dynamics and spin-blockade in this hybrid double quantum dot-donor has been demonstrated [120].

One drawback of this geometry is the inability to operate on each corner dot separately since the top gate is the same for both corner dots. While interfacial disorder and random charge traps break this symmetry, allowing distinction between each corner dot [181], the relative tunability on each dot is limited. One possibility to overcome this limitation is to split the top gate into two well differentiated gates separated by a spacer (typically Si_3N_4) [179]. This geometry can be seen in Fig. 6.1(Right). In this way, different gate voltages can be applied to each corner dot, allowing us to increase or decrease the confinement of each dot separately, or detune one dot respect to the other, recovering the flexibility of other quantum dot systems.

In this chapter the valley physics of corner dots is analyzed, similarly as in Chapter 5. Since these dots are confined in two directions, it is easy to predict that, although geometry, confinement and disorder will favor a particular pair of valley states, up to four valley states are relevant for the low energy physics. Since all these valley states are expected to be in a narrow range of energies, they will play a role in the qubit dynamics of each dot. The spectrum of the lowest valley states will be obtained for different angles of the corners and gate voltages. Both EMA and TB approaches will be used to understand the valley physics of this geometry.

6.2 Nanowire simulations

In order to obtain the value of the valley splitting as a function of the different parameters of the device, it is necessary to quantify how these parameters affect the voltage within the nanowire. Not only different voltages in each gate will affect the voltage distribution within the nanowire, other structural aspects such as the nanowire dimensions, the SiO_2 barriers width, or the angles at the corners are relevant. The effect of all these parameters cannot be accounted analytically and, hence, a numerical approach is necessary. The method we use to analyze the electrostatics of this geometry is a finite difference method using a software suited for this purpose: COMSOL [279]. In Fig. 6.2 the structure of the device used in the simulations is shown. This includes the backgate, top gate, BOX, the nanowire, and the SiO_2 barrier between top gate and nanowire. In the split gate case, a Si_3N_4 spacer is added in between the left and right gates. The dimensions of each component are shown in Table 6.1.

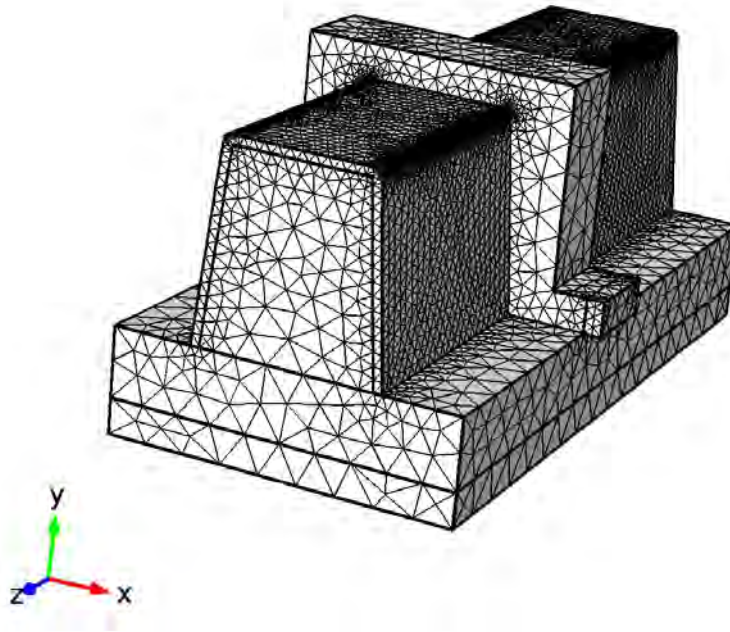


FIGURE 6.2: Discretized nanowire geometry simulated in the finite difference software COMSOL. The different parts are not in scale to help visualization.

	NW L	NW W	NW D	BOX	SiO ₂	HfSiON	TiN	poly-Si	Si ₃ N ₄
Single gate	200	40	11	145	0.8	1.9	5	50	
Split gate	200	40	11	145	1.3				5

TABLE 6.1: Dimensions used in the simulations, unless stated otherwise, in nm. Based on [179] and [181].

In actual devices the nanowire cross section is not a square but, typically the nanowire top width is narrower than the bottom one, see Fig. 6.2. This device variability is taken into account by considering a left top angle deviation from $\pi/2$ (α) and a right top angle deviation from $\pi/2$ (β).

The mesh in Fig. 6.2 was chosen to aid in the visualization. The actual mesh used in the simulations depends on position: The finest tetrahedra allowed in COMSOL are used within the nanowire for accuracy, while, outside the nanowire, much thicker tetrahedra are chosen to reduce complexity.

Gate voltages are chosen to be constants at the gate-barrier interface. The backgate voltage would correspond to V_{BG} at the bottom interface of the BOX, while the topgate voltage would correspond to V_{TG} at the top SiO₂ interface barrier. The voltage within the nanowire is obtained using these boundary conditions in the Maxwell equations

$$\begin{aligned} \mathbf{E} &= -\nabla V \\ \nabla \cdot (\epsilon_0 \epsilon_r \mathbf{E}) &= \rho, \end{aligned} \quad (6.1)$$

and the relation

$$\mathbf{n} \cdot \mathbf{D} = 0. \quad (6.2)$$

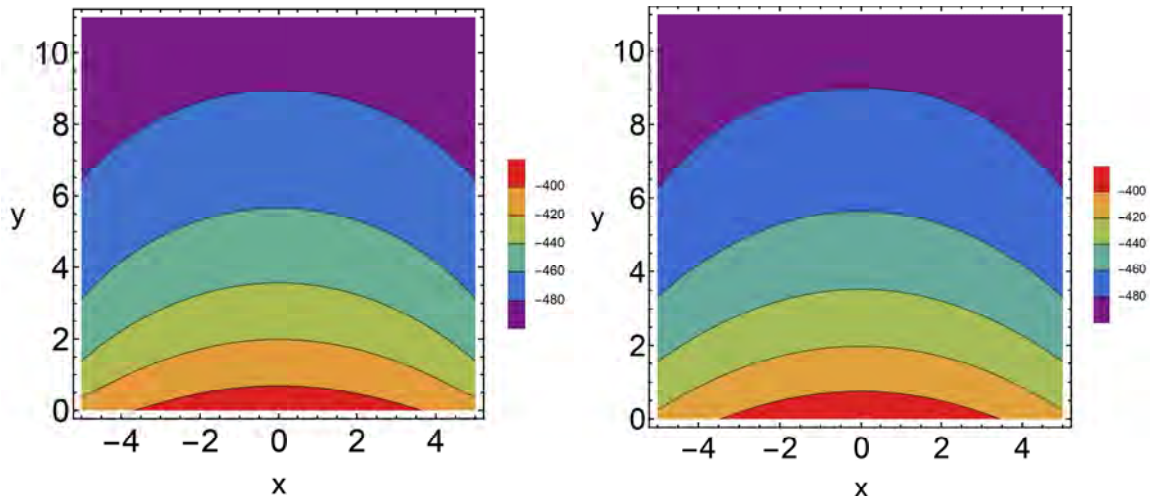


FIGURE 6.3: (Left) Simulated voltage distribution in a section of nanowire with right angles (square cross section) when $V_{bg} = 0$ and $V_{TG} = -0.5V$. (Right) Approximated voltage using expression 6.5.

Since the gate voltage in the z direction is slowly varying (long nanowire and top gates), being the bound states 1D corner states confined in x and y , the relevant directions for valley physics are x and y . As a result the relevant information about the gate voltage distribution can be seen already by plotting the nanowire middle section $z = 0$. In the following, any figure showing a gate voltage distribution will be shown as a function of x and y for $z = 0$.

6.2.1 Gate voltages

We start by simulating the simplest case where the top angles are right angles: $\alpha = \beta = 0$. The nanowire width is chosen to be $w = 10$ nm while the other parameters are chosen as in table 6.1. The results of the simulations can be seen in Fig. 6.3(Left). In this case $V_{TG} = -0.5V$ while the backgate is off $V_{bg} = 0$. The top gate is shown to generate a voltage distribution in which the top corners are the most attractive or repulsive points, depending on the voltage sign. The electric field can be obtained from the gate voltage using Eq. 6.1, resulting in an electric field pointing towards the corners. As a result electrons can be bound to these top corners to form quantum dot states.

In this particular case, all the boundaries are perfectly flat and no random charge traps are considered so each corner has identical voltage distribution. In realistic devices, interfacial disorder and charge trapping is the source of the different charging energy of otherwise identical corners [181]. Another consequence of the lack of disorder is that the backgate voltage induces a voltage distribution identical to the top gate, except for being proportional to V_{bg} . This is a result of the superposition theorem in electrodynamics [280].

6.2.1.1 Analytical approximation

It can be useful to find an analytical approximation for the voltage distribution in the nanowire section. This approximation can then be used to model an analytic Hamiltonian, or to approximate the behavior of similar devices. In order to build an analytical approximation

we can start with the solution of a rectangle whose faces have different gate voltages. The solution to this problem can be found analytically in series form [280]. When we consider two opposite faces (x faces) with the same gate voltages and the other two (y faces) with a difference in gate voltage, the analytical solution is of the form:

$$V(x, y) = \sum_n a_n \sin\left(\frac{n\pi x}{L_x}\right) \exp\left(\frac{-n\pi y}{L_y}\right), \quad (6.3)$$

where a_n are coefficients that can be obtained from the boundary conditions. According to this equation, the solution in the x axis, where both faces have the same gate voltage, is periodic and in the form of a trigonometric function, while in the y axis, where there is difference of potential, the voltage exponentially decays from one face to the opposite.

In our case however, the result is more complex since the interfaces with constant voltage are not the nanowire faces, and there are materials with different geometries and permittivities. In particular, the gate voltage at one corner is not the same potential as in the center of a face. In any case, the qualitative behavior will be similar to that in the rectangular case: periodic behavior in x and decaying behavior in y . The simplest ansatz with this characteristic can then be chosen to be:

$$V(x, y) = A + B \cos\left(\frac{\pi x}{2L_x}\right) \exp\left(-\gamma \frac{y}{L_y}\right), \quad (6.4)$$

where the origin in x is in the middle of the nanowire, and the origin in y is at the bottom interface. The fitting parameters are A , B , and γ .

Using the superposition method, we can fit the contributions of each gate voltage to the values of the three fitting parameters. The resulting formula for the voltage in the nanowire section is then:

$$V(x, y) = -8.30597 \cdot 10^{-4} V_{bg} + 1.00008 V_{tg} + 1.23514 \cdot 10^{-2} (V_{bg} - V_{tg}) \cos\left(\frac{\pi x}{2L_x}\right) \exp\left(-1.84169 \frac{y}{L_y}\right). \quad (6.5)$$

Being all voltages in the same units. The comparison of this formula with a simulation can be seen in Fig. 6.3. As can be seen in this figure, this ansatz can give accurate results. We can estimate the error defining:

$$\text{Err} = 100 \max \left| \frac{V_{sim}(x, y) - V(x, y)}{V_{sim}(x, y)} \right|, \quad (6.6)$$

and obtain an average relative error of 0.02%.

6.2.2 Corner angles

The simulations in COMSOL can be easily adapted to non right angles. As a direct effect the width of the nanowire depends on the particular values of α and β . The result of a simulation with $\alpha = \beta = 6^\circ$ can be seen in Fig. 6.4(Left). The results are qualitatively similar to those in Fig. 6.3, being the obvious difference the width variation with y . Consequently, the voltages adapt to the geometry and the electric field points towards the corner angles.

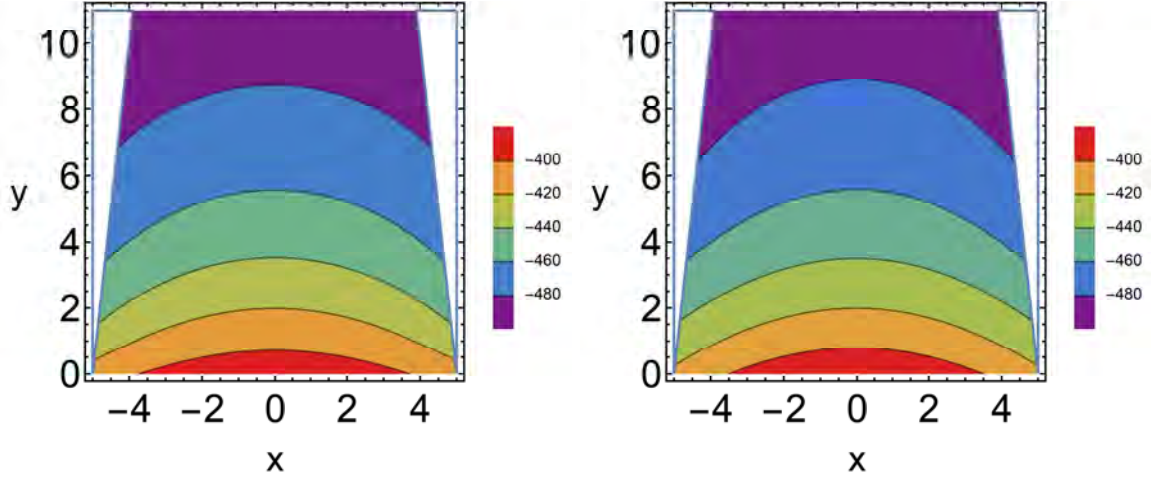


FIGURE 6.4: (Left) Simulated voltage distribution in a section of nanowire with angles $\alpha = \beta = 6^\circ$, when $V_{bg} = 0$ and $V_{tg} = -0.5V$. (Right) Approximated voltage using expression 6.8.

6.2.2.1 Adding angles to the analytical expression

Since the voltage distribution behavior with non right angles is qualitatively similar to the one with right angles, it is possible to simply adapt the formula in Eq. 6.5 to consider the non right angles. This can be easily done by considering the width dependence on the angle and height. We can then redefine the width $L_x(y, \alpha, \beta)$ and define $x_0(y, \alpha, \beta)$ as the center of the NW at height y (x_0 is not necessarily 0 now):

$$\begin{aligned} x_0(y, \alpha, \beta) &= \frac{y}{2}(\sin \alpha - \sin \beta) \\ L_x(y, \alpha, \beta) &= L_x - y(\sin \alpha + \sin \beta). \end{aligned} \quad (6.7)$$

We can use these expressions in Eq. 6.5 to obtain a good approximation to the gate voltage:

$$V(x, y, \alpha, \beta) = A + B \cos \left(\frac{\pi x - x_0(y, \alpha, \beta)}{2 L_x(y, \alpha, \beta)} \right) \exp \left(-\gamma \frac{y}{L_y} \right), \quad (6.8)$$

where A , B and γ take the same values as before. The result of applying this formula is shown in Fig. 6.4, which compares very well to the numeric results. The average error now depends on the angles, getting a better approximation for positive α and β ($\approx 0.03\%$) in comparison with negative values ($\approx 0.1\%$).

6.2.3 Split gates

Finally, it is possible to add a Si_3N_4 spacer in the middle of the top gate to have independent left and right gates. Simulations have been performed in COMSOL, see Fig. 6.5. In particular, in Fig. 6.5(Left) the small difference in gate voltage between left and right dots is enough to induce a voltage distribution where a single face dominates over the others. This effect can be alleviated by the presence of a backgate voltage as in Fig. 6.5(Right), where a strong backgate voltage is used. Unlike in previous cases, where the effect of the backgate voltage was not very relevant due to the lack of disorder and charge traps, now a backgate voltage can be used to modulate the voltage distribution, acting similarly to a tunnel gate. The split

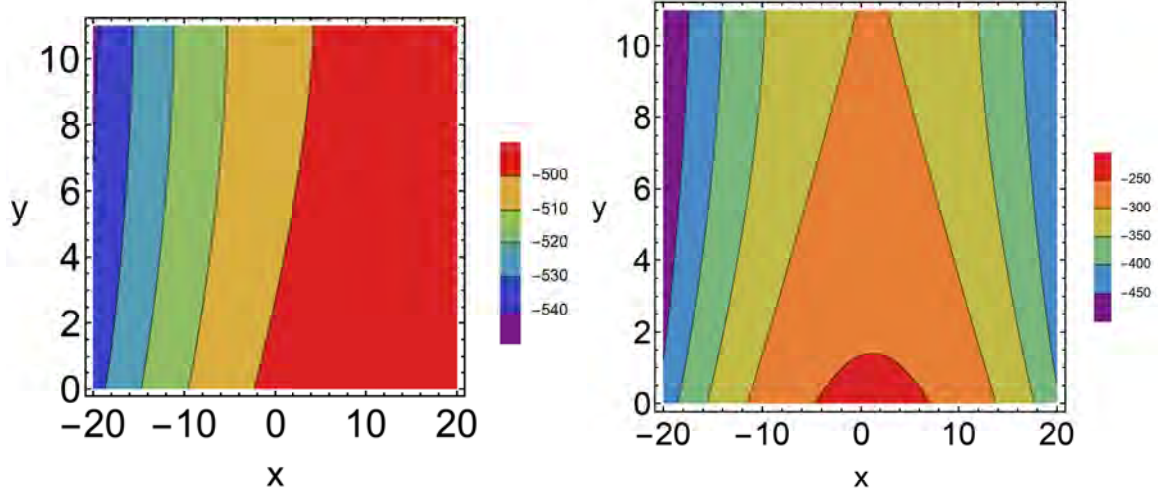


FIGURE 6.5: (Left) Simulated voltage distribution in a section of nanowire with right angles, when $V_{bg} = 0$, $V_R = -0.5\text{V}$, and $V_L = -0.55\text{V}$. (Right) Voltage distribution in a section of nanowire with right, when $V_{bg} = 10\text{V}$, $V_R = -0.5\text{V}$, and $V_L = -0.55\text{V}$.

gate device is then clearly more versatile in comparison to conventional NWFETs, allowing to tune each corner separately with the left and right gates while the backgate voltage can be used together with the others to increase or decrease the interactions between dots.

6.2.3.1 Analytical expression for the split gates

In this case we will focus on a regime where both corner dots are well defined, such as in Fig. 6.5(Right). In this case, the voltage difference between left and right gates is a small perturbation in comparison to the total voltage. Assuming $V_R = V_{TG}$ and $V_L = V_{TG} - V_{\text{diff}}$, the only new contribution to Eq. 6.8 can be approximated to:

$$V_{\text{left}} = -V_{\text{diff}}(x - L_x(y, \alpha, \beta)/2)/L_x(y, \alpha, \beta), \quad (6.9)$$

which can be seen as a detuning voltage. As long as the difference between left and right gate voltages is small enough to maintain dots at each corner, this expression can be accurate. The relative errors in this regime are between 0.1% and 2%, depending on the relative difference values.

6.3 Valley splitting in the EMA

Once we have calculated the voltage distribution within the nanowire, we proceed to calculate the valley spectrum of the corner dots in the NWFET. First of all, it is useful to obtain a simple analytical expression for the potential at a single corner. The results of the simulations are then fitted to the following polynomial:

$$V_{\text{corner}}(x, y) = V_0 + a_1x + a_2y + a_3x^2 + a_4y^2 + a^5xy. \quad (6.10)$$

The expansion is around the corner, meaning that the origin in x and y is set at the position of the left or right corner. From here we can consider the physical meaning of each term: (a) the constant V_0 is a simple constant in the Hamiltonian and will be of no relevance to

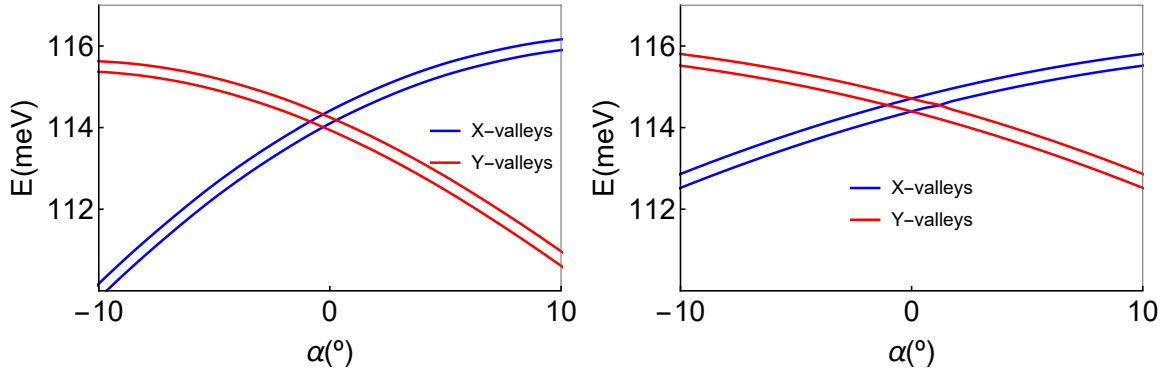


FIGURE 6.6: (Left) Energies of the four lowest valley states under the EMA as a function of the angle, for a fixed modulus of the electric field $F = 14.1\text{MV/m}$. The energies were calculated using the voltages obtained in the simulations. (Right) Same energies obtained assuming the simplification in Eq.6.11.

the valley physics, (b) a_1 and a_2 , the linear terms in x and y , are the electric fields in each direction, (c) the quadratic terms a_3 and a_4 can be seen as corrections to the electric fields, (d) a_5 is a term mixing x and y , this term is very relevant since it will determine whether the Hamiltonian and wavefunction can be separated into x and y terms with accuracy.

After fitting the different terms, we found that a_5 is at least one order of magnitude smaller than the next smallest parameter and thus, negligible. The problem can then be assumed to be separable, as long as we consider the interaction between orthogonal valley states negligible. The values of a_3 and a_4 are also smaller than a_2 and a_1 , meaning that the potential at the corners can be successfully approximated by electric fields in each direction corrected by smaller quadratic terms. Moreover, we find that, despite of the non constant potential at the nanowire faces, the voltage near the corner can be approximated in the linear approximation to a potential created by an equipotential corner of angle η in Ref. [280]:

$$V_{\text{corner}}(x, y) \approx V_0 + F \cos(\eta/2)x + F \sin(\eta/2)y \quad (6.11)$$

We can now use the EMT to obtain the energies of the lowest valley states. Since the wavefunction is confined in two directions, we need to consider four valley states. Assuming a separable problem, both the Hamiltonian $H = H_x + H_y$ and the wavefunction $\Psi(x, y) = \psi(x)\psi(y)$, are separable. The effective Hamiltonian of a single electron in each direction is

$$\begin{aligned} H_x &= -\frac{\hbar^2 \partial_x^2}{2m_{\text{eff}}} + ea_1x + ea_3x^2 + V_b(x) \\ H_y &= -\frac{\hbar^2 \partial_y^2}{2m_{\text{eff}}} + ea_1y + ea_3y^2 + V_b(y). \end{aligned} \quad (6.12)$$

Where V_b is the potential at the barrier, which is $V_b = 3\text{eV}$ inside the SiO_2 barrier, 0 elsewhere. To solve this Hamiltonian we use the following variational guess for the envelope wavefunction:

$$\psi(x_i) = 1/N \exp(-(x_i - x_0)^2/l^2), \quad (6.13)$$

being N a normalization constant, and x_0 and l variational parameters related to the wavefunction center of mass and dispersion, respectively. The problem is then reduced to obtaining the valley splitting of wavefunctions pushed against a single interface, which is a

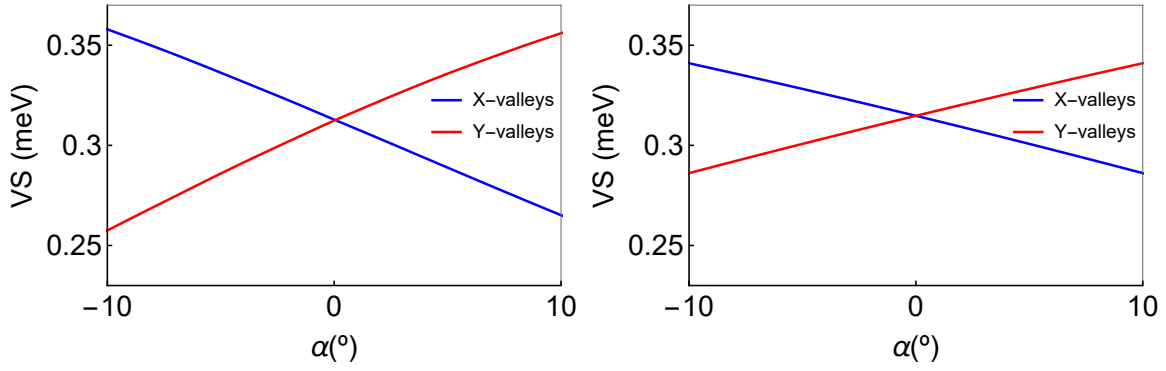


FIGURE 6.7: (Left) Valley splitting in the EMA as a function of the angle, for a fixed modulus of the electric field $F = 14.1\text{MV/m}$. The energies were calculated using the voltages obtained in the simulations. (Right) Same valley splittings obtained assuming the simplification in Eq.6.11.

problem already addressed in the literature [156]. It is important to note that we have made the approximation that V_b is also separable which is only exact if $\alpha = \beta = 0$. This approximation can also be used if α and β are assumed to be small, allowing a great simplification of the problem. Consequently, the valley-orbit coupling of each valley couple is a direct measurement of the electron density of probability right at the interface ($x_i = 0$). The 4×4 effective valley Hamiltonian is then:

$$H = \begin{pmatrix} H_x & \Delta_x & 0 & 0 \\ \Delta_x^* & H_x & 0 & 0 \\ 0 & 0 & H_y & \Delta_y \\ 0 & 0 & \Delta_y^* & H_y \end{pmatrix} \quad (6.14)$$

Using the electric fields from Eq. 6.10 and the variational ansatz in Eq. 6.13, we can minimize the energy and obtain an upper bound to the valley states energy. The results are shown in Figures 6.6 to 6.8.

In 6.6(Left) the energies of the lowest corner states are shown for a single top gate NWFET. Note that the positive energy comes from the inclusion of the constant V_0 . For negative values of α the valleys in the horizontal direction are the lowest states, while positive values of α favor valley states in the vertical direction. This can be expected from the results of the simulations since a negative angle is associated to $F_x \geq F_y$, while a positive angle corresponds to $F_y \geq F_x$. Acute angles confine more the electron in the x direction while obtuse angles confine more in the y direction. The plot also shows an asymmetry between negative and positive angles which is associated to a different behavior of a_3 and a_4 . Horizontal and vertical valleys are easily split for non right angles, for instance, for $\alpha = 10^\circ$ the energy difference can be already of 5 meV, which is similar to the energy difference with higher orbital states [181]. This would explain why in Ref. [181] the first excited states found above the lowest valley couple were orbital excited states. Alternatively, the same calculation was performed using the simpler formula in Eq. 6.11. The results in 6.6(Right) are qualitatively similar to those obtained with the quadratic corrections, showing that the linear approximation already gives the qualitative picture. Quantitatively however, there are some differences such as the symmetry of α under reflections or the smaller energy difference between pairs of valley states. We proceed now to calculate the valley splitting according to Ref. [156]. The

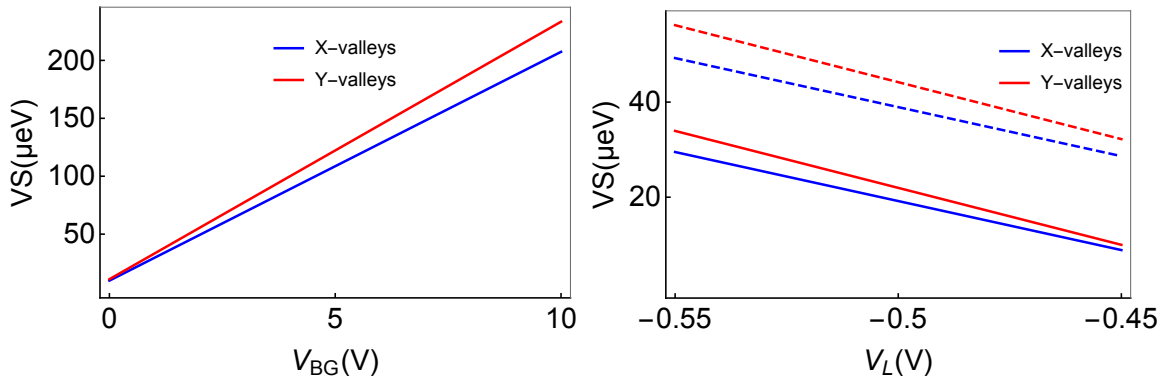


FIGURE 6.8: (Left) Valley splitting in the EMA as a function of the V_{bg} for right angles and $V_{tg} = -0.5V$. (Right) Valley splitting in the EMA as a function of the V_L for right angles, and $V_R = -0.5V$. $V_{bg} = 0$ for solid lines and V_{tg} for dashed lines.

interface induced valley-orbit constant is

$$\Delta_{VO} = -0.02907iV_b a_{Si} |\psi(0)|^2. \quad (6.15)$$

The valley splitting is shown in Fig. 6.7 as a function of the angle for the same device. Again, for the sake of comparison, the results obtained in the linear approximation are shown in Fig. 6.6(Right). In both cases the valley splitting is shown to change linearly with α , indicating how the electric field increases or decreases in each direction. In this case, a really big electric field was chosen and the valley splitting is estimated to be around 0.3 meV.

Lastly, the valley splitting is shown for realistic gate voltages in Fig. 6.8. This shows a highly tunable valley splitting by changing the different gate voltages. In 6.8(Left) the top gate is fixed and the backgate is changed, the valley splitting ranges from ten μeV to 0.25 meV, which is in a similar order to those obtained in [181] or [179]. In Fig. 6.8(Right) a split gate is considered where V_L is changed (the voltage associated to the corner). Again a linear behavior is shown, similar to the behavior under a single interface [156]. In both cases the horizontal and vertical valleys show slightly different behaviors, this is due to the different lengths in each direction and the different behavior of the quadratic terms since the considered angles are right.

6.4 Valley splitting in TB simulations

The EMA is a good approximation to obtain the average behavior of the valley physics, but it is inherently oblivious to atomistic details that may be relevant and depend on the particular device. In particular we have considered the angular dependence through the potential distribution, however, we have assumed a separable $V_b(x, y)$, which is unrealistic. The tight binding method described in the introduction, and used in Chapter 5, can take into account atomistic details, such as the real orientation of the barriers, and is still easy to implement computationally [152, 156, 251]. Its main drawback is the assumption that only two valley states are relevant. In our case, we need to generalize the TB method to include valley states in two confinement directions, being z the only irrelevant direction for the low energy valley physics. Based on the experimental results from references [179, 181, 278], we can assume that generally the valley states in each direction are separated by a few meV

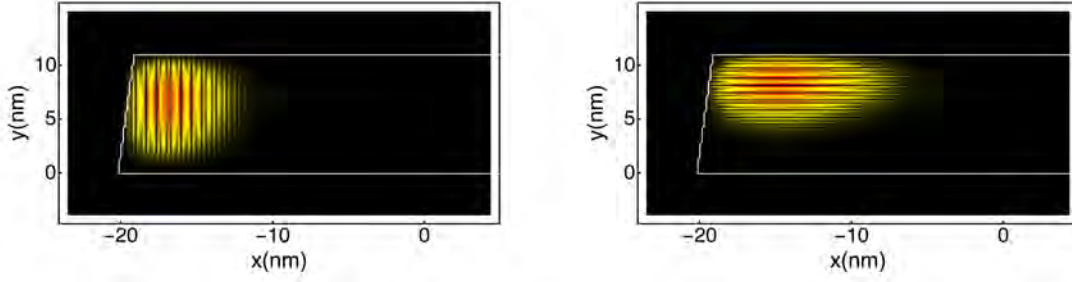


FIGURE 6.9: Valley states localized at the top left corner of the nanowire. An angle $\alpha = 5^\circ$ is used. The white lines illustrate the boundary between the Si nanowire and the SiO₂ barriers. Note that a significant amount of disorder is required to simulate $\alpha = 5^\circ$. (Left) X-valley. (Right) Y-valley.

due to different confinement conditions in the x and y directions. Consequently, we can approximately say that the x and y valley states are non-interacting states, simplifying the problem. Considering independent valley states allows us to separate a huge TB problem including valley states in both directions, into two simpler TB problems for valley oscillations in each direction.

The procedure to calculate valley states is then based in separating the TB Hamiltonians for each pair of valleys H_x and H_y . Each Hamiltonian is then defined as in Chapter 5, with the difference being in choosing the transverse or longitudinal masses. For H_x the longitudinal mass and valley oscillations are in the x direction, being the transverse mass in the y direction. On the other hand, for H_y the longitudinal mass and valley oscillations are in the y direction, with transverse mass in the x direction. This means that for H_i , direction i nearest- and next-nearest neighbor hopping parameters $u_i^{(i)} = 0.68\text{eV}$ and $v_i^{(i)} = 0.61\text{eV}$ are required to account for the valley oscillations and the longitudinal mass, while in direction $j \neq i$ only requires the nearest neighbor term $u_j^{(i)} = -10.91\text{eV}$ to account for the transversal mass. In total these hopping terms contribute to the kinetic energy H_K^i , while the barrier energy of 3 eV is added to the SiO₂ atoms. The on-site term of 23.23 eV is used to set the minimum of the conduction band to zero. Lastly, the voltage distribution extracted from the simulations is added directly as on-site terms that depend on the atom position. In total, the valley Hamiltonian in direction i is simply:

$$H_i = H_K^i + H_{\text{barriers}} + H_{\text{Fields}}, \quad (6.16)$$

where only the hopping terms in H_K^i depend on the valley states to calculate.

With this simple method we can easily modify the position of H_{barriers} to account for interfacial disorder or to consider non right angles. In order to define the latter, atomic disorder is a requirement since the TB method is inherently discrete while angles are continuous variables. Non right angles require then the presence of atomic steps. However, multiple different step distributions will give the same angle on average. We have then an extra freedom when defining the disorder profile that, on average, corresponds to a given angle. We have chosen to consider the disorder profile that best fits, locally and globally, a given angle: we fix the height of the top face and atomic steps are distributed as in a stair in the lateral faces, with step length chosen to get the corresponding corner angle, see Fig. 6.9. As a result the top and bottom interfaces are disorder free, while the lateral faces are very disordered or full of atomic steps when α and/or β are non zero.

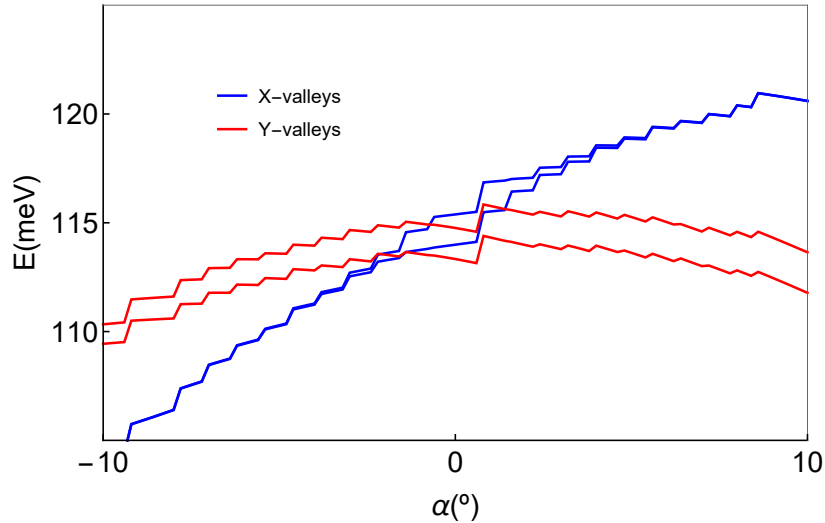


FIGURE 6.10: Energies of the four lowest valley states as a function of the angle, for a fixed modulus of the electric field $F = 14.1\text{MV/m}$, using a TB. The discrete jumps of energy are a result of the discretization of the corner angles.

The tight binding Hamiltonians are then diagonalized and the spectrum is obtained and eigenfunctions are obtained. In Fig. 6.9 both horizontal and vertical valley states are shown. The stair-like disorder profile in the lateral direction can also be seen. The electric fields confining both wavefunctions are the same, however, the envelope function of each valley state is different, showing the effects of the different anisotropy in the effective masses of each valley state.

In Fig. 6.10 the resulting lowest valley-orbit energy levels of the top left corner are shown as a function of the angle α . Unlike in Fig. 6.6, it shows clearly discrete jumps in energy as the value of α changes. This can be easily understood when taking into account the discrete nature of angles in the TB as discussed before. Slight changes of α correspond to sharp changes in the disorder profile in the lateral faces of the nanowire and, as a result, sharp jumps in energy are observed as a function of α . Apart from that difference, the energy spectrum is similar. For acute angles the confinement is stronger in the x direction and the lowest valley states are those corresponding to the oscillations in x . Obtuse angles on the other hand, increase the confinement in the y direction, giving rise to y valley ground states. The plot also presents a reflection asymmetry. As in the EMA case, this is due to the different behavior of the quadratic terms in the voltage distribution.

Bigger differences are observed in the valley splitting in Fig. 6.11. Ignoring the sharp jumps due to different disorder arrangements, the valley splitting for y -valleys can be considered linear, similarly to the one obtained through EMT. This is again due to the increased electric field in the y direction for obtuse angles: the more confined the wavefunction against the top barrier, the bigger the valley splitting. On the other hand, the valley splitting in the horizontal direction is clearly suppressed for angles far from $\alpha = 0$, where it is maximized. From the EMA calculations in Fig. 6.7 another linear behavior with increasing valley splitting for negative α would be expected. In the TB however, the lateral barriers are highly disordered for $\alpha \neq 0$, as a result the valley splitting is strongly affected. In particular for the stair disorder pattern, the multiple steps affect, on average, in a similar way to the ground and valley excited states in the horizontal direction. In consequence, the valley splitting is strongly suppressed. This is particularly alleviated when disorder is reduced or non present when $\alpha \approx 0$.

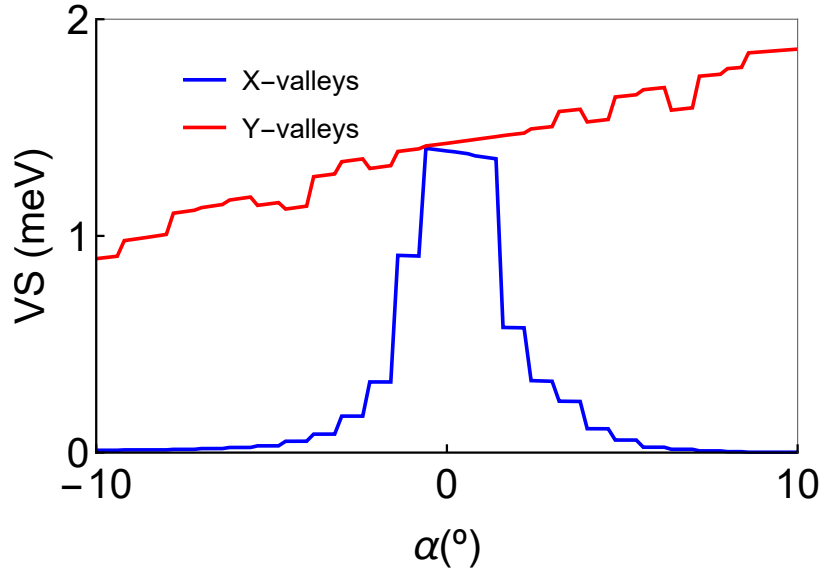


FIGURE 6.11: Valley splitting obtained in the TB simulations as a function of the angle, for a fixed modulus of the electric field $F = 14.1\text{MV/m}$.

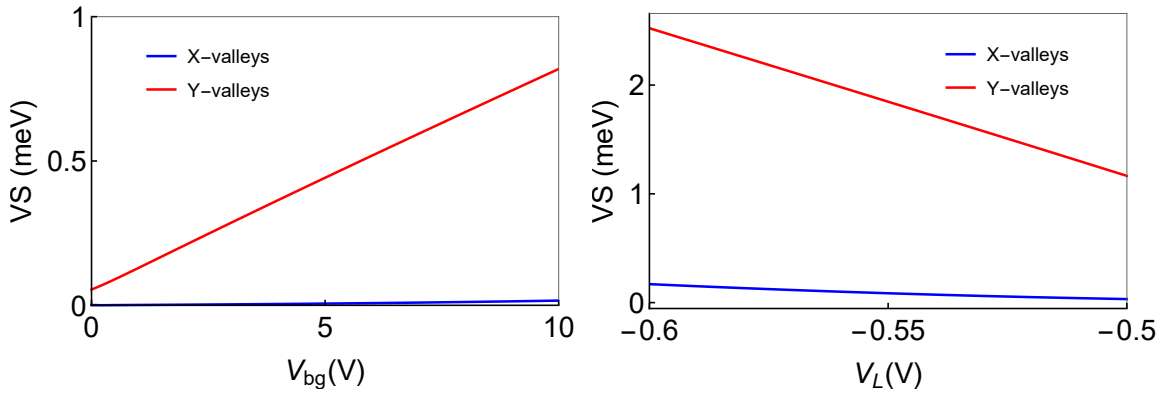


FIGURE 6.12: (Left) Valley splitting obtained in the TB simulations as a function of the V_{bg} for right angles and $V_{tg} = -0.5V$ and $\alpha = 5^\circ$. (Right) Valley splitting obtained in the TB simulations as a function of the V_L for $V_{bg} = 0$, $V_R = -0.5V$, and $\alpha = 5^\circ$.

In Fig. 6.12 the valley splitting is shown for realistic device configurations. As in Fig. 6.8, a linear behavior is shown for $\alpha = 5^\circ$. The x -valley splitting is suppressed due to disorder and, as in Fig. 6.12(Left), this may induce a non linear dependence. The biggest difference compared to Fig. 6.8 is a higher estimation of the valley splitting. In this case, the non suppressed valley splitting is still in the same order of magnitude but can range from 0.2 to 2 meV. This is in good agreement with experimental results such as in references [179, 181, 278]. This also shows a great tunability for non disorder suppressed valley states, even better when using split gates such as in 6.12(Right).

6.5 Conclusions

We have analyzed the valley physics in NWFETs using both atomistic and effective mass methods. The NWFET potential generated by the different gate voltages confines electronic states near the top corners, creating 1D dots along the z direction. We have obtained the

potential distribution within the nanowire using the COMSOL finite difference software as a function of the different gate voltages and the angle in the corners. The numeric results can be easily fitted to analytical expressions, simplifying the expressions for the valley analysis.

The effective mass method was used to calculate the lowest valley states by considering the wavefunction penetration inside the two different barriers. In this case, we approximated the Hamiltonian and wavefunctions to be separable, simplifying the problem. The results show that acute angles correspond to lower valley states in the horizontal direction, while obtuse angles correspond to vertical valley ground states. The energy difference between the two types of valley states can go to several meV for non right angles, in the order of orbital excited states, difficulting its finding. The different gates were shown to be able to tune the valley splitting of the valley states in a wide range, which can be useful for quantum computation purposes, where the valley splitting is a very important quantity.

Qualitatively similar results were found using more atomistic methods such as the described TB. In this case, atomistic interfacial disorder had to be included in order to account for non right angles. As a consequence, the TB results can be quantitatively different from those obtained in the EMA. Sharp steps in the energies were found as a function of the angles, due to the different disorder arrangements required for each angle. The valley splitting of the horizontal valley states was shown to be suppressed for $\alpha \neq 0$ due to the presence of atomic disorder, but the vertical valleys shown behavior qualitatively similar to the one in the EMA. In general, the vertical valley splitting was found to be higher, although in the same order of magnitude, in the TB simulations. Consequently, the TB simulations reveal a more tunable valley splitting than the EMA calculations.

The valley splitting tunability shows the potential of this architecture, particularly with split gates. This implies that the properties of quantum dots in this devices would be electrically tunable for quantum computation purposes. The developed methods also pave the way for the calculation of other relevant quantities, such as tunnel couplings, energy diagrams as a function of detuning, or charge noise susceptibility.

Part III

2D materials

Dopants in 2D materials for Quantum Computing.¹

7.1 Introduction

Defects are an essential ingredient in semiconductor technology as they provide proper carriers to intrinsically insulating semiconductors, being the basis for transistor operations. The miniaturisation of these devices has moved defects to the forefront research, as their number and location may affect device performance and reproducibility [282]. Few-donor configurations were explored by Kane [27] in his Si quantum computer proposal, based on an array of donors in which each of them acts like a spin qubit. This in principle leads to a scalable quantum computer, and would be compatible with the existing Si-based transistor industry. For spin qubits, Si has the additional advantage of sustaining very long spin coherence times, up to seconds for isotopically purified Si [35].

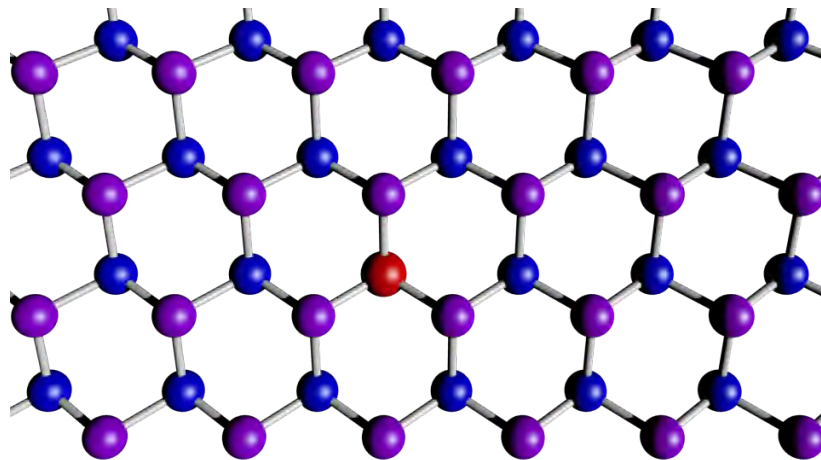


FIGURE 7.1: Dopant placed in a 2D structure, in this case, a Silicene layer. The structure of Silicene is similar to a graphene honeycomb lattice, but slightly buckled. Blue and purple dots indicate Si atoms in different sublattices, being the position in the third dimension the main difference between them. The red dot indicates the donor atom.

¹Published in [281].

The effort to understand single donor behavior has led to progress on the manipulation and control of states bound to donors in the last few years [28, 116, 283–285]. One problem of using donors in Si for qubits is that interference among the multiple degenerate Si conduction band minima states leads to a sensitive and oscillatory behavior of tunnel [52] and exchange [38] coupling of electrons bound to pairs of donors as the relative positions of the donors vary. Although no oscillatory behavior is expected for coplanar dopant pairs relative to (001) planes under tensile stress, any individual dopant deviation in the z direction restores the oscillations [84]. This problem can be deterrent to quantum computing implementation in Si due to the relative lack of control on the exact position of dopants in the bulk. Alternative proposals suggested to overcome this difficulty include hybrid dopant-quantum dot structures [286], a charge-spin hybrid qubit [165], optical manipulation [287] and dipole coupling with electrons [104] or holes [125?].

Here we propose an alternative which relies on 2D semiconductor materials instead of bulk Si for host material, see Fig. 7.1, as precise positioning of donors on a surface may be simpler than in the bulk, i.e., it involves control over two coordinates, avoiding the z -component uncertainties. Moreover, many of the existing 2D materials have a direct gap at Γ which naturally gets rid of oscillatory exchange and tunnel couplings [288]. Among the 2D materials, graphene is the most studied but it has a zero-gap electronic structure. The structural counterpart of graphene in Si, silicene, is a candidate to play the role of 2D host since it has a direct gap for certain structural reconstructions [289]. There are alternatives of monolayer compounds with nonzero direct gaps, such as SiC in its monolayer form [288].

The family of 2D materials comprises an increasing number of elemental and compound semiconductors [290–292]. Many have been experimentally isolated already and the research is very active in this area. In the case of non-metallic behaviour their band gaps range from meV to a few eV. They can also be stacked in van der Waals heterostructures [291, 293, 294] which favors miniaturization and device integration. Incorporation of dopants affects the properties of isolated or stacked monolayers [295, 296], as they do in bulk systems. Here we explore doping in the very low density limit such that electrons can be bound to single and pairs of donors in a 2D environment in the context of quantum computation.

In order to analyze the behavior of the dopants in 2D materials we use the effective mass approximation, discussed in 1.4.1. Single and double dopants, including ions, are taken into account. These dopants are analogous in the EMA to the hydrogen atom H and ion H^- , and the hydrogen molecule H_2 and ion H_2^+ . The validity of the EMA will be discussed in the context of different material properties such as the gap, electron effective mass and dielectric permittivity.

7.2 Effective mass method

We consider neutral, negatively charged donors and donor pairs in 2D. Within EMA the discrete crystal structure of the device is described by a continuum characterized by the effective mass m_{eff} and the dielectric screening ϵ of the host materials. In atomic units, the binding energy in 2D is larger than in 3D for a particular m_{eff} and ϵ . The effective Rydberg is defined as

$$Ry^* = \frac{m_{\text{eff}}e^4}{2\hbar^2\epsilon^2}, \quad (7.1)$$

while the effective length unit is

$$a^* = \frac{\hbar^2 \epsilon}{m_{\text{eff}} e^2}. \quad (7.2)$$

In 2D systems the dielectric function is non-local. As discussed in Ref. [297], it may be written as $\epsilon(\mathbf{q}) = 1 + 2\pi\alpha$, with α the polarizability. Hence for the description of the impurity potential we should take into account the dependence of the screening ϵ with distance from the donor. However, it has been recently found that the effect of a non-local dielectric function can be reproduced by a dielectric constant given by its average within the radius of the wave-function [298], dramatically simplifying the energy calculations. We adopt this approach below. Finally, in order to simplify the discussion, an isotropic effective mass is considered.

7.2.1 Hydrogen atom: H

A single donor impurity can be considered like a H atom in the EMA. The Hamiltonian of the H atom is:

$$H = -\frac{\hbar^2}{2m_{\text{eff}}} \nabla^2 - \frac{e^2}{\epsilon r} \quad (7.3)$$

In terms of the effective units defined in Eqs. 7.1 and 7.2 the Hamiltonian becomes:

$$H = -\nabla^2 - \frac{2}{r} \quad (7.4)$$

In this case it is possible to obtain an analytical solution for the ground state, applying the time independent Schrödinger equation with the Hamiltonian in 7.4. Separating variables in the wavefunction we obtain that the wavefunction is:

$$\Psi_{\text{atom}}(r, \theta) = \sqrt{\frac{8}{\pi}} e^{-2r}, \quad (7.5)$$

which corresponds to an energy of $-4Ry^*$. The differences with the 3D case can already be observed: The binding energy of the electron bound to a single dopant in 3D is $E_B^{3D} = Ry^*$ while in 2D it is $E_B^{2D} = 4Ry^*$. The respective Bohr radii are $a^{3D} = a^*$ while $a^{2D} = a^*/2$. Which means that the electron in a 2D hydrogen atom is four times more bound than in 3D and also more localized, since the electron wavefunction is forced to stay in 2D, enhancing the effects of the attractive Coulomb potential.

7.2.2 Hydrogen ion: H⁻

The hydrogen atomic ion H⁻ includes a second electron, which can be interesting for creating readout protocols based on the Pauli spin blockade: Depending on the spin state, one dopant will bind an extra electron, generating a charge signature that can be measured by a charge sensor. Independently of the spin, we are interested in knowing whether a second electron can be bound to a hydrogen atom in 2D. The Hamiltonian for this problem is:

$$H = -\frac{\hbar^2}{2m_{\text{eff}}} \nabla_1^2 - \frac{\hbar^2}{2m_{\text{eff}}} \nabla_2^2 - \frac{e^2}{\epsilon r_1} - \frac{e^2}{\epsilon r_2} + \frac{e^2}{\epsilon r_{12}}, \quad (7.6)$$

where subindexes 1 and 2 indicate the first and second electron, respectively. The term proportional to $1/r_{12}$ is the repulsion between electrons, being $r_{12} = |\mathbf{r}_1 - \mathbf{r}_2|$ the distance

between electrons. In effective units the Hamiltonian becomes:

$$H = -\nabla_1^2 - \nabla_2^2 - 2/r_1 - 2/r_2 + 2/r_{12}. \quad (7.7)$$

Here we use a variational trial wavefunction with two parameters based on hydrogenic orbitals. In order to construct a wavefunction with two parameters we need to take into account all the possible terms that come from the Slater determinants with the required symmetry. It is also necessary to take the symmetric combination of all the terms because the ground state is also a gerade state (symmetric under reflections):

$$\Psi_{\text{ion}}(\mathbf{r}_1, \mathbf{r}_2) = N(e^{-\alpha r_1 - \beta r_2} + e^{-\alpha r_2 - \beta r_1} + e^{-\alpha(r_1+r_2)} + e^{-\beta(r_1+r_2)}) \quad (7.8)$$

With this wavefunction we minimize the energy and obtain that the minimum corresponds to $a = \frac{1}{\alpha} = 0.287a^*$ and $b = \frac{1}{\beta} = 1.015a^*$, and the upper limit for the energy is $E \leq -4.455Ry^*$. For the sake of comparison, using only the first two terms (single variational parameter) in 7.8 the resulting upper limit is slightly worse $E \leq -4.307Ry^*$.

The two Bohr radii indicate that one electron stays closer to the Coulomb potential than the other; this is due to the repulsion between electrons. The total energy of $-4.455Ry^*$ is only $0.455Ry^*$ smaller than the energy of a hydrogen atom. This means that the binding energy of the second electron is very small, thus, this electron is not very stable. The lifetime of a D^- donor state would be then very short.

7.2.3 Hydrogen molecule ion: H_2^+

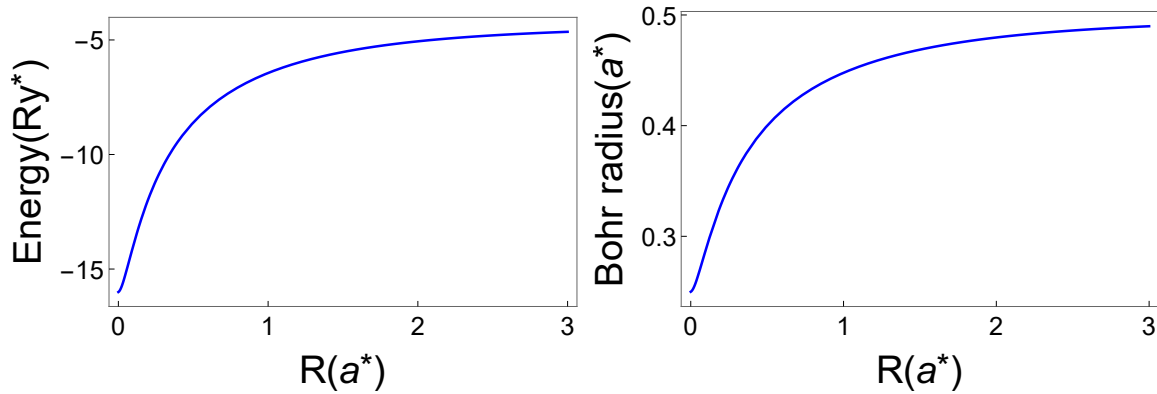


FIGURE 7.2: (Left) Energy of the 2D hydrogen molecule ion in the EMA as a function of the distance between dopants R , see Eq. 7.10. (Right) Bohr radius $1/\alpha$ that minimizes the energy as a function of R .

Two donors sharing a single electron are equivalent in the EMA to the hydrogen molecule ion H_2^+ . This state could be useful for quantum computation when considering qubits encoded in the charge state rather than the spin state. The Hamiltonian of the hydrogen molecule ion is:

$$H = -\frac{\hbar^2}{2m_{\text{eff}}}\nabla^2 - \frac{e^2}{\epsilon r_a} - \frac{e^2}{\epsilon r_b} + 2/R, \quad (7.9)$$

where now subindexes a and b indicate donors a and b respectively, and the term $2/R$ is the repulsion between donors. Note that this term for the interaction between nuclei is

irrelevant for dopants in semiconductors, where the distance would be determined by the placement of the donors.

In effective units, the Hamiltonian is then:

$$H = -\nabla^2 - \frac{2}{r_a} - \frac{2}{r_b} + \frac{2}{R}. \quad (7.10)$$

For this case it is possible to solve analytically the time independent Schrödinger equation without any approximation for the wavefunction or the Hamiltonian [299]. In this case the Hamiltonian is written in spheroidal coordinates:

$$\begin{aligned} \lambda &= \frac{r_a + r_b}{R} \\ \mu &= \frac{r_a - r_b}{R}, \end{aligned} \quad (7.11)$$

which range $1 < \lambda < \infty$ and $-1 < \mu < 1$. In this variables, the Schrödinger equation becomes:

$$\begin{aligned} \sqrt{\lambda^2 - 1} \frac{\partial}{\partial \lambda} \left(\sqrt{\lambda^2 - 1} \frac{\partial \Psi}{\partial \lambda} \right) + \sqrt{1 - \mu^2} \frac{\partial}{\partial \mu} \left(\sqrt{1 - \mu^2} \frac{\partial \Psi}{\partial \mu} \right) \\ + \left(\frac{R^2}{4} E(\lambda^2 - \mu^2) + 2R\lambda \right) \Psi = 0, \end{aligned} \quad (7.12)$$

In these coordinates the Schrödinger equation is separable, hence, the wavefunction can be written as:

$$\Psi(\lambda, \mu) = L(\lambda)M(\mu). \quad (7.13)$$

Plugging Eq. 7.13 into Eq. 7.12, we get the following differential equations for each term of the wavefunction:

$$\begin{aligned} \sqrt{\lambda^2 - 1} \frac{d}{d\lambda} \left(\sqrt{\lambda^2 - 1} \frac{dL(\lambda)}{d\lambda} \right) + \left(A + 2R\lambda + \frac{R^2}{4} \lambda^2 E \right) L(\lambda) = 0 \\ \sqrt{1 - \mu^2} \frac{d}{d\mu} \left(\sqrt{1 - \mu^2} \frac{dM(\mu)}{d\mu} \right) - \left(A + \frac{R^2}{4} \mu^2 E \right) M(\mu) = 0, \end{aligned} \quad (7.14)$$

being A a separation constant. The solution to the first differential equation is obtained in series form:

$$L(\lambda) = (\lambda + 1)^{2/\sqrt{-E}-1/2} e^{-\sqrt{-E}R\lambda/2} \sum_{n=0}^{\infty} a_n \frac{\lambda - 1}{\lambda + 1}, \quad (7.15)$$

The coefficients a_n can be obtained for a given E and A, see [299] for the recurrence relation. Regarding the equation for $M(\mu)$, we can define the variable $Z = \arccos \mu$, and function $F(Z) = M(\mu)$ such that the differential equation becomes:

$$\frac{d^2 F(Z)}{dZ^2} + (\omega - 2q \cos(2Z))F(Z) = 0, \quad (7.16)$$

being $\omega = -C - R^2 E/8$ and $q = -R^4 E^2/16$. The solutions to this equation are known in terms of the even and odd Mathieu functions $C(\omega, q, Z)$ and $S(\omega, q, Z)$, respectively:

$$F(Z) = c_1 C(\omega, q, Z) + c_2 S(\omega, q, Z), \quad (7.17)$$

with c_1 and c_2 constants that depend on the boundary conditions.

We can now use plug these solutions for a given R to obtain the values of R and A . The ground state solution corresponds to an even solution under inversion symmetry (gerade wavefunction).

In order to obtain a Bohr radius we try a variational wavefunction in the form:

$$\Psi_{\text{var}} = N(e^{-\alpha r_a} + e^{-\alpha r_b}) \quad (7.18)$$

The resulting energies from the analytic method and Bohr radius ($1/\alpha$) from the variational wavefunction are shown in Fig. 7.2. The result shows that $R = 0$, which corresponds to the He^+ limit (hydrogen atom with twice the charge at the nucleus), has a binding energy of $16 Ry^*$ (not considering the $2/R$ term) and Bohr radius $0.25 a^*$. The binding energy decreases with R and tends to $4 Ry^*$ when $R \rightarrow \infty$, which corresponds to an electron bound to a single donor (hydrogen atom).

7.2.4 Hydrogen molecule: H_2

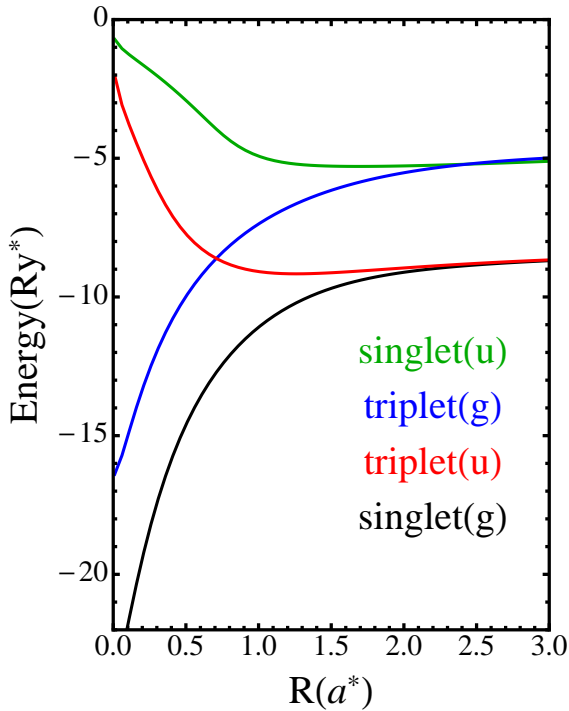


FIGURE 7.3: Energy of the four lowest molecular states in the EMA as a function of R , see Eq. 7.20.

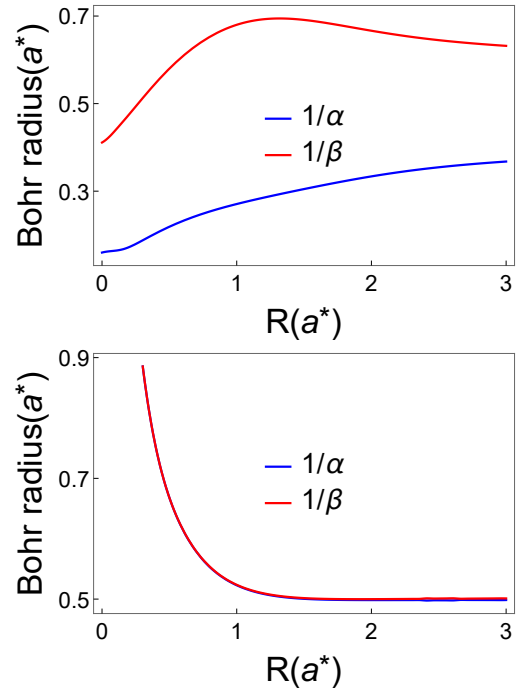


FIGURE 7.4: Bohr radius of the two electrons in the lowest states at large R . (Top) Singlet gerade. (Bottom) Triplet ungerade.

This case corresponds to a couple of dopants sharing two electrons, a very relevant case since entanglement between pairs of qubits is a fundamental requirement for a quantum computer. The Hamiltonian of the hydrogen molecule is:

$$H = -\frac{\hbar^2}{2m_{\text{eff}}}(\nabla_1^2 + \nabla_2^2) - \frac{e^2}{\epsilon r_{1a}} - \frac{e^2}{\epsilon r_{1b}} - \frac{e^2}{\epsilon r_{2a}} - \frac{e^2}{\epsilon r_{2b}} + \frac{e^2}{\epsilon r_{12}} + 2/R. \quad (7.19)$$

In effective units it becomes:

$$H = -\nabla_1^2 - \nabla_2^2 - \frac{2}{r_{1a}} - \frac{2}{r_{1b}} - \frac{2}{r_{2a}} - \frac{2}{r_{2b}} + \frac{2}{r_{12}} + \frac{2}{R}. \quad (7.20)$$

This Hamiltonian cannot be solved analytically, thus, we use a variational approach. We define a two parameter variational wavefunction based in hydrogenic orbitals. This approach assumes that the 2-electron ground state wavefunction is just a combination of 1-electron ground state orbitals. A naive generalization for two parameters such as $\Psi = N(e^{-\alpha r_{1a} - \beta r_{2b}} \pm e^{-\alpha r_{2a} - \beta r_{1b}})$ breaks the symmetry under reflections (equivalent to $a \leftrightarrow b$ symmetry) so we need to generalize the wavefunction inserting more terms from the Slater determinants to keep that symmetry. Consequently, we consider a basis set formed of four states with different symmetry properties: singlet and triplet states, which are antisymmetric and symmetric in the spin part, being symmetric and antisymmetric in their orbital part; and gerade and ungerade states, symmetric and antisymmetric under inversion.

$$\begin{aligned} \Psi_{singlet}^g(\mathbf{r}_1, \mathbf{r}_2) = N[& (e^{-\alpha r_{1a} - \beta r_{2b}} + e^{-\alpha r_{2a} - \beta r_{1b}}) + (e^{-\alpha r_{1b} - \beta r_{2a}} + e^{-\alpha r_{2b} - \beta r_{1a}}) \\ & + e^{i\phi}(e^{-\alpha(r_{1a} + r_{2b})} + e^{-\alpha(r_{2a} + r_{1b})}) + e^{i\theta}(e^{-\beta(r_{1a} + r_{2b})} + e^{-\beta(r_{2a} + r_{1b})})], \end{aligned} \quad (7.21)$$

$$\Psi_{singlet}^u(\mathbf{r}_1, \mathbf{r}_2) = N[(e^{-\alpha r_{1a} - \beta r_{2b}} + e^{-\alpha r_{2a} - \beta r_{1b}}) - (e^{-\alpha r_{1b} - \beta r_{2a}} + e^{-\alpha r_{2b} - \beta r_{1a}})] \quad (7.22)$$

$$\Psi_{triplet}^g(\mathbf{r}_1, \mathbf{r}_2) = N[(e^{-\alpha r_{1a} - \beta r_{2b}} - e^{-\alpha r_{2a} - \beta r_{1b}}) + (e^{-\alpha r_{1b} - \beta r_{2a}} - e^{-\alpha r_{2b} - \beta r_{1a}})] \quad (7.23)$$

$$\begin{aligned} \Psi_{triplet}^u(\mathbf{r}_1, \mathbf{r}_2) = N[& (e^{-\alpha r_{1a} - \beta r_{2b}} - e^{-\alpha r_{2a} - \beta r_{1b}}) - (e^{-\alpha r_{1b} - \beta r_{2a}} - e^{-\alpha r_{2b} - \beta r_{1a}}) \\ & + e^{i\phi}(e^{-\alpha(r_{1a} + r_{2b})} - e^{-\alpha(r_{2a} + r_{1b})}) + e^{i\theta}(e^{-\beta(r_{1a} + r_{2b})} - e^{-\beta(r_{2a} + r_{1b})})], \end{aligned} \quad (7.24)$$

with α and β variational parameters. The inversion symmetry can be seen by exchanging a and b , while the orbital symmetry can be seen by exchanging 1 and 2. The phases ϕ and θ are added to consider the most general case with two variational Bohr radii. The most symmetric wavefunction, hence best candidate for ground state, would then be the singlet gerade. With Eqs. 7.21-7.24 we are able to approximate not only the ground state but also the three first excited states.

Most of the integrals involved in the variational method are complex integrals of exponentials that can be calculated analytically in spheroidal coordinates. The results, however, are quite complex, involving combinations of hypergeometric and Bessel functions. In order to handle these solutions the software Mathematica was used [300]. On the other hand, the integrals related with $1/r_{12}$ are non trivial [301, 302], so instead of an analytical method a numerical calculation was made by approximating the exponentials in (7.21-7.24) by Gaussian functions [303], whose integrals can be performed analytically in Mathematica. Naming $\phi(\alpha, r)$ one orbital with variational parameter α , the approximations to each orbital are made assuming $\alpha = 1$ and then, the orbitals are scaled:

$$\phi(\alpha, r) = \alpha \phi(1, \alpha r). \quad (7.25)$$

The single orbitals are then approximated by six gaussian functions:

$$\psi(1, r) = \sum_{k=0}^6 a_k e^{-\gamma_k r^2}. \quad (7.26)$$

The values of the fitting parameters were obtained using a least squares method. a_k and γ_k are tabulated in Table 7.1. The estimated relative error is 0.02% in six atomic units of length. It is important to note that gaussians and exponentials decay differently, hence, the relative error is higher at longer distances, however, after six atomic units both the exponential and

Parameter	$k = 1$	$k = 2$	$k = 3$	$k = 4$	$k = 5$	$k = 6$
a_k	0.094187	0.0183017	0.173445	0.284744	0.264034	0.14852
γ_k	91.613805	0.061649	8.649974	0.473985	1.723872	0.160028

TABLE 7.1: Values of the fitting parameters a_k and γ_k used to approximate the electron wavefunctions by Gaussians (see Eqs 7.25-7.26). This is a useful approximation in order to calculate the electron-electron interaction.

gaussian wavefunctions are almost zero and then, irrelevant for the variational calculation. The energy is calculated as a function of the variational parameters and R . For a given R the variational parameters are chosen to minimize the energy. For the single gerade state we get $\phi = \theta = 0$ while for the triplet ungerade we get $\phi = 0$ and $\theta = \pi$.

7.2.4.1 Binding energies

The energies as a function of R of the four lowest states are shown in Fig. 7.3. As expected from symmetry arguments, the singlet gerade is the ground state. The singlet ungerade is the highest excited state while the second and third excited states depends on the distance between nuclei: For short distances $R \leq 0.6a^*$ the triplet gerade is the first excited state, while for longer distances the triplet ungerade becomes the first excited state. While both states are triplet states, the different inversion symmetry of the states allows the crossing between them.

For short distances the energy of the ground state is near $24 Ry^*$, which corresponds to the He limit. In the long distance, two clear limits are observed: The singlet gerade and triplet ungerade tend to $-8 Ry^*$, while the singlet ungerade and triplet gerade tend to $-4.5 Ry^*$. These limits can associated to physical cases already analyzed H and H^- . In the case of the singlet gerade and triplet ungerade the energy tends to two simple hydrogen atoms: by separating the two nuclei, both electrons go with each one of the nuclei. On the other hand, the singlet ungerade and triplet ungerade tend to the hydrogen atomic ion: both electrons in a single atom.

7.2.4.2 Bohr radius

The Bohr radii obtained using the variational method are shown in Fig. 7.4. In the case of the singlet gerade, there are two different Bohr radii, one closer to the nuclei than the other. In particular, both Bohr radii tend to 0.5 when R goes to infinity. This is related to the tendency of this state to divide into two hydrogen atoms for large R . In the triplet ungerade however, both Bohr radii are identical and large for close distances, indicating an excited state in comparison to the singlet gerade. Both radii tend to 0.5 as R grows, again, due to the tendency to become two separated hydrogen atoms.

7.3 Parameters of 2D materials

The EMA host parameters m_{eff} and ϵ can be very different for 2D and 3D materials with the same chemical composition and also for 2D materials with different number of layers [309]. They also depend on the distance between the layers [308] or the nature of the substrate.

Material	Effective mass (m_e)	Gap (eV)	Dielectric constant (ϵ_0)
ZnS	0.187	2.58-4.5	-
CdS	0.167	1.72-3.23	-
CdSe	0.127	1.30-2.47	-
SiC	0.645	2.55-3.63	-
MoS ₂	0.37 [304]-0.45 [305]	1.3-1.9 [290]	4 [306]
h-BN	1.175	5.9 [290]	2.31 [307]

TABLE 7.2: Effective masses and gaps of some 2D materials. ZnS, CdS, CdSe and SiC have a direct gap with their conduction band minimum at Γ . h-BN and MoS₂ have it at K. In the literature, values for the dielectric constants (mostly calculated) can be found for only for a few cases and, as discussed in the text, they are dependent on external conditions. Therefore, we consider the dielectric constant as a parameter. Unless otherwise stated, the data are taken from Ref. [308].

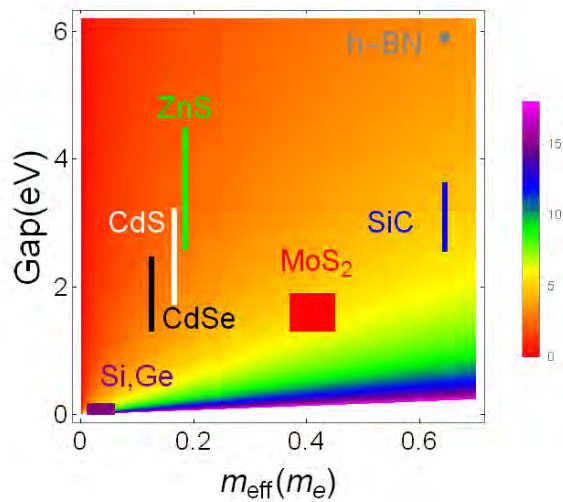


FIGURE 7.5: Critical value of ϵ for the validity of the EMA when considering a single donor atom.

The size and nature (direct-indirect) of the gap of a 2D material also depends on all these factors and can be sometimes tuned with electric field, as for the buckled silicene and germanene [310]. This variability on the physical properties can affect very strongly the possible binding energies. It has been shown, using first-principles calculations, that the binding energy of dopants in transition metal dichalcogenides can be tuned from deep to shallow by using different substrates [311]. This modulation of ionization energy has been studied in the context of achieving p-type/n-type doping for transistor-like devices, but it certainly remains relevant for the donor quantum manipulation proposed here.

The EMA is appropriate to describe shallow states in semiconductors, thus the gap of the considered material has to be much larger than the binding energy E_B . In order to do this comparison, we consider the generally unknown dielectric constant ϵ as a free parameter and estimate its minimum value required for the existence of isolated dopants and dopant pairs as a function of the gap E_g and the effective mass on the conduction band. We use the criterion that the binding energy has to fulfill $E_B < E_g/2$. This is equivalent to

$$\frac{E_g(\text{eV})}{2} \geq E_B(\text{eV}) = 13.6 \frac{m_{\text{eff}}}{\epsilon^2} E_B(\text{Ry}^*). \quad (7.27)$$

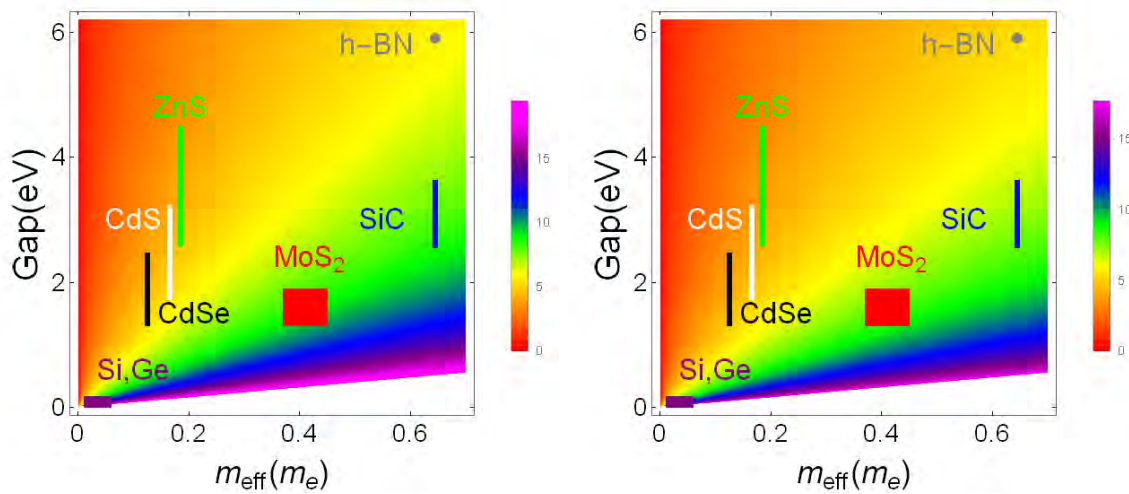


FIGURE 7.6: Critical value of ϵ for the validity of the EMA when considering a donor pair. (Left) $R = 1a^*$. (Right) $R = 2a^*$.

By imposing this criterion, we can get a critical value of the dielectric permittivity:

$$\epsilon_{\text{crit}} = \sqrt{27.2E_B(Ry^*) \frac{m_{\text{eff}}}{E_g}}. \quad (7.28)$$

Below ϵ_{crit} the EMA cannot be considered valid, since it implies that the binding energy is more than half of the gap, and interactions with the valence bands should be taken into account.

In order to put our results in the perspective of actual 2D materials, we introduce in Figures 7.5 and 7.6 the data corresponding to various 2D materials (see Table 7.2) showing the feasibility, in terms of energetics, of using single and pairs of dopants for the definition of qubits.

In Fig. 7.5 the value of ϵ_{crit} for a single dopant is shown as a function of the electron effective mass and energy bandgap of a material. Materials with heavy electrons and narrow bandgaps would require larger ϵ than materials with light effective masses and wide bandgaps. In the case of h-BN, the dielectric constant has been calculated, in the monolayer form, to be 2.31 [307] while the critical value is $\epsilon_{\text{crit}} = 4.65$. In the case of MoS₂ the critical value is $4.6 \leq \epsilon_{\text{crit}} \leq 5.56$, which again is above its dielectric constant. In these two cases, the dopants would be too deep to be described by EMA. Other materials, such as ZnS or CdSe impose softer restrictions due to their small effective mass. Silicene and Germanene, since they are expected to have a very small bandgap and effective masses (almost Dirac cone energy dispersions) that strongly depends on the substrate, have a very wide potential critical permittivities. In some 2D materials, the bandgap has been shown to be tunable [310, 312], which would give an extra tunability.

Since the molecular states are more bound, the critical value of the permittivities is expected to be more restrictive for the donor pair. This can be seen in Fig. 7.6 for two different separations $R = 1a^*$ and $R = 2a^*$. For $R = 1a^*$ we get the worst case scenario, where only CdSe, CdS, ZnS and, potentially, Silicene and Germanene would have critical values of the permittivities below 5. This problem is alleviated at larger distances as can be seen in the right side plot.

In order to give an estimate binding energies and Bohr radii for 2D materials, we need to assume a particular value for the dielectric constant. Assuming $\epsilon \sim 5$, the Bohr radii for electrons bound to single dopants would be between 5\AA and 1nm a factor of ~ 3 smaller than the typical Bohr radii in 3D silicon [67].

7.4 Application to quantum computing

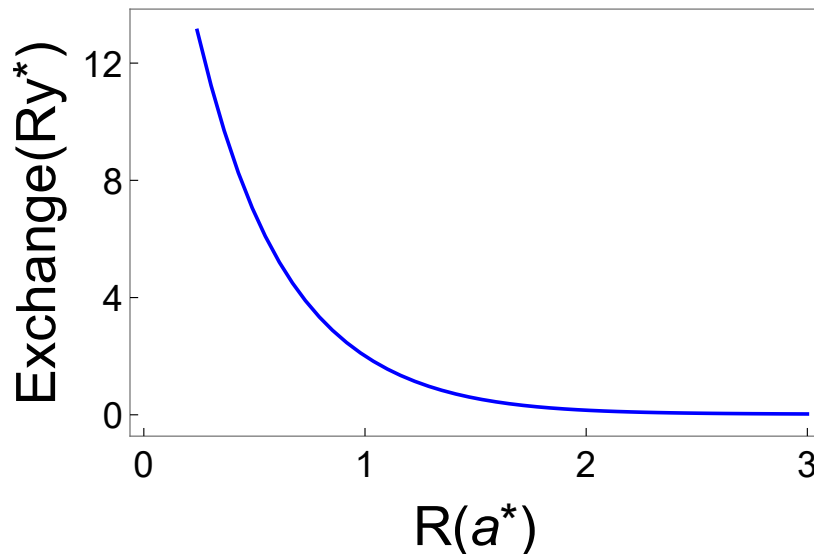


FIGURE 7.7: Exchange, as a function of R , defined as the energy difference between the singlet gerade and triplet ungerade.

For a single donor with 2 electrons there are 2 low-energy levels well separated from the next excited state, one singlet and one triplet, which allows to map the lower-energy states problem to the Heisenberg spin-1/2 Hamiltonian. The spin states could then be addressed by an oscillating magnetic field. On the other hand, since some of these 2D materials exhibit spin-orbit interactions, single qubit manipulation might also be possible via electric fields. In particular, for Silicene and Germanene the bandgaps are tunable via vertical electric fields. As a result, a top gate could be used to tune the energy levels and Bohr radii of the dopants. The ability to manipulate the Bohr radii could be very interesting to move between regimes in which the radius is shorter or larger, associated to different binding energies. In the small wavefunction radius regime, it would reduce the exposure to charge traps or magnetic impurities that could induce decoherence. In the large wavefunction radius regime, interactions with other qubits might become enhanced, switching on and off the two qubit operations.

As already mentioned, the donor state with two electrons is not very stable, being the ionization energy of the second electron of $0.5 Ry^*$. The lifetime of this state would be short, and potentially useful for readout in a Pauli spin blockade protocol. On the other hand, the double donor state with a single electron could be used to define a charge qubit, where the qubit can be encoded as $|0\rangle$ or $|1\rangle$, depending on the electron position at one nucleus or the other.

With 2 donors and 2 electrons, there are 4 possible states, see subsection 7.2.4. We label the expectation values of these states in increasing order E_1 , E_2 , E_3 and E_4 , and assign

a spin hamiltonian to this problem if $E_2 - E_1 \ll E_3 - E_2$ so that only the two lowest levels are relevant at low temperatures, and the spin-1/2 hamiltonian may be defined as for a 2-level system. It has been shown that the 2 lowest levels are a singlet (GS) and a triplet, as illustrated in 7.3. The two lowest states can be used to define a single-qubit. This qubit would not require magnetic fields, and electrical manipulation could be performed. On the other hand, if the double donor is used to define two qubits in the spin degree of freedom of each electron, two-qubit operations are driven by exchange gates, i.e., exchange coupling J pulses between electrons bound to neighboring donors.

Fig. 7.7 shows the exchange interaction J , the difference between the lowest singlet and triplet levels, as a function of R in a physically accessible range of inter donor distances. The Hamiltonian in the two-qubit subspace of the exchange interaction is [26, 27]:

$$H_{\text{int}} = J\sigma^1 \cdot \sigma^2. \quad (7.29)$$

This interaction can be used to perform a SWAP operation, and, together with single-qubit operations, a CNOT gate. The time for performing a $\sqrt{\text{SWAP}}$ operation is $\tau = h/4J$. Using the expression for the Rydberg unit in Eq. 7.1, we can get the expression of τ as a function of ϵ and m_{eff} :

$$\tau = \frac{1}{4 \cdot 13594} \frac{h\epsilon^2}{m_{\text{eff}}J(Ry^*)}. \quad (7.30)$$

For a separation of $2a^*$ the exchange is $J = 0.16Ry^*$. To give an idea of the relevant numbers, this corresponds to the order of ps for $\epsilon = 10$ and an effective mass of $0.05m_0$. Larger values of ϵ would make it slower, while a larger effective mass would make it faster. In any case, the numbers for the exchange interaction indicate extremely fast two-qubit operations that would need to be benchmarked against the coherence times. While this operations would be fast, the small Bohr radius makes the exchange interaction to decrease strongly with R . At the same time, while coherence times in this context are not available, the confinement of the wavefunction in a small Bohr radius indicate potentially good coherence properties.

The stronger confinement in 2D than in 3D, requires closer dopants for 2-qubit exchange coupling. This demands higher accuracy in the placement of gates on top and between donors, and nano-electrodes (as for example carbon nanotubes) may be needed in the final device.

7.5 Conclusions

Dopants in 2D imply stronger confinement and states more bound than in 3D. Consequently, the donor states are, in general, more stable in 2D, and the small Bohr radius would imply better coherence properties. At the same time, this would require closer dopants for multiple qubit operations, which implies a higher accuracy in the placement of gates.

While single dopants can be manipulated with magnetic fields, the strong SOC in several 2D materials could be used to induce transitions via EDSR. Two electrons bound to two donors can be used to perform fast two-qubit operations via exchange gates, although it also allows to define a singlet-triplet qubit, which would not require a magnetic field to define the qubit. The single donor ion state does not have a high binding energy for the second electron, which allows to define a readout procedure based on the Pauli spin blockade.

The variability of binding energies as a function of substrate or number of layers, opens up a wide range of possibilities for the potential use of dopants in 2D materials for quantum computation. The synergy of the different experimental techniques for dopant positioning in 3D semiconductors and the recent quick advancement in 2D materials-based electronics provides with all the technical ingredients required to explore the practical feasibility of this proposal.

Conclusions

We have studied several alternatives for quantum computing in semiconductor nanostructures. We have emphasized the importance of electric manipulation and tunability of the quantum system since magnetic manipulations constraints the scalability of quantum devices. Spin-orbit qubits, such as those that can be defined in the degrees of freedom of holes bound to acceptors, are naturally susceptible to electrical manipulation. We also analyzed the electrical tunability of quantum properties, due to the valley physics, in quantum dot systems such as the quantum dot hybrid qubit and nanowire Field Effect Transistors. Finally, an alternative platform based on 2D materials was presented and analyzed.

The main results of the thesis can be summarized as follows:

- In Chapter 2 we analyzed the effects of quantum confinement in the low energy physics of acceptor bound states. We focused on the effects of hard wall interfaces, such as SiO₂ barriers, and SiGe quantum wells. To quantify the effects of both types of confinement, we developed an effective mass approach to variationally solve the total Hamiltonian. The central cell radius r_{cc} was obtained for each one of the group III acceptors inside both Si and Ge. Confinement against a single interface was found to reduce the binding energy and compress the spectrum of the acceptors, while an acceptor inside a quantum well can increase its binding energy due to the increasing confinement in the impurity. The four-fold degenerate ground state of bulk acceptors is broken due to the inversion asymmetry into two Kramer doublets with heavy-hole and light-hole nature respectively. The effects of electric and magnetic fields, strain and tetrahedral symmetry terms, were taken into account to obtain a low energy Hamiltonian that can be used to analyze the physics of qubits defined in the lowest heavy-hole light-hole manifold.
- The effective Hamiltonian of SiGe quantum wells obtained in Chapter 2, is used to analyze the different forms of manipulation of a qubit in Chapter 3. Both heavy-hole and light-hole qubits were considered. In the case where quantum confinement and strain conditions implied a heavy-hole ground state, we found that manipulation through g-tensor modulation resonance was the fastest method for manipulation. In exchange, this method would make a heavy-hole qubit sensitive to charge noise that would induce g-factor fluctuations. Electric dipole spin resonance, although not so sensitive to charge noise, was found to be suppressed by the strain induced heavy-hole

light-hole splitting. In the case of light-hole qubits, we considered electric dipole spin resonance for two cases, depending on the curvature of the g-factor with electric fields: Concave or convex light-hole qubits. In both cases, several sweet spots, where charge noise is suppressed, were found. At the same time, the Rabi frequency in these sweet spots was found to be maximized and one order of magnitude faster (\approx GHz) than in the best case for heavy-holes (\approx 100 MHz).

- In Chapter 4 we generalize the theory of single acceptor qubits to increase the tunability, coherence and entanglement properties of acceptors near an interface. We found that the tetrahedral symmetry terms is responsible for a strong anisotropy in light-hole qubits. This anisotropy can be used to tune the coherence properties in the different sweet spots, by changing the curvature and finding a second-order sweet spot or by finding a decoherence free subspace, where the qubit cannot decohere to first order under any kind of perturbation. Moreover, the electric field was found to significantly affect the spin properties of the four level system. The electrical tunability of this spin properties allows to exploit the dipolar-dipolar interactions to define two different protocols where entanglement can be switched on and off only by electric means. At the same time, both entanglement protocols take advantage of the coherence properties: One protocol reduces charge noise exposure during the entanglement procedure, while the other exploits single-qubit operations near the decoherence free subspace.
- The valley physics of the quantum dot hybrid qubit was evaluated in Chapter 5. The inevitable presence of interfacial disorder was considered in a 2D single-electron double quantum dot tight-binding that captures the physics of a more complex system: the quantum dot hybrid qubit. This simple tight-binding captured the relevant valley physics, allowing us to simulate the effects of the electric fields on the valley degree of freedom under multiple interfacial disorder profiles. This interfacial disorder was found to induce changes in both the envelope and valley degrees of freedom of electron wavefunction thus affecting the valley splitting and tunnel couplings under vertical electric fields and detuning. Most importantly, this dependence was found to be similar to the reported in the experiments, and predicted the existence of regions in detuning where the coherence properties can be enhanced (sweet spots) or suppressed (hot spots).
- In Chapter 6 the effects of geometry and electric fields on the valley splitting in nanowire Field Effect Transistors was analyzed. The electrostatics of the device was simulated using a finite element method software. The results of these simulations were used in both an effective mass approach and a tight-binding method to simulate the valley physics of corner dots. We found that, although four valley states can be expected to be relevant, defects in the geometry, such as non right angles, can separate the horizontal and vertical valley states up to a few meV. Each valley couple in the corner dot was found to behave similarly to valley doublets near a single interface, allowing linear tunability of the valley splitting by further increasing the confinement against the walls.
- In Chapter 7 we proposed the use of 2D materials as devices for quantum computation. An effective mass approach was used to obtain the lowest levels of a single impurity atom, and a molecule of two impurities sharing one or two electrons. We evaluated the applicability of the effective mass approach for several 2D materials. Most of these materials are direct bandgap semiconductors, with no valley degeneracy, which is a property that would help to simplify the problems of entanglement since the exchange interaction would not oscillate with defect position. In particular, Silicene and Germanene are predicted to have a tunable bandgap, what would allow to change the

effective mass, the binding energies, and the Bohr radius, thus modifying the Larmor energies and exchange of the qubits. These platforms, while experimentally challenging, would have less restrictions than other semiconducting platforms for quantum computing.

Conclusiones

Hemos estudiado varias alternativas para computación cuántica en nanoestructuras semiconductoras. Se ha dado importancia a la manipulación eléctrica y a la capacidad para modificar las propiedades de los sistemas cuánticos dado que la manipulación por medios magnéticos limita la escalabilidad de los dispositivos. Qubits basados en espín-órbita, son susceptibles a la manipulación eléctrica de forma natural. También analizamos la capacidad para modificar las propiedades cuánticas, relacionadas con la física de valles, en sistemas de puntos cuánticos tales como el qubit híbrido en puntos cuánticos o el nanohilo transistor de efecto campo. Finalmente, una plataforma alternativa, basada en materiales bidimensionales fue presentada y analizada.

Los resultados principales de la tesis se pueden resumir en los siguientes puntos:

- En el capítulo 2 analizamos los efectos del confinamiento cuántico en la física de baja energía de estados ligados de aceptores. Nos centramos en el efecto de intercaras, tal como una barrera de SiO_2 , o pozos cuánticos de SiGe . Para cuantificar los efectos de ambos tipos de confinamiento desarrollamos un método de masa efectiva para resolver variacionalmente el Hamiltoniano del sistema. El radio de celda central r_{cc} fue obtenido para cada uno de los aceptores del grupo III tanto en Si como en Ge. El confinamiento cerca de una intercara demostró reducir la energía de ligadura y comprimir el espectro de los aceptores, mientras que un aceptor dentro de un pozo cuántico puede aumentar su energía de ligadura debido al aumento de la función de onda alrededor de la impureza. El cuatro veces degenerado estado fundamental de un aceptor en bulk se degenera en dos pares de Kramer de naturaleza hueco-pesado y hueco-ligero respectivamente. Los efectos de los campos eléctricos y magnéticos, estrés o la simetría tetrahédrica, fueron considerados para obtener el Hamiltonian de baja energía que puede ser usado para analizar la física de qubits definidos en la variedad de los estados fundamentales de hueco-pesado y hueco-ligero.
- El Hamiltonian efectivo de aceptores en pozos cuánticos de SiGe obtenido en el capítulo 2, es usado para analizar las distintas formas de manipulación de un qubit en el capítulo 3. Tanto qubits basados en estados de hueco-pesado como qubits basados en huecos-ligeros fueron considerados. En el caso en que el confinamiento y el estrés implican un estado fundamental de hueco-pesado, encontramos que la manipulación a través de resonancia de la modulación del tensor-g fue el método mas rápido para

manipulación. A cambio, este método incrementaría la sensibilidad al ruido de carga, a través de fluctuaciones del factor-g, a un qubit de huecos-pesados. La resonancia del dipolo eléctrico de espín, aunque no tan sensible al ruido de carga, estaría suprimida por la separación de energías inducida por estrés entre los estados fundamentales de hueco-pesado y hueco-ligero. En el caso de los qubits de hueco-ligero, consideramos la manipulación a través de la resonancia del dipolo eléctrico de espín en dos casos, dependiendo de la curvatura del factor-g respecto al campo eléctrico: Qubits de huecos-ligeros cóncavos o convexos. En ambos casos, varios puntos dulces, donde el efecto del ruido de carga está suprimido, fueron encontrados. Además, la frecuencia de Rabi en estos puntos dulces está maximizada y es un orden de magnitud mayor (\approx GHz) que en el mejor caso para huecos-pesados (\approx 100 MHz).

- En el capítulo 4 generalizamos la teoría de qubits aceptores para aumentar las posibilidades de manipulación, mejorar la coherencia y las propiedades de entrelazamiento de aceptores cercanos a una intercara. Encontramos que los términos de simetría tetrahédrica son responsables de una fuerte anisotropía en las propiedades de los qubits basados en huecos-ligeros. Esta anisotropía puede ser usada para modificar las propiedades de coherencia en los distintos puntos dulces, cambiando la curvatura y dando lugar a un punto dulce de segundo orden, o un subespacio libre de decoherencia, donde el qubit no puede ser influido por procesos de decoherencia de primer orden. Además, encontramos que el campo eléctrico afecta las propiedades de espín del sistema de cuatro niveles. Esta capacidad para manipular las propiedades de espín eléctricamente nos permite aprovechar la interacción dipolo-dipolo para definir dos protocolos distintos en los que el entrelazamiento puede activarse o desactivarse por medios puramente eléctricos. A su vez, ambos protocolos de entrelazamiento pueden aprovecharse de las propiedades de coherencia: Un protocolo se puede usar para reducir la exposición a ruido de carga durante el procedimiento para entrelazar qubits, mientras el otro puede aprovecharse del número de operaciones de un qubit cerca del subespacio libre de decoherencia.
- La física de valles del qubit híbrido de puntos cuánticos fue evaluado en el capítulo 5. La presencia inevitable de desorden en las intercaras fue considerada en un modelo de aproximación de enlace fuerte bidimensional de un solo electron en un doble punto cuántico que captura la física de un sistema mas complejo: el qubit híbrido de puntos cuánticos. Este simple modelo captura la física de valles mas relevante, permitiéndonos simular los efectos de campos eléctricos en el grado de libertad de los valles bajo múltiples perfiles de desorden en la intercara. Este desorden en la intercara induce cambios tanto en la envoltura como en las oscilaciones de valle de la función de onda, afectando por tanto la separación de energía de valles y los acoplos túnel bajo campos eléctricos verticales como detuning. Aún mas importante, esta dependencia es similar a la reportada en experimentos, y predice la existencia de regiones en detuning donde las propiedades de coherencia pueden estar mejoradas (puntos dulces) o suprimidas (puntos calientes).
- En el capítulo 6 los efectos de la geometría y el campos eléctricos sobre la separación de energía entre valles en nanohilos de transistores de efecto campo fueron analizados. La electrostática del dispositivo fue simulada usando un software del método de elementos finitos. Los resultados de estas simulaciones fueron usados tanto en un método de masa efectiva como en la aproximación de enlace fuerte para simular la física de valles de los puntos cuánticos en esquinas. Encontramos que, aunque se puede esperar que hasta cuatro valles puedan ser relevantes, defectos en la geometría, tales como ángulos no rectos, pueden separar los valles horizontales de los verticales en varios meV. Cada

pareja de estados valle in los puntos cuánticos de esquinas se comporta de una forma similar a los dobletes de valle confinados contra una intercara, dando lugar a la capacidad para incrementar linealmente la diferencia de energía entre valles al incrementar el confinamiento contra la intercara.

- En el capítulo 7 se propuse el uso de materiales bidimensionales como dispositivos para la computación cuántica. El método de masa efectiva se usó para obtener los niveles de energía mas bajos de una impureza atómica, así como de una molécula formada por dos impurezas que comparten uno o dos electrones. Evaluamos la pertinencia del método de masa efectiva para distintos materiales bidimensionales. La mayor parte de estos materiales son semiconductores de gap directo, sin degeneración de valles, propiedad que simplificaría los problemas de entrelazamiento dado que la interacción de intercambio no oscilaría con la posición de los dopantes. En particular, se espera que el gap en Siliceno y el Germaneno sea modificable, lo que permitiría cambiar la masa efectiva, las energías de ligadura, o el radio de Bohr, modificando por tando la energía de Larmor o la interacción de intercambio los qubits. Estas plataformas, aunque complicadas experimentalmente, reducirían las restricciones para computación cuántica que tienen que otras plataformas semiconductoras.

Appendices

Relevant integrals for Chapter 2

The calculation of the matrix elements $H_{i,j}$ and $S_{i,j}$ have required the evaluation of integrals involving products of wavefunctions (2.11) and the expected values of the different operators 2.3. The analytical solutions to these integrals are not tabulated. We summarize here most of the integrals used in this work.

The general form of the integrals involved in the calculations of the matrix elements in the hard wall case is

$$I(c, n, k') = \int_{-d}^{\infty} dz \int_{|z|}^{\infty} dr z^c r^n \left(\sqrt{r^2 - z^2} \right)^{k'} e^{-\alpha r}. \quad (\text{A.1})$$

The evaluation of this integral depends strongly on the parity of the exponent k' . When $k' = 2k$ being k any positive integer and defining for convenience $\gamma = 2k + n + c + 2$:

$$I(c, n, 2k) = \frac{1}{\alpha^\gamma} \left[\frac{k! \Gamma(\frac{c+1}{2})}{2\Gamma(\frac{c+3}{2} + k)} \left(\Gamma(\gamma) (1 + (-1)^c) + (-1)^{c+1} \Gamma(\gamma, \alpha d) \right) + \sum_{l=0}^k (-1)^{l+c} \binom{k}{l} \frac{(\alpha d)^{2l+c+1}}{2l+c+1} \Gamma(\gamma - 2l - c - 1) \right], \quad (\text{A.2})$$

being $\Gamma(a, z)$ the incomplete gamma function.

When k' is an odd number $k' = 2k + 1$, the parity of the exponent n becomes relevant. If n is even

$$I(c, n, k') = \sum_{m=0}^k (-1)^m \sum_{u=1}^{\frac{\gamma-c}{2}-m} \left(\prod_{l=0}^{u-1} 2l+1 \right) \binom{k}{m} \frac{1}{\alpha^u} \binom{n/2+k-m}{u-1} \left[\frac{2^{\gamma-u-1}}{\alpha^{\gamma+u+1}} \Gamma\left(\frac{\gamma+1}{2}\right) \Gamma\left(\frac{\gamma+1-2u}{2}\right) + (-1)^{c-2u-2} d^{\gamma+1-u} (\alpha d)^{-u} \pi \csc(u\pi) \left(4^u \Gamma\left(\frac{\gamma+1-2u}{2}\right) {}_1\tilde{F}_2\left(\frac{\gamma+1-2u}{2}; 1-u, \frac{\gamma+3-2u}{2}; \frac{\alpha^2 d^2}{4}\right) - (\alpha d)^{2u} \Gamma\left(\frac{\gamma+1}{2}\right) {}_1\tilde{F}_2\left(\frac{\gamma+1}{2}; \frac{\gamma+3}{2}, u+1; \frac{\alpha^2 d^2}{4}\right) \right) \right] \quad (\text{A.3})$$

being \tilde{F} the hypergeometric regularized function. And when n is odd

$$I(c, n, k') = \sum_{m=0}^k (-1)^m \sum_{u=1}^{\frac{\gamma-1-c}{2}-m} \left(\prod_{l=0}^{u-1} 2l+1 \right) \binom{k}{m} \frac{1}{\alpha^u} \binom{n/2+k-m-1/2}{u-1} \left[\frac{2^{\gamma-u-1}}{\alpha^{\gamma+u+1}} \Gamma\left(\frac{\gamma+2}{2}\right) \Gamma\left(\frac{\gamma-2u}{2}\right) \right. \\ \left. + (-1)^c 2^{-u-3} d^{\gamma+1-u} (\alpha d)^{-u-1} \pi \csc(u\pi) \left(4^u \Gamma\left(\frac{\gamma-2u}{2}\right) {}_1\tilde{F}_2\left(\frac{\gamma-2u}{2}; -u, \frac{\gamma+2-2u}{2}; \frac{\alpha^2 d^2}{4}\right) \right. \right. \\ \left. \left. - (\alpha d)^{2u+2} \Gamma\left(\frac{\gamma+2}{2}\right) {}_1\tilde{F}_2\left(\frac{\gamma+2}{2}; \frac{\gamma+4}{2}, u+2; \frac{\alpha^2 d^2}{4}\right) \right) \right] \quad (\text{A.4})$$

The exponent n can be negative for certain operators. When this is the case, the integrals can be transformed into the previous integrals by using the method of differentiation on α under the integral sign. For example, when $n = -1$

$$I(c, -1, k') = - \int d\alpha I(c, 0, k') + C, \quad (\text{A.5})$$

where C is a constant that can be obtained using $I(c, n, k) = 0$ when $\alpha \rightarrow \infty$. The rest of negative n integrals can be obtained using this method recursively.

Regarding the integrals for SiGe quantum wells, those integrals involving the z components are simple combinations of trigonometric functions and exponentials. However, the integrals involving the ρ coordinate can be complex. The most general integral involving this coordinate is

$$\int_0^\infty \rho^n \exp(-\alpha\rho) d\rho = \frac{\Gamma(n+1)}{\alpha^{n+1}}. \quad (\text{A.6})$$

The Coulomb integrals can be performed analytically only in the z direction. The numerical integral in the ρ coordinate is performed using Mathematica [300].

Schrieffer-Wolff transformation

. Let H be a total Hamiltonian that can be divided in two parts: H_0 , whose eigenvalues and eigenfunctions are known, and H_1 , which can be considered as a perturbation to the total Hamiltonian H :

$$H = H_0 + H_1 \tag{B.1}$$

$$H_0|\psi_n\rangle = E_n|\psi_n\rangle \tag{B.2}$$

Assuming that we are not interested in the effect of the perturbation on all the eigenstates but on a rather small subset, we can divide the eigenstates into those of our interest *subset A*, with eigenfunctions $|\psi_m\rangle$, and those not relevant *subset B*, with eigenfunctions $|\psi_l\rangle$. A unitary operator e^{-S} can be found such that it transforms the total Hamiltonian to an effective Hamiltonian \tilde{H} where the states in A and B do not interact to a desired order in H_1 . In this way, the effect of irrelevant excited states in subset B can be mapped onto an effective Hamiltonian of the states we are interested in (subset A). This is particularly useful for constructing low energy effective Hamiltonians. The construction of the matrix S can be found in Ref. [182].

Here I summarize the relevant results for the construction of the construction of the effective Hamiltonians in Chapters 2, 3, and 4, and the calculation of their parameters. Let the indices m, m' and m'' correspond to subset A, indices l, l' and l'' to subset B, $H_{ml} = \langle\psi_m|H|\psi_l\rangle$. The effective Hamiltonian \tilde{H} of subset A to order n is

$$\tilde{H} = H^{(0)} + H^{(1)} + H^{(2)} + \dots H^{(n)} \tag{B.3}$$

Where the matrix elements, up to third order, to each Hamiltonian are (see Ref. [182] for higher orders):

$$H_{mm'}^{(0)} = H_{mm'}^0 \quad (\text{B.4})$$

$$H_{mm'}^{(1)} = H_{mm'}^1 \quad (\text{B.5})$$

$$H_{mm'}^{(2)} = \frac{1}{2} \sum_l H_{ml}^1 H_{lm'}^1 \quad (\text{B.6})$$

$$H_{mm'}^{(3)} = -\frac{1}{2} \sum_{l,m''} \left[\frac{H_{ml}^1 H_{lm''}^1 H_{m''m}^1}{(E_{m'} - E_l)(E_{m''} - E_l)} + \frac{H_{mm''}^1 H_{m''l}^1 H_{lm'}^1}{(E_m - E_l)(E_{m''} - E_l)} \right] \\ + \frac{1}{2} \sum_{l,l'} H_{ml'}^1 H_{ll'}^1 H_{l'm'}^1 \left[\frac{1}{(E_m - E_l)(E_m - E_{l'})} + \frac{1}{(E_{m'} - E_l)(E_{m'} - E_{l'})} \right] \quad (\text{B.7})$$

This formulas are used with the first four states of the acceptor Hamiltonian in subset A and the next four excited states in subset B. As an example of the use of this formula, the value of the Rashba coefficient to first order is simply:

$$H_{1,2}^{\text{Rashba}} = \alpha F_- = \langle 3/2 | eF_- x^+ | 1/2 \rangle \quad (\text{B.8})$$

References

- [1] G. C. Dacey and I. M. Ross. The field effect transistor. *The Bell System Technical Journal*, 34(6):1149–1189, Nov 1955. (Cited on page 1).
- [2] G. E. Moore. Electron devices meeting. *IEEE International*, 21:11–13, 1975. (Cited on page 1).
- [3] A. Kaneko, A. Yagishita, K. Yahashi, T. Kubota, M. Omura, K. Matsuo, I. Mizushima, K. Okano, H. Kawasaki, S. Inaba, T. Izumida, T. Kanemura, N. Aoki, K. Ishimaru, H. Ishiuchi, K. Suguro, K. Eguchi, and Y. Tsunashima. Sidewall transfer process and selective gate sidewall spacer formation technology for sub-15nm finfet with elevated source/drain extension. In *IEEE International Electron Devices Meeting, 2005. IEDM Technical Digest.*, pages 844–847, Dec 2005. (Cited on page 1).
- [4] A. Asenov, A. R. Brown, J. H. Davies, S. Kaya, and G. Slavcheva. Simulation of intrinsic parameter fluctuations in decananometer and nanometer-scale mosfets. *IEEE Transactions on Electron Devices*, 50(9):1837–1852, Sept 2003. (Cited on page 1).
- [5] Richard P. Feynman. Simulating physics with computers. *International Journal of Theoretical Physics*, 21(6):467–488, Jun 1982. (Cited on page 1).
- [6] D. Deutsch. Quantum theory, the church-turing principle and the universal quantum computer. *Proceedings of the Royal Society of London A: Mathematical, Physical and Engineering Sciences*, 400(1818):97–117, 1985. (Cited on pages 1 and 7).
- [7] Michael A. Nielsen and Isaac L. Chuang. *Quantum Computation and Quantum Information: 10th Anniversary Edition*. Cambridge University Press, New York, NY, USA, 10th edition, 2011. (Cited on page 1).
- [8] F. Bloch. Nuclear induction. *Phys. Rev.*, 70:460–474, Oct 1946. (Cited on page 1).
- [9] Ross Anderson and Roger Needham. Robustness principles for public key protocols. In *Crypto*, volume 95, pages 236–247. Springer, 1995. (Cited on page 2).
- [10] Peter W. Shor. Polynomial-time algorithms for prime factorization and discrete logarithms on a quantum computer. *SIAM Review*, 41(2):303–332, 1999. (Cited on page 2).
- [11] Charles H Bennett and Gilles Brassard. Quantum cryptography: Public key distribution and coin tossing. (Cited on page 2).
- [12] Artur K. Ekert. Quantum cryptography based on bell’s theorem. *Phys. Rev. Lett.*, 67:661–663, Aug 1991. (Cited on page 2).

- [13] William K Wootters and Wojciech H Zurek. A single quantum cannot be cloned. *Nature*, 299(5886):802–803, 1982. (Cited on page 2).
- [14] Lov K. Grover. Quantum mechanics helps in searching for a needle in a haystack. *Phys. Rev. Lett.*, 79:325–328, Jul 1997. (Cited on page 2).
- [15] Seth Lloyd. Universal quantum simulators. *Science*, 273(5278):1073–1078, 1996. (Cited on page 2).
- [16] Kaushik Raha, Martin B Peters, Bing Wang, Ning Yu, Andrew M Wollacott, Lance M Westerhoff, and Kenneth M Merz. The role of quantum mechanics in structure-based drug design. *Drug Discovery Today*, 12(17):725–731, 2007. (Cited on page 2).
- [17] Benjamin P Lanyon, James D Whitfield, Geoff G Gillett, Michael E Goggin, Marcelo P Almeida, Ivan Kassal, Jacob D Biamonte, Masoud Mohseni, Ben J Powell, Marco Barbieri, et al. Towards quantum chemistry on a quantum computer. *Nature chemistry*, 2(2):106–111, 2010. (Cited on page 2).
- [18] Joseph W. Britton, Brian C. Sawyer, Adam C. Keith, C. C. Joseph Wang, James K. Freericks, Hermann Uys, Michael J. Biercuk, and John J. Bollinger. Engineered two-dimensional ising interactions in a trapped-ion quantum simulator with hundreds of spins. *Nature*, 484(7395):489–492, 04 2012. (Cited on page 2).
- [19] R. Islam, C. Senko, W. C. Campbell, S. Korenblit, J. Smith, A. Lee, E. E. Edwards, C.-C. J. Wang, J. K. Freericks, and C. Monroe. Emergence and frustration of magnetism with variable-range interactions in a quantum simulator. *Science*, 340(6132):583–587, 2013. (Cited on page 2).
- [20] A. Friedenauer, H. Schmitz, J. T. Glueckert, D. Porras, and T. Schaetz. Simulating a quantum magnet with trapped ions. *Nat Phys*, 4(10):757–761, 10 2008. (Cited on page 2).
- [21] David P DiVincenzo et al. The physical implementation of quantum computation. *arXiv preprint quant-ph/0002077*, 2000. (Cited on page 2).
- [22] J. I. Cirac and P. Zoller. Quantum computations with cold trapped ions. *Phys. Rev. Lett.*, 74:4091–4094, May 1995. (Cited on page 3).
- [23] Lilian Childress and Ronald Hanson. Diamond nv centers for quantum computing and quantum networks. *MRS bulletin*, 38(2):134–138, 2013. (Cited on page 3).
- [24] Michel H Devoret and Robert J Schoelkopf. Superconducting circuits for quantum information: an outlook. *Science*, 339(6124):1169–1174, 2013. (Cited on page 3).
- [25] Michael Freedman, Alexei Kitaev, Michael Larsen, and Zhenghan Wang. Topological quantum computation. *Bulletin of the American Mathematical Society*, 40(1):31–38, 2003. (Cited on page 3).
- [26] Daniel Loss and David P. DiVincenzo. Quantum computation with quantum dots. *Phys. Rev. A*, 57:120–126, Jan 1998. (Cited on pages 3, 7, and 130).
- [27] B. E. Kane. A silicon-based nuclear spin quantum computer. *Nature*, 393(6681):133–137, 05 1998. (Cited on pages 3, 5, 119, and 130).

- [28] Floris A Zwanenburg, Andrew S Dzurak, Andrea Morello, Michelle Y Simmons, Lloyd CL Hollenberg, Gerhard Klimeck, Sven Rogge, Susan N Coppersmith, and Mark A Eriksson. Silicon quantum electronics. *Reviews of modern physics*, 85(3):961, 2013. (Cited on pages 3, 9, and 120).
- [29] Silicon bandstructure. <http://www.globalsino.com/micro/1/1micro9968.html>. (Cited on page 4).
- [30] Otfried Madelung. *Semiconductors: data handbook*. Springer Science & Business Media, 2012. (Cited on pages 4, 32, 33, and 76).
- [31] Bernard Pajot and Bernard Clerjaud. *Optical Absorption of Impurities and Defects in Semiconducting Crystals: Electronic Absorption of Deep Centres and Vibrational Spectra*, volume 169. Springer Science & Business Media, 2012. (Cited on pages 4, 16, 17, 22, 25, and 33).
- [32] W. Kohn and J. M. Luttinger. Theory of donor states in silicon. *Phys. Rev.*, 98:915–922, May 1955. (Cited on pages 5, 9, 10, and 15).
- [33] David G. Cory, Amr F. Fahmy, and Timothy F. Havel. Ensemble quantum computing by nmr,Åâspectroscopy. *Proceedings of the National Academy of Sciences*, 94(5):1634–1639, 1997. (Cited on page 5).
- [34] JR Klauder and PW Anderson. Spectral diffusion decay in spin resonance experiments. *Physical Review*, 125(3):912, 1962. (Cited on page 5).
- [35] Alexei M Tyryshkin, Shinichi Tojo, John JL Morton, Helge Riemann, Nikolai V Abrosimov, Peter Becker, Hans-Joachim Pohl, Thomas Schenkel, Michael LW Thewalt, Kohei M Itoh, et al. Electron spin coherence exceeding seconds in high-purity silicon. *Nature Materials*, 11(2), 2012. (Cited on pages 5, 11, 22, and 119).
- [36] Juha T. Muhonen, Juan P. Dehollain, Arne Laucht, Fay E. Hudson, Rachpon Kalra, Takeharu Sekiguchi, Kohei M. Itoh, David N. Jamieson, Jeffrey C. McCallum, Andrew S. Dzurak, and Andrea Morello. Storing quantum information for 30 seconds in a nanoelectronic device. *Nat Nano*, 9(12):986–991, 12 2014. (Cited on pages 5 and 11).
- [37] G Feher. Electron spin resonance experiments on donors in silicon. i. electronic structure of donors by the electron nuclear double resonance technique. *Physical Review*, 114(5):1219, 1959. (Cited on page 5).
- [38] Belita Koiller, Xuedong Hu, and S. Das Sarma. Exchange in silicon-based quantum computer architecture. *Phys. Rev. Lett.*, 88:027903, Dec 2001. (Cited on pages 7, 10, and 120).
- [39] LCL Hollenberg, CJ Wellard, Christopher Ian Pakes, and AG Fowler. Single-spin readout for buried dopant semiconductor qubits. *Physical Review B*, 69(23):233301, 2004. (Cited on pages 7 and 10).
- [40] JM Elzerman, R Hanson, Van Beveren LH Willems, B Witkamp, LM Vandersypen, and LP Kouwenhoven. Single-shot read-out of an individual electron spin in a quantum dot. *Nature*, 430(6998):431–435, 2004. (Cited on pages 8 and 11).
- [41] Franck HL Koppens, Joshua A Folk, Jeroen M Elzerman, Ronald Hanson, LH Willems Van Beveren, Ivo T Vink, Hans-Peter Tranitz, Werner Wegscheider, Leo P Kouwenhoven, and Lieven MK Vandersypen. Control and detection of singlet-triplet mixing in a random nuclear field. *Science*, 309(5739):1346–1350, 2005. (Cited on pages 8 and 11).

- [42] J. R. Petta, A. C. Johnson, J. M. Taylor, E. A. Laird, A. Yacoby, M. D. Lukin, C. M. Marcus, M. P. Hanson, and A. C. Gossard. Coherent manipulation of coupled electron spins in semiconductor quantum dots. *Science*, 309(5744):2180–2184, 2005. (Cited on pages 8 and 11).
- [43] WM Witzel and S Das Sarma. Quantum theory for electron spin decoherence induced by nuclear spin dynamics in semiconductor quantum computer architectures: Spectral diffusion of localized electron spins in the nuclear solid-state environment. *Physical Review B*, 74(3):035322, 2006. (Cited on pages 8 and 22).
- [44] J. M. Luttinger and W. Kohn. Motion of electrons and holes in perturbed periodic fields. *Phys. Rev.*, 97:869–883, Feb 1955. (Cited on pages 9, 15, 17, 22, 24, and 50).
- [45] A A Larionov, L E Fedichkin, A A Kokin, and K A Valiev. The nuclear magnetic resonance spectrum of 31 p donors in a silicon quantum computer. *Nanotechnology*, 11(4):392, 2000. (Cited on page 9).
- [46] C J Wellard, L C L Hollenberg, and C I Pakes. Single-qubit operations on the kane quantum computer. *Nanotechnology*, 13(5):570, 2002. (Cited on page 9).
- [47] C J Wellard and L C L Hollenberg. Thermal noise in a solid state quantum computer. *Journal of Physics D: Applied Physics*, 35(20):2499, 2002. (Cited on page 9).
- [48] L. M. Kettle, H.-S. Goan, Sean C. Smith, C. J. Wellard, L. C. L. Hollenberg, and C. I. Pakes. Numerical study of hydrogenic effective mass theory for an impurity p donor in si in the presence of an electric field and interfaces. *Phys. Rev. B*, 68:075317, Aug 2003. (Cited on pages 9 and 23).
- [49] C. J. Wellard and L. C. L. Hollenberg. Donor electron wave functions for phosphorus in silicon: Beyond effective-mass theory. *Phys. Rev. B*, 72:085202, Aug 2005. (Cited on pages 9 and 10).
- [50] Mark Friesen. Theory of the stark effect for p donors in si. *Phys. Rev. Lett.*, 94:186403, May 2005. (Cited on page 9).
- [51] A. Debernardi, A. Baldereschi, and M. Fanciulli. Computation of the stark effect in p impurity states in silicon. *Phys. Rev. B*, 74:035202, Jul 2006. (Cited on page 9).
- [52] M. J. Calderón, A. Saraiva, Belita Koiller, and S. Das Sarma. Quantum control and manipulation of donor electrons in si-based quantum computing. *Journal of Applied Physics*, 105(12):122410, 2009. (Cited on pages 9 and 120).
- [53] G. D. J. Smit, S. Rogge, J. Caro, and T. M. Klapwijk. Gate-induced ionization of single dopant atoms. *Phys. Rev. B*, 68:193302, Nov 2003. (Cited on pages 9 and 10).
- [54] G. D. J. Smit, S. Rogge, J. Caro, and T. M. Klapwijk. Stark effect in shallow impurities in Si. *Phys. Rev. B*, 70:035206, Jul 2004. (Cited on pages 9 and 23).
- [55] A. S. Martins, R. B. Capaz, and Belita Koiller. Electric-field control and adiabatic evolution of shallow donor impurities in silicon. *Phys. Rev. B*, 69:085320, Feb 2004. (Cited on page 9).
- [56] A. S. Martins, Timothy B. Boykin, Gerhard Klimeck, and Belita Koiller. Conduction-band tight-binding description for si applied to p donors. *Phys. Rev. B*, 72:193204, Nov 2005. (Cited on page 9).

- [57] F. R. Bradbury, A. M. Tyryshkin, Guillaume Sabouret, Jeff Bokor, Thomas Schenkel, and S. A. Lyon. Stark tuning of donor electron spins in silicon. *Phys. Rev. Lett.*, 97:176404, Oct 2006. (Cited on page 9).
- [58] Rajib Rahman, Cameron J. Wellard, Forrest R. Bradbury, Marta Prada, Jared H. Cole, Gerhard Klimeck, and Lloyd C. L. Hollenberg. High precision quantum control of single donor spins in silicon. *Phys. Rev. Lett.*, 99:036403, Jul 2007. (Cited on page 9).
- [59] M. J. Calderón, Belita Koiller, and S. Das Sarma. Exchange coupling in semiconductor nanostructures: Validity and limitations of the heitler-london approach. *Phys. Rev. B*, 74:045310, Jul 2006. (Cited on page 10).
- [60] M. J. Calderón, Belita Koiller, and S. Das Sarma. External field control of donor electron exchange at the Si/SiO₂ interface. *Phys. Rev. B*, 75:125311, Mar 2007. (Cited on page 10).
- [61] M. J. Calderón, Belita Koiller, and S. Das Sarma. Model of valley interference effects on a donor electron close to a Si/SiO₂ interface. *Phys. Rev. B*, 77:155302, Apr 2008. (Cited on page 10).
- [62] Y. L. Hao, A. P. Djotyan, A. A. Avetisyan, and F. M. Peeters. Shallow donor states near a semiconductor-insulator-metal interface. *Phys. Rev. B*, 80:035329, Jul 2009. (Cited on page 10).
- [63] Rajib Rahman, G. P. Lansbergen, Seung H. Park, J. Verduijn, Gerhard Klimeck, S. Rogge, and Lloyd C. L. Hollenberg. Orbital stark effect and quantum confinement transition of donors in silicon. *Phys. Rev. B*, 80:165314, Oct 2009. (Cited on page 10).
- [64] Sokrates T. Pantelides. The electronic structure of impurities and other point defects in semiconductors. *Rev. Mod. Phys.*, 50:797–858, Oct 1978. (Cited on page 10).
- [65] R. A. Faulkner. Higher donor excited states for prolate-spheroid conduction bands: A reevaluation of silicon and germanium. *Phys. Rev.*, 184:713–721, Aug 1969. (Cited on page 10).
- [66] Angbo Fang, Yia-Chung Chang, and J. R. Tucker. Simulation of si:p spin-based quantum computer architecture. *Phys. Rev. B*, 72:075355, Aug 2005. (Cited on page 10).
- [67] A L Saraiva, A Baena, M J Calderón, and Belita Koiller. Theory of one and two donors in silicon. *Journal of Physics: Condensed Matter*, 27(15):154208, 2015. (Cited on pages 10, 15, 32, and 129).
- [68] A K Ramdas and S Rodriguez. Spectroscopy of the solid-state analogues of the hydrogen atom: donors and acceptors in semiconductors. *Reports on Progress in Physics*, 44(12):1297, 1981. (Cited on page 10).
- [69] Marco Fanciulli. *Electron spin resonance and related phenomena in low-dimensional structures*, volume 115. Springer Science & Business Media, 2009. (Cited on page 10).
- [70] Xuedong Hu, Belita Koiller, and S. Das Sarma. Charge qubits in semiconductor quantum computer architecture: Tunnel coupling and decoherence. *Phys. Rev. B*, 71:235332, Jun 2005. (Cited on page 10).

- [71] C. J. Wellard, L. C. L. Hollenberg, and S. Das Sarma. Theory of the microwave spectroscopy of a phosphorus-donor charge qubit in silicon: Coherent control in the Si : P quantum-computer architecture. *Phys. Rev. B*, 74:075306, Aug 2006. (Cited on page 10).
- [72] R. Rahman, G. P. Lansbergen, J. Verduijn, G. C. Tettamanzi, S. H. Park, N. Collaert, S. Biesemans, G. Klimeck, L. C. L. Hollenberg, and S. Rogge. Electric field reduced charging energies and two-electron bound excited states of single donors in silicon. *Phys. Rev. B*, 84:115428, Sep 2011. (Cited on page 10).
- [73] Angbo Fang, Y. C. Chang, and J. R. Tucker. Effects of j-gate potential and uniform electric field on a coupled donor pair in si for quantum computing. *Phys. Rev. B*, 66:155331, Oct 2002. (Cited on page 10).
- [74] Rajib Rahman, Seung H. Park, Timothy B. Boykin, Gerhard Klimeck, Sven Rogge, and Lloyd C. L. Hollenberg. Gate-induced g -factor control and dimensional transition for donors in multivalley semiconductors. *Phys. Rev. B*, 80:155301, Oct 2009. (Cited on page 10).
- [75] Austin G. Fowler, Cameron J. Wellard, and Lloyd C. L. Hollenberg. Error rate of the kane quantum computer controlled-not gate in the presence of dephasing. *Phys. Rev. A*, 67:012301, Jan 2003. (Cited on page 10).
- [76] Charles D. Hill and Hsi-Sheng Goan. Fast nonadiabatic two-qubit gates for the kane quantum computer. *Phys. Rev. A*, 68:012321, Jul 2003. (Cited on page 10).
- [77] A Kerridge, S Savory, A H Harker, and A M Stoneham. Time dependent quantum simulations of two-qubit gates based on donor states in silicon. *Journal of Physics: Condensed Matter*, 18(21):S767, 2006. (Cited on page 10).
- [78] D B Tsai and H S Goan. Gradient ascent pulse engineering approach to cnot gates in donor electron spin quantum computing. *AIP Conference Proceedings*, 1074(1):50–53, 2008. (Cited on page 10).
- [79] Dong-Bang Tsai, Po-Wen Chen, and Hsi-Sheng Goan. Optimal control of the silicon-based donor-electron-spin quantum computing. *Phys. Rev. A*, 79:060306, Jun 2009. (Cited on page 10).
- [80] C. J. Wellard, L. C. L. Hollenberg, F. Parisoli, L. M. Kettle, H.-S. Goan, J. A. L. McIntosh, and D. N. Jamieson. Electron exchange coupling for single-donor solid-state spin qubits. *Phys. Rev. B*, 68:195209, Nov 2003. (Cited on page 10).
- [81] Belita Koiller, Xuedong Hu, H. D. Drew, and S. Das Sarma. Disentangling the exchange coupling of entangled donors in the si quantum computer architecture. *Phys. Rev. Lett.*, 90:067401, Feb 2003. (Cited on page 10).
- [82] Belita Koiller, R. B. Capaz, Xuedong Hu, and S. Das Sarma. Shallow-donor wave functions and donor-pair exchange in silicon: Ab initio theory and floating-phase heitler-london approach. *Phys. Rev. B*, 70:115207, Sep 2004. (Cited on page 10).
- [83] B. Koiller and Xuedong Hu. Nanofabrication aspects of silicon-based spin quantum gates. *IEEE Transactions on Nanotechnology*, 4(1):113–115, Jan 2005. (Cited on page 10).

- [84] Belita Koiller, Xuedong Hu, and S. Das Sarma. Strain effects on silicon donor exchange: Quantum computer architecture considerations. *Phys. Rev. B*, 66:115201, Sep 2002. (Cited on pages 10 and 120).
- [85] M. J. Testolin, Andrew D. Greentree, C. J. Wellard, and L. C. L. Hollenberg. Optically induced spin-to-charge transduction in donor-spin readout. *Phys. Rev. B*, 72:195325, Nov 2005. (Cited on page 10).
- [86] Jared H Cole, Simon J Devitt, and Lloyd C L Hollenberg. Precision characterization of two-qubit hamiltonians via entanglement mapping. *Journal of Physics A: Mathematical and General*, 39(47):14649, 2006. (Cited on page 10).
- [87] Simon J. Devitt, Jared H. Cole, and Lloyd C. L. Hollenberg. Scheme for direct measurement of a general two-qubit hamiltonian. *Phys. Rev. A*, 73:052317, May 2006. (Cited on page 10).
- [88] Serguei Vorojtsov, Eduardo R. Mucciolo, and Harold U. Baranger. Spin qubits in multielectron quantum dots. *Phys. Rev. B*, 69:115329, Mar 2004. (Cited on page 10).
- [89] Xuedong Hu and S. Das Sarma. Charge-fluctuation-induced dephasing of exchange-coupled spin qubits. *Phys. Rev. Lett.*, 96:100501, Mar 2006. (Cited on page 10).
- [90] Rutger Vrijen, Eli Yablonovitch, Kang Wang, Hong Wen Jiang, Alex Balandin, Vwani Roychowdhury, Tal Mor, and David DiVincenzo. Electron-spin-resonance transistors for quantum computing in silicon-germanium heterostructures. *Phys. Rev. A*, 62:012306, Jun 2000. (Cited on page 10).
- [91] A A Larionov, L E Fedichkin, and K A Valiev. A silicon-based nuclear magnetic resonance (nmr) quantum computer using resonant transfer of a single electron for the inter-qubit interaction. *Nanotechnology*, 12(4):536, 2001. (Cited on page 10).
- [92] A. J. Skinner, M. E. Davenport, and B. E. Kane. Hydrogenic spin quantum computing in silicon: A digital approach. *Phys. Rev. Lett.*, 90:087901, Feb 2003. (Cited on page 10).
- [93] A M Stoneham, A J Fisher, and P T Greenland. Optically driven silicon-based quantum gates with potential for high-temperature operation. *Journal of Physics: Condensed Matter*, 15(27):L447, 2003. (Cited on page 10).
- [94] Rogerio de Sousa, J. D. Delgado, and S. Das Sarma. Silicon quantum computation based on magnetic dipolar coupling. *Phys. Rev. A*, 70:052304, Nov 2004. (Cited on pages 10 and 63).
- [95] L. C. L. Hollenberg, A. S. Dzurak, C. Wellard, A. R. Hamilton, D. J. Reilly, G. J. Milburn, and R. G. Clark. Charge-based quantum computing using single donors in semiconductors. *Phys. Rev. B*, 69:113301, Mar 2004. (Cited on page 10).
- [96] L. C. L. Hollenberg, A. D. Greentree, A. G. Fowler, and C. J. Wellard. Two-dimensional architectures for donor-based quantum computing. *Phys. Rev. B*, 74:045311, Jul 2006. (Cited on page 10).
- [97] T. Schenkel, A. Persaud, S. J. Park, J. Nilsson, J. Bokor, J. A. Liddle, R. Keller, D. H. Schneider, D. W. Cheng, and D. E. Humphries. Solid state quantum computer development in silicon with single ion implantation. *Journal of Applied Physics*, 94(11):7017–7024, 2003. (Cited on page 10).

- [98] D. N. Jamieson, C. Yang, T. Hopf, S. M. Hearne, C. I. Pakes, S. Prawer, M. Mitic, E. Gauja, S. E. Andresen, F. E. Hudson, A. S. Dzurak, and R. G. Clark. Controlled shallow single-ion implantation in silicon using an active substrate for sub-20-Å keV ions. *Applied Physics Letters*, 86(20):202101, 2005. (Cited on page 10).
- [99] A. Batra, C. D. Weis, J. Reijonen, A. Persaud, T. Schenkel, S. Cabrini, C. C. Lo, and J. Bokor. Detection of low energy single ion impacts in micron scale transistors at room temperature. *Applied Physics Letters*, 91(19):193502, 2007. (Cited on page 10).
- [100] J. A. Seamons, E. Bielejec, M. S. Carroll, and K. D. Childs. Room temperature single ion detection with geiger mode avalanche diode detectors. *Applied Physics Letters*, 93(4):043124, 2008. (Cited on page 10).
- [101] T Shinada, T Kurosawa, H Nakayama, Y Zhu, M Hori, and I Ohdomari. A reliable method for the counting and control of single ions for single-dopant controlled devices. *Nanotechnology*, 19(34):345202, 2008. (Cited on page 10).
- [102] C. D. Weis, A. Schuh, A. Batra, A. Persaud, I. W. Rangelow, J. Bokor, C. C. Lo, S. Cabrini, E. Sideras-Haddad, G. D. Fuchs, R. Hanson, D. D. Awschalom, and T. Schenkel. Single atom doping for quantum device development in diamond and silicon. *Journal of Vacuum Science & Technology B: Microelectronics and Nanometer Structures Processing, Measurement, and Phenomena*, 26(6):2596–2600, 2008. (Cited on page 10).
- [103] E Bielejec, J A Seamons, and M S Carroll. Single ion implantation for single donor devices using geiger mode detectors. *Nanotechnology*, 21(8):085201, 2010. (Cited on page 10).
- [104] Guilherme Tosi, Fahd A. Mohiyaddin, Vivien Schmitt, Stefanie Tenberg, Rajib Rahman, Gerhard Klimeck, and Andrea Morello. Silicon quantum processor with robust long-distance qubit couplings. *Nature Communications*, 8(1):450, 2017. (Cited on pages 10, 11, 63, and 120).
- [105] S.-J. Park, A. Persaud, J.A. Liddle, J. Nilsson, J. Bokor, D.H. Schneider, I.W. Rangelow, and T. Schenkel. Processing issues in top-down approaches to quantum computer development in silicon. *Microelectronic Engineering*, 73:695 – 700, 2004. *Micro and Nano Engineering 2003*. (Cited on page 10).
- [106] B. C. Johnson, G. C. Tettamanzi, A. D. C. Alves, S. Thompson, C. Yang, J. Verduijn, J. A. Mol, R. Wacquez, M. Vinet, M. Sanquer, S. Rogge, and D. N. Jamieson. Drain current modulation in a nanoscale field-effect-transistor channel by single dopant implantation. *Applied Physics Letters*, 96(26):264102, 2010. (Cited on page 10).
- [107] Enrico Prati, Marco De Michielis, Matteo Belli, Simone Cocco, Marco Fanciulli, Dharmraj Kotekar-Patil, Matthias Ruoff, Dieter P Kern, David A Wharam, Jan Verduijn, Giuseppe C Tettamanzi, Sven Rogge, Benoit Roche, Romain Wacquez, Xavier Jehl, Maud Vinet, and Marc Sanquer. Few electron limit of n-type metal oxide semiconductor single electron transistors. *Nanotechnology*, 23(21):215204, 2012. (Cited on page 10).
- [108] Jessica van Donkelaar, C Yang, A D C Alves, J C McCallum, C Hougaard, B C Johnson, F E Hudson, A S Dzurak, A Morello, D Spemann, and D N Jamieson. Single atom devices by ion implantation. *Journal of Physics: Condensed Matter*, 27(15):154204, 2015. (Cited on page 10).

- [109] J. L. O'Brien, S. R. Schofield, M. Y. Simmons, R. G. Clark, A. S. Dzurak, N. J. Curson, B. E. Kane, N. S. McAlpine, M. E. Hawley, and G. W. Brown. Towards the fabrication of phosphorus qubits for a silicon quantum computer. *Phys. Rev. B*, 64:161401, Sep 2001. (Cited on page 10).
- [110] S. R. Schofield, N. J. Curson, M. Y. Simmons, F. J. Rueß, T. Hallam, L. Oberbeck, and R. G. Clark. Atomically precise placement of single dopants in si. *Phys. Rev. Lett.*, 91:136104, Sep 2003. (Cited on page 10).
- [111] Frank J. Ruess, Lars Oberbeck, Michelle Y. Simmons, Kuan Eng J. Goh, Alex R. Hamilton, Toby Hallam, Steven R. Schofield, Neil J. Curson, and Robert G. Clark. Toward atomic-scale device fabrication in silicon using scanning probe microscopy. *Nano Letters*, 4(10):1969–1973, 2004. (Cited on page 10).
- [112] M.Y. Simmons, F.J. Ruess, K.E.J. Goh, T. Hallam, S.R. Schofield, L. Oberbeck, N.J. Curson, A.R. Hamilton, M.J. Butcher, R.G. Clark, and T.C.G. Reusch. Scanning probe microscopy for silicon device fabrication. *Molecular Simulation*, 31(6-7):505–515, 2005. (Cited on page 10).
- [113] F. Ruess, W. Pok, T. C. Reusch, M. J. Butcher, K. J. Goh, L. Oberbeck, G. Scappucci, A. R. Hamilton, and M. Y. Simmons. Realization of atomically controlled dopant devices in silicon. *Small*, 3(4):563–567, 2007. (Cited on page 10).
- [114] Jason R. Petta. Atom-by-atom construction of a quantum device. *ACS Nano*, 11(3):2382–2386, 2017. PMID: 28281744. (Cited on page 11).
- [115] A. Morello, C. C. Escott, H. Huebl, L. H. Willems van Beveren, L. C. L. Hollenberg, D. N. Jamieson, A. S. Dzurak, and R. G. Clark. Architecture for high-sensitivity single-shot readout and control of the electron spin of individual donors in silicon. *Phys. Rev. B*, 80:081307, Aug 2009. (Cited on page 11).
- [116] JJ Pla, KY Tan, JP Dehollain, WH Lim, JJ Morton, DN Jamieson, AS Dzurak, and A Morello. A single-atom electron spin qubit in silicon. *Nature*, 489(7417):541–545, 2012. (Cited on pages 11 and 120).
- [117] JJ Pla, KY Tan, JP Dehollain, WH Lim, JJL Morton, FA Zwanenburg, DN Jamieson, AS Dzurak, and A Morello. High-fidelity readout and control of a nuclear spin qubit in silicon. *NATURE*, 496(7445):334–338, 2013. (Cited on page 11).
- [118] Arne Laucht, Juha T Muhonen, Fahd A Mohiyaddin, Rachpon Kalra, Juan P Dehollain, Solomon Freer, Fay E Hudson, Menno Veldhorst, Rajib Rahman, Gerhard Klimeck, et al. Electrically controlling single-spin qubits in a continuous microwave field. *Science advances*, 1(3):e1500022, 2015. (Cited on page 11).
- [119] J T Muhonen, A Laucht, S Simmons, J P Dehollain, R Kalra, F E Hudson, S Freer, K M Itoh, D N Jamieson, J C McCallum, A S Dzurak, and A Morello. Quantifying the quantum gate fidelity of single-atom spin qubits in silicon by randomized benchmarking. *Journal of Physics: Condensed Matter*, 27(15):154205, 2015. (Cited on page 11).
- [120] Matias Urdampilleta, Anasua Chatterjee, Cheuk Chi Lo, Takashi Kobayashi, John Mansir, Sylvain Barraud, Andreas C. Betz, Sven Rogge, M. Fernando Gonzalez-Zalba, and John J. L. Morton. Charge dynamics and spin blockade in a hybrid double quantum dot in silicon. *Phys. Rev. X*, 5:031024, Aug 2015. (Cited on pages 11, 13, 14, and 105).

- [121] M. Rudolph, P. Harvey-Collard, R. Jock, T. Jacobson, J. Wendt, T. Pluym, J. Domínguez, G. Ten-Eyck, R. Manginell, M. P. Lilly, and M. S. Carroll. Coupling mos quantum dot and phosphorous donor qubit systems. In *2016 IEEE International Electron Devices Meeting (IEDM)*, pages 34.1.1–34.1.4, Dec 2016. (Cited on page 11).
- [122] Guilherme Tosi, Fahd A. Mohiyaddin, Hans Huebl, and Andrea Morello. Circuit-quantum electrodynamics with direct magnetic coupling to single-atom spin qubits in isotopically enriched ^{28}Si . *AIP Advances*, 4(8):087122, 2014. (Cited on page 11).
- [123] Arne Laucht, Rachpon Kalra, Stephanie Simmons, Juan P Dehollain, Juha T Muhonen, Fahd A Mohiyaddin, Solomon Freer, Fay E Hudson, Kohei M Itoh, David N Jamieson, et al. A dressed spin qubit in silicon. *Nature Nanotechnology*, 2016. (Cited on page 11).
- [124] Brage Golding and MI Dykman. Acceptor-based silicon quantum computing. *arXiv preprint cond-mat/0309147*, 2003. (Cited on pages 11, 22, and 41).
- [125] Joe Salfi, Jan A. Mol, Dimitrie Culcer, and Sven Rogge. Charge-insensitive single-atom spin-orbit qubit in silicon. *Phys. Rev. Lett.*, 116:246801, Jun 2016. (Cited on pages 11, 22, 23, 26, 35, 37, 38, 40, 41, 48, 49, 56, 57, 60, 63, 64, 65, 68, 74, 76, 77, 81, 83, 84, 85, 86, 87, 88, 89, 90, 91, 92, 93, 94, 95, 96, 97, 98, 99, 100, 101, 102, 103, 104, 105, 106, 107, 108, 109, 110, 111, 112, 113, 114, 115, 116, 117, 118, 119, 120, 121, 122, 123, 124, 125, 126, 127, 128, 129, 130, 131, 132, 133, 134, 135, 136, 137, 138, 139, 140, 141, 142, 143, 144, 145, 146, 147, 148, 149, 150, 151, 152, 153, 154, 155, 156, 157, 158, 159, 160, 161, 162, 163, 164, 165, 166, 167, 168, 169, 170, 171, 172, 173, 174, 175, 176, 177, 178, 179, 180, 181, 182, 183, 184, 185, 186, 187, 188, 189, 190, 191, 192, 193, 194, 195, 196, 197, 198, 199, 200, 201, 202, 203, 204, 205, 206, 207, 208, 209, 210, 211, 212, 213, 214, 215, 216, 217, 218, 219, 220, 221, 222, 223, 224, 225, 226, 227, 228, 229, 230, 231, 232, 233, 234, 235, 236, 237, 238, 239, 240, 241, 242, 243, 244, 245, 246, 247, 248, 249, 250, 251, 252, 253, 254, 255, 256, 257, 258, 259, 260, 261, 262, 263, 264, 265, 266, 267, 268, 269, 270, 271, 272, 273, 274, 275, 276, 277, 278, 279, 280, 281, 282, 283, 284, 285, 286, 287, 288, 289, 290, 291, 292, 293, 294, 295, 296, 297, 298, 299, 300, 301, 302, 303, 304, 305, 306, 307, 308, 309, 310, 311, 312, 313, 314, 315, 316, 317, 318, 319, 320, 321, 322, 323, 324, 325, 326, 327, 328, 329, 330, 331, 332, 333, 334, 335, 336, 337, 338, 339, 340, 341, 342, 343, 344, 345, 346, 347, 348, 349, 350, 351, 352, 353, 354, 355, 356, 357, 358, 359, 360, 361, 362, 363, 364, 365, 366, 367, 368, 369, 370, 371, 372, 373, 374, 375, 376, 377, 378, 379, 380, 381, 382, 383, 384, 385, 386, 387, 388, 389, 390, 391, 392, 393, 394, 395, 396, 397, 398, 399, 400, 401, 402, 403, 404, 405, 406, 407, 408, 409, 410, 411, 412, 413, 414, 415, 416, 417, 418, 419, 420, 421, 422, 423, 424, 425, 426, 427, 428, 429, 430, 431, 432, 433, 434, 435, 436, 437, 438, 439, 440, 441, 442, 443, 444, 445, 446, 447, 448, 449, 450, 451, 452, 453, 454, 455, 456, 457, 458, 459, 460, 461, 462, 463, 464, 465, 466, 467, 468, 469, 470, 471, 472, 473, 474, 475, 476, 477, 478, 479, 480, 481, 482, 483, 484, 485, 486, 487, 488, 489, 490, 491, 492, 493, 494, 495, 496, 497, 498, 499, 500, 501, 502, 503, 504, 505, 506, 507, 508, 509, 510, 511, 512, 513, 514, 515, 516, 517, 518, 519, 520, 521, 522, 523, 524, 525, 526, 527, 528, 529, 530, 531, 532, 533, 534, 535, 536, 537, 538, 539, 540, 541, 542, 543, 544, 545, 546, 547, 548, 549, 550, 551, 552, 553, 554, 555, 556, 557, 558, 559, 560, 561, 562, 563, 564, 565, 566, 567, 568, 569, 570, 571, 572, 573, 574, 575, 576, 577, 578, 579, 580, 581, 582, 583, 584, 585, 586, 587, 588, 589, 590, 591, 592, 593, 594, 595, 596, 597, 598, 599, 600, 601, 602, 603, 604, 605, 606, 607, 608, 609, 610, 611, 612, 613, 614, 615, 616, 617, 618, 619, 620, 621, 622, 623, 624, 625, 626, 627, 628, 629, 630, 631, 632, 633, 634, 635, 636, 637, 638, 639, 640, 641, 642, 643, 644, 645, 646, 647, 648, 649, 650, 651, 652, 653, 654, 655, 656, 657, 658, 659, 660, 661, 662, 663, 664, 665, 666, 667, 668, 669, 670, 671, 672, 673, 674, 675, 676, 677, 678, 679, 680, 681, 682, 683, 684, 685, 686, 687, 688, 689, 690, 691, 692, 693, 694, 695, 696, 697, 698, 699, 700, 701, 702, 703, 704, 705, 706, 707, 708, 709, 710, 711, 712, 713, 714, 715, 716, 717, 718, 719, 720, 721, 722, 723, 724, 725, 726, 727, 728, 729, 730, 731, 732, 733, 734, 735, 736, 737, 738, 739, 740, 741, 742, 743, 744, 745, 746, 747, 748, 749, 750, 751, 752, 753, 754, 755, 756, 757, 758, 759, 760, 761, 762, 763, 764, 765, 766, 767, 768, 769, 770, 771, 772, 773, 774, 775, 776, 777, 778, 779, 780, 781, 782, 783, 784, 785, 786, 787, 788, 789, 790, 791, 792, 793, 794, 795, 796, 797, 798, 799, 800, 801, 802, 803, 804, 805, 806, 807, 808, 809, 810, 811, 812, 813, 814, 815, 816, 817, 818, 819, 820, 821, 822, 823, 824, 825, 826, 827, 828, 829, 830, 831, 832, 833, 834, 835, 836, 837, 838, 839, 840, 841, 842, 843, 844, 845, 846, 847, 848, 849, 850, 851, 852, 853, 854, 855, 856, 857, 858, 859, 860, 861, 862, 863, 864, 865, 866, 867, 868, 869, 870, 871, 872, 873, 874, 875, 876, 877, 878, 879, 880, 881, 882, 883, 884, 885, 886, 887, 888, 889, 890, 891, 892, 893, 894, 895, 896, 897, 898, 899, 900, 901, 902, 903, 904, 905, 906, 907, 908, 909, 910, 911, 912, 913, 914, 915, 916, 917, 918, 919, 920, 921, 922, 923, 924, 925, 926, 927, 928, 929, 930, 931, 932, 933, 934, 935, 936, 937, 938, 939, 940, 941, 942, 943, 944, 945, 946, 947, 948, 949, 950, 951, 952, 953, 954, 955, 956, 957, 958, 959, 960, 961, 962, 963, 964, 965, 966, 967, 968, 969, 970, 971, 972, 973, 974, 975, 976, 977, 978, 979, 980, 981, 982, 983, 984, 985, 986, 987, 988, 989, 990, 991, 992, 993, 994, 995, 996, 997, 998, 999, 1000).
- [126] Joe Salfi, Mengyang Tong, Sven Rogge, and Dimitrie Culcer. Quantum computing with acceptor spins in silicon. *Nanotechnology*, 27(24):244001, 2016. (Cited on pages 11, 22, 26, 37, 38, 39, 41, 48, 49, 57, 59, and 86).
- [127] G. Katsaros, P. Spathis, M. Stoffel, F. Fournel, M. Mongillo, V. Bouchiat, F. Lefloch, A. Rastelli, O. G. Schmidt, and S. De Franceschi. Hybrid superconductor-semiconductor devices made from self-assembled sige nanocrystals on silicon. *Nat Nano*, 5(6):458–464, 06 2010. (Cited on pages 11 and 49).
- [128] Hannes Watzinger, Christoph Kloeffel, Lada Vukusic, Marta D. Rossell, Violetta Sessi, Josip Kukucka, Raimund Kirchschrager, Elisabeth Lausecker, Alisha Truhlar, Martin Glaser, Armando Rastelli, Andreas Fuhrer, Daniel Loss, and Georgios Katsaros. Heavy-hole states in germanium hut wires. *Nano Letters*, 16(11):6879–6885, 2016. (Cited on pages 11 and 49).
- [129] A. V. Nenashev, A. V. Dvurechenskii, and A. F. Zinovieva. Wave functions and g factor of holes in Ge/Si quantum dots. *Phys. Rev. B*, 67:205301, May 2003. (Cited on pages 11 and 49).
- [130] H. Malissa, W. Jantsch, M. Muhlberger, F. Schaffler, Z. Wilamowski, M. Draxler, and P. Bauer. Anisotropy of g -factor and electron spin resonance linewidth in modulation doped SiGe quantum wells. *Applied Physics Letters*, 85(10):1739–1741, 2004. (Cited on pages 11, 31, and 49).
- [131] N. Ares, V. N. Golovach, G. Katsaros, M. Stoffel, F. Fournel, L. I. Glazman, O. G. Schmidt, and S. De Franceschi. Nature of tunable hole g factors in quantum dots. *Phys. Rev. Lett.*, 110:046602, Jan 2013. (Cited on pages 11 and 49).
- [132] A. Srinivasan, K. L. Hudson, D. Miserev, L. A. Yeoh, O. Klochan, K. Muraki, Y. Hiramaya, O. P. Sushkov, and A. R. Hamilton. Electrical control of the sign of the g factor in a gaas hole quantum point contact. *Phys. Rev. B*, 94:041406, Jul 2016. (Cited on page 11).

- [133] S. J. Prado, C. Trallero-Giner, A. M. Alcalde, V. López-Richard, and G. E. Marques. Influence of quantum dot shape on the landé g -factor determination. *Phys. Rev. B*, 69:201310, May 2004. (Cited on page 11).
- [134] M. Kugler, T. Andlauer, T. Korn, A. Wagner, S. Fehringer, R. Schulz, M. Kubová, C. Gerl, D. Schuh, W. Wegscheider, P. Vogl, and C. Schüller. Gate control of low-temperature spin dynamics in two-dimensional hole systems. *Phys. Rev. B*, 80:035325, Jul 2009. (Cited on page 11).
- [135] Till Andlauer and Peter Vogl. Electrically controllable g tensors in quantum dot molecules. *Phys. Rev. B*, 79:045307, Jan 2009. (Cited on page 11).
- [136] Anthony J. Bennett, Matthew A. Pooley, Yameng Cao, Niklas Sköld, Ian Farrer, David A. Ritchie, and Andrew J. Shields. Voltage tunability of single-spin states in a quantum dot. *Nature Communications*, 4:1522, 02 2013. (Cited on page 11).
- [137] Joost Van der Heijden, Joe Salfi, Jan A. Mol, Jan Verduijn, Giuseppe C. Tettamanzi, Alex R. Hamilton, Nadine Collaert, and Sven Rogge. Probing the spin states of a single acceptor atom. *Nano Letters*, 14(3):1492–1496, 2014. (Cited on page 11).
- [138] L. E. Calvet, R. G. Wheeler, and M. A. Reed. Observation of the linear stark effect in a single acceptor in si. *Phys. Rev. Lett.*, 98:096805, Mar 2007. (Cited on pages 11 and 23).
- [139] L. E. Calvet, R. G. Wheeler, and M. A. Reed. Effect of local strain on single acceptors in si. *Phys. Rev. B*, 76:035319, Jul 2007. (Cited on pages 11 and 23).
- [140] J. A. Mol, J. Salfi, R. Rahman, Y. Hsueh, J. A. Miwa, G. Klimeck, M. Y. Simmons, and S. Rogge. Interface-induced heavy-hole/light-hole splitting of acceptors in silicon. *Applied Physics Letters*, 106(20):203110, 2015. (Cited on pages 11, 24, 33, 34, 35, 47, and 48).
- [141] J. Salfi, J. A. Mol, R. Rahman, G. Klimeck, M. Y. Simmons, L. C. L. Hollenberg, and S. Rogge. Quantum simulation of the hubbard model with dopant atoms in silicon. 7:11342 EP –, 04 2016. (Cited on page 11).
- [142] J. van der Heijden, T. Kobayashi, M.G. House, J. Salfi, S. Barraud, R. Lavieville, M.Y. Simmons, and S. Rogge. Spin-orbit dynamics of single acceptor atoms in silicon. *arXiv:1703.03538 [cond-mat.mes-hall]*, 2017. (Cited on page 11).
- [143] Hendrik Bluhm, Sandra Foletti, Izhar Neder, Mark Rudner, Diana Mahalu, Vladimir Umansky, and Amir Yacoby. Dephasing time of gaas electron-spin qubits coupled to a nuclear bath exceeding 200[thinsp][mu]s. *Nat Phys*, 7(2):109–113, 02 2011. (Cited on page 12).
- [144] Tim Botzem, Robert P. G. McNeil, Jan-Michael Mol, Dieter Schuh, Dominique Bougeard, and Hendrik Bluhm. Quadrupolar and anisotropy effects on dephasing in two-electron spin qubits in gaas. 7:11170 EP –, 04 2016. (Cited on page 12).
- [145] Filip K. Malinowski, Frederico Martins, Peter D. Nissen, Edwin Barnes, CywińskiŁukasz, Mark S. Rudner, Saeed Fallahi, Geoffrey C. Gardner, Michael J. Manfra, Charles M. Marcus, and Ferdinand Kuemmeth. Notch filtering the nuclear environment of a spin qubit. *Nat Nano*, 12(1):16–20, 01 2017. (Cited on page 12).

- [146] F. Simmel, David Abusch-Magder, D. A. Wharam, M. A. Kastner, and J. P. Kotthaus. Statistics of the coulomb-blockade peak spacings of a silicon quantum dot. *Phys. Rev. B*, 59:R10441–R10444, Apr 1999. (Cited on page 12).
- [147] C. B. Simmons, Madhu Thalakulam, Nakul Shaji, Levente J. Klein, Hua Qin, R. H. Blick, D. E. Savage, M. G. Lagally, S. N. Coppersmith, and M. A. Eriksson. Single-electron quantum dot in Si, δ SiGe with integrated charge sensing. *Applied Physics Letters*, 91(21):213103, 2007. (Cited on pages 12 and 89).
- [148] F. A. Zwanenburg, A. A. van Loon, G. A. Steele, C. E. W. M. van Rijmenam, T. Balder, Y. Fang, C. M. Lieber, and L. P. Kouwenhoven. Ultrasmall silicon quantum dots. *Journal of Applied Physics*, 105(12):124314, 2009. (Cited on page 12).
- [149] Floris A. Zwanenburg, Cathalijn E. W. M. van Rijmenam, Ying Fang, Charles M. Lieber, and Leo P. Kouwenhoven. Spin states of the first four holes in a silicon nanowire quantum dot. *Nano Letters*, 9(3):1071–1079, 2009. PMID: 19226128. (Cited on page 12).
- [150] Friedrich Schäffler. High-mobility Si and Ge structures. *Semiconductor Science and Technology*, 12(12):1515, 1997. (Cited on page 12).
- [151] Timothy B. Boykin, Gerhard Klimeck, M. A. Eriksson, Mark Friesen, S. N. Coppersmith, Paul von Allmen, Fabiano Oyafuso, and Seungwon Lee. Valley splitting in strained silicon quantum wells. *Applied Physics Letters*, 84(1):115–117, 2004. (Cited on pages 12, 17, and 92).
- [152] Timothy B. Boykin, Gerhard Klimeck, Mark Friesen, S. N. Coppersmith, Paul von Allmen, Fabiano Oyafuso, and Seungwon Lee. Valley splitting in low-density quantum-confined heterostructures studied using tight-binding models. *Phys. Rev. B*, 70:165325, Oct 2004. (Cited on pages 12, 92, and 113).
- [153] Timothy B. Boykin, Neerav Kharche, and Gerhard Klimeck. Valley splitting in finite barrier quantum wells. *Phys. Rev. B*, 77:245320, Jun 2008. (Cited on page 12).
- [154] Mark Friesen, Sucismita Chutia, Charles Tahan, and S. N. Coppersmith. Valley splitting theory of SiGe/Si/SiGe quantum wells. *Phys. Rev. B*, 75:115318, Mar 2007. (Cited on pages 12 and 15).
- [155] Dimitrie Culcer, Łukasz Cywiński, Qiuzi Li, Xuedong Hu, and S. Das Sarma. Quantum dot spin qubits in silicon: Multivalley physics. *Phys. Rev. B*, 82:155312, Oct 2010. (Cited on pages 12 and 89).
- [156] A. L. Saraiva, M. J. Calderón, Rodrigo B. Capaz, Xuedong Hu, S. Das Sarma, and Belita Koiller. Intervalley coupling for interface-bound electrons in silicon: An effective mass study. *Phys. Rev. B*, 84:155320, Oct 2011. (Cited on pages 12, 17, 112, and 113).
- [157] John King Gamble, Mark Friesen, S. N. Coppersmith, and Xuedong Hu. Two-electron dephasing in single si and gaas quantum dots. *Phys. Rev. B*, 86:035302, Jul 2012. (Cited on pages 12 and 17).
- [158] Neil M. Zimmerman, Peihao Huang, and Dimitrie Culcer. Valley phase and voltage control of coherent manipulation in si quantum dots. *Nano Letters*, 17(7):4461–4465, 2017. PMID: 28657758. (Cited on page 12).

- [159] Mark Friesen and S. N. Coppersmith. Theory of valley-orbit coupling in a Si/SiGe quantum dot. *Phys. Rev. B*, 81:115324, Mar 2010. (Cited on pages 12, 13, 16, 89, and 92).
- [160] Charles Tahan, Mark Friesen, and Robert Joynt. Decoherence of electron spin qubits in si-based quantum computers. *Phys. Rev. B*, 66:035314, Jul 2002. (Cited on page 12).
- [161] Charles Tahan and Robert Joynt. Rashba spin-orbit coupling and spin relaxation in silicon quantum wells. *Phys. Rev. B*, 71:075315, Feb 2005. (Cited on page 12).
- [162] Qiuzi Li, Łukasz Cywiński, Dimitrie Culcer, Xuedong Hu, and S. Das Sarma. Exchange coupling in silicon quantum dots: Theoretical considerations for quantum computation. *Phys. Rev. B*, 81:085313, Feb 2010. (Cited on page 12).
- [163] Rifat Ferdous, Erika Kawakami, Pasquale Scarlino, Michał P Nowak, DR Ward, DE Savage, MG Lagally, SN Coppersmith, Mark Friesen, Mark A Eriksson, et al. Valley dependent anisotropic spin splitting in silicon quantum dots. *arXiv preprint arXiv:1702.06210*, 2017. (Cited on page 12).
- [164] Yue Wu and Dimitrie Culcer. Coherent electrical rotations of valley states in si quantum dots using the phase of the valley-orbit coupling. *Phys. Rev. B*, 86:035321, Jul 2012. (Cited on pages 12 and 89).
- [165] Zhan Shi, C. B. Simmons, J. R. Prance, John King Gamble, Teck Seng Koh, Yun-Pil Shim, Xuedong Hu, D. E. Savage, M. G. Lagally, M. A. Eriksson, Mark Friesen, and S. N. Coppersmith. Fast hybrid silicon double-quantum-dot qubit. *Phys. Rev. Lett.*, 108:140503, Apr 2012. (Cited on pages 12, 13, 89, and 120).
- [166] E. P. Nordberg, H. L. Stalford, R. Young, G. A. Ten Eyck, K. Eng, L. A. Tracy, K. D. Childs, J. R. Wendt, R. K. Grubbs, J. Stevens, M. P. Lilly, M. A. Eriksson, and M. S. Carroll. Charge sensing in enhancement mode double-top-gated metal-oxide-semiconductor quantum dots. *Applied Physics Letters*, 95(20):202102, 2009. (Cited on page 12).
- [167] Robert R Hayes, Andrey A Kiselev, Matthew G Borselli, Steven S Bui, Edward T Croke III, Peter W Deelman, Brett M Maune, Ivan Milosavljevic, Jeong-Sun Moon, Richard S Ross, et al. Lifetime measurements (t_1) of electron spins in Si/SiGe quantum dots. *arXiv preprint arXiv:0908.0173*, 2009. (Cited on page 12).
- [168] C. B. Simmons, J. R. Prance, B. J. Van Bael, Teck Seng Koh, Zhan Shi, D. E. Savage, M. G. Lagally, R. Joynt, Mark Friesen, S. N. Coppersmith, and M. A. Eriksson. Tunable spin loading and T_1 of a silicon spin qubit measured by single-shot readout. *Phys. Rev. Lett.*, 106:156804, Apr 2011. (Cited on page 12).
- [169] C. H. Yang, W. H. Lim, F. A. Zwanenburg, and A. S. Dzurak. Dynamically controlled charge sensing of a few-electron silicon quantum dot. *AIP Advances*, 1(4):042111, 2011. (Cited on page 12).
- [170] J. Gorman, D. G. Hasko, and D. A. Williams. Charge-qubit operation of an isolated double quantum dot. *Phys. Rev. Lett.*, 95:090502, Aug 2005. (Cited on pages 12 and 89).
- [171] Akira Fujiwara, Hiroshi Inokawa, Kenji Yamazaki, Hideo Namatsu, Yasuo Takahashi, Neil M. Zimmerman, and Stuart B. Martin. Single electron tunneling transistor with tunable barriers using silicon nanowire metal-oxide-semiconductor field-effect transistor. *Applied Physics Letters*, 88(5):053121, 2006. (Cited on page 12).

- [172] Mark Friesen, Joydip Ghosh, MA Eriksson, and SN Coppersmith. A decoherence-free subspace in a charge quadrupole qubit. *Nature Communications*, 8, 2017. (Cited on page 12).
- [173] C. B. Simmons, Madhu Thalakulam, B. M. Rosemeyer, B. J. Van Bael, E. K. Sackmann, D. E. Savage, M. G. Lagally, R. Joynt, Mark Friesen, S. N. Coppersmith, and M. A. Eriksson. Charge sensing and controllable tunnel coupling in a Si/SiGe double quantum dot. *Nano Letters*, 9(9):3234–3238, 2009. PMID: 19645459. (Cited on page 12).
- [174] Madhu Thalakulam, C. B. Simmons, B. M. Rosemeyer, D. E. Savage, M. G. Lagally, Mark Friesen, S. N. Coppersmith, and M. A. Eriksson. Fast tunnel rates in Si/SiGe one-electron single and double quantum dots. *Applied Physics Letters*, 96(18):183104, 2010. (Cited on page 12).
- [175] A. Wild, J. Kierig, J. Sailer, J. W. Ager III, E. E. Haller, G. Abstreiter, S. Ludwig, and D. Bougeard. Few electron double quantum dot in an isotopically purified ^{28}Si quantum well. *Applied Physics Letters*, 100(14):143110, 2012. (Cited on page 12).
- [176] H. W. Liu, T. Fujisawa, Y. Ono, H. Inokawa, A. Fujiwara, K. Takashina, and Y. Hirayama. Pauli-spin-blockade transport through a silicon double quantum dot. *Phys. Rev. B*, 77:073310, Feb 2008. (Cited on pages 12 and 89).
- [177] C. B. Simmons, Teck Seng Koh, Nakul Shaji, Madhu Thalakulam, L. J. Klein, Hua Qin, H. Luo, D. E. Savage, M. G. Lagally, A. J. Rimberg, Robert Joynt, Robert Blick, Mark Friesen, S. N. Coppersmith, and M. A. Eriksson. Pauli spin blockade and lifetime-enhanced transport in a Si/SiGe double quantum dot. *Phys. Rev. B*, 82:245312, Dec 2010. (Cited on pages 12 and 89).
- [178] NS Lai, WH Lim, CH Yang, FA Zwanenburg, WA Coish, F Qassemi, A Morello, and AS Dzurak. Pauli spin blockade in a highly tunable silicon double quantum dot. *Scientific reports*, 1:110, 2011. (Cited on pages 12 and 89).
- [179] AC Betz, R Wacquez, M Vinet, X Jehl, AL Saraiva, M Sanquer, AJ Ferguson, and MF Gonzalez-Zalba. Dispersively detected pauli spin-blockade in a silicon nanowire field-effect transistor. *Nano letters*, 15(7):4622–4627, 2015. (Cited on pages 12, 13, 14, 89, 104, 105, 106, 113, and 116).
- [180] DJ Reilly, CM Marcus, MP Hanson, and AC Gossard. Fast single-charge sensing with a rf quantum point contact. *Applied Physics Letters*, 91(16):162101, 2007. (Cited on page 13).
- [181] Benoit Voisin, Viet-Hung Nguyen, Julien Renard, Xavier Jehl, Sylvain Barraud, Francois Triozon, Maud Vinet, Ivan Duchemin, Yann-Michel Niquet, Silvano de Franceschi, and Marc Sanquer. Few-electron edge-state quantum dots in a silicon nanowire field-effect transistor. *Nano Letters*, 14(4):2094–2098, 2014. PMID: 24611581. (Cited on pages 13, 14, 104, 105, 106, 107, 112, 113, and 116).
- [182] Roland Winkler. *Spin-orbit coupling effects in two-dimensional electron and hole systems*. Springer tracts in modern physics. Springer, Berlin, 2003. (Cited on pages 13, 17, 22, 141, and 142).
- [183] Gustav Bihlmayer, O Rader, and R Winkler. Focus on the rashba effect. *New journal of physics*, 17(5):050202, 2015. (Cited on page 13).

- [184] M. F. Gonzalez-Zalba, S. Barraud, A. J. Ferguson, and A. C. Betz. Probing the limits of gate-based charge sensing. *Nature Communications*, 6:6084 EP –, 01 2015. (Cited on pages 14, 104, and 105).
- [185] Sucismita Chutia, S. N. Coppersmith, and Mark Friesen. Multiscale theory of valley splitting in the conduction band of a quantum well. *Phys. Rev. B*, 77:193311, May 2008. (Cited on page 16).
- [186] A. L. Saraiva, M. J. Calderón, Xuedong Hu, S. Das Sarma, and Belita Koiller. Physical mechanisms of interface-mediated intervalley coupling in Si. *Phys. Rev. B*, 80:081305, Aug 2009. (Cited on pages 16 and 92).
- [187] Mark Friesen, M. A. Eriksson, and S. N. Coppersmith. Magnetic field dependence of valley splitting in realistic Si/SiGe quantum wells. *Applied Physics Letters*, 89(20):202106, 2006. (Cited on pages 16 and 89).
- [188] Peter Y Yu and Manuel Cardona. *Fundamentals of semiconductors: physics and materials properties*. Springer, 2010. (Cited on page 17).
- [189] J C Abadillo-Uriel and M J Calderón. Interface effects on acceptor qubits in silicon and germanium. *Nanotechnology*, 27(2):024003, 2016. (Cited on pages 22 and 60).
- [190] J C Abadillo-Uriel and M J Calderón. Spin qubit manipulation of acceptor bound states in group iv quantum wells. *New Journal of Physics*, 19(4):043027, 2017. (Cited on pages 22 and 49).
- [191] K. C. Nowack, F. H. L. Koppens, Yu. V. Nazarov, and L. M. K. Vandersypen. Coherent control of a single electron spin with electric fields. *Science*, 318(5855):1430–1433, 2007. (Cited on pages 22 and 49).
- [192] S. Nadj-Perge, S. M. Frolov, E. P. A. M. Bakkers, and L. P. Kouwenhoven. Spin-orbit qubit in a semiconductor nanowire. *Nature*, 468(7327):1084–1087, 12 2010. (Cited on page 22).
- [193] András Pályi, P. R. Struck, Mark Rudner, Karsten Flensberg, and Guido Burkard. Spin-orbit-induced strong coupling of a single spin to a nanomechanical resonator. *Phys. Rev. Lett.*, 108:206811, May 2012. (Cited on page 22).
- [194] Denis V. Bulaev and Daniel Loss. Electric dipole spin resonance for heavy holes in quantum dots. *Phys. Rev. Lett.*, 98:097202, Feb 2007. (Cited on page 22).
- [195] P. Szumniak, S. Bednarek, B. Partoens, and F. M. Peeters. Spin-orbit-mediated manipulation of heavy-hole spin qubits in gated semiconductor nanodevices. *Phys. Rev. Lett.*, 109:107201, Sep 2012. (Cited on page 22).
- [196] R Winkler, Dimitrie Culcer, S J Papadakis, B Habib, and M Shayegan. Spin orientation of holes in quantum wells. *Semiconductor Science and Technology*, 23(11):114017, 2008. (Cited on page 22).
- [197] Dimitrie Culcer, C. Lechner, and R. Winkler. Spin precession and alternating spin polarization in spin-3/2 hole systems. *Phys. Rev. Lett.*, 97:106601, Sep 2006. (Cited on page 22).
- [198] G.L. Bir, E.I. Butikov, and G.E. Pikus. Spin and combined resonance on acceptor centres in Ge and Si type crystals I. *Journal of Physics and Chemistry of Solids*, 24(12):1467 – 1474, 1963. (Cited on pages 22, 23, 26, 49, and 50).

- [199] G.L. Bir, E.I. Butikov, and G.E. Pikus. Spin and combined resonance on acceptor centres in Ge and Si type crystals II. *Journal of Physics and Chemistry of Solids*, 24(12):1475 – 1486, 1963. (Cited on pages 22, 23, 26, 49, and 50).
- [200] Rusko Ruskov and Charles Tahan. On-chip cavity quantum phonodynamics with an acceptor qubit in silicon. *Phys. Rev. B*, 88:064308, Aug 2013. (Cited on pages 22 and 41).
- [201] B. Eble, C. Testelin, P. Desfonds, F. Bernardot, A. Balocchi, T. Amand, A. Miard, A. Lemaître, X. Marie, and M. Chamarro. Hole-nuclear spin interaction in quantum dots. *Phys. Rev. Lett.*, 102:146601, Apr 2009. (Cited on page 22).
- [202] P. Fallahi, S. T. Yılmaz, and A. Imamoglu. Measurement of a heavy-hole hyperfine interaction in ingaas quantum dots using resonance fluorescence. *Phys. Rev. Lett.*, 105:257402, Dec 2010. (Cited on page 22).
- [203] E. A. Chekhovich, A. B. Krysa, M. S. Skolnick, and A. I. Tartakovskii. Direct measurement of the hole-nuclear spin interaction in single InP/GaInP quantum dots using photoluminescence spectroscopy. *Phys. Rev. Lett.*, 106:027402, Jan 2011. (Cited on page 22).
- [204] C. Testelin, F. Bernardot, B. Eble, and M. Chamarro. Hole-spin dephasing time associated with hyperfine interaction in quantum dots. *Phys. Rev. B*, 79:195440, May 2009. (Cited on page 22).
- [205] Jan Fischer, W. A. Coish, D. V. Bulaev, and Daniel Loss. Spin decoherence of a heavy hole coupled to nuclear spins in a quantum dot. *Phys. Rev. B*, 78:155329, Oct 2008. (Cited on page 22).
- [206] E. A. Chekhovich, M. M. Glazov, A. B. Krysa, M. Hopkinson, P. Senellart, A. Lemaitre, M. S. Skolnick, and A. I. Tartakovskii. Element-sensitive measurement of the hole-nuclear spin interaction in quantum dots. *Nat Phys*, 9(2):74–78, 02 2013. (Cited on page 22).
- [207] Christophe Jean Delerue and Michel Lanoo. *Nanostructures: Theory and Modelling*. Springer-Verlag Berlin Heidelberg, 2004. (Cited on pages 23 and 33).
- [208] J. A. Mol, J. Salfi, J. A. Miwa, M. Y. Simmons, and S. Rogge. Interplay between quantum confinement and dielectric mismatch for ultrashallow dopants. *Phys. Rev. B*, 87:245417, Jun 2013. (Cited on pages 23, 33, and 47).
- [209] Garnett W. Bryant. Hydrogenic impurity states in quantum-well wires. *Phys. Rev. B*, 29:6632–6639, Jun 1984. (Cited on page 23).
- [210] Mikael T. Bjork, Heinz Schmid, Joachim Knoch, Heike Riel, and Walter Riess. Donor deactivation in silicon nanostructures. *Nat Nano*, 4(2):103–107, 02 2009. (Cited on page 23).
- [211] J. Broeckx and J. Vennik. Interpretation of acceptor excitation spectra in uniaxially stressed germanium. *Phys. Rev. B*, 35:6165–6168, Apr 1987. (Cited on pages 23, 27, and 33).
- [212] T H Wang and S T Yen. Electric-dipole transitions between group-iii acceptor states in uniaxially compressed ge. *Journal of Physics: Condensed Matter*, 22(34):345801, 2010. (Cited on pages 23, 27, and 33).

- [213] H. Sellier, G. P. Lansbergen, J. Caro, S. Rogge, N. Collaert, I. Ferain, M. Jurczak, and S. Biesemans. Transport spectroscopy of a single dopant in a gated silicon nanowire. *Phys. Rev. Lett.*, 97:206805, Nov 2006. (Cited on pages 24 and 104).
- [214] Pierre M., Wacquez R., Jehl X., Sanquer M., Vinet M., and Cueto O. Single-donor ionization energies in a nanoscale cmos channel. *Nat Nano*, 5(2):133–137, 02 2010. (Cited on page 24).
- [215] A. M. Yakunin, A. Yu. Silov, P. M. Koenraad, J. H. Wolter, W. Van Roy, J. De Boeck, J.-M. Tang, and M. E. Flatté. Spatial structure of an individual mn acceptor in gaas. *Phys. Rev. Lett.*, 92:216806, May 2004. (Cited on page 24).
- [216] J. Salfi, J. A. Mol, R. Rahman, G. Klimeck, M. Y. Simmons, L. C. L. Hollenberg, and S. Rogge. Spatially resolving valley quantum interference of a donor in silicon. 13:605 EP –, 04 2014. (Cited on page 24).
- [217] A. Baldereschi and Nunzio C. Lipari. Energy levels of direct excitons in semiconductors with degenerate bands. *Phys. Rev. B*, 3:439–451, Jan 1971. (Cited on pages 24 and 50).
- [218] N.O. Lipari and A. Baldereschi. Interpretation of acceptor spectra in semiconductors. *Solid State Communications*, 25(9):665 – 668, 1978. (Cited on pages 24, 27, and 50).
- [219] N.O. Lipari, A. Baldereschi, and M.L.W. Thewalt. Central cell effects on acceptor spectra in Si and Ge. *Solid State Communications*, 33(3):277 – 279, 1980. (Cited on pages 24, 32, and 50).
- [220] M. J. Calderón, Belita Koiller, Xuedong Hu, and S. Das Sarma. Quantum control of donor electrons at the Si–sio₂ interface. *Phys. Rev. Lett.*, 96:096802, Mar 2006. (Cited on pages 25 and 28).
- [221] M. J. Calderón, J. Verduijn, G. P. Lansbergen, G. C. Tettamanzi, S. Rogge, and Belita Koiller. Heterointerface effects on the charging energy of the shallow D^- ground state in silicon: Role of dielectric mismatch. *Phys. Rev. B*, 82:075317, Aug 2010. (Cited on pages 25 and 33).
- [222] Y. Sun, S. E. Thompson, and T. Nishida. Physics of strain effects in semiconductors and metal-oxide-semiconductor field-effect transistors. *Journal of Applied Physics*, 101(10):104503, 2007. (Cited on pages 26, 27, 32, and 37).
- [223] Andreas Köpf and Kurt Lassmann. Linear stark and nonlinear zeeman coupling to the ground state of effective mass acceptors in silicon. *Phys. Rev. Lett.*, 69:1580–1583, Sep 1992. (Cited on pages 26, 32, 38, 39, 46, and 60).
- [224] A. Baldereschi and Nunzio O. Lipari. Cubic contributions to the spherical model of shallow acceptor states. *Phys. Rev. B*, 9:1525–1539, Feb 1974. (Cited on page 27).
- [225] D. B. Tran Thoai, R. Zimmermann, M. Grundmann, and D. Bimberg. Image charges in semiconductor quantum wells: Effect on exciton binding energy. *Phys. Rev. B*, 42:5906–5909, Sep 1990. (Cited on page 29).
- [226] D. V. Ushakov and V. K. Kononenko. Calculation of energy characteristics for Si_{1-x}Ge_xSi structures with single quantum wells. *Journal of Applied Spectroscopy*, 78(1):59–68, 2011. (Cited on page 30).

- [227] Lianfeng Yang, Jeremy R Watling, Richard C W Wilkins, Mirela Borici, John R Barker, Asen Asenov, and Scott Roy. Si/SiGe heterostructure parameters for device simulations. *Semiconductor Science and Technology*, 19(10):1174, 2004. (Cited on page 30).
- [228] Q. X. Zhao and M. Willander. Theoretical investigation of shallow acceptors confined in Si/Si_{1-x}Ge_x quantum well structures. *Journal of Applied Physics*, 86(10):5624–5629, 1999. (Cited on page 30).
- [229] N. Fraj, I. Saidi, S. Ben Radhia, and K. Boujdaria. Band structures of alas, gap, and SiGe alloys: A 30 $k \times p$ model. *Journal of Applied Physics*, 102(5), 2007. (Cited on page 30).
- [230] S. E. Thompson, Guangyu Sun, Youn Sung Choi, and T. Nishida. Uniaxial-process-induced strained-Si: extending the CMOS roadmap. *IEEE Transactions on Electron Devices*, 53(5):1010–1020, May 2006. (Cited on pages 32 and 37).
- [231] A.F. Kovalenko, E.N. Sovyak, and M.F. Holovko. Quantum properties of a hydrogen-like particle near a hard wall. *Electrochimica Acta*, 36(11):1711 – 1713, 1991. (Cited on page 33).
- [232] A. L. Saraiva, J. Salfi, J. Bocquel, B. Voisin, S. Rogge, Rodrigo B. Capaz, M. J. Calderón, and Belita Koiller. Donor wave functions in si gauged by stm images. *Phys. Rev. B*, 93:045303, Jan 2016. (Cited on page 47).
- [233] S. Nadj-Perge, S. M. Frolov, E. P. A. M. Bakkers, and L. P. Kouwenhoven. Spin-orbit qubit in a semiconductor nanowire. *Nature*, 468(7327):1084–1087, 12 2010. (Cited on page 49).
- [234] Y. Kato, R. C. Myers, D. C. Driscoll, A. C. Gossard, J. Levy, and D. D. Awschalom. Gigahertz electron spin manipulation using voltage-controlled g-tensor modulation. *Science*, 299(5610):1201–1204, 2003. (Cited on page 49).
- [235] R. Maurand, X. Jehl, D. Kotekar-Patil, A. Corna, H. Bohuslavskyi, R. Laviéville, L. Hutin, S. Barraud, M. Vinet, M. Sanquer, and S. De Franceschi. A CMOS silicon spin qubit. *Nature Communications*, 7:13575 EP –, 11 2016. (Cited on pages 49 and 104).
- [236] N. Ares, G. Katsaros, V. N. Golovach, J. J. Zhang, A. Prager, L. I. Glazman, O. G. Schmidt, and S. De Franceschi. SiGe quantum dots for fast hole spin rabi oscillations. *Applied Physics Letters*, 103(26):263113, 2013. (Cited on pages 49, 54, and 55).
- [237] B. Voisin, R. Maurand, S. Barraud, M. Vinet, X. Jehl, M. Sanquer, J. Renard, and S. De Franceschi. Electrical control of g-factor in a few-hole silicon nanowire mosfet. *Nano Letters*, 16(1):88–92, 2016. (Cited on page 49).
- [238] M. V. Fischetti and S. E. Laux. Band structure, deformation potentials, and carrier mobility in strained Si, Ge, and SiGe alloys. *Journal of Applied Physics*, 80(4):2234–2252, 1996. (Cited on page 60).
- [239] A. P. Higginbotham, T. W. Larsen, J. Yao, H. Yan, C. M. Lieber, C. M. Marcus, and F. Kuemmeth. Hole spin coherence in a ge/si heterostructure nanowire. *Nano Letters*, 14(6):3582–3586, 2014. (Cited on page 60).
- [240] Dimitrie Culcer and Neil M. Zimmerman. Dephasing of si singlet-triplet qubits due to charge and spin defects. *Applied Physics Letters*, 102(23):232108, 2013. (Cited on page 60).

- [241] J. C. Abadillo-Uriel, Joe Salfi, Xuedong Hu, Sven Rogge, M. J. Calderón, and Dimitrie Culcer. Fully tunable coherence and control of acceptor qubits in si. *arXiv:1706.08858*, 2017. (Cited on page 63).
- [242] Mircea Trif, Vitaly N. Golovach, and Daniel Loss. Spin dynamics in inas nanowire quantum dots coupled to a transmission line. *Phys. Rev. B*, 77:045434, Jan 2008. (Cited on page 63).
- [243] Christoph Kloeffel, Mircea Trif, Peter Stano, and Daniel Loss. Circuit qed with hole-spin qubits in ge/si nanowire quantum dots. *Phys. Rev. B*, 88:241405, Dec 2013. (Cited on page 63).
- [244] Dimitrie Culcer, Xuedong Hu, and S. Das Sarma. Dephasing of si spin qubits due to charge noise. *Applied Physics Letters*, 95(7):073102, 2009. (Cited on pages 75 and 86).
- [245] J. C. Abadillo-Uriel, Brandur Thorgrimsson, Dohun Kim, L. W. Smith, C. B. Simmons, Daniel R. Ward, Ryan H. Foote, J. Corrigan, D. E. Savage, M. G. Lagally, M. J. Calder on, S. N. Coppersmith, M. A. Eriksson, and Mark Friesen. Tunable energy dispersion in si quantum dot qubits with atomic-scale disorder. *In preparation*, 2018. (Cited on page 89).
- [246] O. E. Dial, M. D. Shulman, S. P. Harvey, H. Bluhm, V. Umansky, and A. Yacoby. Charge noise spectroscopy using coherent exchange oscillations in a singlet-triplet qubit. *Phys. Rev. Lett.*, 110:146804, Apr 2013. (Cited on pages 89, 96, and 99).
- [247] K. D. Petersson, J. R. Petta, H. Lu, and A. C. Gossard. Quantum coherence in a one-electron semiconductor charge qubit. *Phys. Rev. Lett.*, 105:246804, Dec 2010. (Cited on pages 89 and 99).
- [248] Dimitrie Culcer, Łukasz Cywiński, Qiuzi Li, Xuedong Hu, and S. Das Sarma. Realizing singlet-triplet qubits in multivalley Si quantum dots. *Phys. Rev. B*, 80:205302, Nov 2009. (Cited on page 89).
- [249] M. O. Nestoklon, L. E. Golub, and E. L. Ivchenko. Spin and valley-orbit splittings in SiGe/Si heterostructures. *Phys. Rev. B*, 73:235334, Jun 2006. (Cited on page 89).
- [250] Neerav Kharche, Marta Prada, Timothy B. Boykin, and Gerhard Klimeck. Valley splitting in strained silicon quantum wells modeled with 2° miscuts, step disorder, and alloy disorder. *App. Phys. Lett.*, 90(9):092109, 2007. (Cited on page 89).
- [251] John King Gamble, M. A. Eriksson, S. N. Coppersmith, and Mark Friesen. Disorder-induced valley-orbit hybrid states in Si quantum dots. *Phys. Rev. B*, 88:035310, Jul 2013. (Cited on pages 89, 92, 95, 96, and 113).
- [252] Niklas Rohling, Maximilian Russ, and Guido Burkard. Hybrid spin and valley quantum computing with singlet-triplet qubits. *Phys. Rev. Lett.*, 113:176801, Oct 2014. (Cited on page 89).
- [253] Péter Boross, Gábor Széchenyi, Dimitrie Culcer, and András Pályi. Control of valley dynamics in silicon quantum dots in the presence of an interface step. *Phys. Rev. B*, 94:035438, Jul 2016. (Cited on page 89).
- [254] John King Gamble, Patrick Harvey-Collard, N. Tobias Jacobson, Andrew D. Baczewski, Erik Nielsen, Leon Maurer, Inès Montaña, Martin Rudolph, M. S. Carroll, C. H. Yang, A. Rossi, A. S. Dzurak, and Richard P. Muller. Valley splitting

- of single-electron Si MOS quantum dots. *App. Phys. Lett.*, 109(25):253101, 2016. (Cited on page 89).
- [255] Teck Seng Koh, S. N. Coppersmith, and Mark Friesen. High-fidelity gates in quantum dot spin qubits. *Proc. Nat. Acad. Sci.*, 110(49):19695–19700, 2013. (Cited on page 89).
- [256] Dohun Kim, Zhan Shi, C. B. Simmons, D. R. Ward, J. R. Prance, Teck Seng Koh, John King Gamble, D. E. Savage, M. G. Lagally, Mark Friesen, S. N. Coppersmith, and Mark A. Eriksson. Quantum control and process tomography of a semiconductor quantum dot hybrid qubit. *Nature*, 511(7507):70–74, 07 2014. (Cited on page 89).
- [257] E. Ferraro, M. De Michielis, G. Mazzeo, M. Fanciulli, and E. Prati. Effective hamiltonian for the hybrid double quantum dot qubit. *Quantum Information Processing*, 13(5):1155–1173, May 2014. (Cited on page 89).
- [258] M De Michielis, E Ferraro, M Fanciulli, and E Prati. Universal set of quantum gates for double-dot exchange-only spin qubits with intradot coupling. *J. Phys. A: Mathematical and Theoretical*, 48(6):065304, 2015. (Cited on page 89).
- [259] Gang Cao, Hai-Ou Li, Guo-Dong Yu, Bao-Chuan Wang, Bao-Bao Chen, Xiang-Xiang Song, Ming Xiao, Guang-Can Guo, Hong-Wen Jiang, Xuedong Hu, and Guo-Ping Guo. Tunable hybrid qubit in a GaAs double quantum dot. *Phys. Rev. Lett.*, 116:086801, Feb 2016. (Cited on page 89).
- [260] Clement H. Wong. High-fidelity ac gate operations of a three-electron double quantum dot qubit. *Phys. Rev. B*, 93:035409, Jan 2016. (Cited on page 89).
- [261] Bao-Bao Chen, Bao-Chuan Wang, Gang Cao, Hai-Ou Li, Ming Xiao, Guang-Can Guo, Hong-Wen Jiang, Xuedong Hu, and Guo-Ping Guo. Spin blockade and coherent dynamics of high-spin states in a three-electron double quantum dot. *Phys. Rev. B*, 95:035408, Jan 2017. (Cited on page 89).
- [262] Brandur Thorgrimsson, Dohun Kim, Yuan-Chi Yang, L. W. Smith, C. B. Simmons, Daniel R. Ward, Ryan H. Foote, J. Corrigan, D. E. Savage, M. G. Lagally, Mark Friesen, S. N. Coppersmith, and M. A. Eriksson. Extending the coherence of a quantum dot hybrid qubit. *npj Quantum Information*, 3(1):32, 2017. (Cited on pages 89, 92, 98, and 99).
- [263] Dohun Kim, Daniel R Ward, Christie B Simmons, Don E Savage, Max G Lagally, Mark Friesen, Susan N Coppersmith, and Mark A Eriksson. High-fidelity resonant gating of a silicon-based quantum dot hybrid qubit. *Npj Quantum Information*, 1:15004 EP –, 10 2015. (Cited on pages 90 and 99).
- [264] C. H. Yang, A. Rossi, R. Ruskov, N. S. Lai, F. A. Mohiyaddin, S. Lee, C. Tahan, G. Klimeck, A. Morello, and A. S. Dzurak. Spin-valley lifetimes in a silicon quantum dot with tunable valley splitting. *Nature Communications*, 4:2069, 06 2013. (Cited on page 91).
- [265] Shiue-yuan Shiau, Sucismita Chutia, and Robert Joynt. Valley kondo effect in silicon quantum dots. *Phys. Rev. B*, 75:195345, May 2007. (Cited on page 92).
- [266] Xian Wu, D. R. Ward, J. R. Prance, Dohun Kim, John King Gamble, R. T. Mohr, Zhan Shi, D. E. Savage, M. G. Lagally, Mark Friesen, S. N. Coppersmith, and M. A. Eriksson. Two-axis control of a singlet–triplet qubit with an integrated micromagnet. *Proc. Nat. Acad. Sci.*, 111(33):11938–11942, 2014. (Cited on page 96).

- [267] D. Vion, A. Aassime, A. Cottet, P. Joyez, H. Pothier, C. Urbina, D. Esteve, and M. H. Devoret. Manipulating the quantum state of an electrical circuit. *Science*, 296(5569):886–889, 2002. (Cited on page 99).
- [268] J. M. Taylor, V. Srinivasa, and J. Medford. Electrically protected resonant exchange qubits in triple quantum dots. *Phys. Rev. Lett.*, 111:050502, Jul 2013. (Cited on page 99).
- [269] J. Medford, J. Beil, J. M. Taylor, E. I. Rashba, H. Lu, A. C. Gossard, and C. M. Marcus. Quantum-dot-based resonant exchange qubit. *Phys. Rev. Lett.*, 111:050501, Jul 2013. (Cited on page 99).
- [270] Jianjia Fei, Jo-Tzu Hung, Teck Seng Koh, Yun-Pil Shim, S. N. Coppersmith, Xuedong Hu, and Mark Friesen. Characterizing gate operations near the sweet spot of an exchange-only qubit. *Phys. Rev. B*, 91:205434, May 2015. (Cited on page 99).
- [271] M. D. Reed, B. M. Maune, R. W. Andrews, M. G. Borselli, K. Eng, M. P. Jura, A. A. Kiselev, T. D. Ladd, S. T. Merkel, I. Milosavljevic, E. J. Pritchett, M. T. Rakher, R. S. Ross, A. E. Schmitz, A. Smith, J. A. Wright, M. F. Gyure, and A. T. Hunter. Reduced sensitivity to charge noise in semiconductor spin qubits via symmetric operation. *Phys. Rev. Lett.*, 116:110402, Mar 2016. (Cited on page 99).
- [272] Frederico Martins, Filip K. Malinowski, Peter D. Nissen, Edwin Barnes, Saeed Fallahi, Geoffrey C. Gardner, Michael J. Manfra, Charles M. Marcus, and Ferdinand Kuemmeth. Noise suppression using symmetric exchange gates in spin qubits. *Phys. Rev. Lett.*, 116:116801, Mar 2016. (Cited on page 99).
- [273] Yun-Pil Shim and Charles Tahan. Charge-noise-insensitive gate operations for always-on, exchange-only qubits. *Phys. Rev. B*, 93:121410, Mar 2016. (Cited on page 99).
- [274] E. Dupont-Ferrier, B. Roche, B. Voisin, X. Jehl, R. Wacquez, M. Vinet, M. Sanquer, and S. De Franceschi. Coherent coupling of two dopants in a Silicon nanowire probed by Landau-Zener-Stückelberg interferometry. *Phys. Rev. Lett.*, 110:136802, Mar 2013. (Cited on page 104).
- [275] H. Sellier, G. P. Lansbergen, J. Caro, S. Rogge, N. Collaert, I. Ferain, M. Jurczak, and S. Biesemans. Subthreshold channels at the edges of nanoscale triple-gate silicon transistors. *Applied Physics Letters*, 90(7):073502, 2007. (Cited on page 104).
- [276] M. Fernando Gonzalez-Zalba, Sergey N. Shevchenko, Sylvain Barraud, J. Robert Johansson, Andrew J. Ferguson, Franco Nori, and Andreas C. Betz. Gate-sensing coherent charge oscillations in a silicon field-effect transistor. *Nano Letters*, 16(3):1614–1619, 2016. (Cited on pages 104 and 105).
- [277] A. C. Betz, M. L. V. Tagliaferri, M. Vinet, M. Broström, M. Sanquer, A. J. Ferguson, and M. F. Gonzalez-Zalba. Reconfigurable quadruple quantum dots in a silicon nanowire transistor. *Applied Physics Letters*, 108(20):203108, 2016. (Cited on page 104).
- [278] Andrea Corna, Leo Bourdet, Romain Maurand, Alessandro Crippa, Dharmraj Kotekar-Patil, Heorhii Bohuslavskiy, Romain Lavieville, Louis Hutin, Sylvain Barraud, Xavier Jehl, Maud Vinet, Silvano De Franceschi, Yann-Michel Niquet, and Marc Sanquer. Electrically driven electron spin resonance mediated by spin-orbit coupling in a silicon quantum dot. *arXiv preprint cond-mat:1708.02903*, 2017. (Cited on pages 104, 113, and 116).

- [279] COMSOL. Comsol multiphysics reference manual, version 5.3. (Cited on page 105).
- [280] John David Jackson. *Classical electrodynamics*. Wiley, New York, NY, 3rd ed. edition, 1999. (Cited on pages 107, 108, and 111).
- [281] J. C. Abadillo-Uriel, Belita Koiller, and M. J. Calderón. 2-dimensional semiconductors pave the way towards dopant based quantum computing. *arXiv:1801.02222*, 2018. (Cited on page 119).
- [282] Takahiro Shinada, Shintaro Okamoto, Takahiro Kobayashi, and Iwao Ohdomari. Enhancing semiconductor device performance using ordered dopant arrays. *Nature*, 437(7062):1128–1131, 2005. (Cited on page 119).
- [283] Andrea Morello, Jarryd J. Pla, Floris A. Zwanenburg, Kok W. Chan, Kuan Y. Tan, Hans Huebl, Mikko Mottonen, Christopher D. Nugroho, Changyi Yang, Jessica A. van Donkelaar, Andrew D. C. Alves, David N. Jamieson, Christopher C. Escott, Lloyd C. L. Hollenberg, Robert G. Clark, and Andrew S. Dzurak. Single-shot readout of an electron spin in silicon. *Nature*, 467(7316):687–691, 10 2010. (Cited on page 120).
- [284] M. F. Gonzalez-Zalba, André Saraiva, María J. Calderón, Dominik Heiss, Belita Koiller, and Andrew J. Ferguson. An exchange-coupled donor molecule in silicon. *Nano Letters*, 14(10):5672–5676, 2014. (Cited on page 120).
- [285] S. Freer, S. Simmons, A. Laucht, J.T. Muhonen, J.P. Dehollain, R. Kalra, F.A. Mohiyaddin, F. Hudson, K.M. Itoh, J.C. McCallum, D.N. Jamieson, A.S. Dzurak, and A. Morello. A single-atom quantum memory in silicon. *arXiv:1608.07109*. (Cited on page 120).
- [286] M Fernando Gonzalez-Zalba, Dominik Heiss, and Andrew J Ferguson. A hybrid double-dot in silicon. *New Journal of Physics*, 14(2):023050, 2012. (Cited on page 120).
- [287] M. Abanto, L. Davidovich, Belita Koiller, and R. L. de Matos Filho. Quantum computation with doped silicon cavities. *Phys. Rev. B*, 81:085325, Feb 2010. (Cited on page 120).
- [288] Kin Fai Mak, Changgu Lee, James Hone, Jie Shan, and Tony F. Heinz. Atomically thin mos₂: A new direct-gap semiconductor. *Phys. Rev. Lett.*, 105:136805, Sep 2010. (Cited on page 120).
- [289] P. Pflugradt, L. Matthes, and F. Bechstedt. Silicene-derived phases on Ag(111) substrate versus coverage: *Ab initio* studies. *Phys. Rev. B*, 89:035403, Jan 2014. (Cited on page 120).
- [290] Andres Castellanos-Gomez. Why all the fuss about 2D semiconductors? *Nat Photon*, 10(4):202–204, 04 2016. (Cited on pages 120 and 127).
- [291] K.S. Novoselov, A. Mishchenko, A. Carvalho, and A.H. Castro-Neto. 2D materials and van der Waals heterostructures. *Science*, 353:6298, 2016. (Cited on page 120).
- [292] R. Roldán, L. Chirolli, E. Prada, J.A. Silva-Guillén, P. San-Jose, and F. Guinea. Theory of 2D crystals: graphene and beyond. 2017. *arXiv:1703.07200*. (Cited on page 120).
- [293] A. K. Geim and I. V. Grigorieva. Van der Waals heterostructures. *Nature*, 499(7459):419–425, 07 2013. (Cited on page 120).

- [294] Riccardo Frisenda, Efren Navarro-Moratalla, Patricia Gant, David Perez De Lara, Pablo Jarillo-Herrero, Roman V. Gorbachev, and Andres Castellanos-Gomez. Recent progress in the assembly of nanodevices and van der Waals heterostructures by deterministic placement of 2D materials. *Chem. Soc. Rev.*, pages –, 2018. (Cited on page 120).
- [295] Zhong Lin, Bruno R Carvalho, Ethan Kahn, Ruitao Lv, Rahul Rao, Humberto Terrones, Marcos A Pimenta, and Mauricio Terrones. Defect engineering of two-dimensional transition metal dichalcogenides. *2D Materials*, 3(2):022002, 2016. (Cited on page 120).
- [296] Simin Feng, Zhong Lin, Xin Gan, Ruitao Lv, and Mauricio Terrones. Doping two-dimensional materials: ultra-sensitive sensors, band gap tuning and ferromagnetic monolayers. *Nanoscale Horiz.*, 2:72–80, 2017. (Cited on page 120).
- [297] Pierluigi Cudazzo, Ilya V. Tokatly, and Angel Rubio. Dielectric screening in two-dimensional insulators: Implications for excitonic and impurity states in graphane. *Phys. Rev. B*, 84:085406, Aug 2011. (Cited on page 121).
- [298] Thomas Olsen, Simone Latini, Filip Rasmussen, and Kristian S. Thygesen. Simple screened Hydrogen model of excitons in two-dimensional materials. *Phys. Rev. Lett.*, 116:056401, Feb 2016. (Cited on page 121).
- [299] Jia-Lin Zhu and Jia-Jiong Xiong. Hydrogen molecular ions in two dimensions. *Phys. Rev. B*, 41:12274–12277, Jun 1990. (Cited on page 123).
- [300] Wolfram Research, Inc. Mathematica, Version 11.2. Champaign, IL, 2017. (Cited on pages 125 and 140).
- [301] M. Fabbri and A. Ferreira da Silva. Variational calculation of the two-dimensional H_2 molecule. *Phys. Rev. A*, 32:1870–1872, Sep 1985. (Cited on page 125).
- [302] Jia-Lin Zhu, Xi Chen, and Jia-Jiong Xiong. Hydrogen molecules in two dimensions. *Journal of Physics: Condensed Matter*, 3(47):9559, 1991. (Cited on page 125).
- [303] W. J. Hehre, R. F. Stewart, and J. A. Pople. Self-consistent molecular, orbital methods. I. Use of Gaussian expansions of Slater, type Atomic Orbitals. *The Journal of Chemical Physics*, 51(6):2657–2664, 1969. (Cited on page 125).
- [304] Diana Y. Qiu, Felipe H. da Jornada, and Steven G. Louie. Optical spectrum of MoS_2 : Many-body effects and diversity of exciton states. *Phys. Rev. Lett.*, 111:216805, Nov 2013. (Cited on page 127).
- [305] Youngki Yoon, Kartik Ganapathi, and Sayeef Salahuddin. How good can monolayer MoS_2 transistors be? *Nano Letters*, 11(9):3768–3773, 2011. PMID: 21790188. (Cited on page 127).
- [306] Elton J. G. Santos and Efthimios Kaxiras. Electrically driven tuning of the dielectric constant in MoS_2 layers. *ACS Nano*, 7(12):10741–10746, 2013. (Cited on page 127).
- [307] Lu Hua Li, Elton J. G. Santos, Tan Xing, Emmanuele Cappelluti, Rafael Roldán, Ying Chen, Kenji Watanabe, and Takashi Taniguchi. Dielectric screening in atomically thin Boron Nitride nanosheets. *Nano Letters*, 15(1):218–223, 2015. (Cited on pages 127 and 128).

-
- [308] Pere Miro, Martha Audiffred, and Thomas Heine. An atlas of two-dimensional materials. *Chem. Soc. Rev.*, 43:6537–6554, 2014. (Cited on pages 126 and 127).
- [309] Di Wu, Alexander J. Pak, Yingnan Liu, Yu Zhou, Xiaoyu Wu, Yihan Zhu, Min Lin, Yu Han, Yuan Ren, Hailin Peng, Yu-Hao Tsai, Gyeong S. Hwang, and Keji Lai. Thickness-dependent dielectric constant of few-layer In_2Se_3 nanoflakes. *Nano Letters*, 15(12):8136–8140, 2015. (Cited on page 126).
- [310] Zeyuan Ni, Qihang Liu, Kechao Tang, Jiaxin Zheng, Jing Zhou, Rui Qin, Zhengxiang Gao, Dapeng Yu, and Jing Lu. Tunable bandgap in Silicene and Germanene. *Nano Letters*, 12(1):113–118, 2012. (Cited on pages 127 and 128).
- [311] Jie Ma, Zhi Gen Yu, and Yong-Wei Zhang. Tuning deep dopants to shallow ones in 2D semiconductors by substrate screening: The case of x_s ($X = \text{Cl}, \text{Br}, \text{I}$) in mos_2 . *Phys. Rev. B*, 95:165447, Apr 2017. (Cited on page 127).
- [312] N. D. Drummond, V. Zólyomi, and V. I. Falkó. Electrically tunable band gap in silicene. *Phys. Rev. B*, 85:075423, Feb 2012. (Cited on page 128).